UNIVERSITY OF BIRMINGHAM

Thermally Induced Sensitisation of Austenitic Stainless Steel for AGR Fuel Cladding

SIBEN JIANG

A thesis submitted for the degree of:

DOCTOR OF PHILOSOPHY

December 2018

School of Metallurgy and Materials
University of Birmingham
United Kingdom
B15 2TT

Preface

This research was carried out by Siben Jiang in School of Metallurgy and Materials, University of Birmingham (from September 2014 to September 2018), under the supervision of Dr. Yu-Lung Chiu and Dr. Brian Connolly.

The work is original and no part has been submitted for another degree at any other university. Wherever other researchers' work has been drawn from or cited, this is acknowledged in the text and the references are listed.

Acknowledgements

I would like to express my sincerest thanks to my supervisor, Dr. Yu-Lung Chiu, for his continual guidance and tutelage throughout this PhD. His patience and enthusiasm have inspired me to achieve more than I thought possible. I would also like to thank my former supervisor, Dr. Brian Connolly who is based in University of Manchester, for his comprehensive help, especially in the early stage of my PhD. I would also like to thank Prof. Ian Jones who is very knowledgeful and kind, for reading the whole thesis and giving useful comments that massively help to step over the final hurdle of the thesis.

I would like to thank all the experimental technicians who have trained me on equipment throughout this project: Mr. Paul Stanley and Mrs. Theresa Morris. I would also like to thank Dr. Christopher Cooper for his help in the early stage of this PhD, and Prof. Alison Davenport for providing the potentiostat to carry out the electrochemical tests, and Dr. Mary Taylor for providing the 20/25/Nb model alloys.

I am grateful to my numerous colleagues from the electron microscopy group who have provided me with many meaningful discussions and have helped me solve many problems during my PhD. I am also thankful to the many friends that I have made throughout my time in Birmingham who have always made time for me.

Finally, I would like to express my sincerest thanks to my family for their continued love and support. I am especially grateful to my mother and my wife who have always supported me throughout my studies.

Abstract

In this thesis, the sensitisation behaviour of thermally treated Advanced Gas-cooled Reactor (AGR) fuel cladding, a Nb stabilised 20 wt.%Cr/25 wt.%Ni (20/25/Nb) austenitic stainless steel was investigated. Three model alloys containing different silicon concentrations (0, 0.56, and 2.25 wt.% Si, termed alloys A, alloy B and alloy C, respectively) and an end cap commercial AGR fuel cladding alloy (termed alloy D) were studied. To produce a sensitised microstructure, all 20/25/Nb samples were solution annealed at 1050 °C for 30 minutes with subsequent ageing at 650 °C for a range of times from 10 minutes to 200 hours. Chromium depletion was measured by Scanning Transmission Electron Microscopy-Energy Dispersive Spectroscopy (STEM-EDS) on samples prepared by twin-jet polishing and Focused Ion Beam (FIB). The degree of sensitisation (DOS) was measured by Double Loop-Electrochemical Potentiokinetic Reactivation (DL-EPR) test followed by surface morphology characterisation using a Scanning Electron Microscope (SEM). The grain boundary misorientation angles were measured by Electron Back-Scattered Diffraction (EBSD).

Silicon bearing alloys exhibit more severe grain boundary chromium depletion during the sensitisation stage while less chromium depletion during the desensitisation stage than the silicon free alloy, and the addition of silicon decreases the time needed to reach the maximum chromium depletion. This might be because silicon increases the diffusion coefficient of chromium atom in austenitic stainless steel. The morphology of sensitised samples after the DL-EPR test are in agreement with the magnitude of chromium depletion at the grain boundary. Whereas, the DOS values and surface morphology obtained from the DL-EPR test show that the effect of silicon on sensitisation is not evident.

In alloy D, an annealing temperature of 930 °C would not produce any chromium depletion or sensitisation at grain boundaries, even after a subsequent ageing of 200 hours at 650 °C. In a sample of alloy D annealed at 1050 °C followed by 24 hours ageing at 650 °C, chromium concentration at grain boundary is about 12.0 wt.%, which is similar to the chromium depletion reported in neutron irradiated AGR fuel cladding. Thus, the sensitisation of neutron irradiated cladding during the post-storage in cooling pond can to some extent be studied by investigating the thermally sensitised cladding, consequently, avoid handling high dose radioactive material.

After the DL-EPR test, low angle grain boundaries (LAGBs) and coincidence site lattice (CSL) Σ3 boundaries are found to be mostly free from attack while the majority of the random high angle grain boundaries (HAGBs) are attacked and the extent of attack depended on the magnitude of chromium depletion at the grain boundary. There exists a threshold grain boundary misorientation angle below which grain boundaries are immune to intergranular attack while grain boundaries with a misorientation higher than this angle are subject to attack and the extent of attack varies from grain boundary to grain boundary. Grain boundary attack starts when the chromium concentration is around 13 wt.% to 14 wt.% and substantial attack occurs when the chromium concentration is less than 12.0 wt.%. At individual random HAGBs, the magnitude of chromium depletion is the key factor affecting sensitisation, rather than the misorientation angle. No obvious relationship is found between the extent of attack and the misorientation angle for random HAGBs, which might be because the misorientation is not the only factor that affect the extent of attack.

Contents

1 Introduction

1.1 Background

Sustainable and affordable energy is regarded as a crucial aspect of global economic prosperity and societal stability. Nuclear energy has been widely exploited across the world over the past 60 years since the first commercial nuclear power plant built in 1956. In 2018, there are 455 reactors operating, which account for 10.5% global electricity generation, 55 reactors under construction [1]. In the UK, 15 reactors generate about 8.9 GW, accounting for 21 % of its electricity in the country but almost half of this capacity is to be retired by 2025 [2]. These reactors include seven twin-unit AGR stations, one pressurized water reactor (PWR). Global warming, which is induced by greenhouse gas emissions, has become a regular topic of international environmental conferences. Nuclear energy has very low carbon emission and therefore increasing the proportion of nuclear power can reduce the consumption of fossil fuel, which is the major source of carbon dioxide emission, and fulfil the global electricity demand in the meantime [3,4].

The UK's second-generation gas-cooled commercial nuclear power plants were developed in the 70s and 80s and the seven AGRs operating in the UK will be decommissioned by 2030 [2]. The AGR reactors have been the backbone of the UK's nuclear energy generation fleet since the 1980s. They use graphite as the neutron moderator and carbon dioxide as the coolant. The mean temperature of the hot coolant leaving the reactor core was designed to be 650 °C [5]. Figure 1-1 is a typical configuration of an AGR fuel element. The fuel element is made up of 34 fuel pins that are held together in a stainless steel support grid and supported by a central brace and a top brace. The grids and braces are held in a graphite

sleeve. Each fuel pin consists of 64 enriched uranium-dioxide (UO_2) pellets with a central bore, encapsulated into the stainless steel cladding. The ^{235}U level in ceramic UO_2 fuel is enriched to 2.5-3.5%, depending on the fuel design and target burn-up. The enriched fuel allows higher neutron losses to the stainless steel cladding which is made from higher neutron absorption cross section elements compared with PWR zirconium fuel cladding [6]. During the operation of an AGR, the outlet temperature reaches around 635 °C at the top of the core, where the coolant gas exits to supply the boilers. The inlet temperature of the coolant gas is about 340 °C [6]. The key operating features of an AGR are shown in Table 1-1. The spent fuel elements are routinely discharged from the reactor core then stored in cooling ponds, initially at the stations and then, following an initial cooling period, to a longer-term storage cooling pond as shown in Figure 1-2.

Table 1-1 Summary of key design of advanced gas-cooled reactor [6].

Generation	Fuel material	Moderator	Coolant	Cladding	Inlet and outlet temperature	Pressure
II	enriched UO_2	Graphite	CO_2	Austenitic stainless steel	340 °C, 635 °C	4 MPa

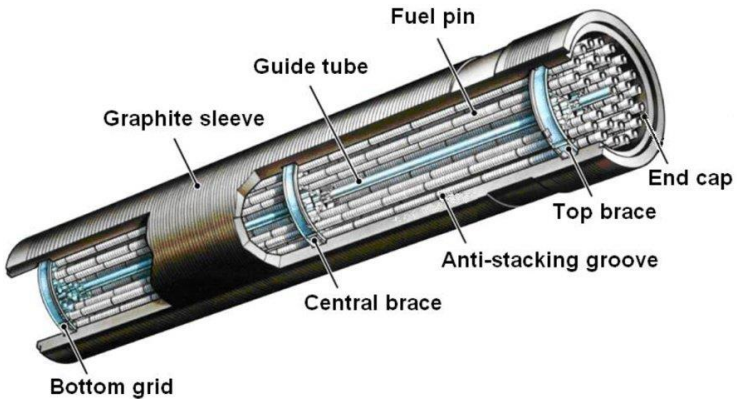

Figure 1-1 Fuel element of advanced gas-cooled reactor [7].

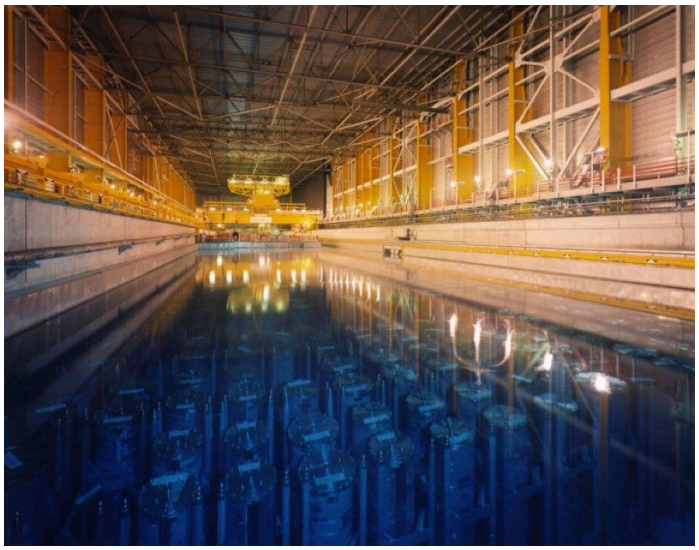

Figure 1-2 Thorp receipt and storage pond at Sellafield [7].

The structural materials in a reactor core are exposed to an extremely harsh environment due to the combination of high temperature, stress, corrosive coolant and, especially, intense neutron irradiation. Thus, good physical, mechanical and corrosion properties and neutron radiation resistance are required for reactor core materials. Lots of nuclear structural material research, in terms of neutron irradiation, has been conducted both at fission and fusion energies [6,8–10]. Energetic neutrons, released by the uranium fuel fission reaction, bombard the lattice atoms of the structural material and impart energy to the lattice atoms, forcing them leave their lattice positions to form point defects, such as vacancies and interstitials. The migration of point defects towards defect sinks such as grain boundaries can cause chromium to move away from the grain boundary to the matrix, which is explained by the inverse Kirkendall (IK) effect [11,12]. The grain boundary will then become vulnerable to intergranular corrosion when it is exposed to a corrosive environment. This process is termed irradiation induced sensitisation. In an AGR, the irradiation induced sensitisation on fuel cladding material caused by irradiation induced chromium depletion at grain boundaries, has been observed for many years. Although the

sensitisation affects a small proportion of the fuel pins, it leads them to be susceptible to intergranular attack when the fuel elements are extracted from the reactor and stored in cooling ponds if physical and chemical conditions are not optimised during the storage. [13,14]

Examining highly radioactive samples irradiated by neutrons needs dedicated testing equipment in shielded experimental facilities, such as hot cell and post-irradiation test equipment, which are costly and time consuming. In order to provide sensitised and low radioactive samples that can be easily examined in general laboratory to illuminate the problems related to sensitised materials, there is a perceived need for relevant and representative means to replicate sensitisation in the stainless steel other than by neutron irradiation. Energetic particles, including protons, electrons and heavy ions, had been used for many years to study a wide range of radiation damage, especially fundamental irradiation damage theories, on much shorter timescales and with low induced radioactivity [15,16]. Proton irradiation has been used to simulate neutron radiation induced segregation (RIS) and its feasibility has been verified by Was et al. [17] by analysing sensitised 304 and 316 stainless steel. The RIS of AGR fuel cladding has been studied by Norris et al. [18–20] in the 1980s. However, an irradiation facility was not accessible for the research in this thesis, therefore a thermal sensitisation method was applied to replicate the behaviours of chromium depletion and sensitisation induced by neutron irradiation on AGR fuel cladding material.

1.2 Arrangement of chapters

In Chapter 1, the research background is briefly introduced and the organisation of this thesis is sketched. In Chapter 2, relevant reported work up to date is reviewed, including:

1) overview of sensitisation on AGR fuel cladding, 2) mechanism of sensitisation, 3) factors affecting sensitisation which mainly focus on the silicon effect and grain boundary misorientation effect, 4) methods to investigate sensitisation and 5) a summary of literature review and objectives of this research. In Chapter 3, the materials and heat treatments are introduced. Research techniques applied in this research are described in detail, including microstructure characterisation, electrochemical testing and elemental segregation analysis at grain boundaries. In Chapters 4, 5 and 6, the obtained results are presented and then discussed thoroughly by referring to the relevant literature, including: 1) silicon effect on chromium depletion at the grain boundary and sensitisation, 2) thermally induced sensitisation behaviour of alloy D, 3) the correlation of grain boundary misorientation angle, chromium depletion and sensitisation of individual grain boundaries. Conclusions are outlined and future work after this thesis is suggested in Chapter 7.

2 Literature Review

Fuel cladding stainless steel degrades in the long term in-reactor service when exposed to intensive neutron irradiation. Two kinds of stress corrosion cracking (SCC), namely, irradiation assisted stress corrosion cracking (IASCC) and intergranular stress corrosion cracking (IGSCC), are observed. IASCC and IGSCC are due to the sensitisation of the stainless steel induced by irradiation and thermal treatment, respectively. In terms of the behaviour of sensitisation, both processes are similar [21]. It is widely accepted that chromium depletion at the grain boundary is the primary cause of sensitisation [22], which is induced by chromium carbide formation at the grain boundary for thermal sensitisation [23] and vacancies diffusion towards grain boundary for irradiation sensitisation [24]. When we refer to the word 'sensitisation', a specific definition should be attached: stainless steel becomes vulnerable to grain boundary attack when exposed to aggressive environment due to the depletion of chromium to a critical value (for stainless steel this value is about 12 to 13 wt.% [25,26]) at the grain boundary.

In this chapter, the sensitisation of AGR fuel cladding steel was reviewed to set up the scenario for the whole thesis. Then the mechanism of sensitisation was briefly explained and the characterisation methods were introduced. Factors affecting sensitisation were reviewed, especially the reported work with respect to the effect of silicon on oxidation and elemental diffusion and grain boundary misorientation angle effect on elemental segregation and sensitisation. Finally, the characterisation methods were reviewed.

2.1 Overview of sensitisation on advanced gas-cooled reactor fuel cladding

As UK's second generation of gas-cooled nuclear reactor, AGR has been developed and been in service for decades [27]. The UO_2-ceramic fuel pellets of AGR are encapsulated into fuel cladding which is manufactured of Fe-20%Cr/25%Ni-Nb stabilized austenitic stainless steel (it is termed 20/25/Nb in this thesis) because of its excellent mechanical performance at high-temperature and good ability to maintain the fuel integrity against excessive swelling during the fission reaction [28]. Figure 2-1 shows a section of commercial AGR fuel cladding and its dimensions. The circumferential threads, 0.31 mm tall at every 2.5 mm pitch, on the cladding surface can improve heat transfer with the circulating CO_2 coolant. As fuel cladding is subject to internal stress that's stem from the fuel pellet swelling, intense neutron irradiation and high temperature during the running of the reactor, adverse degradation of the cladding is unavoidable, including mechanical properties, thermal properties, dimensional changes and corrosion susceptibility.

After the removal of the fuel element from an AGR core, the extracted fuel element is stored as spent fuel in a cooling water pond prior to further reprocessing [14]. The fuel cladding has been exposed to neutron irradiation to a high dose level (as it is next to the UO_2 fuel) when it is retracted from the reactor. The diffusion of neutron irradiation induced vacancies towards grain boundaries causes chromium depletion which leads to the sensitisation of the fuel cladding [24]. As direct assessment of the sensitisation of the irradiated AGR fuel cladding material is costly and time consuming, and requires dedicated testing equipment, most of the work on the 20/25/Nb alloy is under thermal sensitisation conditions to simulate the sensitisation induced by in-reactor conditions, such as elemental

segregation at the grain boundary [18–20,29], localised pitting corrosion [30,31], intergranular corrosion [32], intergranular stress corrosion cracking [33], oxidation behaviour [34,35] and susceptibility to creep at elevated temperature [34,36–38].

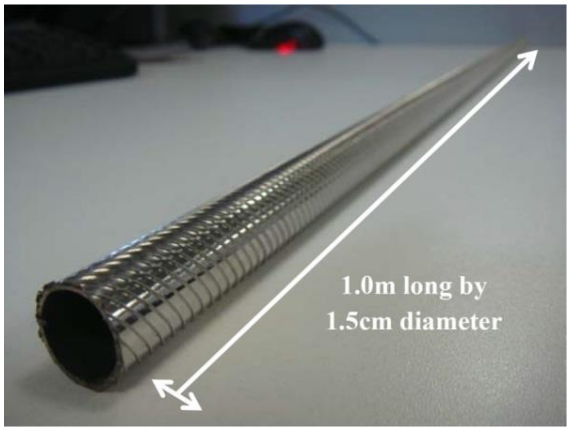

Figure 2-1 A section of commercial AGR fuel cladding tube and its dimensions [39].

2.1.1 Sensitisation of AGR fuel cladding material

In general, for austenitic stainless steel to be resistant to intergranular corrosion, the chromium concentration needs to be higher than 10.5 wt.% [40]. In AGR fuel cladding material, 20 wt.% chromium is higher than many other stainless steels, which gives the alloy remarkable corrosion and oxidation resistance. 0.7 wt.% niobium is doped as a 'stabiliser' to form niobium carbide and improve the resistance to sensitisation and have better creep and structural strength [31]. The addition of a stabiliser can protect material from sensitisation by preventing the formation of intergranular chromium carbides. Niobium, tantalum and titanium can all be used as a 'stabiliser' to remove the carbon in the matrix by forming carbides. For application in a nuclear reactor core, a good neutron economy of the fuel cladding is desirable. As the neutron absorption cross section of Nb is only about 1.150 Barn, which is much lower than that of Ta and Ti (5.6 and 21.0 Barn, respectively), Nb is preferred as stabiliser for fuel cladding in a nuclear reactor [6].

Irradiation induced sensitisation is caused by chromium depletion at the grain boundary, and the chromium depletion is induced by the vacancy diffusion towards the grain boundary (IK effect). A model for simulating the depletion of chromium in Fe-Cr -Ni cladding alloy via the IK mechanism was firstly introduced by Perks et al. [41,42], based on the previous work of Marwick [11]. Later a modified model was proposed by Allen and Was [43] to include the composition dependent migration energies and short-range ordering effects. For predictive purposes, Norris [44] used the width of the chromium depleted zone (i.e., the total width on both sides of the boundary over which the chromium concentration is below 12 wt.%) to show the extent of sensitisation in 20/25/Nb alloy, with a zone width of 4 nm taken as the onset level. Figure 2-2(a) shows the predicted width of chromium depleted zone as a function of temperature at various irradiation levels. Sensitisation was predicted to be most severe at irradiation temperatures between about 380 and 455 °C, with a high temperature cut-off of about 470 °C. It might be because vacancies are immobile and point defects are annihilated by mutual recombination at lower temperatures, and back diffusion and lower vacancy supersaturating at higher temperature supress the chromium depletion at the grain boundary [45]. Figure 2-2(b) shows another interesting result that illustrates the effect of initial dislocation density, with dislocation densities above 10^{13} m^{-2} expected to significantly inhibit sensitisation. As dislocation is the dominant sink of point defects, increasing the initial dislocation density in the alloy can lead to the annihilation of irradiation induced point defects in the matrix resulting in fewer point defects migrate to the grain boundary, consequently, reduce chromium depletion at the grain boundary [46].

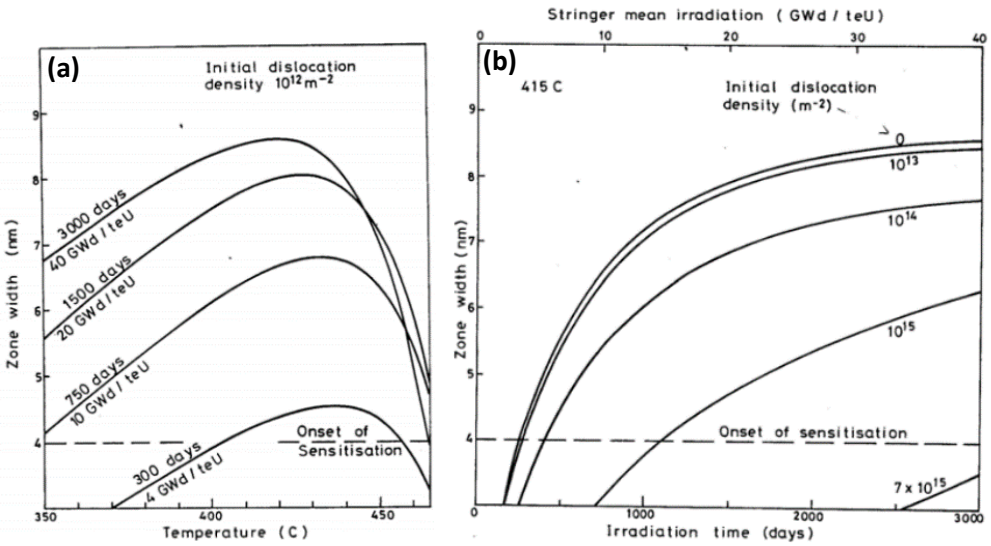

Figure 2-2 Predicted width of chromium depleted zone as a function of (a) irradiation temperature, (b) initial dislocation density irradiated at 415 °C [44] (quoted in [46]).

Norris, et al. [18] studied RIS on neutron irradiated 20/25/Nb alloy which was retrieved from the AGR. They examined, using analytical TEM and Strauss test, the elemental segregation and corrosion on alloy irradiated to various dose levels at different temperatures, taken from different AGRs. Silicon, a fast diffusion element, is enriched at the grain boundary due to the interstitial-solute drag mechanism [45]. Figure 2-3 shows that compositional profiles at the grain boundary become wider but smaller magnitude with increasing irradiation temperature, which might be because of the diffusion rate of atoms is rising at higher temperature. As shown in Figure 2-4, RIS is shown to be alleviated by annealing at 600 °C for 2 hours due to the migration of atoms towards the grain boundary from the matrix during the annealing process. Figure 2-5(a) shows that modified Strauss test results revealed the cladding material within the temperature range 350 °C to 520 °C with the most severe effects at 420 °C. Figure 2-5(b) shows that the depth of attack increases with chromium depleted zone width [18].

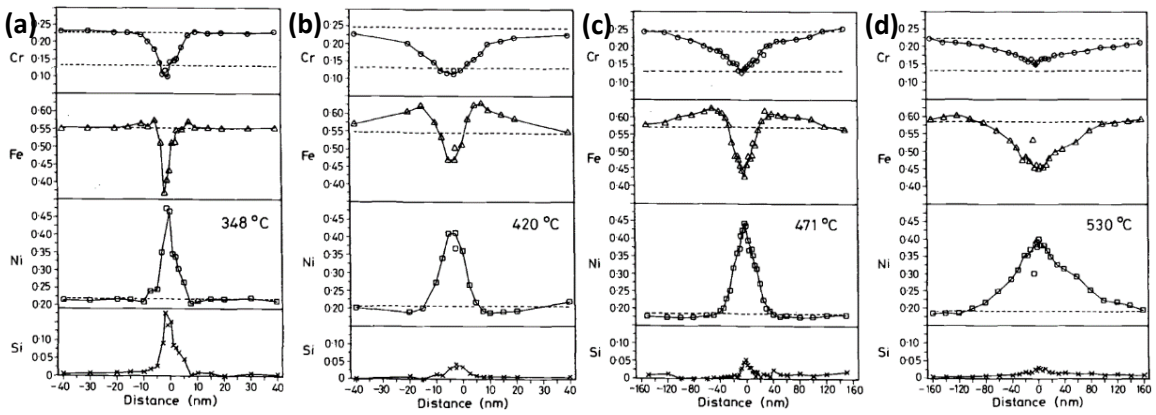

Figure 2-3 Elemental segregation profiles across grain boundaries from four positions along a 20/25/Nb fuel cladding tube retrieved from the reactor at different temperatures: (a) 348 °C, (b) 420 °C, (c) 471 °C and (d) 530 °C [18].

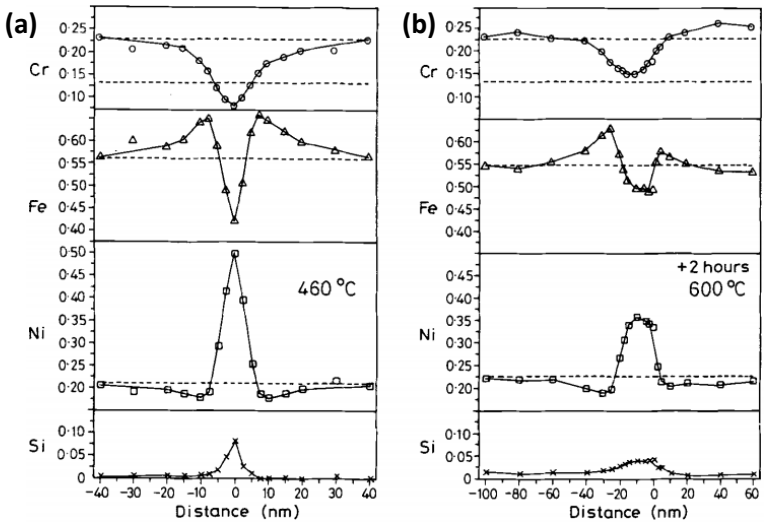

Figure 2-4 The comparison of elemental segregation profiles between (a) as-irradiated and (b) 600 °C annealed 20/25/Nb sample [18].

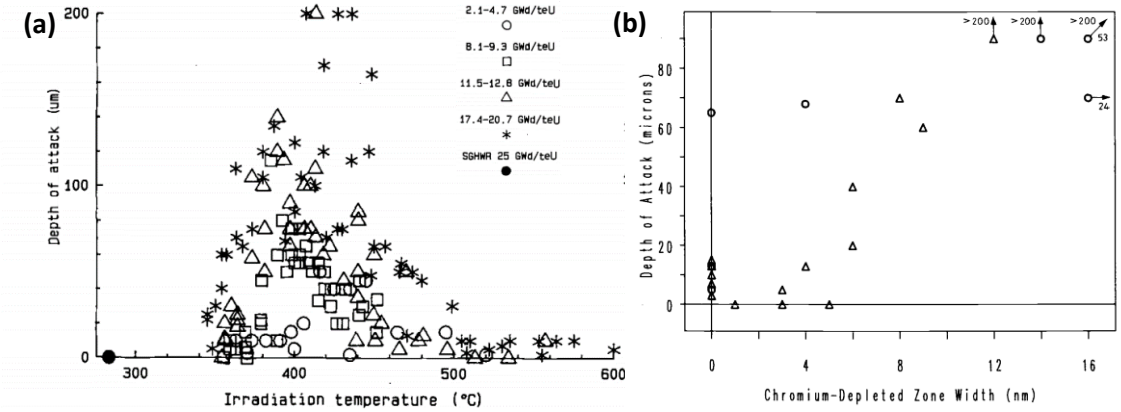

Figure 2-5 Depth of attack measured by Strauss test on 20/25/Nb alloys as a function of: (a) temperature at different burn-ups, (b) chromium-depleted zone width [18].

Ashworth et al. [19] studied the grain boundary segregation behaviour in a commercial 20/25/Nb alloy and a series of model alloys irradiated in a high voltage electron microscope (HVEM) by 1 MeV electrons, at temperatures ranging from 250 °C to 500 °C and dose ranging from 0.6 dpa to 7.2 dpa. They found that grain boundary migration has a strong effect on RIS. Cold work was beneficial in reducing segregation at low dose but not at higher irradiation dose due to the extensive grain boundary migration. As depicted in Figure 2-6, they also found a significant variation of chromium depletion at different grain boundaries, which might be because of the variation of chromium carbides nucleation on the grain boundaries. This extent of chromium depletion scatter is also observed on the thermally sensitised 20/25/Nb alloy in this thesis.

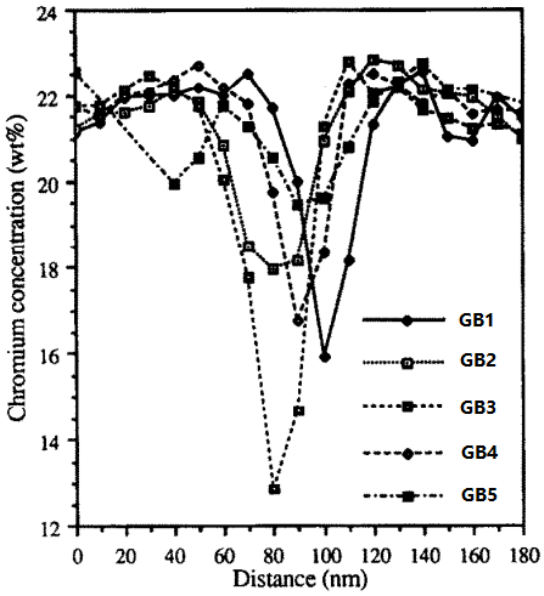

Figure 2-6 The variability of the extent of chromium depletion detected from five grain boundaries in 20/25/Nb/Pd alloy irradiated for 0.6 dpa at 450 °C [19].

As shown in Figure 2-7, Moss and Sykes [32] studied the sensitisation of 20/25/Nb tube material, bar material and reworked bar material heat treated at two different solution annealing temperatures (1050 °C and 1150 °C) using Strauss test and EPR test. In their

work, DOS was characterised by the penetration depth of the Strauss test and the peak current of the EPR test. Figure 2-7(a), which is the Strauss test results on tube samples, shows that ageing at 550 °C produces a delayed increase of DOS. At higher ageing temperatures, 600 °C and 650 °C, the maximum DOS increases when the solution annealing is carried out at 1150 °C. Ageing at 600 °C and 650 °C can produce sensitised samples quickly, even in less than 50 hours. The slow increasing DOS in the 550 °C aged sample might be because the formation of chromium carbides on grain boundaries is slow at lower temperature. Figure 2-7(b), EPR test results obtained from the bar and reworked bar materials, shows that the reworked bar material has a substantially higher EPR peak current due to the difference in thermo-mechanical treatment which leaves higher carbon level in the reworked bar.

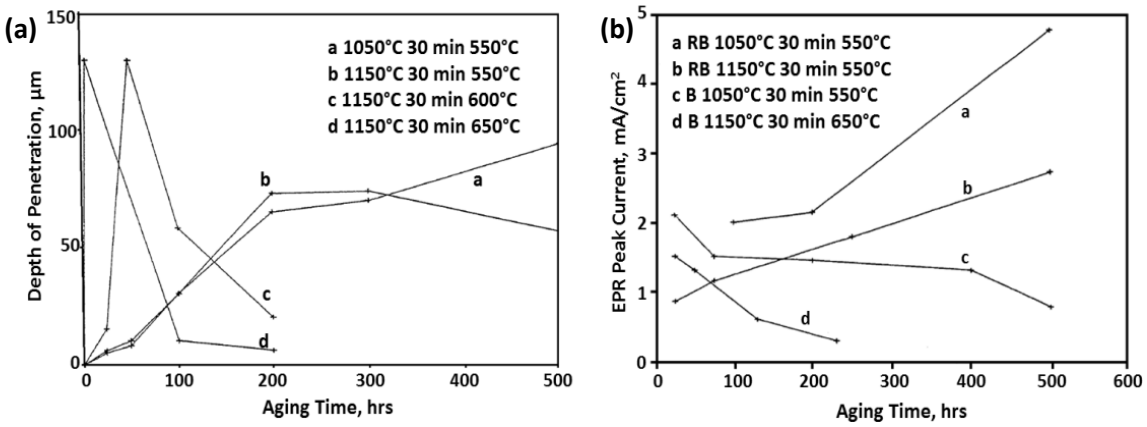

Figure 2-7 Results of (a) Strauss tests on aged AGR tube material and (b) EPR tests on aged AGR reworked bar (RB) and AGR bar (B) [32].

Recently, a preliminary study of chromium depletion profile and IGSCC on AGR fuel cladding material was carried out by Whillock et al. [29]. They found that samples annealed at 1050 °C with subsequent ageing, viz. 550 °C (for 500, 1055 and 1605 hours), 600 °C for 48 hours and 650 °C (for 5 and 1000 hours) led to no crack in the screening test. This might be due to insufficient carbon being released back into the austenite matrix, whereas, in

Moss and Sykes's work [32], substantial susceptibility to intergranular corrosion was detected in 1050 °C annealed samples in Strauss test. This might be because the solution used in screening test in Whillock's work was less aggressive than that in the Strauss test. As shown in Figure 2-8(a) and (b), in 1150 °C solution anneal followed by 600 °C 48 hours aged 20/25/Nb, cracks were found after the screening test due to the chromium depletion at grain boundary (Figure 2-8(c)), which suggests that higher annealing temperature results in more carbon being released back to the matrix.

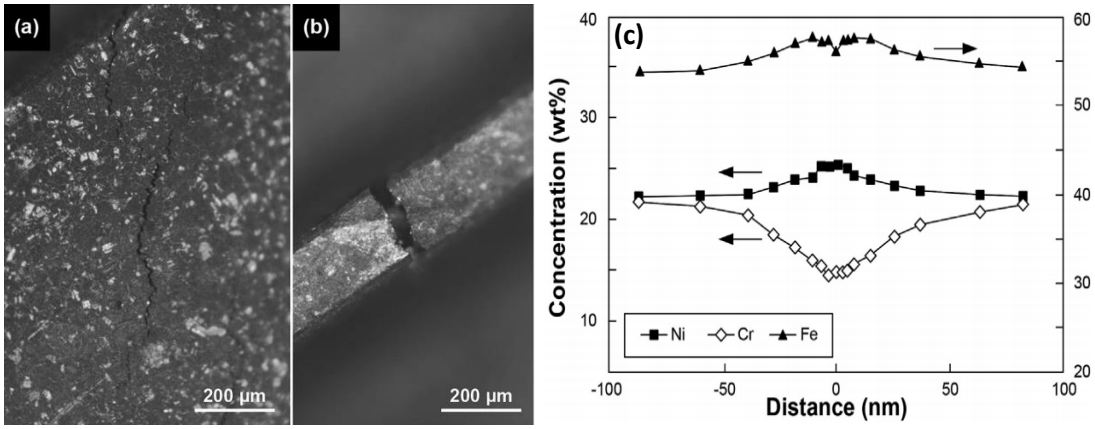

Figure 2-8 Screening test response for 20/25/Nb solution annealed at 1150 °C for 0.5 hour then aged at 600 °C for 48 hours: (a) sample surface, (b) view of rib; (c) is the elemental segregation profiles [29].

Two different types of AGR fuel cladding materials, cylindrical fuel cladding and end cap, was studied by Chan [30]. The samples were all solution annealed at 1200 °C with subsequent ageing at various temperatures from 550 °C to 930 °C, for different times, from 0.8 hour to 1000 hours. Electrochemical corrosion tests were carried out in different testing conditions. Chan suggested that niobium carbide plays a crucial role on in-pond localised corrosion of AGR fuel cladding material. In a neutral pH, large niobium carbides are cathodically active sites which promote the anodic dissolution of the surrounding alloy. The behaviour of large NbC precipitates was also examined in caustic soda solution with pH 11.5. Chan suggested that the NbC precipitates act as anodically active sites and

dissolve preferentially from the surrounding alloy in caustic pH, which was observed in the heat treated samples but not in the as-received material when tested 60 °C. Grain boundary corrosion was also observed on a sensitised end cap sample tested in 10 ppm chloride solution at 50 °C. Chan suggested that the possible reason for the grain boundary attack is that NaOH becomes an etchant for chromium carbides at elevated temperature. He also proposed that a caustic pH has a beneficial effect on long term safe storage of spent AGR fuel due to the dissolution of large NbC precipitate.

Phuah [31] studied the behaviour of NbC precipitates in commercial AGR fuel cladding sourced from Sellafield Ltd. which has been annealed at 1050 °C for 2 hours. The ageing was conducted over a temperature range from 400 °C to 800 °C and a time range from 24 hours to 192 hours. Phuah suggested that NbC precipitates have a critical role in the pitting corrosion process. As shown in Figure 2-9, pitting corrosion was observed to preferentially initiate around NbC precipitates, which was in agreement with the results reported in Chan's work [30]. The geometry of these NbC precipitates were well maintained even though extensive corrosion occurred around them, suggesting that NbC precipitates act as a cathode and is relatively stable to the matrix.

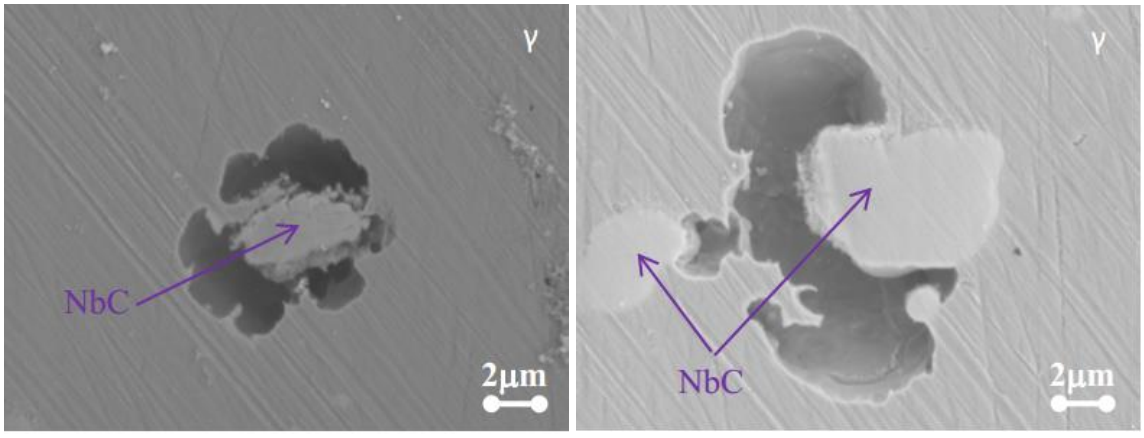

Figure 2-9 The dissolution of alloy surrounding NbC precipitates observed in an AGR fuel cladding sample aged at 800 °C for 192 hours after polarisation [31].

Al-Shater, et al. [33] studied the SCC behaviour of thermally sensitised 20/25/Nb in a simulated cooling pond environment. To simulate the behaviour of sensitised AGR fuel cladding when stored in a post-processing water storage pond environment, in their work, 20/25/Nb samples were solution annealed at 1150 °C for 30 minutes then sensitised at 650 °C for 5 hours (Heat Treatment 1, HT1) and 600 °C for 50 hours (Heat Treatment 2, HT2) and then the samples were assessed for their susceptibility to pitting corrosion and stress corrosion cracking using slow strain rate testing (SSRT) in elevated chloride (10 ppm) neutral pH solution. As shown in Figure 2-10, all samples have the yield strength between 200 and 300 MPa and the elongation varying severely depends on the applied anodic potential. The samples tested at a potential higher than + 200 mV show much lower strain due to higher pit (acting as nucleation sites for SCC initiation) density on the sample surface. Figure 2-11 shows the time required for fracture and the ratios of strain to fracture in a corrosive environment to that in air ($\varepsilon_a/\varepsilon_i$). It shows that the time to fracture (t_f) and the elongations after both heat treatments suddenly drop by 4 or 5 times when the anodic potential is higher than + 200 mV which is because of the increased pit density on the sample fracture surface and flanks when the anodic potential is higher than + 200 mV. By examining the fracture surface after the SSRT, they found that in samples tested in the potential range from + 100 mV to + 200 mV the ductile fracture was indicated by the presence of micro-void coalescence in the form of dimples. Thus, a potential of + 200 mV was suggested as the threshold potential for the initiation of IGSCC in 10 ppm chloride solution at 80 °C. They also found that the pitting potential was between + 375 mV and + 400 mV when samples were tested in 10 ppm chloride solution at 80 °C.

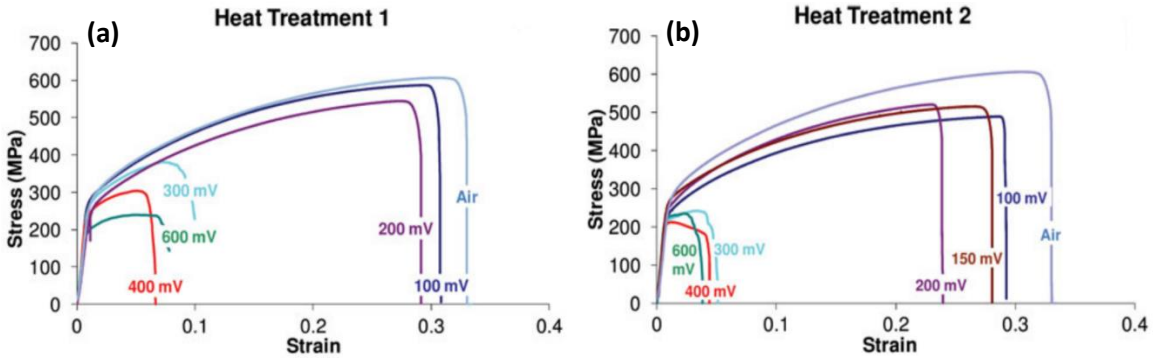

Figure 2-10 Stress-strain behaviour of samples polarised in 10 ppm chloride at 80 °C at + 100 to + 600 mV (SCE) during SSRT: (a) sensitised at 650 °C for 5 hours (HT1), (b) sensitised at 600 °C for 50 hours (HT2) [33].

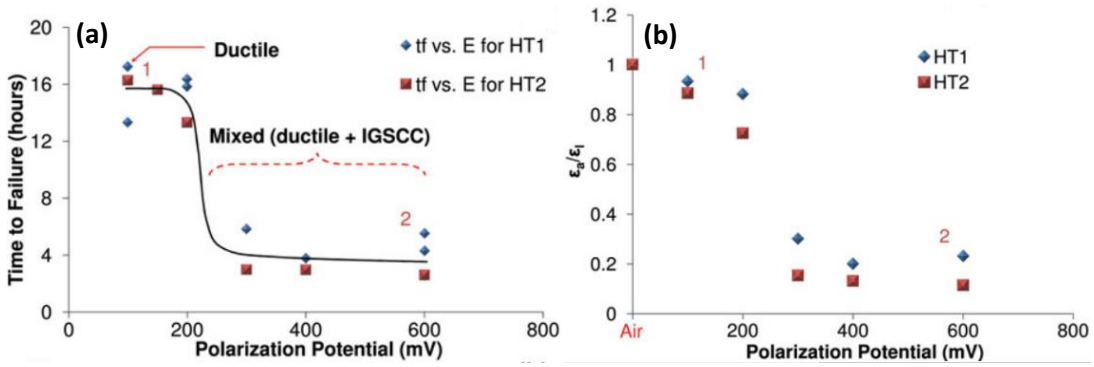

Figure 2-11 (a) Time to failure (t_f), (b) the ratio of strain of fracture in a corrosive environment vs. in air as a function of anodic potential during SSRT at 80 °C [33].

2.1.2 The consequences of sensitisation of AGR fuel cladding

Sensitisation of the AGR fuel cladding austenitic stainless steel due to the depletion of chromium at grain boundaries is caused by intense fission neutron irradiation [47]. During in-reactor service, AGR fuel cladding must not show any intergranular attack and maintain integrity, otherwise it will be disastrous. The capture of carbon from carbon dioxide coolant might make the depletion of chromium on the cladding surface more serious. After being extracted from the reactor, the spent-fuel elements which have been partly sensitised during the service are nominally stored in a demineralised water pond. During the pond storage, the consequences of sensitisation on AGR fuel cladding are closely inspected and well

reported. The first ever failures of AGR fuel cladding was found on fuel elements that had been discharged from the Windscale advanced gas-cooled reactor (WAGR) in 1974, which was stored under dry condition via dry storage route [48]. It had been proposed that the failure was a result of the attack of sensitised grain boundaries by nitric acid produced by radiolysis of moist air. As shown in Figure 2-12, broad front attack was also observed during the pond storage, which was because of the poor pond condition, such as poorly demineralised water, increased chloride concentration and a dramatic pH drop to as low as 4 [49]. Since the introduction of caustic dosing water to a target pH of 11.4, the broad front attack never happened again. Intergranular attack has been regarded as the only mode of attack during pond storage [50].

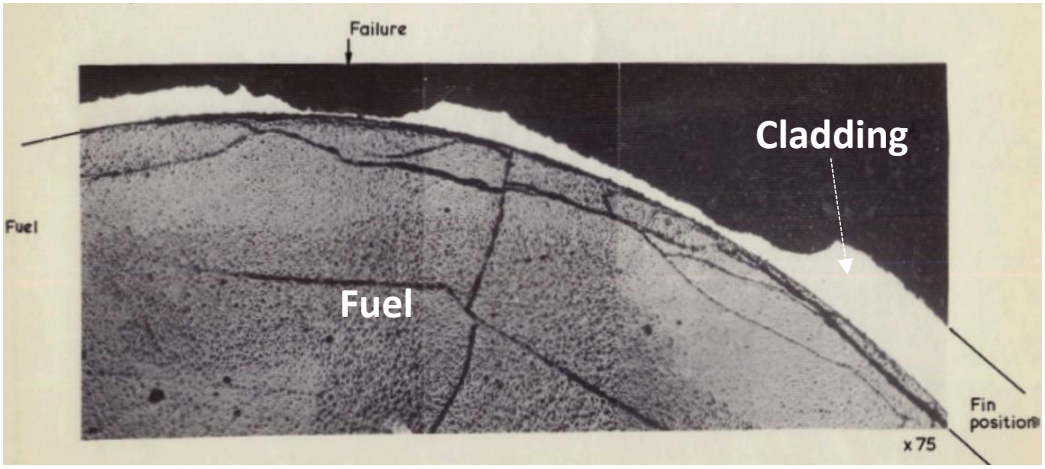

Figure 2-12 A cross-section through a fuel pellet and its cladding to show the broad front attack of AGR fuel cladding during the pond storage [51].

Figure 2-13, which shows the morphology of an AGR fuel cladding section (380 μm in width) retracted from the reactor and stored in the storage pond, features the intergranular attack exhibiting different morphologies depending on exposure circumstances. Figure 2-13(a) shows how intergranular attack leads to a network of loose grains with no

associated cracking while, in Figure 2-13(b), IGSCC leads to a deeper penetration of the crack with less overall corrosion.

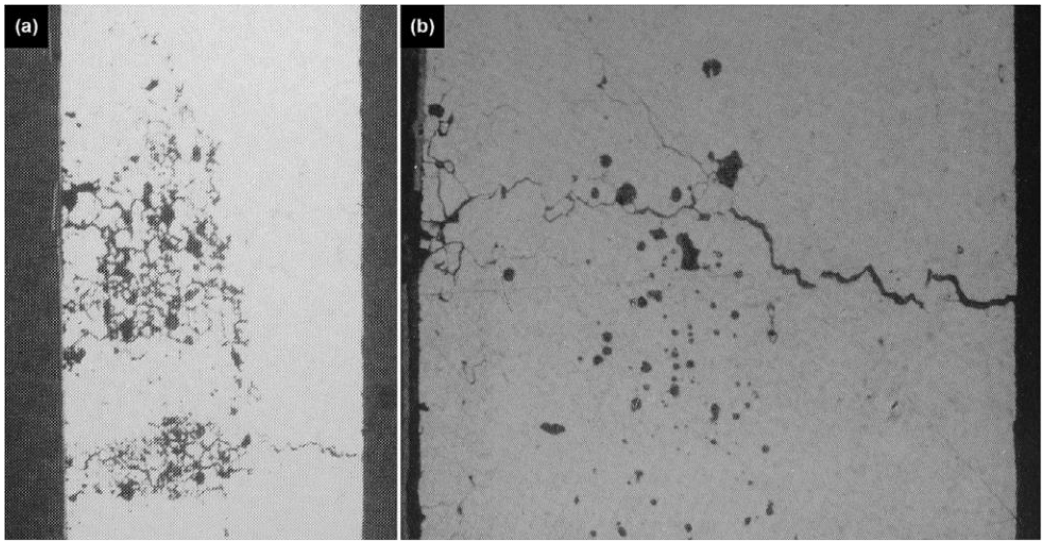

Figure 2-13 Typical morphology of intergranular attack in irradiation induced sensitised AGR fuel cladding, (a) network of loose grains with no associated cracking, (b) a deeper penetration of the crack with less overall corrosion [52].

2.1.3 Precipitates in AGR fuel cladding

Thermally induced sensitisation is because of the formation of chromium carbides at the grain boundary, which causes the depletion of chromium at the chromium carbides-matrix interface and the grain boundary, consequently, leads the alloy susceptible to intergranular corrosion. In solution annealed 20/25/Nb alloy, the carbon used to nucleate chromium carbides is from the niobium carbides which dissolve at high solution annealing temperature. Thus, it is necessary to know the precipitation behaviour in the 20/25/Nb alloy under different heat treatment conditions, especially the formation chromium carbides and niobium carbides.

Powell et al. [53] studied the precipitation characteristics of 20/20/Nb alloy over the ageing temperature range 500 °C – 850 °C and the alloy was treated under two different conditions

before the ageing, (1) annealed at 930 °C for 1 hours, and (2) thermo-mechanical treatment to let dislocation network presents in the alloy. They found that there are four types of precipitates formed at grain boundaries and in the matrix, namely, Nb(CN), $M_{23}C_6$, G-phase and sigma-phase. The time-temperature-precipitation (TTP) diagram of the AGR fuel cladding material was plotted as shown in Figure 2-14 to show the stability of these phase over different time and temperature. The ageing temperature and maximum ageing time applied in this thesis are indicated by a red and black arrow in Figure 2-14 respectively, which shows that the majority of the precipitates present in the 20/25/Nb alloy will be the residual Nb(CN), intergranular $M_{23}C_6$ and G-phase. The characteristics of these precipitates are summarised in Table 2-1.

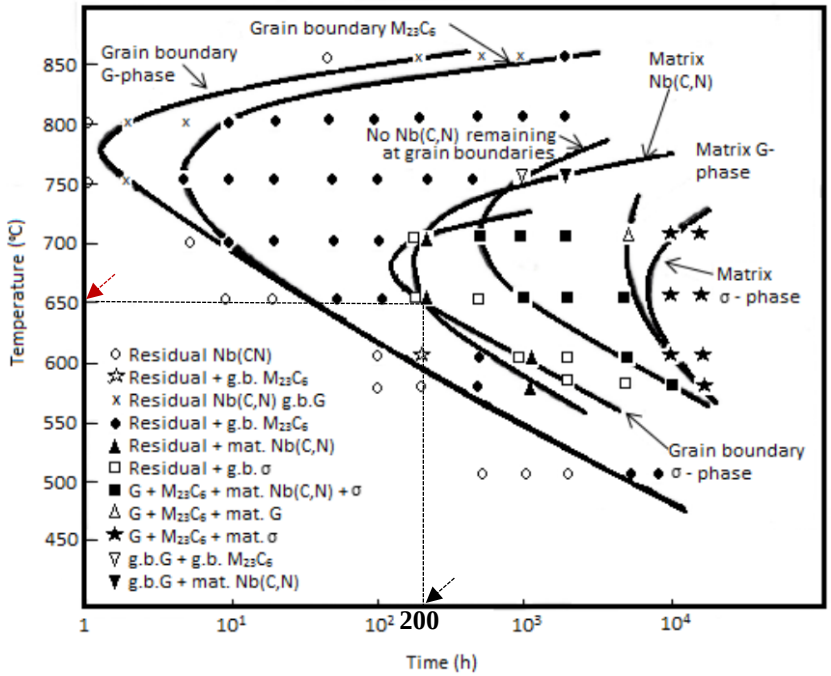

Figure 2-14 Time-temperature-precipitation (TTP) diagram of AGR fuel cladding material [53].

Table 2-1 Precipitates that might present in AGR fuel cladding alloy, modified from [53].

Phase type	Crystal structure	Lattice parameter (Å)	Compositions from EDS analysis (wt.%)	Morphology of the precipitate
Nb(CN)	FCC	4.41	99Nb, 1Ti	Spherical
$M_{23}C_6$	FCC	10.62	83Cr, 16Fe, 1Ni	0.5 µm at the grain boundary
G-phase	cF116 a variant of FCC [54]	11.20	51Ni, 29Nb, 14Si, 4.5Fe, 1.5Cr	Plate-like
Sigma phase	BCT	8.85	48Cr, 42Fe, 8.5Ni, 1.5Si	Blocky angular type phase

Lee et al. [55] studied the dissolution behaviour of NbC in alloy slab as a function of temperature under different heating rates, as shown in Figure 2-15. The solution annealing carried out in this thesis is 1050 °C for 30 minutes with a heating rate close to 0.13 °C/s, which corresponds to the blue curve in Figure 2-15. It shows that part of the NbC precipitates dissolve at 1050 °C. Thus, the dissolution of NbC precipitates at 1050 °C in AGR fuel cladding release carbon back to the matrix, consequently, facilitate the formation of chromium carbides at the grain boundary in the following ageing process, which makes the study of sensitisation behaviour of AGR cladding viable in this thesis.

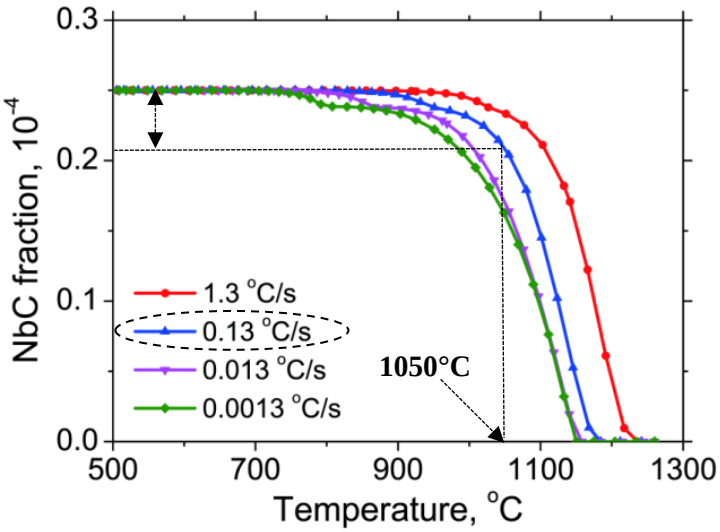

Figure 2-15 Calculated NbC dissolution behaviour for different heating rates [55].

2.2 Mechanism of sensitisation

IASCC has been used to explain the intergranular cracking in heavily irradiated structural material in nuclear reactor core which subsequently shows little or no ductility [56]. IASCC has been considered as one of the most serious degradation phenomena affecting the integrity of the reactor core components and is the major concern for the life span extension of current light water reactors [8,57–59]. From the reported results, irradiation induced sensitisation, localized deformation and irradiation hardening play important roles in IASCC [60–62]. The amount of IASCC increases with neutron damage dose [59]. Both irradiation and thermally induced sensitisation are due to the depletion of chromium at a grain boundary. However, the mechanisms of chromium segregation are different between the two modes of sensitisation [46]. The mechanisms of thermally and irradiation induced sensitisation are reviewed in detail in this section.

2.2.1 Thermally induced sensitisation

It is widely accepted that thermally induced sensitisation in austenitic stainless steel is due to the formation of intergranular chromium carbides, which leads to the depletion of chromium at grain boundaries and causes the material to be susceptible to intergranular corrosion. The carbon content of austenitic stainless steel can be up to 0.15 wt.% which leaves substantial amounts of free solid solution carbon after solution annealing at temperatures >= 1050 °C. The free carbon becomes supersaturated when the steel is cooled rapidly (such as water quenching) from the solution annealing temperature as the carbon solubility in steel is less at lower temperatures. If the supersaturated steel is continuously

heated (aged) in the medium temperature range of 450-850 °C [63], chromium carbides will nucleate along the grain boundaries because of the high diffusion rate of carbon towards the grain boundary, which is several orders of magnitude higher than that of chromium. Compared with carbon, chromium diffuses much slower and leaves the chromium depleted to a level in equilibrium with the growing carbides. It is not just the interface between the chromium carbide and matrix, which becomes chromium depleted, but the grain boundary. Chromium depleted region at the grain boundary causes the material to be sensitised and vulnerable to intergranular corrosion [32,64].

Sensitisation observed in stainless steel has been explained by three major theories, namely noble carbide theory, segregation theory and chromium depletion theory [65]. The first two theories can be used to explain sensitisation in certain conditions, such as the alloy is not in the carbide-sensitised condition or the environment is highly oxidising. The third theory (chromium depletion theory) is the most widely accepted, which can be used to explained the carbide induced sensitisation. Dayal et al. [66] summarized the three theories. Initially, the chromium depletion theory was proposed by Bain et al. [67]. According to this theory, sensitisation is due to the formation of chromium carbide precipitates at the grain boundary, which causes the chromium concentration at the grain boundary area to be depleted to a level below that required for passivation. After a long time of ageing, complete recovery from sensitisation could take place. Self-healing can occur simultaneously with the precipitation of chromium carbides due to chromium migration to the grain boundary from the matrix [68], and it becomes more obvious when all the free carbon has been used up to form chromium carbides.

Sensitisation is normally caused by the depletion of chromium from the grain boundaries in stainless steel induced during welding or an improper heat treatment process [26,69,70]. The alloy becomes vulnerable to corrosion if chromium depleted to less than about 12-13 wt.% [25,26], as the protective passive chromia film at such low chromium concentration is not strong enough to prohibit an attack from an aggressive environment. In the niobium stabilised stainless steel, such as an AGR fuel cladding material, carbon in the matrix is combined with niobium to form NbC precipitates and leave a very low carbon concentration in the bulk material.

Two theories, reaction theory and kinetic theory, to explain thermally induced chromium depletion at grain boundaries in austenitic steel are reviewed in Yin's work [71]. Both theories agree that chromium depletion is because of the nucleation of chromium carbides at grain boundaries in thermally treated austenitic steel. In the reaction theory, the carbon distribution is uniform throughout the bulk matrix and its concentration is the highest before any chromium carbides precipitates nucleate at the grain boundary. Thus, carbon activity is the highest at the beginning (time = 0). As heat treatment is carried out, the nucleation of chromium carbide precipitates takes carbon from the matrix, which causes a decrease of carbon activity due to the decreasing carbon concentration. Thus, the chromium concentration is at the lowest level when the nucleation of chromium carbides at grain boundary starts to initiate. Chromium concentration increases as the carbide precipitation continues, which decreases the carbon activity.

In kinetic theory, the chromium concentration at the grain boundary is determined by the net amount of chromium taken by chromium carbide as chromium diffuses toward the grain boundary from the matrix. Thus, the chromium concentration at the grain boundary

decreases as chromium carbide grows. As shown in Figure 2-16, there is a delay in reaching the minimum chromium concentration at the grain boundary. The time for chromium concentration to reach the minimum is different at different heat treatment temperatures.

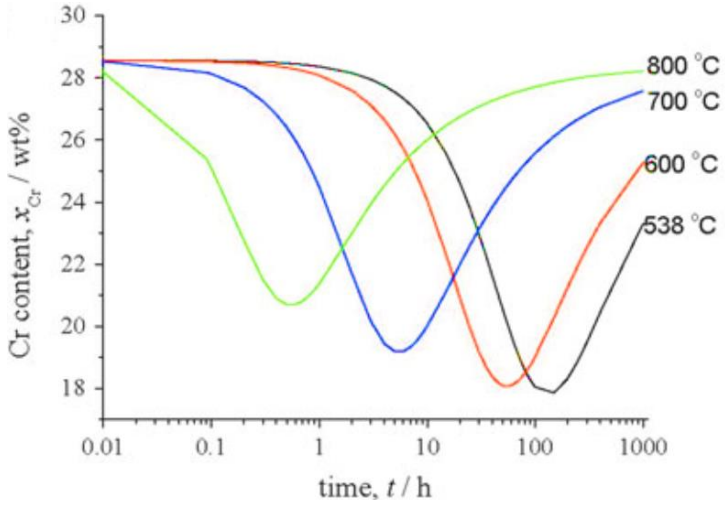

Figure 2-16 A schematic figure to show the minimum chromium concentration at the grain boundary as a function of heat treatment time at different temperatures in the kinetic theory [71].

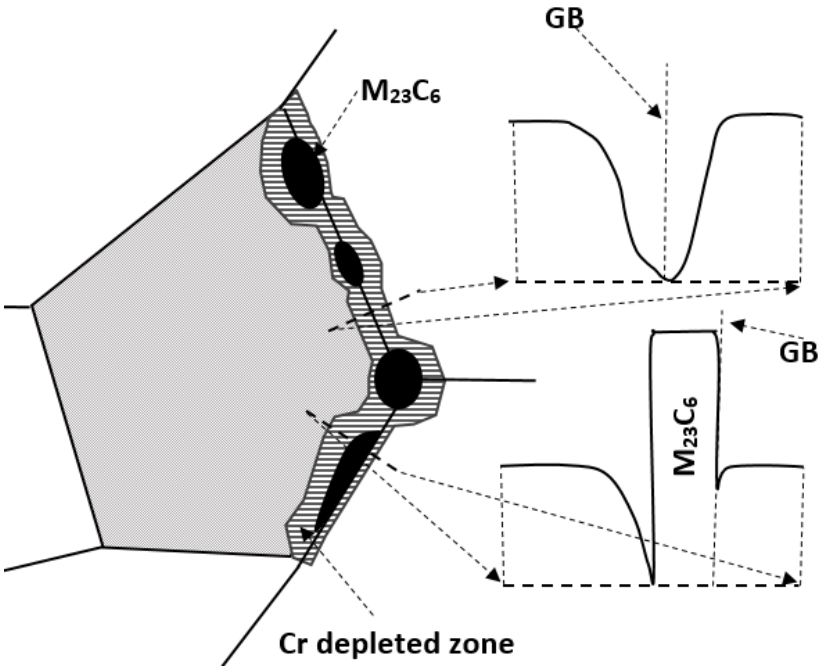

Figure 2-17 Schematic of chromium depletion at the grain boundary due to the growth of chromium carbides.

Figure 2-17 is a schematic drawing of chromium carbide precipitation and chromium depletion profiles. It shows that the extent of chromium depletion at a coherent interface between the carbide and matrix is much lower than the incoherent interface. In thermally sensitised material, grain boundaries become unprotected by a passive film when chromium concentration depleted to a critical value. The exposure of sensitised material to an aggressive environment may cause catastrophic failure. The activated region of low chromium concentration at the grain boundary and the passive matrix form a local electrochemical battery cell with the grain boundary acting as anode and the matrix acting as cathode, as shown in Figure 2-18.

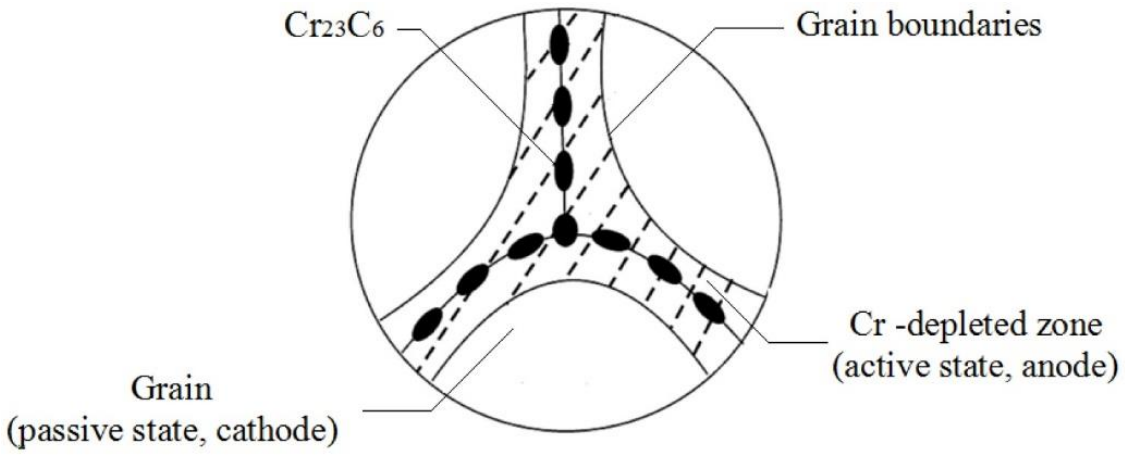

Figure 2-18 Schematic of electrochemical cell involving chromium depleted zone (anode) and passive matrix (cathode) [72].

Chromium depletion at grain boundaries and sensitisation of stainless steels [66,71,73,74] and nickel alloys [75–78] have been widely investigated by experimental and modelling methods [79,80]. Sahlaoui et al. [74] investigated the long time ageing up to 80000 hours at different temperatures including the effect on precipitate evolution, chromium depletion and intergranular corrosion susceptibility of low carbon AISI 316L austenitic stainless steel.

Figure 2-19 shows that chromium carbides form not only intergranularly at incoherent twin boundary and low energy coherent twin boundary stainless steel, but also intragranularly on dislocation networks in low carbon 316L after long time ageing. Figure 2-20(a), which shows the chromium concentration at the carbide-matrix interface, shows that the minimum chromium concentration decreases from 14 wt.% at an ageing temperature of 700 °C to 7 wt.% at 550 °C, which might be because the chromium atoms diffuse quicker towards the interface from the matrix at higher temperature. The ageing time required for chromium to reach the minimum decreases with increasing ageing temperature. Figure 2-20(b) and Figure 2-20(c), which are chromium profiles for samples aged at 550 °C and 600 °C for various long-time scales, show that the width of chromium depletion at the grain boundary increases with both ageing temperature and time. This might be because the increasing ageing temperature and time can add to the diffusion of chromium atoms towards the grain boundary resulting in the broadening of the chromium depletion width. Figure 2-21 is the chromium depletion profile of Inconel 690 aged at different temperatures for various times reported as in the work of Kai et al. [77]. It shows that the minimum chromium concentration at the grain boundary decreases at the beginning and then increases with the increasing ageing time at 538 °C, 600 °C and 700 °C, and the lowest minimum chromium depletion at 700 °C is higher than that at 538 °C and 600 °C, which might be because chromium depletion can be replenished quicker at higher temperature. In the 800 °C aged samples, the minimum chromium concentration increases with ageing time from 1 hour to

10 hours, which suggests that chromium carbides might have stopped growth after 1 hour ageing.

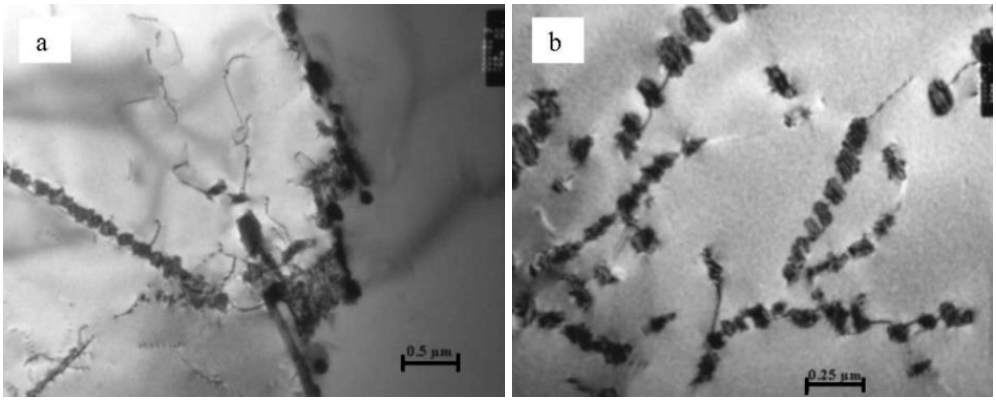

Figure 2-19 Chromium carbides formation in AISI 316L at (a) both coherent and incoherent twin boundaries at 600 °C for 30000 hours, (b) dislocation networks at 550 °C for 80000 hours [74].

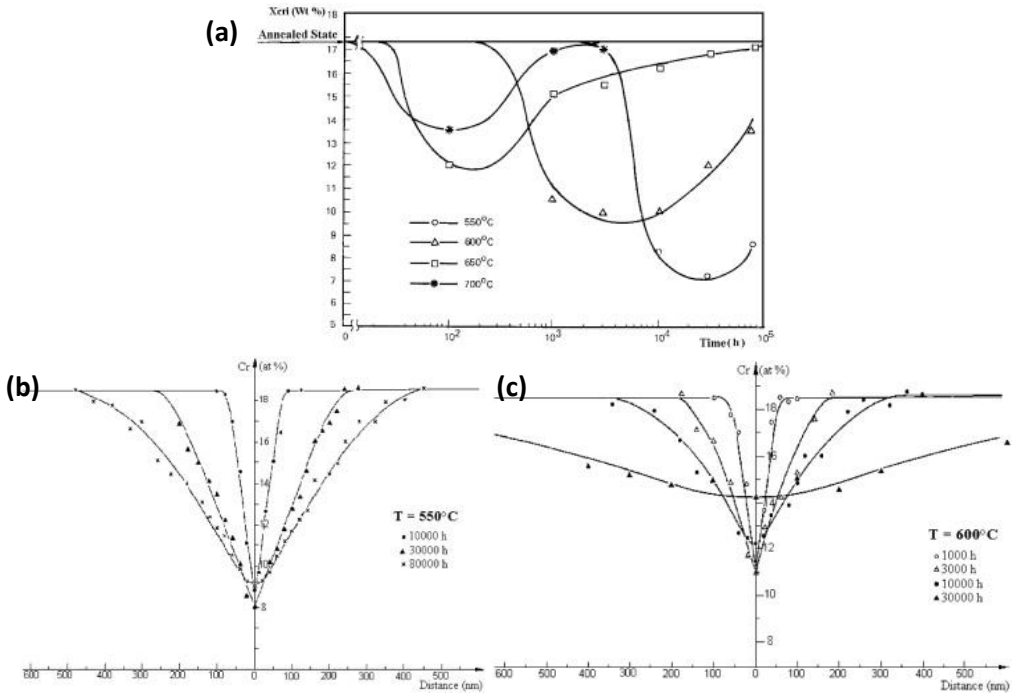

Figure 2-20 Chromium depletion at: (a) chromium carbide-matrix interface, (b) and (c) grain boundaries at 550 °C and 600 °C, respectively [74].

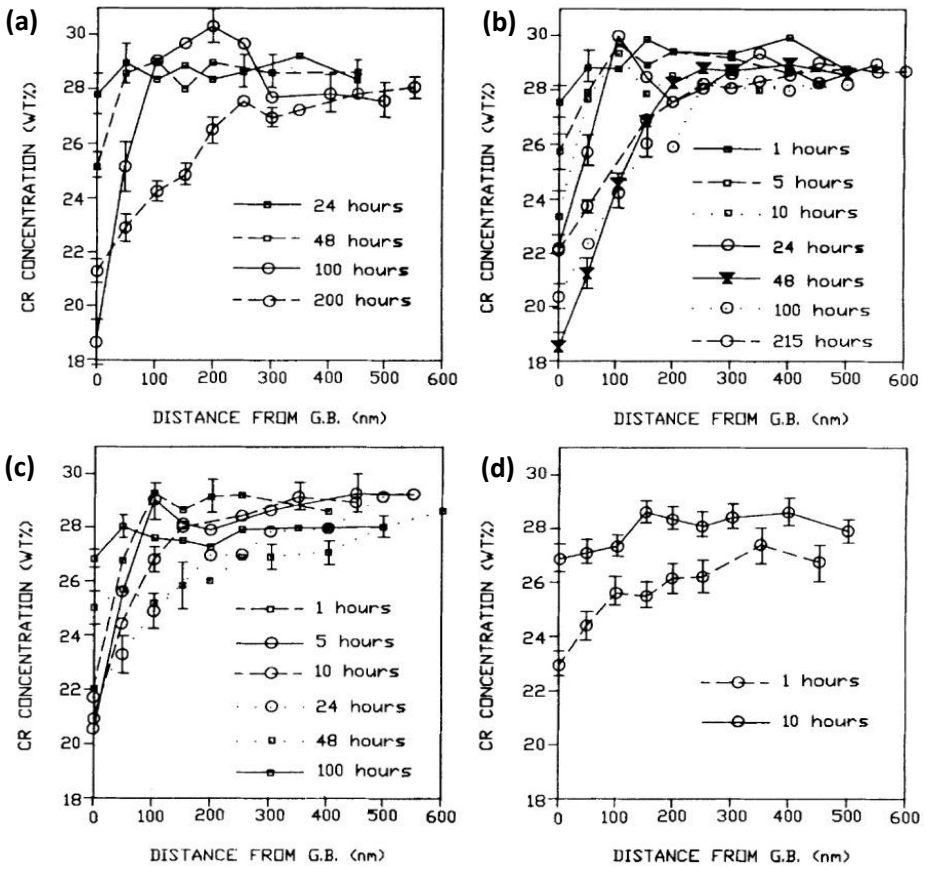

Figure 2-21 Chromium depletion profiles for Inconel 690, annealed at 1150 °C for 60 minutes and aged at: (a) 538 °C, (b) 600 °C, (c) 700 °C, and (d) 800 °C for various times [77].

The non-destructive DL-EPR test has been widely used to assess the DOS behaviour in austenitic stainless steels and nickel-based alloys [81–84]. This method provides a simple, rapid, non-destructive and quantitative approach to determine DOS in stainless steels and nickel alloys which is more reliable than the methods based on weight loss or intergranular attack depth measurements for samples that are not fully sensitised [66,83]. Rahimi et al. [84] developed a new data processing method to make the DOS calculation using the DL-EPR test more accurate by analysing the grain boundary network, which can be applied to compare the DOS in samples with different grain size and grain boundary character distribution. Figure 2-22 is a time-temperature-sensitisation (TTS) diagram superimposed on the time-temperature-phase (TTP) diagram for austeno-ferritic duplex stainless steel,

which shows the dependence of sensitisation in the material on ageing temperature and time [85].

According to a large amount of studies on localized corrosion in stainless steel, it is widely accepted that the character of the grain boundary can strongly affect its susceptibility to grain boundary attack [86–88]. Normally, low angle and CSL boundaries are categorised as low energy boundaries while random HAGBs are high energy boundaries. In general, low energy grain boundaries have better resistance to intergranular corrosion than random HAGBs. Based on this idea (grain boundary engineering [89]), thermo-mechanical treatment can be used to increase the fraction of CSL grain boundaries and, consequently, improve the intergranular corrosion property without altering the alloy chemical composition [90–93].

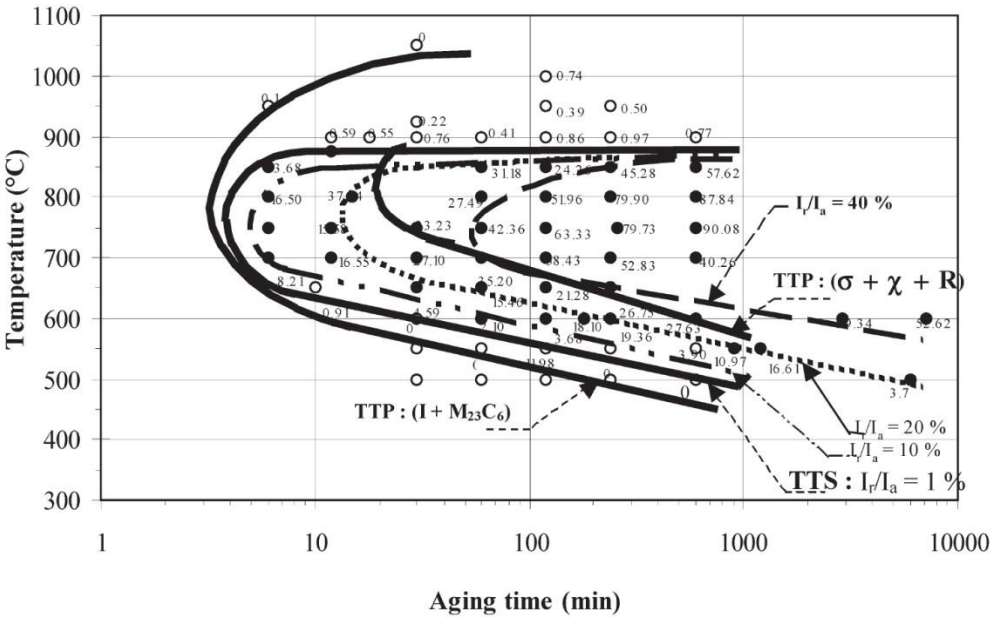

Figure 2-22 TTP and TTS of austeno-ferritic duplex stainless steel based on DL-EPR test [85].

2.2.2 Irradiation induced sensitisation

Stainless steels as fuel cladding materials in a nuclear reactor core would be exposed to intense neutron irradiation that can cause the material to be sensitised. Irradiation induced sensitisation and thermally induced sensitisation in stainless steel are both induced by the depletion of chromium at grain boundaries. However, the mechanism of chromium depletion is different. Thermally induced chromium depletion at the grain boundary is described in section 2.2.1. Iradiation induced chromium depletion is introduced in this section.

The motion of irradiation induced point defects to sinks (dislocations, grain boundaries, free surface and other defect sinks) will cause the migration of lattice atoms in the opposite direction. Continuous irradiation sustains fluxes of point defects that move towards these point defect sinks and, in case of any preferential transport of one of the alloy components, leads to a local chemical redistribution. This phenomenon is very common in alloys under irradiation and has important technological implications [45,94]. Wiedersich [95] developed a model to illustrate this. The relation between the direction of the gradient of alloy component A and that of the vacancy gradient is determined by the relative magnitudes of the ratios [60]:

$$\frac{d_{Av}}{d_{Bv}} - \frac{d_{Ai}}{d_{Bi}} \tag{1}$$

where, d_{Ai},d_{Bi}, d_{Av}, d_{Bv} are the interstitial diffusivity coefficient via atom A, interstitial diffusivity coefficient via atom B, vacancy diffusivity coefficient via atom A and vacancy diffusivity coefficient via atom B, respectively. During irradiation, the vacancy

concentration always decreases towards a defect sink, and if $\frac{d_{Av}}{d_{Bv}} > \frac{d_{Ai}}{d_{Bi}}$,the element A will become depleted at sinks [60].

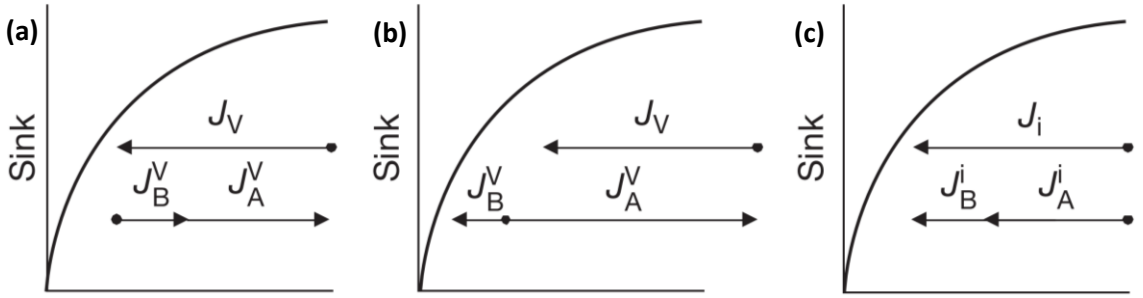

Figure 2-23 Radiation-induced segregation mechanisms due to coupling between point defect and solute fluxes in a binary A-B alloy [45].

Figure 2-23 shows the mechanism of RIS in a binary A-B alloy refer to the point defects and solutes diffusion direction and diffusion rate. Figure 2-23(a) shows vacancy and solute atom flux diffuse in the opposite direction. An enrichment of atom B will be near the sink, if d_{Bv} is lower than d_{Av}. This model is illustrated as segregation by the IK effect [95]. Atom A and B fluxes do not necessarily diffuse in the same direction (Figure 2-23(b)). If B is strongly bound to the vacancy and dragged to the sink, an enrichment of B will be expected. The formation of an interstitial-solute complex is the solute drag mechanism (Figure 2-23(c)). If interstitial-solute complex diffusion coefficient d_{Ai} is lower than d_{Bi}, atom B will enrich at the interstitial sink. The two kinds of RIS, IK effect (driven by vacancy gradients) and the migration of solute-defect complexes, generally occur over different temperature stages [96].

In terms of neutron irradiated stainless steel, sensitisation is generally attributed to RIS effects, in particular with the depletion of chromium from grain boundaries to adjacent zones. RIS is a non-equilibrium effect, which arises from the flux of point defects created

by atomic displacement events. The IK effect is applied to explain the major element segregation in irradiated material, whereby slower diffusing solutes (Ni) are enriched at point defects sinks such as grain boundaries and free surfaces [11]. This process occurs because the migration of vacancies to a sink requires a flux of atoms in the opposite direction, so that the faster diffusing solutes (chromium and iron) become depleted. RIS may also occur via the migration of point defect-solute complexes (in which a solute atom is bound to vacancy or interstitial, generally because of differences in the size of solute and matrix atoms) [97]. The migration of point defect-solute complexes causes solute segregation at the point defect sink for example the segregation of Si to grain boundaries is thought to result from the migration of Si-interstitial complexes [98]. Then, after one element of the alloy exceeds the level of solubility, local supersaturation can provide the driving force for the formation of precipitate. Figure 2-24 shows the element concentration profile across a grain boundary in a stainless steel irradiated by neutrons to several dpa at about 300 °C. Chromium depletion in austenitic steels is highly consistent and repeatable, even if subjected to varying irradiation conditions. However, in low chromium concentration ferritic-martensitic (F-M) alloys, both chromium depletion and enrichment were observed at grain boundaries after irradiation under different conditions [99,100]. Wharry and Was [98] studied the mechanism of RIS in F-M alloys using modelling and compared it to experimental results over a range of alloys with varying chromium concentration, irradiation temperature and dose. They suggested that chromium and iron segregation induced by irradiation in F-M alloys were still dominated by the IK effect. The

direction of RIS (depletion or enrichment) at the grain boundary was determined by the relative magnitudes of the diffusion coefficient ratios at a given temperature, as shown in equation 1. As shown in Figure 2-25, the diffusion coefficient ratios intersect at a "crossover" temperature, below which chromium enrichment via interstitials is dominant, and above which chromium depletion via vacancies is dominant [98]. They also found that the magnitude of chromium enrichment decreases with increasing bulk chromium concentration. The decreasing of Cr:Fe diffusion coefficient ratio for interstitials with increasing bulk chromium concentration causes the crossover temperature to decrease. This also accounts for the fact that almost all reported results show an enrichment of chromium at the grain boundary in the high chromium concentration austenitic steel.

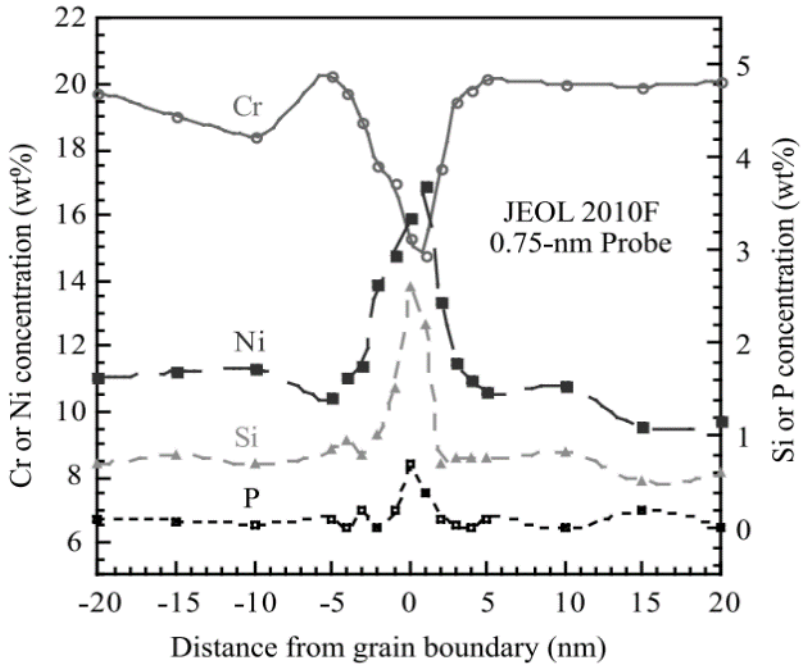

Figure 2-24 RIS at the grain boundary of a stainless steel in a LWR core to several dpa at about 300 °C [101].

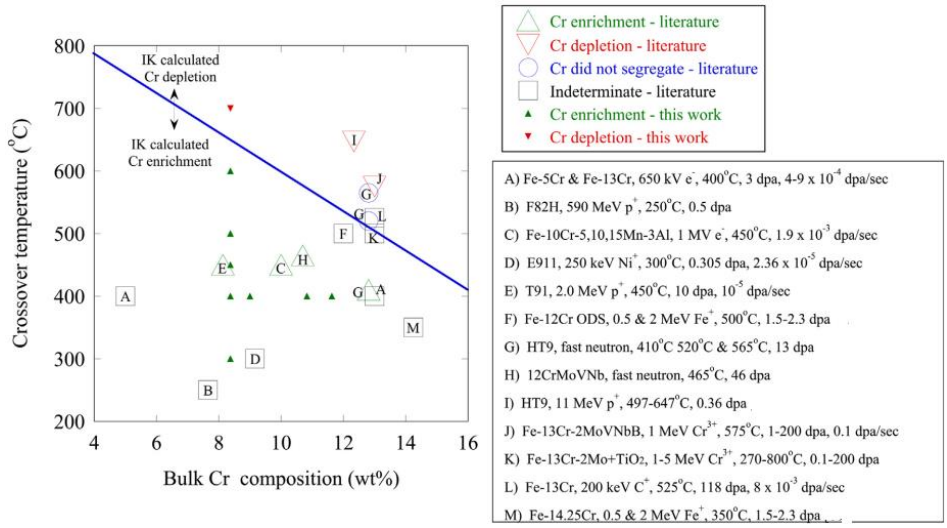

Figure 2-25 Reported experimental results of segregation directions of Cr in irradiated F-M alloys, as compared to the crossover temperature calculated in Wharry and Was' work [98].

Both thermally and irradiation induced sensitisation are due to the chromium depletion at the grain boundary. However, there are some obvious differences [13] in terms of the elemental segregation mechanism and microstructure, such as:

1) For niobium stabilised alloy, niobium carbides still present in the matrix after irradiation at the medium temperature. In thermally sensitised alloy, solution anneal is carried out to dissolve the niobium carbides to make the material ready to be sensitised by a subsequent ageing process;
2) Chromium carbides at the grain boundary together with a chromium depletion region adjacent to the carbides are induced by thermal sensitisation. By contrast, irradiation produced chromium depletion at the grain boundary is simply by elemental segregation and point defects gradients;
3) Thermally induced sensitisation will produce a comparatively broad extent of chromium depletion (minimum 30 nm), whereas RIS due to the IK effect

produces much narrower zones of chromium depletion (about 5 to 15 nm) and no grain boundary chromium carbide precipitates.

2.3 Factors affecting sensitisation

Sensitisation can be affected by the chemical composition, grain boundary character and thermo-mechanical treatment parameters [66]. 1) Chemical composition: carbon is the major element that causes sensitisation because of the formation of chromium carbides at the grain boundary. An increase of carbon content in stainless steel leads to more chromium carbides being produced at the grain boundary, which increases the magnitude and width of the chromium depletion zone and the tendency to intergranular attack [23]. The addition of Ti and Nb can form stable carbides that hugely decrease the concentration of free carbon to prevent the nucleation of chromium carbides at the grain boundary. Figure 2-26 is a comparison of unstrained samples and 20% strained samples [23], with different carbon concentration, on DOS vs. ageing time, which shows that samples with higher carbon content tend to have higher DOS due to the formation of large number of chromium carbides in the high carbon alloy. The strained samples are desensitised (re-healed) after 200 hours ageing at 670 °C, which is quicker than the unstrained samples. 2) Grain boundary characters: special grain boundaries (such as Σ3 twin boundaries) have lower energy than random grain boundaries, and show much less chromium depletion and chromium carbide precipitation [102,103]. 3) Heat treatment parameters: the sensitisation temperature is about 450-850 °C, ageing temperature out of this range can hardly form chromium carbide to produce a chromium depletion zone. Long-time ageing will also let

the sensitised grain boundary to be self-healed because chromium carbides only form at the early stage of a prolonged ageing process [74]. 4) Cold work and grain size: studies have found that a small amount of prior cold work (about 5-20%) obviously increase the susceptibility to sensitisation in various stainless steels. In general, the time required for starting intergranular corrosion is reduced at a given sensitisation temperature if cold work is applied up to 15%. On further cold work, no significant decrease in sensitisation time is obtained. This effect is because large number of in-grain carbides are produced and relatively fewer carbides nucleated at the grain boundary after cold work [66,104,105]. The grain size also plays a role in sensitisation, which has been reported by Pascali et al. [106] and Beltran [107]. Their results suggested that increasing grain size delays the initiation of sensitisation. As shown in Figure 2-27, the reduction of grain size accelerates the sensitisation-desensitisation process suggesting that carbide nucleation is accelerated as grain size decreases, which might be because the average length of carbon atoms diffusing from the mid-grain to the grain boundary decreases for smaller grain size material [66].

Reported work shows that increase the residual strain can increase the diffusion rate of chromium in matrix [108] due to more chromium diffused via the dislocation pipe, which leads to more chromium carbides form at the grain boundary in a given time and increase the magnitude of chromium depletion. Thus, the increasing of cold work lead to the increase of sensitisation. Previous work in 304 stainless steel showed that a low level of residual strain has less extent of sensitisation due to lower chromium diffusion rate [109].

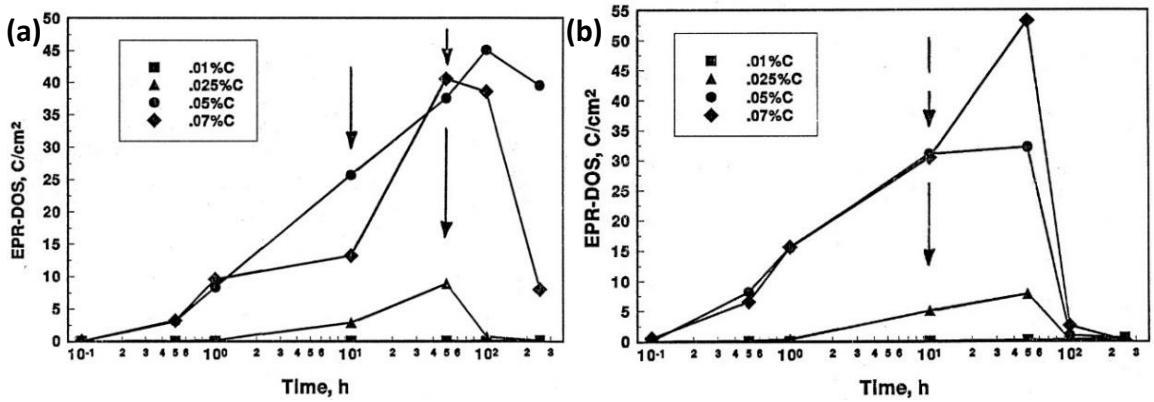

Figure 2-26 DOS vs. ageing time of 304 stainless with varying carbon content steels at 670 °C: (a) unstrained, (b) 20% strained [23].

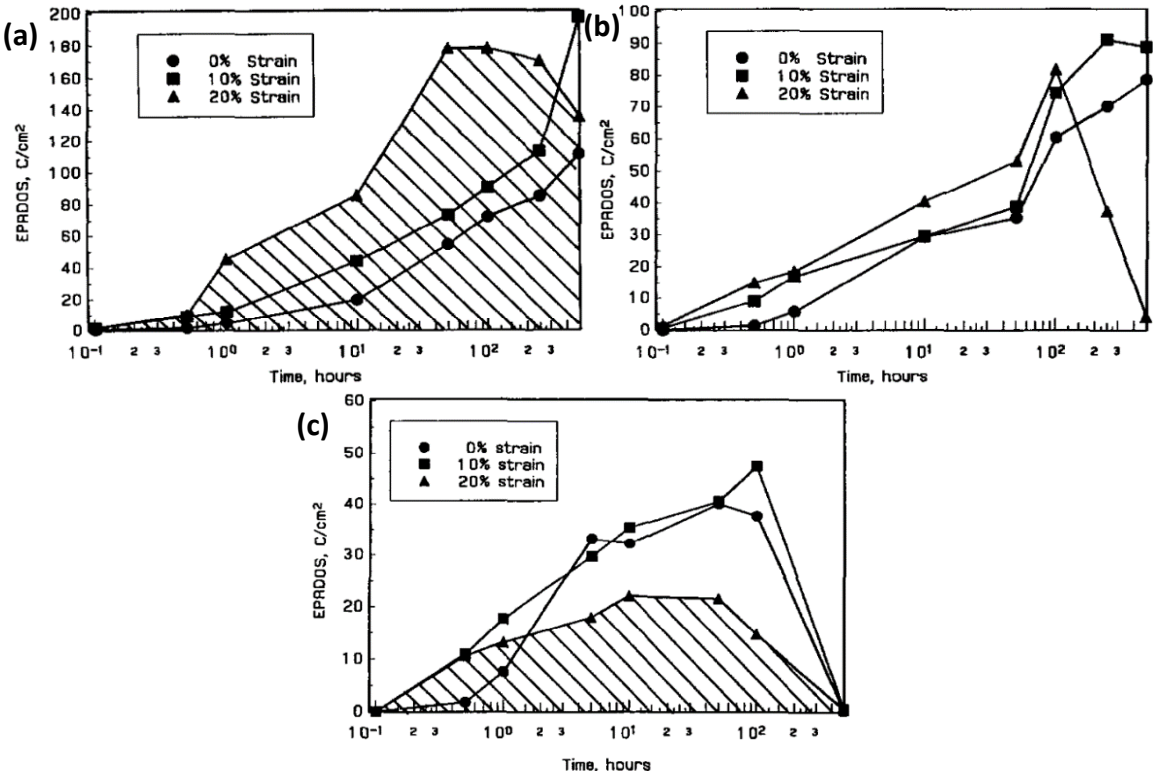

Figure 2-27 DOS as a function of ageing time of 304 stainless steel with three strain levels aged at 625 °C: (a) 150 µm grain size, (b) 40 µm grain size and (c) 15 µm grain size [110].

2.3.1 The effect of the minor alloying element silicon on sensitisation

2.3.1.1 Silicon effect on sensitisation

The effects of silicon on high temperature oxidation [111–113], intergranular corrosion [114–116] and stress corrosion cracking [117–121] have been widely investigated.

According to published work [112], a relatively small silicon addition is known to have beneficial effects on the oxidation resistance due to the formation of a layer of silica, as shown in Figure 2-28, adjacent to the metal, which could act either as a diffusion barrier to both outward diffusion of iron and chromium, and inward diffusion of carbon-bearing species, or as a structure supporting the formation of an outer layer of chromia [112]. The formation of iron oxides is suppressed by silicon and oxidation of alloy dramatically slowed by slowing the outward diffusion of iron. It has long been known that the oxidation resistance of steels in various gases (H_2O, H_2-H_2O, CO_2-CO, O_2 and air) can be improved by silicon addition [112]. A dense and slow-growing silica layer formed at the interface of the chromium oxide film and the bulk alloy, which contributes to the improvement of the oxidation resistance of a chromium steel.

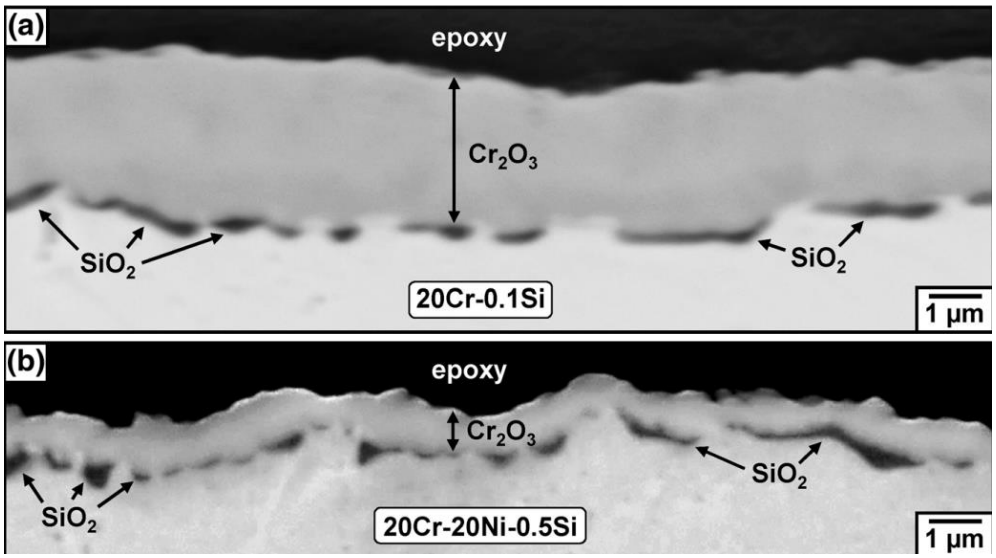

Figure 2-28 BSE cross-sections of (a) Fe-20%Cr-0.1%Si and (b) Fe-20%Cr-20%Ni-0.5%Si, after reaction for 240 hours at 818 °C [112].

In austenitic stainless steel, the alloying element silicon is introduced to achieve high corrosion resistance to oxidising nitric acid and specially to inhibit the intergranular corrosion. The ability of silicon-doped steel to resist intergranular corrosion depends on

silicon content and its distribution, as well as the conditions and composition of the corrosive environment [122,123]. Suppressed intergranular corrosion was observed in silicon doped 304LN stainless steel in [124]. Attempts have been made to explain the reason for the intergranular corrosion suppression in silicon doped stainless steel, which were briefly reviewed in [125]. The potential difference between the grain surface and the grain boundary was thought to be the cause of this phenomenon, as preferential attack was observed at grain boundaries in non-sensitised stainless steel containing moderate silicon addition (between 0.5 and 1 wt.%). Desestret et al. [126] proposed that the potential difference was because of Si segregation to the grain boundary. This was supported by Armijo et al. [115] who measured the anodic current between grain surface faces and grain boundary separately on an alloy containing 0.95 wt.% Si, whereas, they did not identify Si segregation to grain boundaries in these alloys. As shown in Figure 2-29, in unsensitised alloys, very low Si content alloys are immune to intergranular corrosion, Si additions about 1 wt.% dramatically increase intergranular corrosion while a further increase in Si concentration would decrease intergranular corrosion.

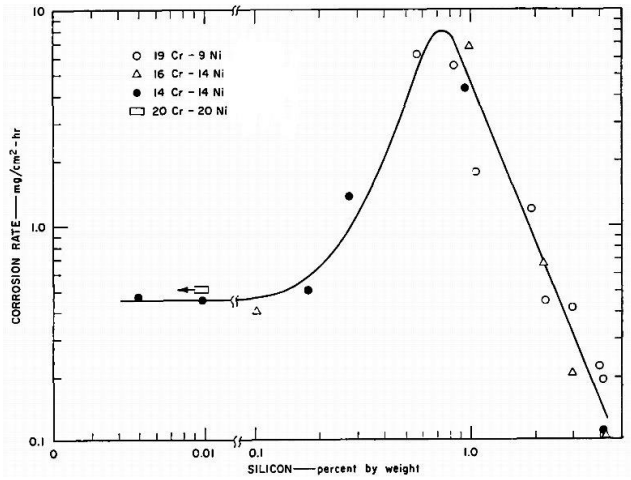

Figure 2-29 The intergranular corrosion rate as a function of Si concentration in stainless steels tested in boiling HNO_3-dichromate solutions [115].

Recently, the effects of silicon on passive and transpassive dissolution on austenitic stainless steel in nitric acid have been studied by Laurent et al. [124,125,127]. Figure 2-30 shows that serious intergranular attack is observed on unsensitised 304LN stainless steel in nitric solution while 3.5 wt.% Si doped stainless steel shows relatively uniform dissolution, except for a few pits observed on the surface. Figure 2-31 shows the elemental profiles across the passive film. Silicon rich oxide film observed in the 3.5 wt.% Si added stainless steel, which accounts for the better corrosion resistance to intergranular attack than the 304LN stainless steel. The passive film formed on the surface in 3.5 wt.% Si added stainless steel was further studied in Laurent et al.'s work [127]. They found that chromium and silicon were the major elements to form the passive oxide film in the silicon doped stainless steel. The passive film consisted of two layers with a silicon rich outer layer and a chromium rich inner layer. Silicon increases the activation potential of the passive film as it contains less chromium and more silicon, which suggests that silicon decrease the affinity of the stainless steel for oxygen. The presence of a high silicon content 3.5 wt.% in the stainless steel could inhibit the dissolution of chromium during the transpassive dissolution [127].

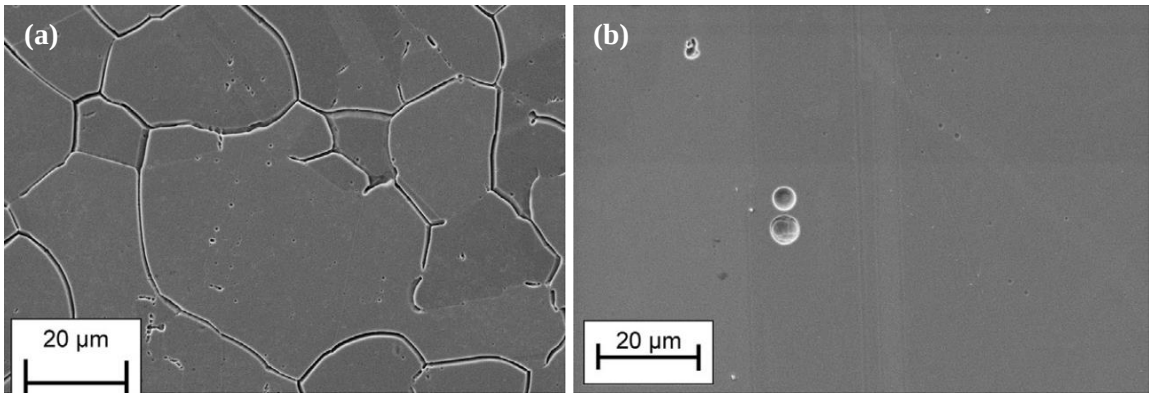

Figure 2-30 Surface morphology of 304LN samples polarised at a potential of 0.65 V(vs. MSE) in 4 mol dm^{-3} HNO_3 at 40 °C for 1000 seconds: (a) 304LN stainless steel, (b) 3.5 wt.% Si containing stainless steel [125].

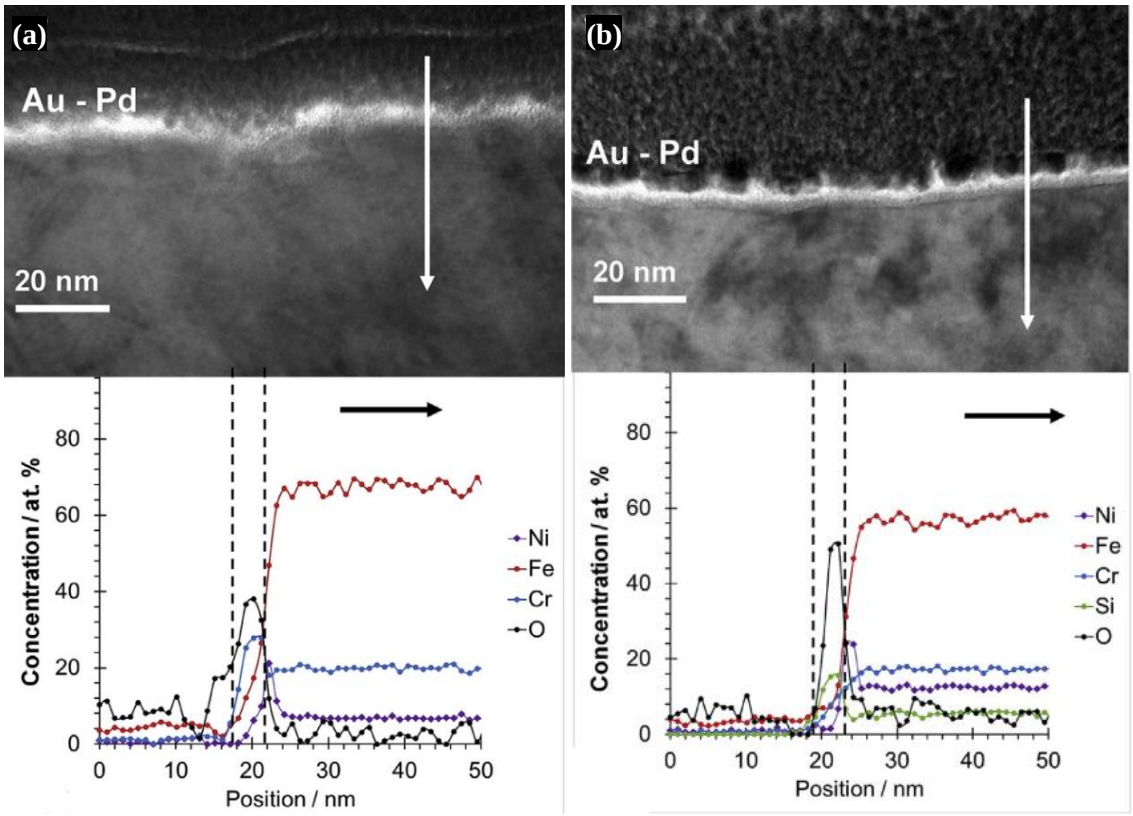

Figure 2-31 Elemental profiles across FIB cross sections through 304LN sample surface after passive layers have been produced in 4 mol dm^{-3} HNO_3 at 100 °C for 24 hours: (a) 304LN stainless steel, (b) 3.5 wt.% Si added stainless steel [125].

In Figure 2-32, the strength of unirradiated 304 SS does not show any dependence on Si concentration. However, the strength slightly decreases as the Si concentration increases to 0.8-1.2 wt.% when irradiated to 0.3×10^{21} neutron/cm^2 because Si supresses the formation of irradiation induced hardening centres and contributes to greater ductility [56]. Silicon atoms are more likely to interact with irradiation induced vacancies so that the formation of vacancy clusters or vacancy-impurity complexes can be inhibited. Therefore, irradiation induced hardening will be less significant. It has been suggested that the addition of Si has beneficial effect to the resistance of stainless steel to IASCC due to the suppression of irradiation induced hardening of these alloys and, consequently, make them less susceptible to IASCC [56]. Three mechanisms were proposed by Li et al. [119] to

explain the detrimental effect of silicon addition on stress corrosion cracking: 1) Stacking fault energy might be decreased, which facilitates the planar slip and the breakdown of the protective passive film; 2) The strength of the passive film is decreased; 3) the susceptibility of the grain boundary to oxidation is increased. However, no direct experimental results could be referred to support these mechanisms proposed by Li et al [119].

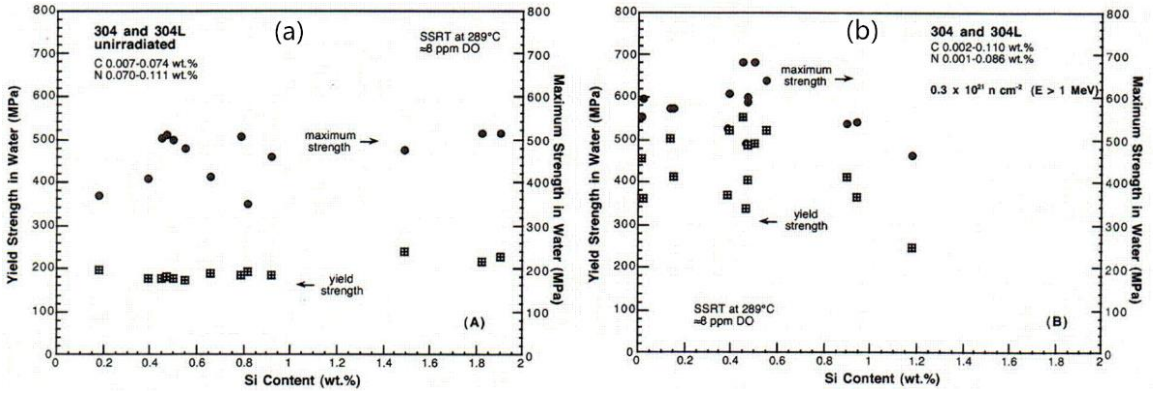

Figure 2-32 Silicon effect on the yield strength and ultimate tensile strength of 304 stainless steel, (a) unirradiated, (b) fast neutron fluence 0.3×10^{21}neutron/cm^2 [56].

The effect of minor element silicon on sensitisation was not well studied in previous work. Norris et al. [18] discussed a little bit about the silicon effect by examining the 20/25/Nb cladding material retrieved from an AGR reactor. Their work revealed that silicon is the most significant minor constituent segregate in cladding material. Because of the limited accuracy of the measurement techniques and the variability of values obtained within grains, they gave just a possible explanation that silicon migrates to intragranular precipitates and grain boundaries and then contributes to the growth of silicon-rich precipitates. These precipitates are incorporated with chromium and niobium [128]. As shown in Figure 2-24, silicon is enriched at the grain boundary after irradiation. However, silicon is an undersized solute atom with a faster diffusion rate than iron. Its enrichment at

grain boundaries can only be explained by the solute-interstitial drag mechanism [129]. The greatest silicon concentrations are shown in the lower temperature irradiated samples. Greater silicon maxima are observed associated with wider chromium depleted zones after examining different boundaries in the same specimen. These discussions did not show any relationship between silicon concentration and DOS in the 20/25/Nb cladding material [18].

2.3.1.2 Silicon effect on chromium diffusion

As described in section 2.3.1.1, the effect of silicon on intergranular corrosion has been widely studied. The main cause of intergranular corrosion in sensitised austenitic stainless steel is induced by the depletion of chromium at the grain boundary. TEM and microprobe studies performed on four stainless steels containing from 1 wt.% to 5 wt.% Si and from 12 wt.% to 19 wt.% Cr by Chou et al. [118], did not show any grain boundary enrichment of Si by natural segregation at ambient temperature. Silicon is known to have a high diffusion rate, several orders of magnitudes larger than the major constituents of austenitic stainless steels [130–132]. A confirmation of the influence of silicon on the overall diffusivity of the solvents, include Fe, Ni, Cr, has been provided by various researchers. Johnston [132] suggested that silicon had a strong effect on the diffusion rate of chromium. An attempt has been made to understand the effect of silicon on diffusion coefficient of chromium at grain boundaries by Assassa and Guiraldenq [133], as shown in Figure 2-33. They found that 1 wt.% Si doped steel had the highest intergranular diffusion coefficient and the lowest activation energy for chromium at lower temperature.

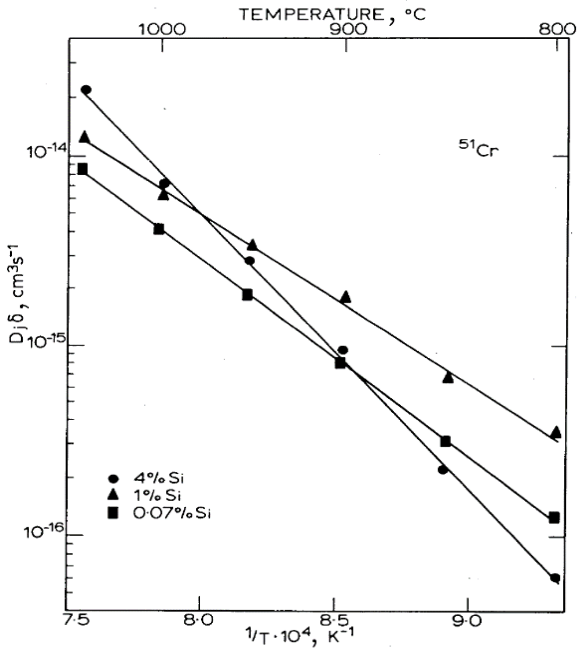

Figure 2-33 Diffusion coefficient of chromium at the grain boundary in stainless steels with different silicon concentrations [133].

The effect of silicon on vacancy diffusion to grain boundaries, consequently affecting RIS, has been studied by Garner and Wolfer [134]. Their results showed that the addition of a small number of fast-diffusing elements to pure nickel decreased void nucleation strongly by increasing the effective vacancy diffusion coefficient D_V^{eff}. Katz & Wiedersich [135] and Russell [136] used a model to describe the dependence of D_V^{eff} on the diffusion coefficient of the solute:

$$D_V^{eff} = (D_V + KC_S D_S)/(1 + KC_S)$$

where, D_V is the diffusion coefficient for migration of a free vacancy in pure nickel and D_S is the diffusion coefficient for a solute-vacancy pair. C_S is the solute concentration, $K = 12\exp(E_b/kT)$ is the mass action constant for solute-vacancy dissolution in an FCC lattice and E_b is the solute-vacancy binding energy. Figure 2-34 shows the effect of silicon on the vacancy diffusion rate, which increases as silicon level increases.

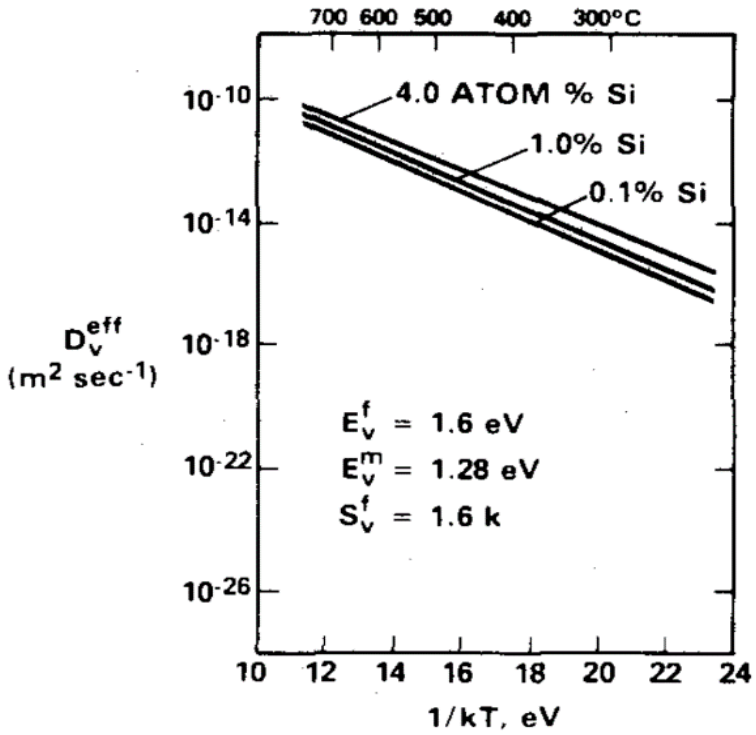

Figure 2-34 Effect of silicon content on the vacancy diffusion coefficient for Fe-16Cr-14Ni-xSi alloys [128,137].

Figure 2-35 shows silicon segregation as a function of irradiation dose. High level Si enrichment was observed at the grain boundary after irradiation. Silicon is soluble in high temperature water, which might enhance the dissolution of the alloy adjacent to the grain boundary, consequently, increase the rates of intergranular corrosion and IGSCC [60].

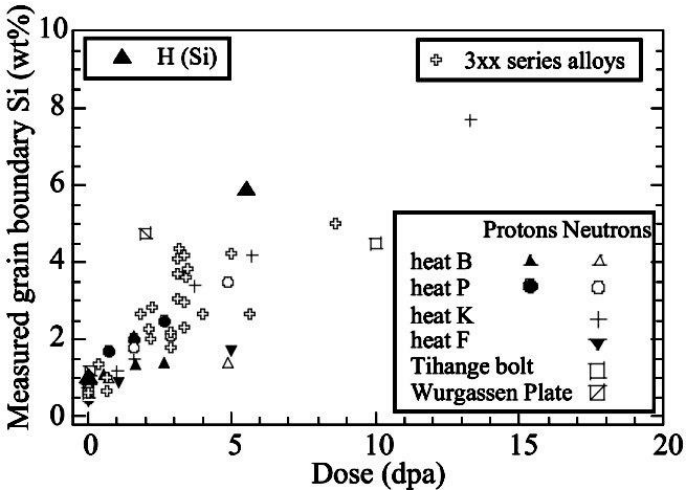

Figure 2-35 grain boundary segregation of silicon in 300 series austenitic alloys irradiated with neutrons or protons to 13 dpa [60].

2.3.2 The effects of grain boundary misorientation on chromium depletion and grain boundary attack

Structural materials exposed to corrosive coolant while subjected to intense neutron irradiation at elevated temperature might suffer from IASCC. IASCC is an important engineering issue for the integrity of both the core components of fission reactors during operation and spent-fuel elements when stored in a cooling pond. Plenty of research has already carried out to investigate the causes of IASCC, which are believed to be one or more of the irradiation induced microstructural defects, coolant chemistry and the stress state. One of the key factors causing IASCC is irradiation induced sensitisation via chromium depletion from the grain boundary which makes the material susceptible to intergranular attack when exposed to a corrosive environment. Grain boundary attack induced by both irradiation and thermal treatment is discussed in the following paragraphs.

2.3.2.1 Basic fundamentals of grain boundaries

The sensitisation of austenitic stainless steels is caused by the depletion of chromium at grain boundaries, which leads to susceptibility to grain boundary attack by corrosive solution. Various magnitudes of chromium depletion have been detected on different types of grain boundaries. Many attempts have been made to understand the effects of grain boundary character on grain boundary sensitisation. Before reviewing these effects, it is desirable firstly to know some fundamentals of grain boundary.

As shown in Figure 2-36(a), grain boundaries can be generally described by the notation $\theta°[h_{\mathbf{O}}k_{\mathbf{O}}l_{\mathbf{O}}]$, $(h_{\mathbf{nA}}k_{\mathbf{nA}}l_{\mathbf{nA}})/(h_{\mathbf{nB}}k_{\mathbf{nB}}l_{\mathbf{nB}})$, where θ is the rotation (misorientation) angle, [hkl] and (hkl) are the Miller indices of the rotation axis and boundary plane, respectively. Four categories of grain boundaries are proposed by Wolf and Lutsko [138], namely twist grain

boundary, asymmetrical tilt grain boundary, symmetrical tilt grain boundary and random grain boundary. The first three categories are shown in Figure 2-36(b). Grain boundaries which are neither twist nor tilt are termed random.

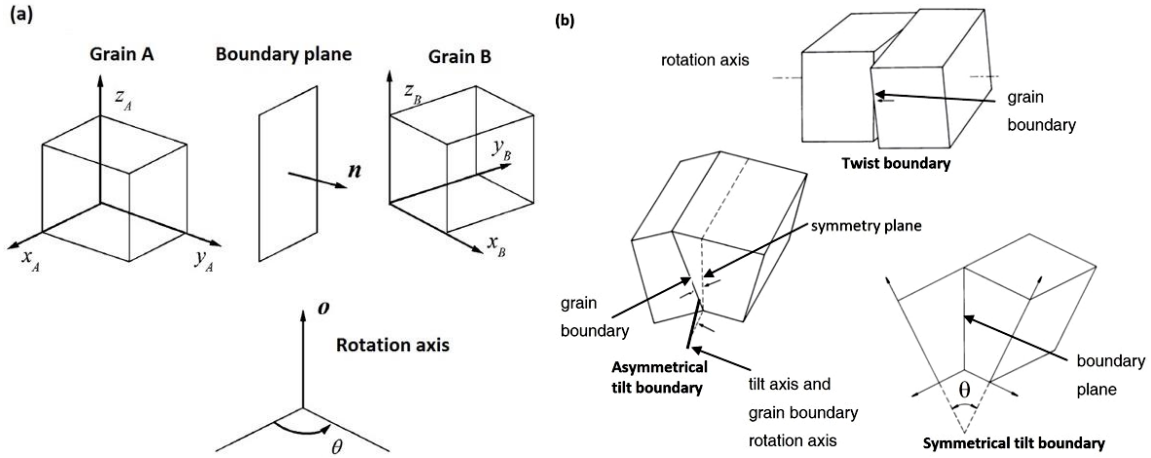

Figure 2-36 (a) Variables that define a grain boundary. **o** is the rotation axis, θ is the rotation angle and n is the grain boundary plane normal [139]. (b) Schematics of three classified grain boundaries.

From the point of view of actual atomic structure [140,141], two groups of grain boundary may be distinguished: low angle grain boundary (LAGB) and high angle grain boundary (HAGB). The misorientation of the grain boundary is accommodated by discrete arrays of dislocations [142–144] when the misorientation angle between two neighbouring grains is small enough. Tilt and twist grain boundaries are formed by edge dislocations and screw dislocation respectively. Generally, it has been accepted that the transition between LAGB and HAGB is 15° [145], this angle might be different depend on the materials. HAGBs are further classified into special and random grain boundaries. The CSL model has been widely used to describe the special grain boundaries [146]. CSL grain boundaries are classified by the Σ value, whose reciprocal gives the density of coincidence sites of the two adjacent grains that share the same grain boundary. In cubic lattices, the Σ value of a symmetrical tilt grain boundary is $\delta(h^2+k^2+l^2)$, where δ is 1 if $(h^2+k^2+l^2)$ is odd and δ is 0.5

if ($h^2+k^2+l^2$) is even. In cubic systems, all Σ values are odd. The grain boundary energy will be lower if the grain boundary plane has a higher density of coincidence site lattice [147,148], which corresponds to a low Σ value. Low Σ value grain boundaries often show special properties, such as higher resistance to intergranular attack, less elemental segregation and less precipitation.

2.3.2.2 The influence of grain boundary misorientation on sensitisation

Grain boundary sensitisation has been regarded as the major cause of both intergranular corrosion and IGSCC [149]. Sensitised grain boundaries are caused by the depletion of chromium because of the formation of chromium rich carbides when materials are exposed to a medium temperature range of 450-850 °C. Lots of research has suggested that each grain boundary has its own sensitivity to grain boundary attack because the characteristics vary between different grain boundary types [88]. Many work has been conducted to investigate how the grain boundary characteristics affect grain boundary attack and how to improve the resistance to intergranular corrosion.

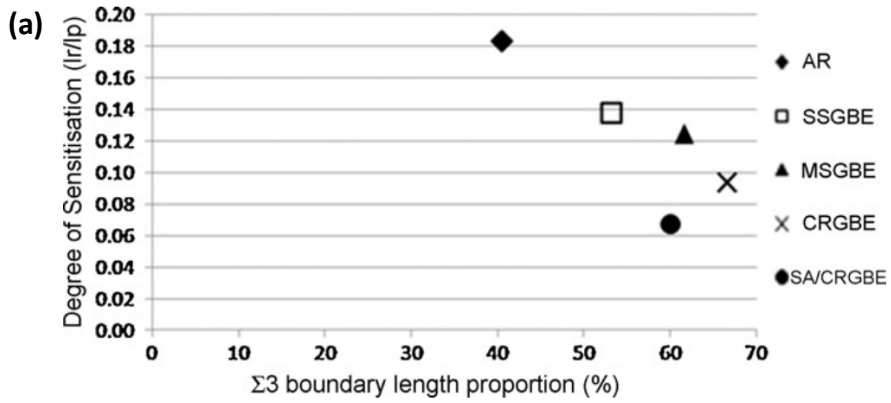

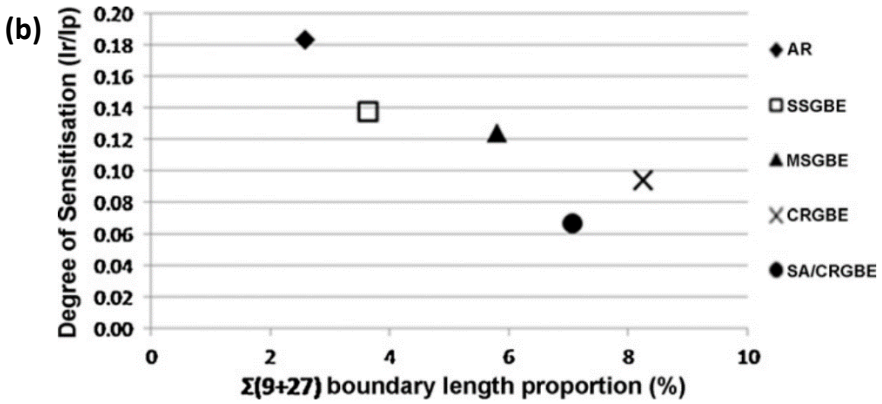

Figure 2-37 DOS as a function of (a) Σ3, (b) Σ(9+27) boundary length proportion in 304 stainless steel subjected to different thermo-mechanical grain boundary engineering (GBE) processing: as received (AR), single-step GBE (SSGBE), multiple-step GBE (MSGBE), cold rolled GBE (CRGBE) and solution annealing (SA) [73].

As shown in Figure 2-37, Jones and Randle [73] studied grain boundary type effects on the sensitisation behaviour of grain boundaries in engineered 304 stainless steel. They found that the DOS, measured by a DL-EPR test, decreased significantly on increasing the proportion of Σ3 and Σ9 boundaries. Σ3 boundaries are almost entirely free from attack. Compared to random grain boundaries, Σ9 grain boundaries are either free or partially free from attack. They also found that all other CSL boundaries and random HAGBs do not free from sensitisation. The resistance to grain boundary attack of these Σ grain boundaries is much stronger than random grain boundaries [150], as their atomic structures are highly regular and coherent compared to the random HAGB. To increase the fraction of CSL grain boundary, the idea of grain boundary engineering has been applied to tailor the grain boundary network by proper thermo-mechanical treatment [151,152]. Hu et al. [153] found that 5% cold work followed by 1100 °C solution annealing for 5 minutes could produce more than 70% low Σ CSL grain boundaries in 304 stainless steel, mainly $\Sigma 3^n$ type. As shown in Figure 2-38, among these CSL grain boundaries, only Σ3 coherent grain boundary entirely prohibits intergranular grain boundary attack. Interconnected $\Sigma 3^n$ type triple

junctions can inhibit the propagation of grain boundary attack thereby improving the resistance to intergranular corrosion [153].

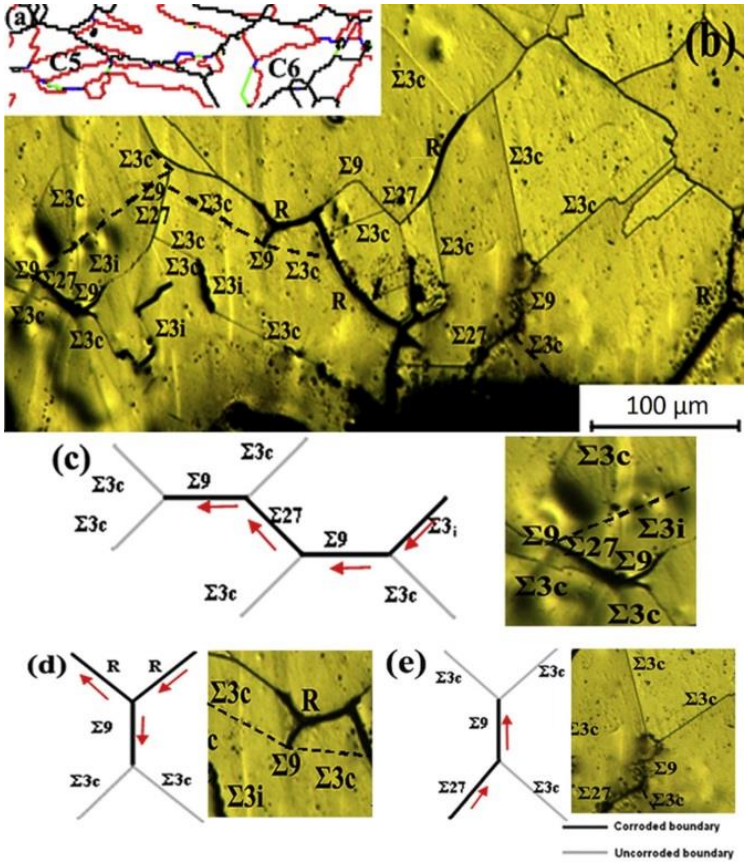

Figure 2-38 The propagation of intergranular attack in 304 stainless steel, (a) the corresponding grain boundary map of (b); (b) optical image showing the propagation path of intergranular attack; (c)-(e) the propagation of intergranular attack is stopped at two coherent Σ3 boundaries, where 'c' is coherent, 'i' is incoherent and 'R' is random [153].

It is well known that the mechanisms of RIS and the thermally induced segregation are different. However, the effects of grain boundary character on intergranular corrosion induced by irradiation and thermal treatment are similar in austenitic stainless steel. Figure 2-39 and Figure 2-40 show the intergranular corrosion at different types of grain boundaries irradiated by protons after electrochemical testing as reported by Sakaguchi et al. [103]. Random grain boundaries are much easily attacked than Σ3 twin boundaries. It is also implied that the corrosion network along the grain boundary is stopped completely by non-

corrosive coherent Σ3 twin boundaries, which is similar to the thermally induced intergranular corrosion shown in Figure 2-38.

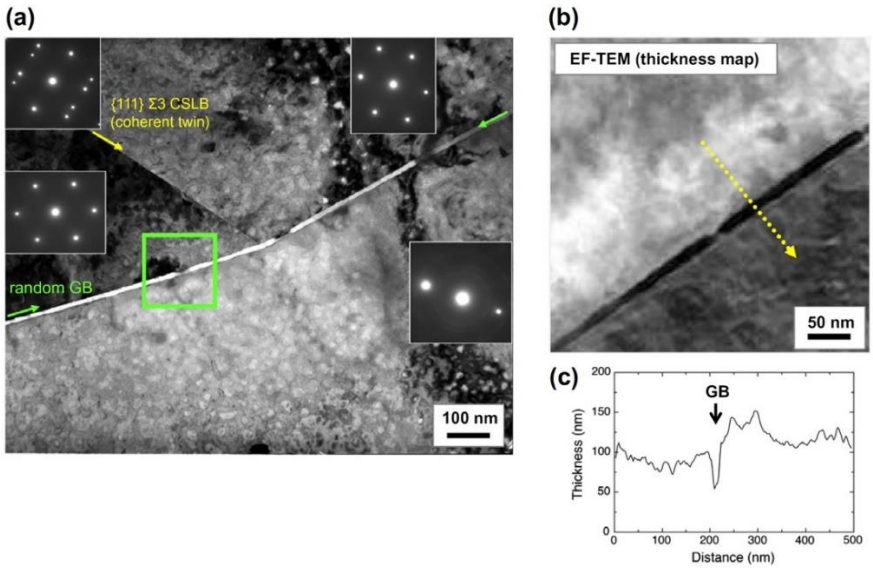

Figure 2-39 (a) TEM image of proton irradiated 316L stainless steel after electrochemical etching, (b) thickness map of random grain boundary acquired by EF-TEM and (c) thickness profile across the random grain boundary [103].

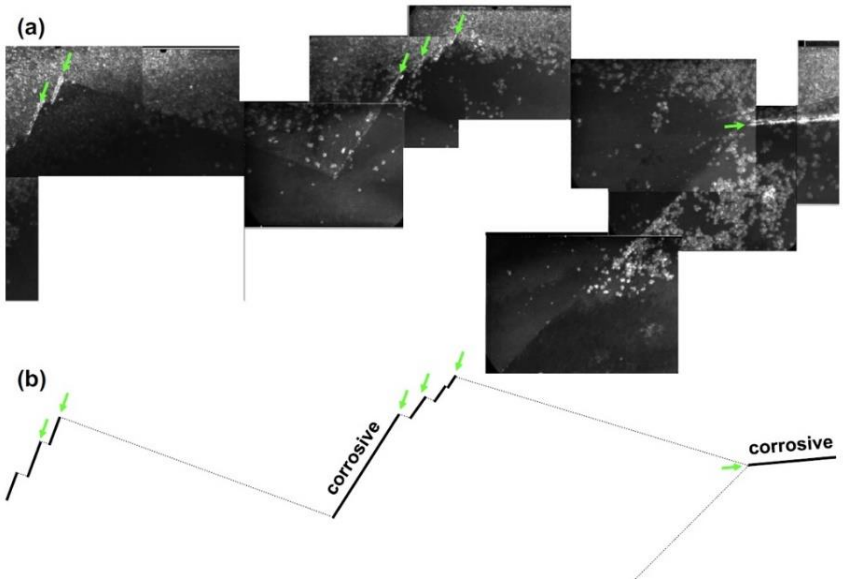

Figure 2-40 (a) Panoramic TEM images of a Σ3 twin boundary network in proton irradiated 316L stainless steel after oxalic acid etching, (b) schematic indication of grain boundary network [103].

2.3.2.3 The influence of grain boundary misorientation on chromium depletion

The formation of chromium carbides on grain boundaries inducing chromium depletion is a non-equilibrium segregation process. The wide variation in the DOS among individual grain boundaries can be explained by the strong dependence of the chromium profile across the sensitised grain boundary on the misorientation angle and the lattice relationship between the two adjacent grains. The character of the grain boundary, as a vacancy sink, plays an important role in the nucleation of chromium carbides and chromium depletion. Random HAGBs have a higher efficiency as vacancy sinks than the special CSL grain boundaries. Thus, the amount of non-equilibrium segregation to the random HAGBs is larger than that to special CSL grain boundaries. Those random HAGBs show a higher driving force for chromium depletion because they are more efficient sinks for vacancies and impurities, which leads to higher magnitude of chromium depletion. It was confirmed experimentally decades ago that no chromium carbide precipitation at Σ3 coherent twin boundaries induced no chromium depletion to them and limited precipitation at Σ3 incoherent twin boundaries caused narrow and low magnitude of chromium depletion region. There are, however, extensive precipitation at random HAGBs leading to wide and deep chromium depletion adjacent to the grain boundary [154,155]. The coherent Σ3 twin boundary interface exhibits no precipitation until an extremely long ageing time [74]. Laws and Goodhew [102] investigated the grain boundary character effect on chromium carbide precipitation at and chromium depletion from grain boundary in 1100 °C solution annealed 316 stainless steel. They found that there was no correlation between chromium depletion width and grain boundary chromium depletion magnitude. The magnitude of chromium depletion along the grain boundary is not affected by the proximity of the chromium carbide.

Many researchers, as reviewed above, have studied the effects of grain boundary character on grain boundary segregation induced by thermal sensitisation decades ago. However, the influence of grain boundary character on the grain boundary segregation induced by irradiation has not been well studied until the last two decades. The correlation between RIS and grain boundary character has been investigated for ion and electron irradiation in austenitic stainless steel [156–160]. These studies indicate that significant RIS is detected at random (general) grain boundaries whereas RIS was obviously suppressed at coincidence site lattice (CSL) grain boundaries, particularly Σ3 twin boundaries, which is similar to the grain boundary character effect on thermally induced chromium depletion from grain boundaries. However, compared with the thermally induced segregation, the width of chromium depletion induced by RIS is much narrower, which is explained by the nature of IK effect. Figure 2-41 and Figure 2-42 show the irradiation-induced segregation at different types of grain boundary as reported by Sakaguchi et al [103]. There is no chromium depletion at low energy coherent Σ3 twin boundaries while remarkable chromium depletion is observed on both incoherent Σ3 twin boundaries and random grain boundaries. Similar results were also reported by Barr et al. [161] in heavy-ion irradiated nickel-based FCC alloys. They found that chromium depletion from Σ3 coherent twin boundary with a {111} grain boundary plane normal is about two to three times smaller than Σ3 incoherent twin boundaries with {112} grain boundary plane normal after irradiation.

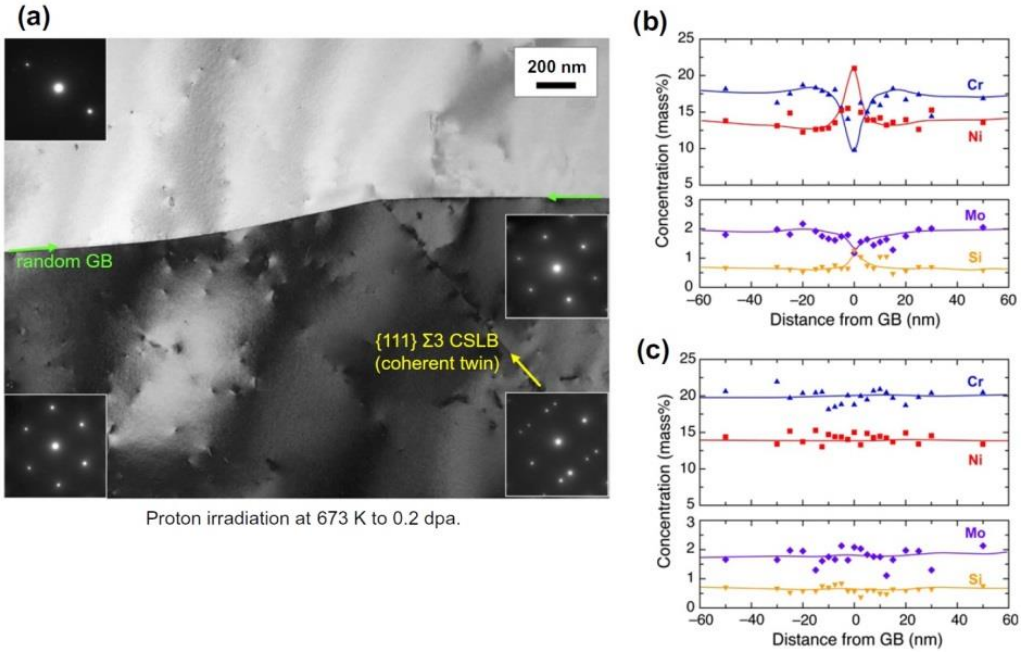

Figure 2-41 (a) TEM image of grain boundaries in proton irradiated 316 SS, (b) and (c) are elemental segregation profiles across a random grain boundary and a coherent Σ3 twin boundary [103].

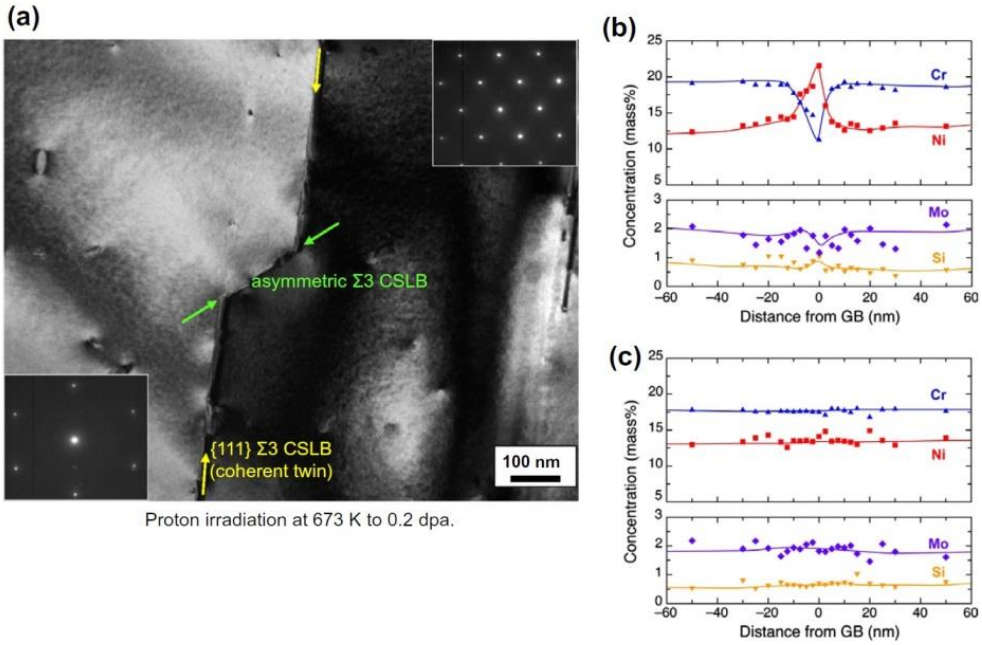

Figure 2-42 (a) TEM image of grain boundaries in proton irradiated 316 stainless steel, (b) and (c) are elemental segregation profile across asymmetric Σ3 twin boundary and coherent Σ3 twin boundary [103].

2.3.3 Methods to improve the resistance to sensitisation

As the mechanism for both thermally and irradiation induced sensitisation has been well understood and the important factors proposed, different methods have been attempted to reduce the extent of sensitisation. 1) Reduce the free carbon content [23]: carbon content is the key factor that causes the population of chromium carbides to form at grain boundaries. Controlling carbon content to a low level (below 0.03%) while manufacturing the material can hugely prohibit thermally induced sensitisation. The free carbon in the matrix can also be reduced by adding stabilising alloying elements Ti, Ta and Nb [162], which could form very stable carbides to prevent the carbon from producing chromium carbide. 2) Annealing heat treatment: solution annealing at high temperature (>= 1050 °C) can dissolve the precipitated chromium carbides and remove the chromium-depleted zone at the grain boundary. Annealing the sensitised material for a long time in the sensitisation temperature range (450-850 °C) can re-heal the sensitised grain boundary by removing the chromium-depleted zone [66]. 3) Grain boundary engineering by thermo-mechanical processes can improve the proportion of low energy Σ3 CSL grain boundaries which shows a much higher resistance to grain boundary sensitisation than a random grain boundary [73,89]. 4) Laser surface treatment [66] by melting, annealing and alloying the surface area, laser treatment can overcome the sensitisation in different materials without affecting the bulk material. Laser surface melting can homogenise the heterogeneous surfaces created during cold work and welding. Carbides can be dissolved by laser treatment and the high cooling rate can avoid the formation of chromium carbides, which can eliminate grain boundary sensitisation.

2.4 Characterisation methods of sensitisation

To apply stainless steel components in an aggressive environment, it is essential to assess the presence or absence of sensitisation in the material prior to service and to monitor the development of sensitisation during service. Different methods have been developed to measure the chromium depletion at grain boundaries, to screen sensitised materials and measure the DOS. These methods have been classified into three categories: elemental analytical methods, chemistry methods and electrochemical methods. Among these methods, the commonly used methods are now introduced.

2.4.1 Elemental analytical methods

The measurement of chromium depletion in stainless steel induced by thermal treatment and irradiation is necessary to explain and assess the sensitisation. High-resolution elemental analytical methods, such as STEM-EDS in TEM and atom probe tomography (APT), have been developed in recent time to measure elemental segregation on the nano-scale.

2.4.1.1 Scanning transmission electron microscopy - energy dispersive X-ray spectroscopy (STEM-EDS)

As a common high-resolution technique, STEM-EDS has been widely used to measure the elemental segregation profiles in thermally and irradiation sensitised samples [163]. Titchmarsh and Vatter [164] summarized the use of high spatial resolution electron microscope to measure RIS profiles across grain boundaries. Their results showed that TEM with sufficient current in a small diameter (< 3 nm) electron probe is necessary to measure RIS concentration profiles. The minimum chromium concentration is strongly

affected by the electron beam broadening and the probe diameter in STEM-EDS. An electron transparent sample is fabricated by twin-jet polishing and focused ion beam (FIB) milling. FIB milling is especially useful for preparing an irradiated sample, as a small volume of the sample prepared by FIB minimises the dose of radioactivity that personnel are exposed to while analysing it. Elemental segregation profiles can easily be measured by performing line-scan cross the grain boundary. Two aspects need specially to be considered to increase the measurement accuracy. The sample thickness needs to be small enough to reduce the interaction volume between the electron probe and the sample. However, to collect enough x-ray counts for quantification, the sample should not be too thin. Thus, it is suggested that sample thickness should not be less than 75 nm for conventional one detector STEM-EDS. A double tilt sample holder is used to tilt the target grain boundary to 'edge-on' position. Edge-on means the incident electron beam is very close to be parallel to the grain boundary plane. To achieve this, the projected grain boundary thickness need to be as small as possible, around 2 nm. To obtain sufficient X-ray counts to quantify the chemical composition at the grain boundary, the STEM-EDS sample thickness need to be larger than 75 nm [163].

2.4.1.2 Atom probe tomography (APT)

As a near atomic-scale (around 0.1-0.3 nm in depth and 0.3-05 nm laterally) and high detection sensitivity 3D imaging and chemical composition analysis technique, APT has become more and more popular recently [165–168]. Elemental segregation, which often involves light elements, can be measured at internal interfaces that take place even within a few angstroms [168,169]. An APT can directly image atoms and local chemistry as shown in Figure 2-43. APT sample is prepared by FIB milling into a small volume needle. This reduces the volume of material required to perform APT analysis and facilitates APT to be a major characterisation technique for high dose irradiated material.

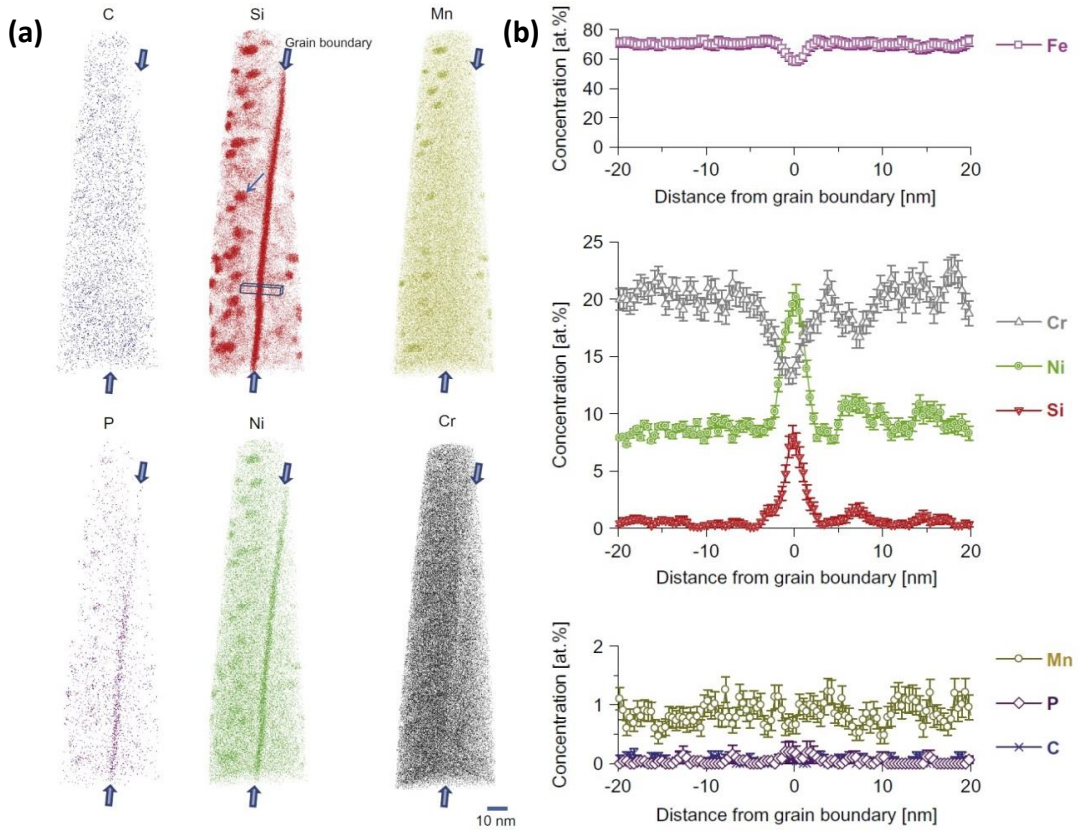

Figure 2-43 (a) Atomic maps of elements in neutron-irradiated 304 stainless steel acquired by APT, (b) concentration profiles obtained from a rectangular parallel-piped region [170].

2.4.2 Chemical etching and electrochemical methods

Chemical etching and electrochemical testing can screen the sensitised material and measure quantitatively the DOS. The most commonly use methods are incorporated in the ASTM standards A-262 [171] Practices A to C, E and F and G-108 [172]. A-262 practice A (Oxalic etching test) is a qualitative and quick screening test. In this test, the metal surrounding chromium carbides at a grain boundary dissolve preferentially; the etch structure gives an idea of chromium depletion which is responsible for intergranular corrosion. After the test, the surface microstructure of the tested samples showing a 'step' or 'duel' morphology will not indicate the presence of sensitisation in the material, but if a

'ditch' is observed along grain boundary, it might indicate sensitised material. If a ditch is obtained, the immersion tests described in A-262 practices B to F should be performed. Sensitised material will be confirmed, if the ditch still turns up after the immersion test.

To determine the DOS quantitatively, the EPR test has been developed. This technique has been standardised in ASTM standard G-108. The EPR test is a quantitative, non-destructive and rapid method [173,174] which has been widely used to evaluate the corrosion resistance of steels and nickel-based alloys [175]. The most common variation of this test used today is the DL-EPR test [84,176] in preference to the single loop EPR (SL-EPR) test due to the cleaning effect on the specimen surface during the forward anodic scan which makes the test independent of surface finish and the presence of random pitting. DL-EPR test involves a forward activation scan from the open circuit potential (OCP) to the passivation potential and a reversal back to OCP. The DOS is determined by the ratio of peak current density I_r/I_a (as shown in Figure 2-44(a)) during reverse and forward scans, which make this method insensitive to surface finish. The sample is polarised anodically by applying a forward potential from the OCP to the passive region to form a very thin (less than 2 nm) passive film across the whole sample surface [177]. The scan direction is then reversed back to the OCP to reactivate the sample. During the reactivation process, the passive film on the sensitised grain boundary is attacked by the electrolyte, which leaves the corresponding grain boundary exposed to the corrosive solution and attacked, while the passive film on the unsensitised grain boundary remain intact and protects the grain boundary underneath. The SL-EPR test has only the reverse scan from the passivation

potential to the OCP. The area under the reactivation peak is directly proportional to the electric charge (Q) (as shown in Figure 2-44(a)) which indicates the DOS. It has been proposed that the reactivation charge should be normalised by the total grain boundary area as different samples might have different grain sizes [178]. Both test methods involve the formation of a passivation oxide film (chromia) during a passivation scan. If the chromium concentration exceeds 12-13 wt.% (this value may vary from material to material), chromium oxide film will protect the grain boundary from attack. Otherwise, the film will be destroyed by the aggressive electrolyte which attack the grain boundary and will contribute to the reactivation current. The SL-EPR test produces a good passive film across the whole sample surface by holding the passivation potential for about 2 minutes before starting the reverse scan.

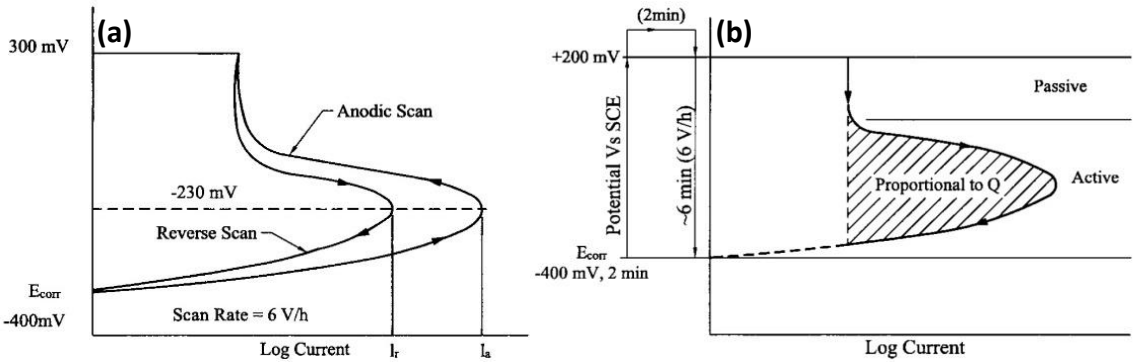

Figure 2-44 Schematic diagrams of (a) a DL-EPR test and (b) a SL-EPR test [66].

2.5 Summary and objectives

2.5.1 Summary

The effects of minor alloying element silicon on stainless steel oxidation have been well studied [111–113]. Silicon doped alloys show better resistance to oxidation because of the

formation of a thin silica layer between the protective chromia film and the bulk material [111]. Some work have been done to investigate the role of the element silicon in intergranular corrosion [114–116]. Assassa and Guiraldenq [133] studied the effect of silicon on the diffusion coefficient of chromium, which might result in different magnitude of chromium depletion at grain boundary, using residual activity method. However, the effect of silicon on chromium depletion which causes the sensitisation of the stainless steel is still unclear. In this work, the effect of silicon on chromium depletion and sensitisation was studied on three AGR fuel cladding model alloys with varying silicon concentrations by measuring the magnitude of chromium depletion at grain boundary.

Reported work on thermally and irradiation induced sensitisation of AGR fuel cladding is reviewed in section 2.1. The spent fuel will be stored in a cooling pond after removal from the reactor. Sensitised fuel cladding might be vulnerable to intergranular attack when exposed to aggressive environment. According to Norris et al.'s work [18], neutron irradiation induced chromium depletion has reached a range of 10.0 wt.%-14.8 wt.% when the irradiation dose is about 1.4 dpa – 5.4 dpa. The irradiation dose is even higher as fuel burn-up increase further. Handling and analysing the radioactive material need dedicated facilities to protect personnel, which is costly and time consuming. Thus, it is attracting to use thermally induced sensitisation to replicate irradiation induced sensitisation. Attempt has been made in this work to verify the feasibility of using thermal treatment to achieve similar magnitude of chromium depletion with the irradiated cladding.

The effect of grain boundary type on chromium depletion and intergranular attack has been well understood [88]. CSL boundaries and LAGBs have lower magnitude of chromium depletion and better corrosion resistance than the random HAGBs due to their lower

boundary energy [109]. For a sensitised stainless steel, the extent of attack at the grain boundary might be different from grain boundary to grain boundary after an electrochemical test, which has been reported by different researchers [25,109,179,180]. An attempt has been made to understand the cause of this difference from the perspective of the grain boundary misorientation angle [179]. However, no reported work has attempted to correlate the chromium depletion directly to the specific grain boundary that has a certain extent of attack. Thus, it is interesting to know the correlation between the sensitisation, the grain boundary misorientation and the chromium depletion. In this work, sensitisation at individual random grain boundary was studied and the sensitisation structure was obtained using DL-EPR test TEM samples were directly lifted from the individual grain boundaries which have various extent of attack using FIB to measure its chromium depletion. In this way, chromium depletion at individual grain boundary can be directly linked to its extent of attack.

2.5.2 Objectives

The aim of this thesis is to improve the understanding of sensitisation behaviour of AGR cladding by achieving the following objectives:

1) To understand the role of silicon in sensitisation and chromium depletion at the grain boundary on model alloys;
2) To study the sensitisation behaviours of the commercial alloy on samples thermally sensitised at different annealing temperatures and ageing times to find out the proper thermal treatment for simulating the in-reactor neutron irradiation induced sensitisation;

3) To understand the correlation between sensitisation, misorientation angle and chromium depletion at the grain boundary.

3 Experimental procedures

3.1 Materials and heat treatment

Four types of 20/25/Nb alloys were investigated in the thesis. Alloys A, B and C are model alloys containing 0 wt.%, 0.56 wt.% and 2.25 wt.% Si, respectively, as shown in Figure 3-1. The as received model alloys came as 0.38 mm thickness sheets. Alloy D is a commercial alloy containing 0.56 wt.% Si and of 1 mm thickness. The chemical compositions of the alloys are shown in Table 3-1. All alloys are Nb stabilised. The alloys are cut into a number of 10 mm × 10 mm coupons from the central area of the metal sheet for subsequent heat treatment.

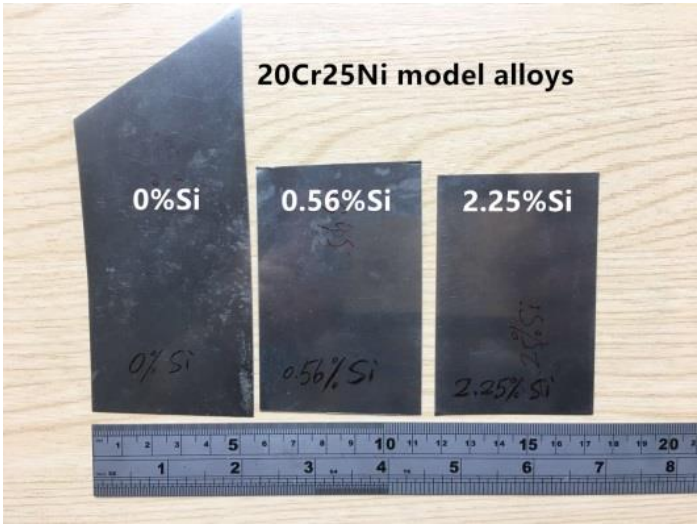

Figure 3-1 20/25/Nb model alloys with varying Si concentrations.

Table 3-1 Chemical compositions of 20/25/Nb austenitic stainless steels (wt.%)

Materials	Cr	Ni	Nb	Si	Mn	C	Fe
Alloy A	19.0	26.5	0.60	0.00	0.67	0.051	Balance
Alloy B	19.2	25.3	0.70	0.56	0.76	0.054	Balance
Alloy C	20.7	24.6	0.73	2.25	0.86	0.052	Balance
Alloy D (Commercial)	19.7	24.6	0.65	0.57	0.75	0.049	Balance

All three model alloys were solution annealed at 1050 °C for 30 minutes. Then the samples were aged at 650 °C, which is very close to the in-reactor service temperature of the cladding, for various times. Alloy D was annealed at 930 °C and 1050 °C for 30 minutes. 930 °C annealing is called stabilisation annealing, which maximises the formation of niobium carbides to decrease the free carbon in the matrix. 1050 °C annealing is called solution annealing, which dissolves carbides to release the carbon into the matrix. Alloy D was then aged at 650 °C for various periods of time.

The annealing was conducted in an air furnace followed by water quenching. After the annealing, samples were ground with 240-grit silica paper to remove the oxidation layer formed during annealing. As shown in Table 3-2, the samples were aged for different periods of time, 10 minutes, 0.5 hour, 1 hour, 5 hours, 24 hours, 96 hours and 200 hours at 650 °C.

Table 3-2 Heat treatment parameters carried out on AGR fuel cladding materials.

Materials	Annealing temperature/ °C	Ageing temperature/ °C	Ageing time/hours
Alloy A (0%Si)	1050	650	0, 0.17, 0.5, 1, 5, 24, 96, 200
Alloy B (0.56%Si)			
Alloy C (2.25%Si)			
Alloy D (commercial alloy)	930		0, 24, 96, 200
	1050		0, 1, 5, 24, 96, 200

3.2 Microstructural characterisation techniques

3.2.1 Scanning Electron Microscope

The SEM used in this project is a Tescan Mira-3 as shown in Figure 3-2. The SEM is equipped with an Oxford X-Max SDD energy dispersive X-ray spectroscopy (EDS) detector and Aztec software for EDS analysis. It is also equipped with a Nordlys EBSD

detector for grain orientation and grain boundary misorientation measurement. All samples for grain structure characterisation underwent 1.5 hours final oxide polishing suspension (OP-S) polishing using colloidal silica suspension. SEM images were taken under backscatter electron (BSE) imaging mode at 10 kV.

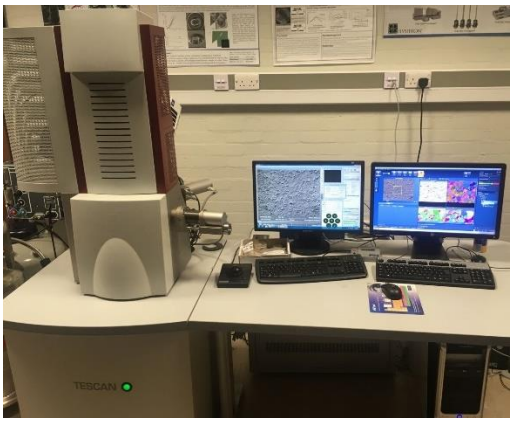

Figure 3-2 Tescan Mira-3 SEM equipped with a Nordlys EBSD detector and an Oxford X-Max SDD EDS detector.

3.2.2 Electron back-scattered diffraction (EBSD) and transmission Kikuchi diffraction (TKD)

As a quicker and straight forward method, transmission electron back-scattered diffraction (t-EBSD or TKD) has been proposed to characterise site-specific grain boundaries in TEM foils. The grain orientations in an electron transparent thin sample can be quantitatively analysed using the TKD technique in a conventional EBSD system [181]. The crystallographic orientation details contained in the diffraction patterns is derived from only the last 10-20 nm of material at the bottom (electron exit) surface [182]. In this thesis, the misorientation angle of grain boundaries in bulk sample and TEM foil is measured by EBSD and TKD respectively. Silver paint was applied to ensure the conductivity between sample and stage. 30 kV beam voltage and a large beam current were used to improve the

EBSD signal intensity. As shown in Figure 3-3, the stage with 70° and 20° pre-tilt angles was used for EBSD and TKD, respectively. The post-processing software Tango was used to determine the grain orientation map and to measure the misorientation angles.

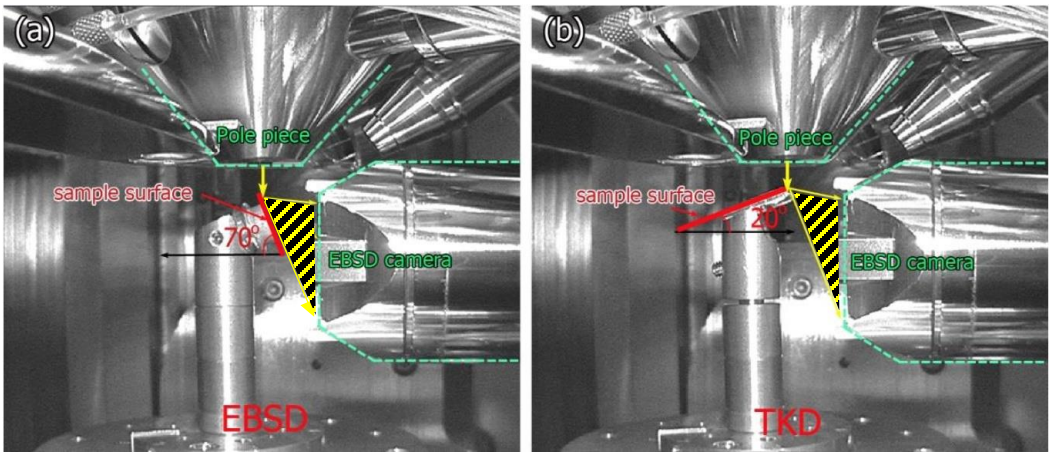

Figure 3-3 (a) conventional EBSD configuration with sample tilt to 70° from horizontal, (b) TKD configuration with sample tilt to 20° [183].

3.3 Double Loop-Electrochemical Potentiokinetic Reactivation (DL-EPR) test

The basis of the DL-EPR technique involves first polarising the sample through the active region before a reactivation scan in the reverse direction is carried out. The DOS is measured by determining the ratio of the maximum current generated by the reactivation (reverse) scan to that of the anodic (forward) scan, I_r/I_a, as shown in Figure 3-4. The procedure used in this study involved holding the specimen at OCP for 10 minutes to allow dynamic stabilisation between the working electrode and the electrolyte. The forward scan was started at 50 mV lower than OCP and polarised to a passive potential of + 300 mV (vs. SCE) using an ACM model 1414 potentiostat. The test setup is shown in Figure 3-5. The scan was reversed to the original value when the forward scan reached the maximum voltage. A scan rate of 100 mV per minute was used for both forward and reverse scans.

All specimens of approximately 10 mm × 10 mm were attached to stainless steel lead wire by a copper tape foil. Silver paint was used to secure the connection and improve the conductivity. Samples were cold mounted with epoxy resin and polished to a mirror surface with 1 μm diamond suspension finish. A 50 × 50 mesh platinum wire and SCE (Saturated Calomel Electrode) were used as counter and reference electrode respectively. The electrolyte used was 0.5 mol/L of reagent grade sulphuric acid (H_2SO_4) and 0.01 mol/L potassium thiocyanate (KSCN) in deionised water. Testing was carried out at room temperature (20 ± 2 °C). Samples were cleaned in the ethanol and then dried with warm air prior to testing. After testing, samples were examined by SEM to observe the morphology and identify the extent of grain boundary attack, specifically to ensure that the reactivation current actually represents attack of the grain boundary areas, (i.e., ditching) rather than being associated with the reactivation of intragranular precipitates that may be present in certain specimens.

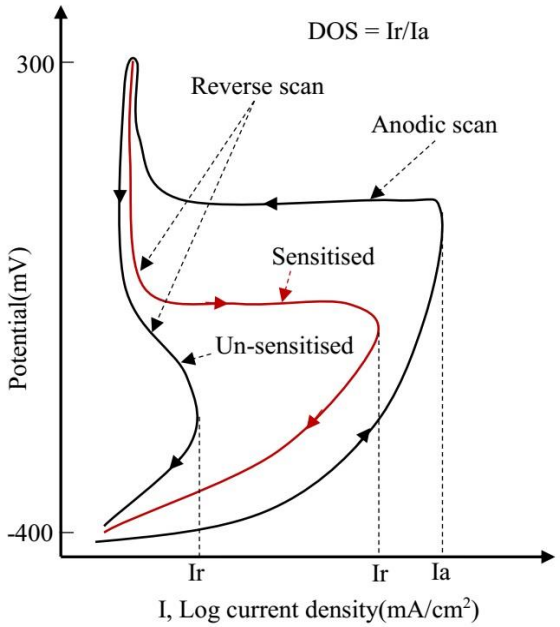

Figure 3-4 Schematic EPR curves for sensitised and solution annealed type 304 stainless steel.

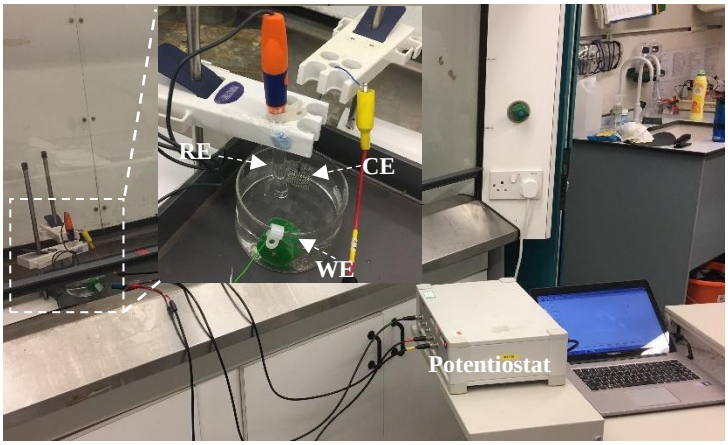

Figure 3-5 The setup of DL-EPR test: work electrode (WE), reference electrode (RE), counter electrode (CE).

3.4 Elemental segregation analytical method: STEM-EDS

3.4.1 TEM sample preparation methods

3.4.1.1 Twin jet polishing

The twin-jet polishing was performed in a solution of 10% perchloric acid and 90% ethanol, using a Struers Tenupol 5 twin-jet electro-polisher as shown in Figure 3-6. The voltage was set at about 20 V with a flowrate of 36. The temperature was monitored by a thermocouple and kept at about -15 °C by pouring liquid nitrogen into the electrolyte tank when the temperature was less than -15 °C. For each heat treatment condition, at least one TEM sample with a shiny thin area was prepared for the subsequent STEM-EDS analysis. Once the twin-jet polishing was finished, the sample was taken out promptly from the holder and then cleaned thoroughly in ethanol.

Figure 3-6 Struers Tenupol 5 twin-jet electro polisher

3.4.1.2 Focused Ion Beam (FIB) milling

To measure the chromium depletion at specific grain boundaries, TEM samples were fabricated by focused ion beam (FIB) on an FEI Quanta 3D FEG FIB as shown in Figure 3-7. The FIB machining procedure involves platinum deposition, milling, lifting and thinning. Firstly, a platinum layer was deposited perpendicularly on the target grain boundary. Secondly, trenches on either side of the platinum deposit were dug out using a high ion current at the beginning then decreasing the beam current as the milling gets close to the platinum layer. After digging the trench, the lamella edge was cut through all around but leaving a bit to keep the lamella with the bulk sample. Then the lamella was attached to a copper TEM grid. Finally, the sample was thinned with a small ion beam current. To reduce ion damage induced by higher energy ion bombardment, cleaning with a low ion beam energy and current of 5 kV and 48 pA was conducted.

Figure 3-7 FEI Quanta 3D FEG FIB

3.4.2 STEM-EDS

To characterise the extent of element segregation to the grain boundary, which is related to the DOS, STEM-EDS was utilised. An FEI Tecnai-F20 TEM (Figure 3-8(a)) with the accelerating voltage of 200 kV and equipped with an Oxford EDS detector was used to measure the element segregation at grain boundaries in thermally sensitised samples prepared by twin-jet. The minimum electron beam probe diameter is about 1 nm. A double tilt low background holder was used and the TEM sample tilted to 15 degrees to maximise the X-ray collection efficiency. An FEI Talso F200 TEM (Figure 3-8(b)) which was equipped with four Super-X EDS detectors was used to measure the chromium depletion on TEM samples prepared by FIB. The four EDS detectors are evenly distributed around the sample, which collect X-ray signals at a large range of tilting angle.

The target grain boundary was adjusted to the edge-on condition as shown in Figure 3-9. This reduces the magnitude to which the grain matrix dilutes the measured grain boundary concentration. Sample drift correction was applied to all segregation measurements by

applying the auto-lock function in the Aztec software. All segregation measurements were conducted on random grain boundaries and at least 50 nm away from any present chromium carbide. The chromium profile was obtained by STEM-EDS line scan across the grain boundary.

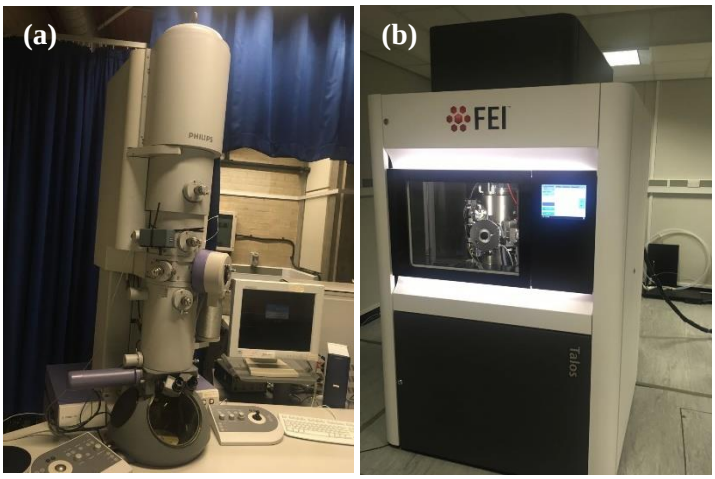

Figure 3-8 The TEM utilised in this work: (a) Tecnai-F20, (b) Talos F200.

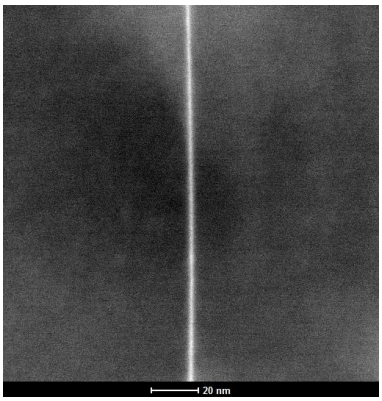

Figure 3-9 High-Angle Annular Dark Field (HAADF) image of an ‘edge-on’ grain boundary.

4 The role of Si in chromium depletion and sensitisation of model alloys

To study the effect of Si on chromium depletion and sensitisation, the model alloys were deliberately sensitised by solution annealing at 1050 °C with subsequent ageing at 650 °C for various times from 10 minutes to 200 hours. The microstructure and precipitates of solution annealed and aged model alloys were characterised. The magnitude of chromium depletion at the grain boundary was measured by STEM-EDS on twin-jet polished TEM samples. The DOS was measured by the DL-EPR test followed by a sensitisation morphology examination using SEM.

4.1 Material characterisation

The microstructure of the investigated alloys, principally the grain structure and precipitation, plays an important role in the thermally induced elemental segregation and sensitisation. To have a better understanding of the investigated alloys under the different heat treatment conditions described in section 3.1, the microstructure and secondary phases are reported here.

4.1.1 Grain structure of the model alloys

Typical low and high magnification BSE images of the model alloys after solution annealing at 1050 °C for 30 minutes are shown in Figure 4-1. Figure 4-1(a) and (c) show that the grain size of alloys A and B after annealing is uniform throughout the whole sample. Many chromium oxides (black particles, indicated by red arrow in Figure 4-1(b)) are observed in the matrix. They might be formed during the fabrication process. As shown in Figure 4-1(b) and (d), which are localised areas from Figure 4-1(a) and (c), respectively,

lots of in-grain twins are observed which might be produced as a result of recrystallization and grain growth during the high temperature annealing. The average grain size of alloys A and B is 18.5 µm and 17.4 µm respectively, which is measured according to the standard ISO 643:2003 [184]. The white particles with irregular shape are shown to be niobium carbides in section 4.1.2.1. Figure 4-1(e) is a BSE image of alloy C after annealing at 1050 °C, which shows that the grain size is not uniform. Figure 4-1(f) is a localised area of Figure 4-1(e), which shows the microstructure of the small grains. The average size of small grains in alloy C is 15.6 µm which is very close to the grain size in alloys A and B, whereas the average size of the large grain is up to about 120 µm.

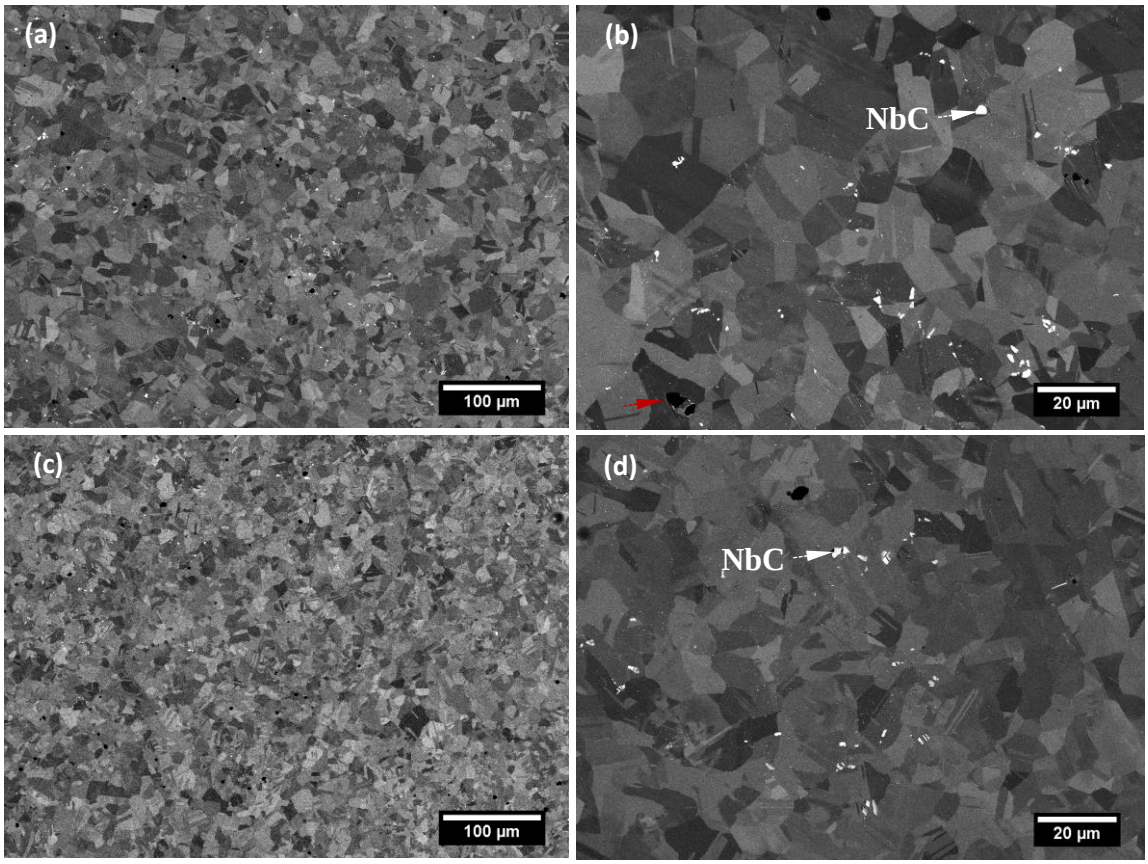

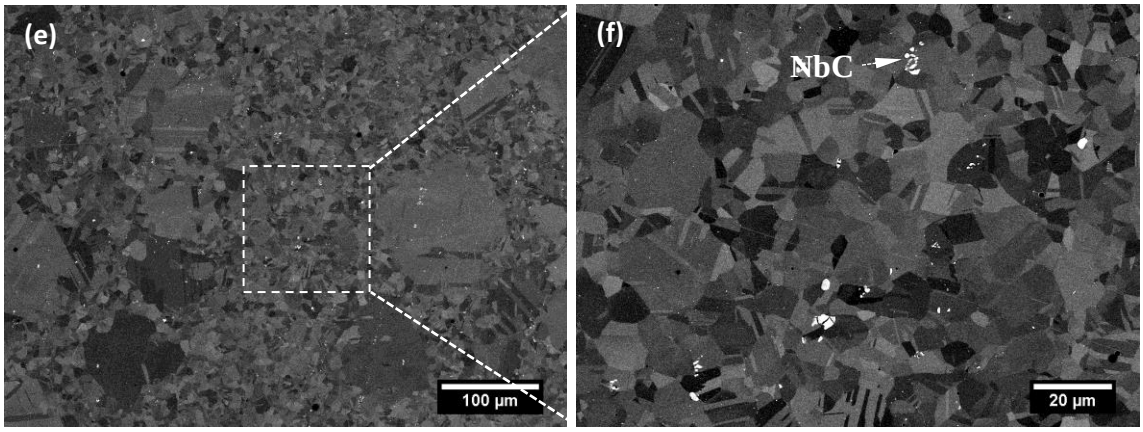

Figure 4-1 BSE micrographs showing the microstructure of the model alloys solution annealed for 30 minutes at 1050 °C: (a)(b) alloy A, (c)(d) alloy B and (e)(f) alloy C.

The images in Figure 4-2 show the grain structure of alloy A after the solution annealing and then ageing at 650 °C for 1 hour, 5 hours and 24 hours. Their grain structures are similar to each other and uniform throughout the whole sample. No obvious grain growth has been found when ageing at 650 °C for up to 24 hours. Niobium carbides with bright contrast are observed in all the samples after the ageing.

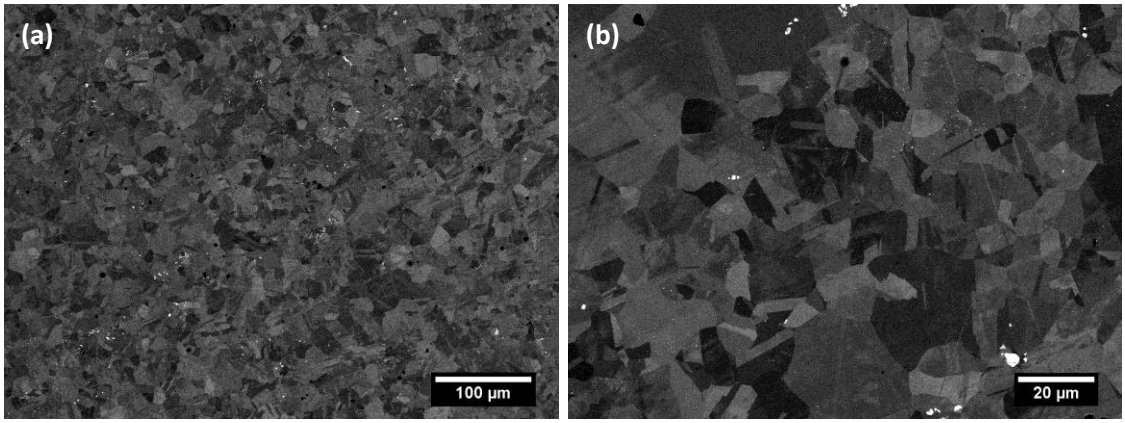

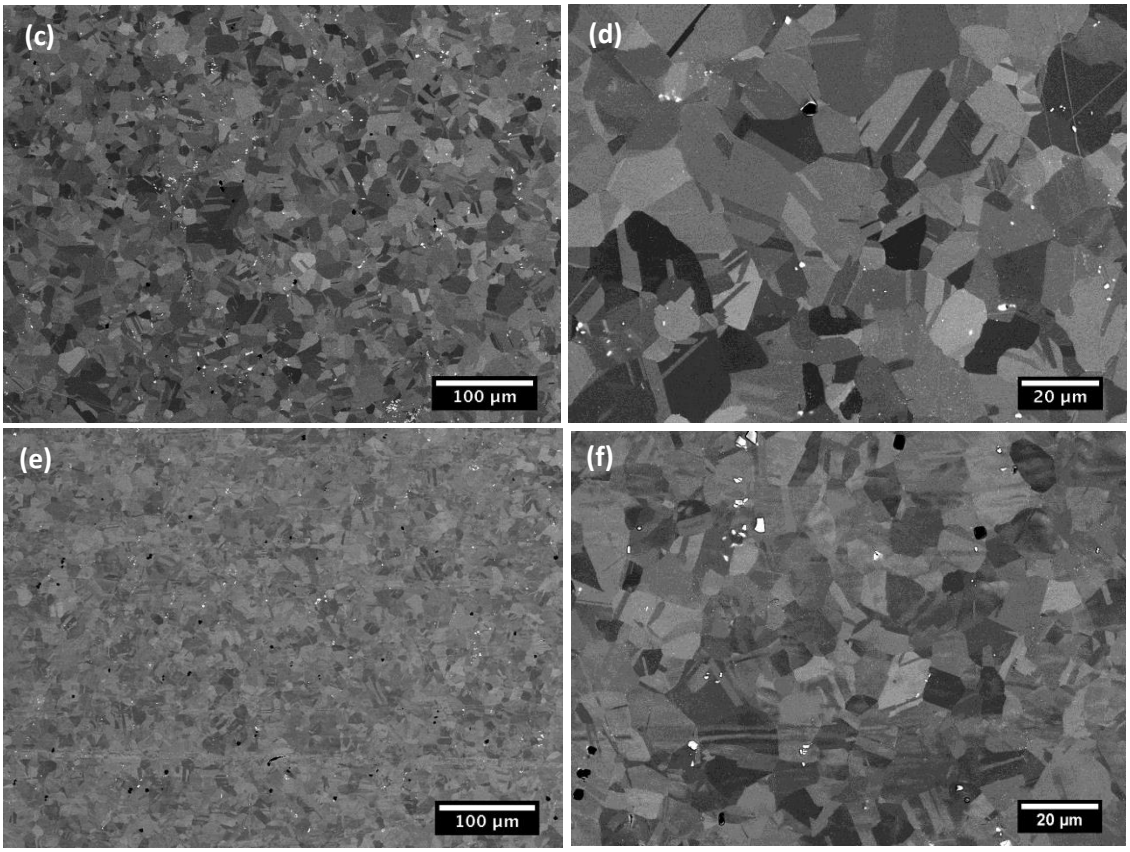

Figure 4-2 BSE micrographs showing the microstructure of alloy A solution annealed at 1050 and then aged at 650 °C for: (a)(b) 1 hour, (c)(d) 5 hours, (e)(f) 24 hours.

The images in Figure 4-3 show the grain structure of alloy B after ageing at 650 °C for 1 hour, 5 hours, 24 hours and 200 hours. Figure 4-3(a), (c) and (e) are low magnification images, which show that the grain size is still uniform throughout the sample and no obvious grain growth is observed when the ageing time increases up to 200 hours at 650 °C. Figure 4-3(b), (d) and (f) are higher magnification images. The grain structure of alloy B is similar to that of alloy A in Figure 4-1. Niobium carbides, which are the white particles, remain in the alloy after the ageing at 650 °C.

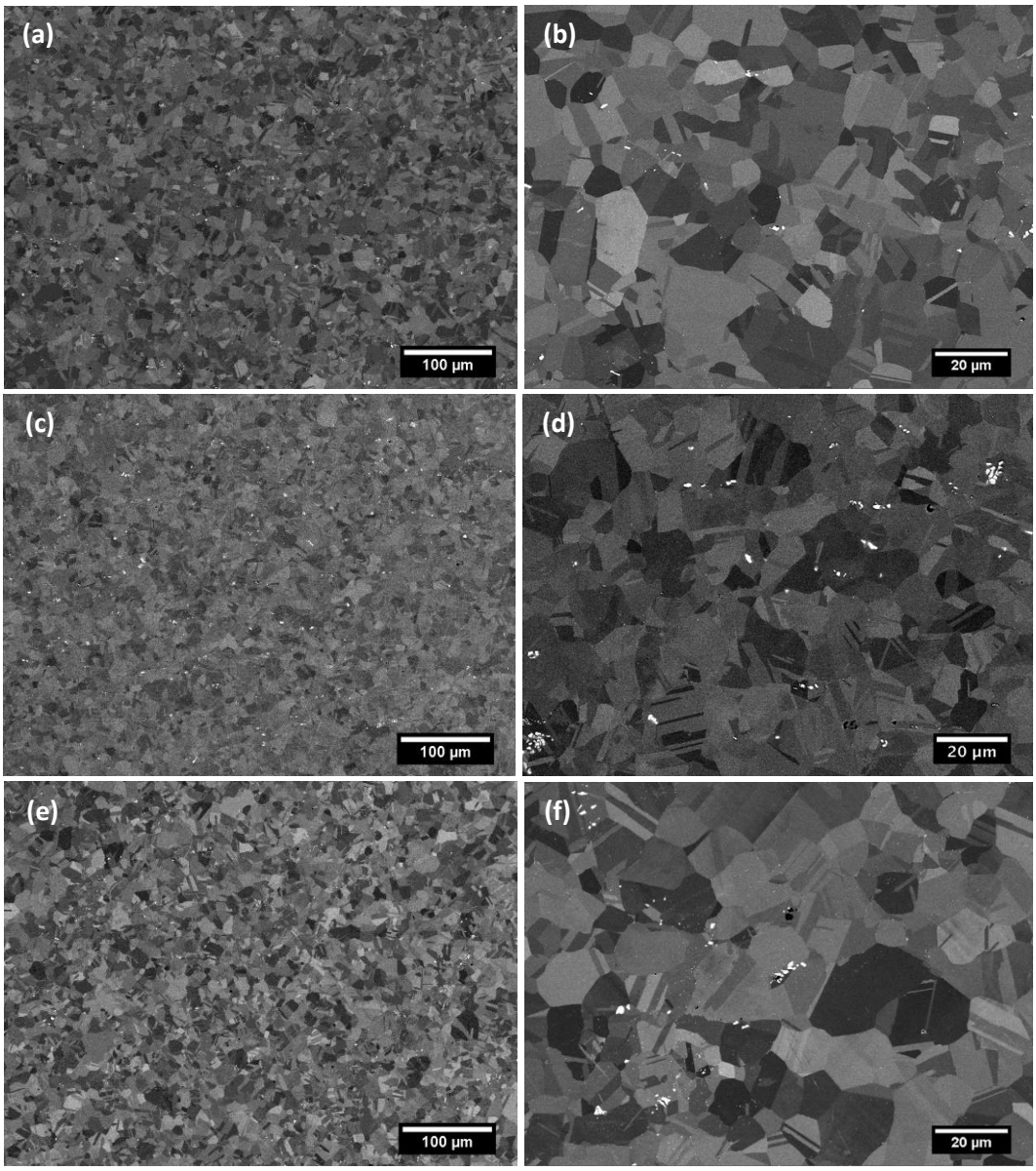

Figure 4-3 BSE micrographs showing the microstructure of alloy B solution annealed at 1050 °C then aged at 650 °C for: (a)(b) 1 hour, (c)(d) 5 hours, (e)(f) 24 hours and (g)(h) 200 hours.

Figure 4-4 shows the grain structure of alloy C aged at 650 °C for 1 hour and 5 hours. As illustrated in the low magnification images (Figure 4-4(a) and (c)), the grain size is not uniform in alloy C after the ageing which is similar to the solution annealed sample in Figure 4-1(e) and (f). Figure 4-4(b) and (d) are higher magnification images that are localised area of small grains from Figure 4-4(a) and (c). Compared with the solution

annealed sample in Figure 4-1(f), no obvious grain growth is observed in the samples after ageing. The grain structure of the small grains is very similar to that of alloy A and B in Figure 4-1. Niobium carbides, which are the white particles, remain in the alloy after the ageing at 650 °C.

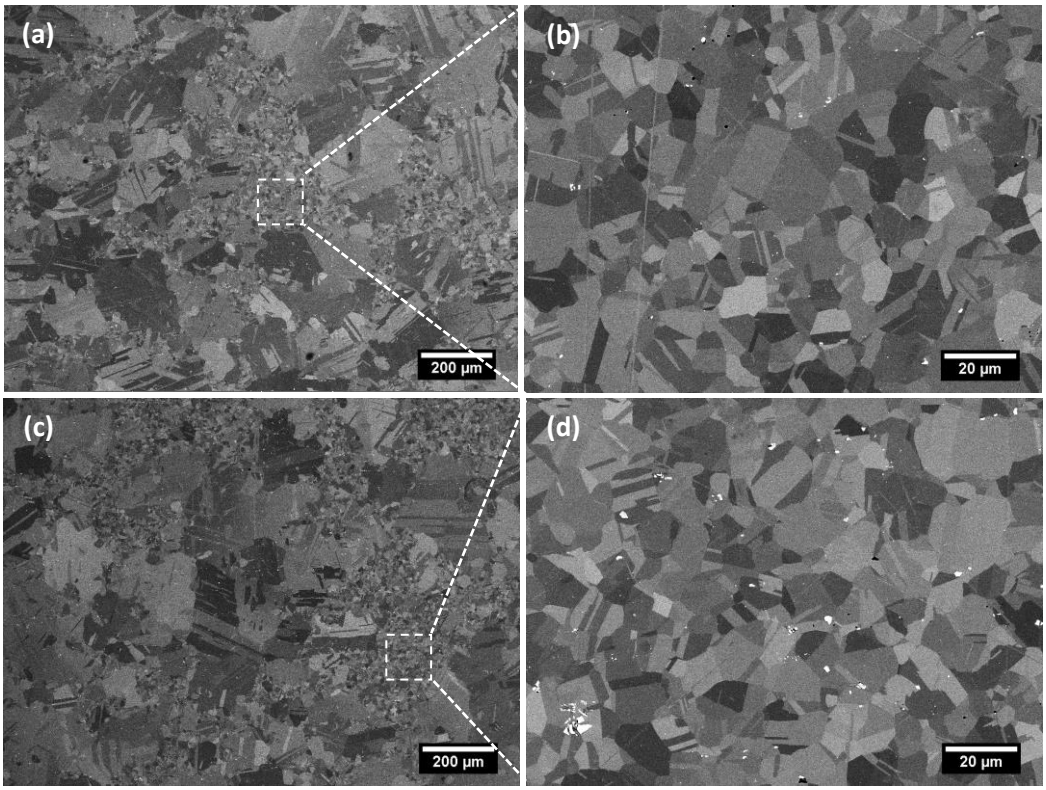

Figure 4-4 BSE micrographs showing the microstructure of alloy C solution annealed at 1050 °C then aged at 650 °C for (a)(b) 1 hour, (c)(d) 5 hours.

The distribution of random HAGBs, LAGBs and special Σ3 boundaries in the solution annealed model alloys were characterised by EBSD as shown in Figure 4-5. The different colours show grains with different orientations. The small black dots in Figure 4-5(a) are zero solution points when conducting the EBSD mapping, which are either polishing defects or small niobium carbides. The small niobium carbides protrude out of the sample surface after OP-S polishing because of the hardness difference between the niobium

carbide and the austenite matrix. To maximise the EBSD signal acquisition, the sample is pre-tilted to 70°, which makes the small spherical niobium carbides even harder to index. A large number of twins is observed in the solution annealed model alloys. As shown in Figure 4-5(b), (e), (h) and (k), the majority of grain boundaries are identified as Σ3 boundaries (red), which suggests that this alloy has good corrosion resistance to intergranular attack. Grain boundaries in black are random HAGBs. Lots of random HAGBs are intercepted by the twin grains, which will have a beneficial effect on the resistance to intergranular corrosion from the perspective of grain boundary engineering [89]. The EBSD maps also confirm that the grain size of alloys A and B is about 15-20 μm which is in agreement with Figure 4-1(b). Figure 4-5(g), (h) and (i) are EBSD maps from a large area of alloy C; the grain size is not uniform in the sample which is in agreement with Figure 4-1(e) and (f). Figure 4-5(j), (k) and (l) are EBSD maps of a localised area of Figure 4-5(g), (h) and (i), which show the grain structure of the small grains. The small grains in alloy C are about 15-20 μm across which is similar to alloys A and B; the large grains are about 120 μm. The area fraction of large grains is larger than that of small grains.

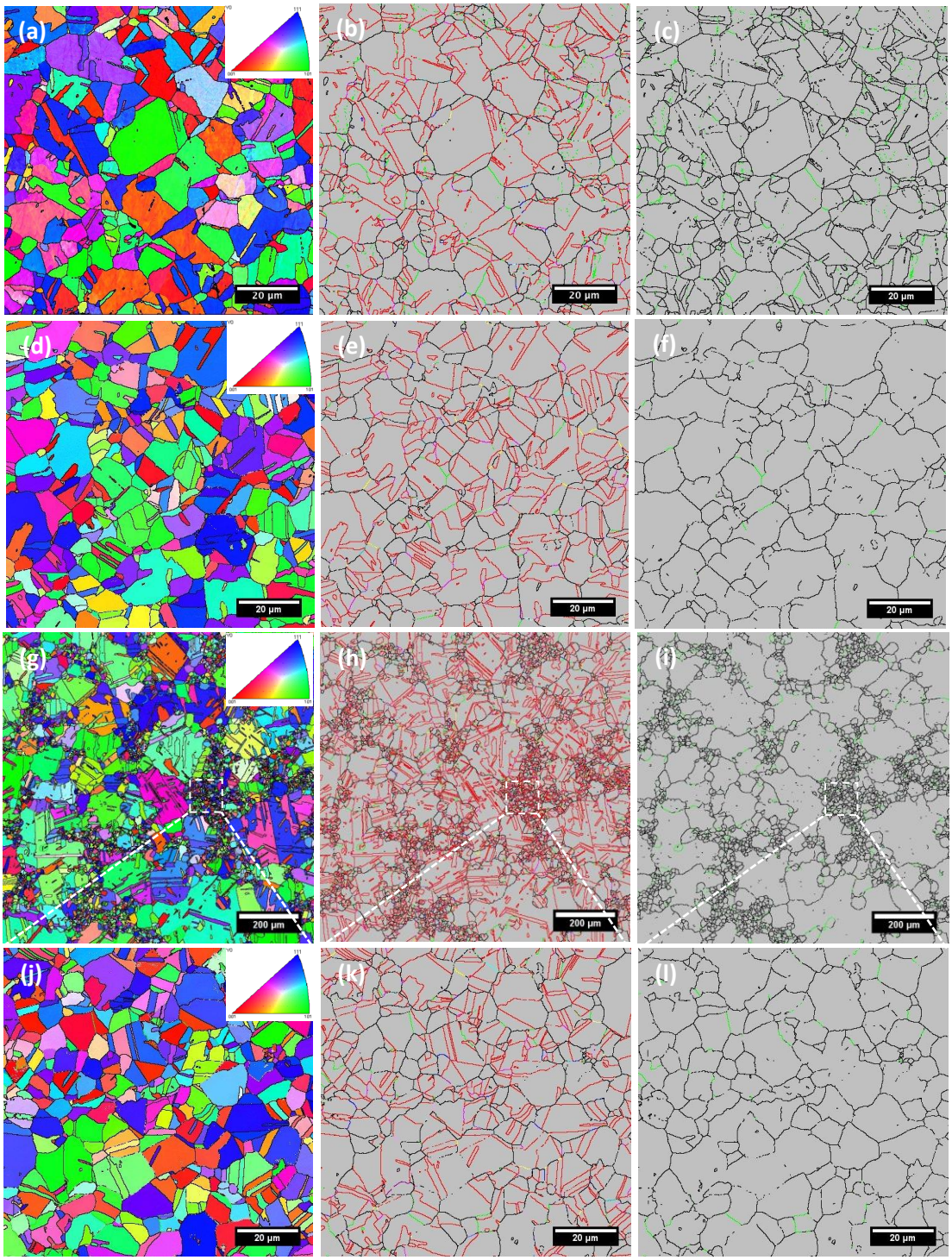

Figure 4-5 EBSD maps obtained from the model alloys annealed at 1050 °C, (a)-(c) from alloy A, (d)-(f) from alloy B, (g)-(l) from alloy C; (a), (d), (g) and (j) are orientation maps in the Y direction (rolling direction). The top-right inset indicates the colour code for the inverse pole image, (b), (e), (h) and (k) show grain boundaries shown in various colours: Σ3 and Σ9 boundaries are red and pink, random HAGBs and LAGBs are black and lime green; (c), (f), (i) and (l) show random grain boundary maps which excludes the CSL boundaries.

4.1.2 Precipitates

The materials investigated in this thesis are niobium stabilized austenitic stainless steels. A large number of niobium carbides were nucleated during the fabrication of these materials, which could eliminate the free carbon in the matrix, and improve their intergranular corrosion and creep properties. Without ageing, the precipitates in the alloy were dominated by niobium carbides after the solution annealing at 1050 °C. After ageing at 650 °C, chromium carbide started to nucleate at the grain boundary in a short time (about 10 minutes). In alloy C which contains 2.25 wt.% Si, G phase was observed both at the grain boundary and in the matrix. Niobium carbide, $M_{23}C_6$ and G phase were briefly characterised in this section using TEM bright field (BF) and dark field (DF) imaging, electron diffraction and EDS.

4.1.2.1 Niobium carbide

Figure 4-6(a) is a BSE image obtained from alloy A annealed at 1050 °C, which shows lots of irregularly shaped white precipitates (1-4 μm). A number of small white spherically shaped precipitates (50 nm-1 μm) are also observed in Figure 4-6(b) which is a higher magnification BSE image. Figure 4-6(c) is an EDS spectrum obtained from one of the big precipitates indicated by the white circle in Figure 4-6(a), which shows only carbon and niobium peaks. This suggests that the large precipitates are niobium carbides.

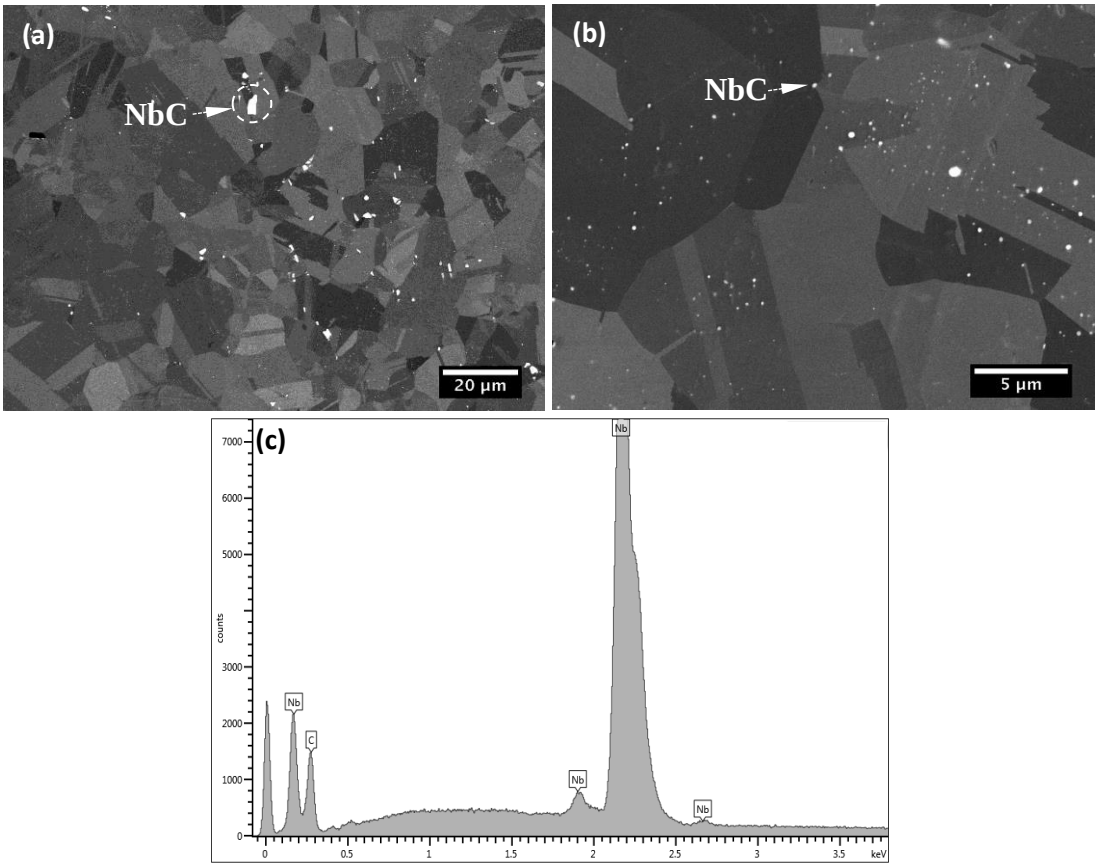

Figure 4-6 BSE images of alloy A solution annealed at 1050 °C at (a) low and (b) high magnification; (c) an EDS spectrum of the large white precipitate indicated by a circle in (a).

Figure 4-7(a) and (b) are TEM BF and HAADF images. They show a number of small spherical niobium carbides after the 1050 °C solution anneal. Figure 4-7(c) is an EDS spectrum obtained from a niobium carbide, indicated by a white arrow, at the edge of the thin area. High niobium and carbon peaks are observed on the spectrum, which indicates that these small particles are likely niobium carbides.

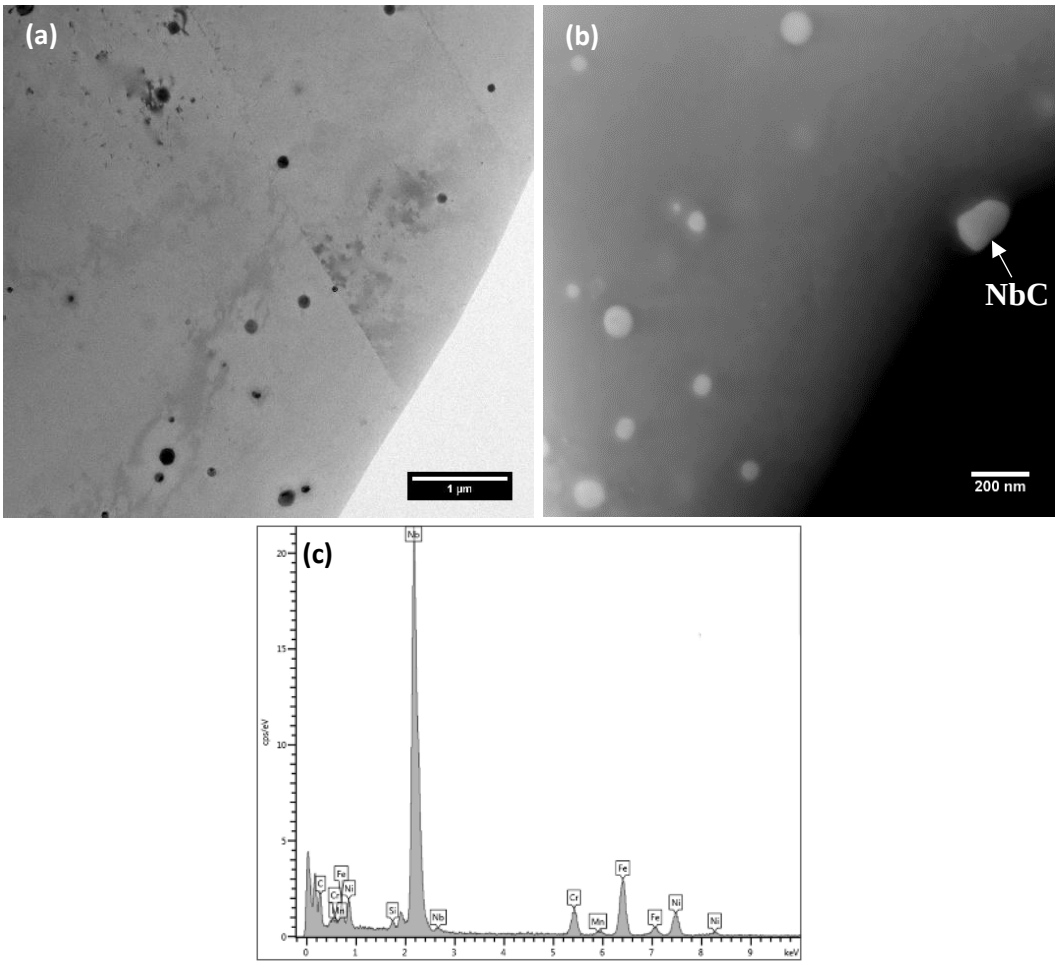

Figure 4-7 TEM images obtained from alloy A solution annealed at 1050 °C: (a) BF image, (b) HAADF image, (c) EDS spectrum obtained from the particle indicated by the white arrow in (b).

Figure 4-8 shows the STEM BF images of alloy B annealed at 1050 °C followed by 5 hours ageing at 650 °C. Figure 4-8(b) is a localized area of Figure 4-8(b), which shows a number of small (50-100 nm) precipitates along the grain boundary as indicated by white arrows. These small intergranular precipitates are elongated along the grain boundary and might have an effect in inhibiting the grain growth. Figure 4-8(c) is an EDS spectrum from one of the intergranular precipitates, which shows a high niobium peak. This suggests that they might be niobium carbides. The partial dissolution of niobium carbides during the solution

annealing at 1050 °C increases the niobium concentration in the matrix. During ageing, the supersaturated niobium atom migrates to grain boundary to form new niobium carbide.

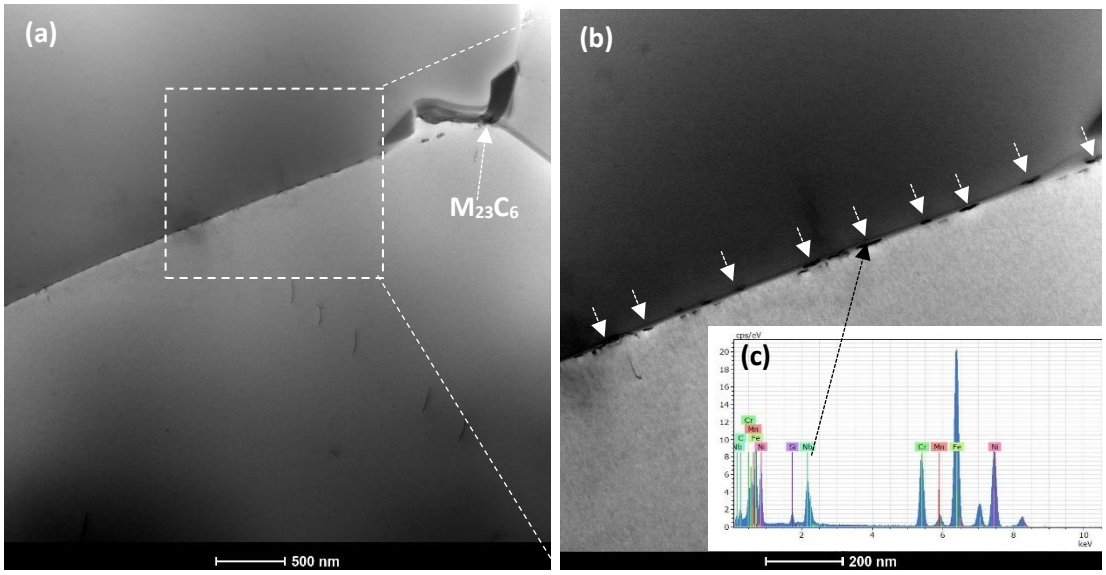

Figure 4-8 (a)(b) STEM BF images of alloy B aged for 5 hours at 650 °C, (c) an EDS spectrum obtained from a small precipitate at the grain boundary.

4.1.2.2 Chromium carbide

Figure 4-9 shows the BSE images obtained from the model alloys solution annealed at 1050 °C without ageing, which shows that the grain boundaries are free from chromium carbide after the solution annealing. The white particles are all niobium carbides.

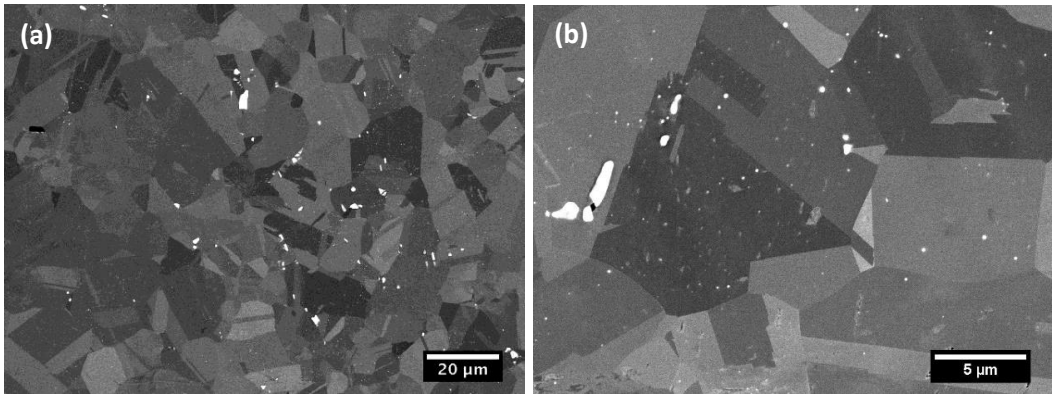

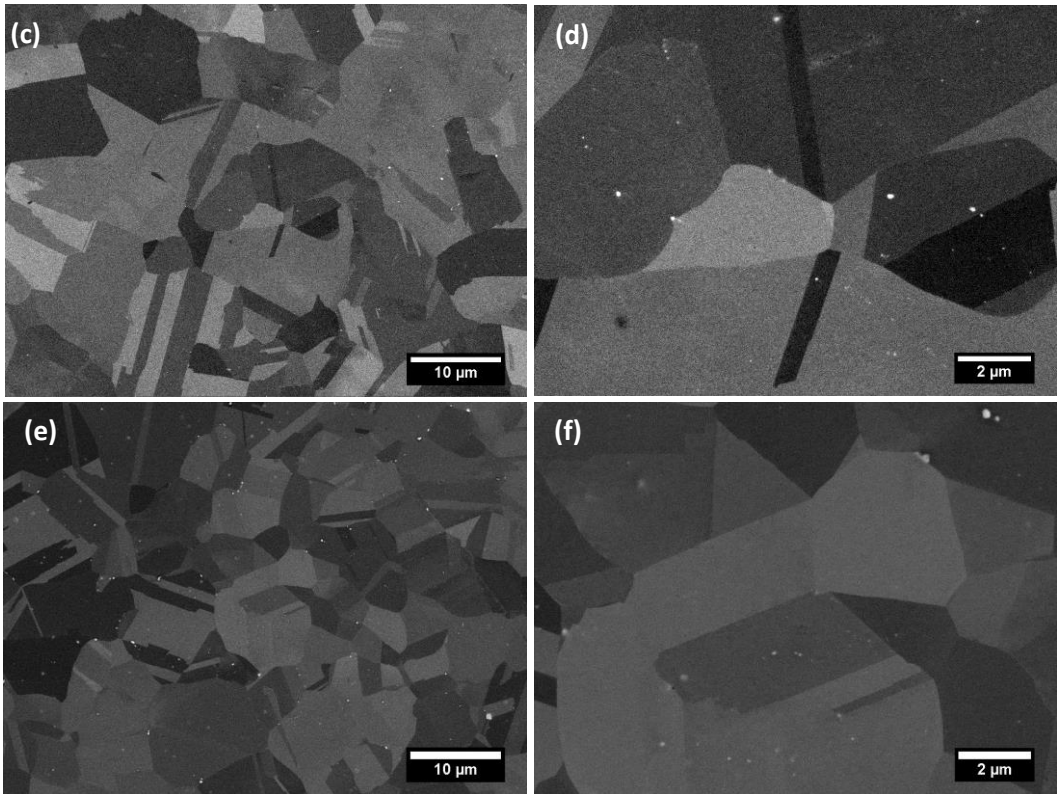

Figure 4-9 BSE micrographs obtained from the model alloys solution annealed at 1050 °C: (a)(b) alloy A, (c)(d) alloy B, (e)(f) alloy C.

Figure 4-10 shows the BSE images with the chromium carbides at the grain boundaries in the model alloys solution annealed with subsequent ageing at 650 °C for 5 hours. As illustrated in the figure, a number of discrete precipitates in dark contrast indicated by white arrows are formed at random grain boundaries after 5 hours ageing. The elemental contrast (Z contrast) of the BSE image gives chromium carbides at the grain boundary dark contrast because of the lower atomic number of chromium than the other main alloying elements iron and nickel. Thus, these precipitates are more likely chromium carbides. No chromium carbide is observed at twin boundaries. Figure 4-10(g) is a comparison of EDS spectra between the chromium carbide and the matrix. The spectra in grey and red colours are obtained from one of the chromium carbides and its adjacent matrix, respectively, which show that the chromium and carbon peaks from the carbide are higher than that from the

matrix. Thus, these precipitates at the grain boundary are chromium rich. The following results confirm that these chromium rich precipitates are $M_{23}C_6$.

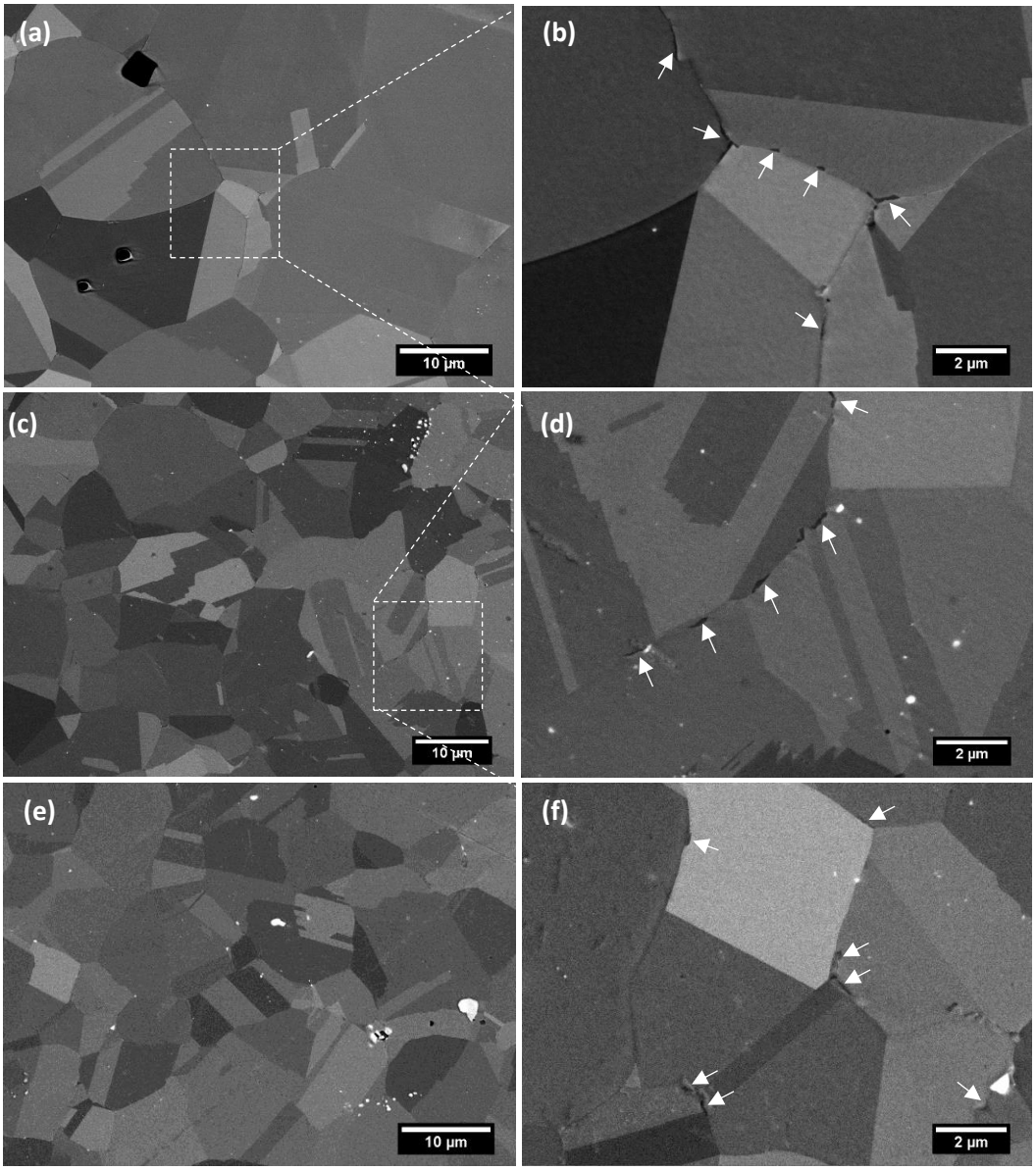

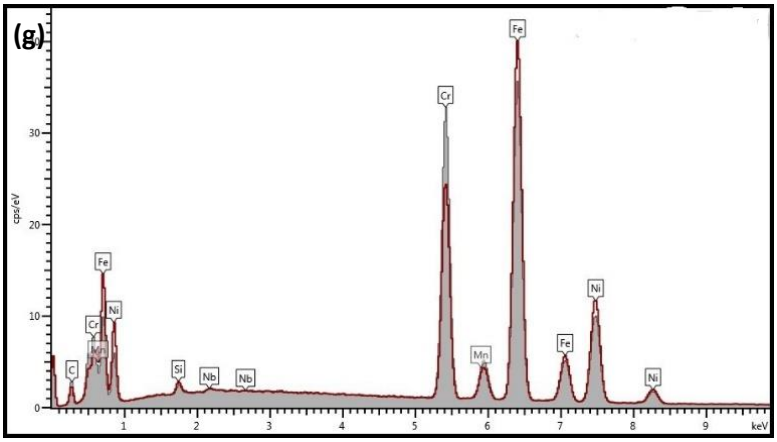

Figure 4-10 BSE micrographs obtained from the model solution annealed at 1050 °C then aged at 650 °C for 5 hours: (a)(b) alloy A, (c)(d) alloy B, (e)(f) alloy C, (g) the comparison of EDS spectra between chromium carbide and the matrix. Red spectrum was obtained from matrix and grey spectrum from $M_{23}C_6$ precipitate.

Figure 4-11(a) is a BF image showing chromium carbides at a grain boundary in alloy B aged for 5 hours at 650 °C. Figure 4-11(b) is a DF image, which shows that the chromium carbides which are coherent with the adjacent grain B are illuminated, whereas the other chromium carbides, indicated by red arrows, which are coherent with grain A, are not illuminated. Figure 4-11 (c) is a diffraction pattern having the contribution from both the austenite matrix and the chromium carbides, acquired by positioning the smallest selected area diffraction aperture, indicated by a red dashed circle in Figure 4-11(b). Two sets of diffraction patterns are obtained. The weaker spots are the diffraction pattern from the chromium carbide while the strong spots are the diffraction pattern from the matrix. Obviously, we can see that the d-spacings of the planes in the [011] zone axis of the chromium carbide are three times those of the austenite matrix, which indicates that these precipitates are $M_{23}C_6$ carbides according to the literature [32].

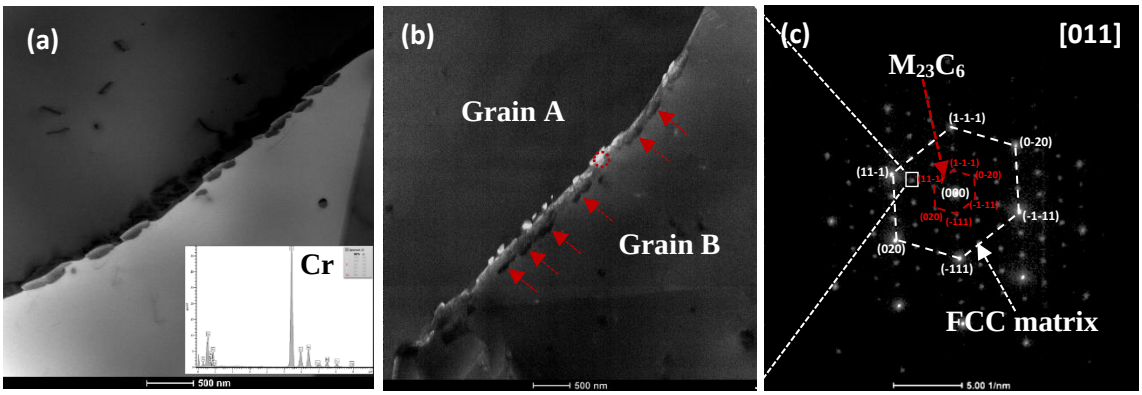

Figure 4-11 Chromium carbides at a grain boundary in alloy B solution annealed at 1050 °C and then aged for 5 hours at 650 °C: (a) BF image, (b) DF image of chromium carbides at the grain boundary, (c) diffraction pattern obtained from the area indicated by a dashed circle in (b).

4.1.2.3 G phase

Figure 4-12(a) is a HAADF image of alloy C after ageing for 200 hours at 650 °C. A precipitate with white contrast is found at the grain boundary. The EDS spectrum obtained from the white precipitate suggests that it is likely to be G phase ($Ni_{16}Nb_6Si_7$). In AGR cladding material, G phase has been reported by Powell et al. [53] after ageing at 650 °C.

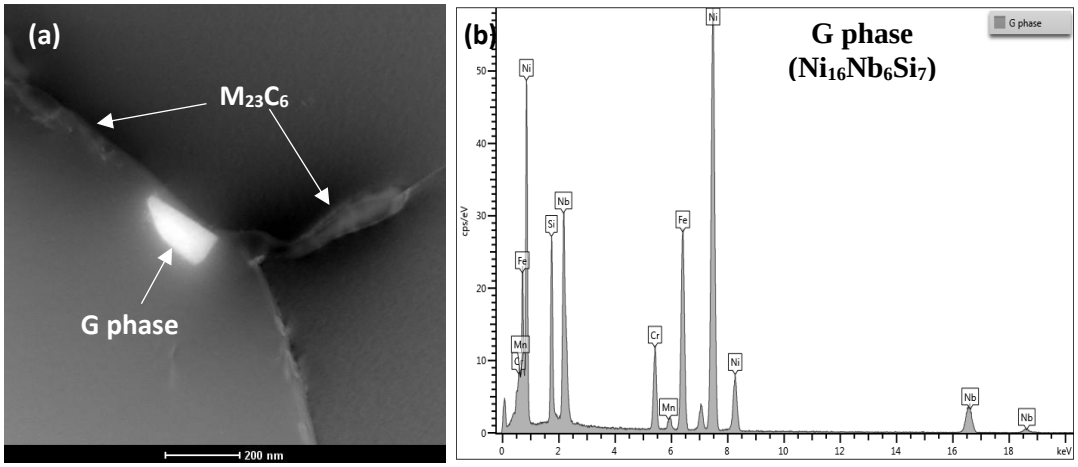

Figure 4-12 G phase in alloy C annealed at 1050 °C followed by 200 hours ageing: (a) HAADF image, (b) EDS spectrum obtained from the G phase precipitate.

Figure 4-13 shows the TEM EDS maps obtained from alloy C annealed at 1050 °C without ageing. In Figure 4-13(a) and (b), a number of precipitates with white contrast are observed in the HAADF images. As alloy C contains 2.25 wt.% Si (which is a very high

concentration in stainless steel) G phase would be expected in alloy C even without ageing. The EDS map was obtained from the whole area of Figure 4-13(b). Reported work [53] has shown that there are four kinds of precipitates found in the 20/25/Nb alloy after ageing, namely, NbC, $M_{23}C_6$, G-phase (Ni-Nb-Si) and sigma phase (Cr-Fe-Ni-Si). By comparing the EDS maps, the precipitates in Figure 4-13(b) are identified as NbC, sigma phase and G phase and arrowed in white, black and red, respectively. As the sample is only solution annealed, without ageing, no $M_{23}C_6$ precipitates are expected.

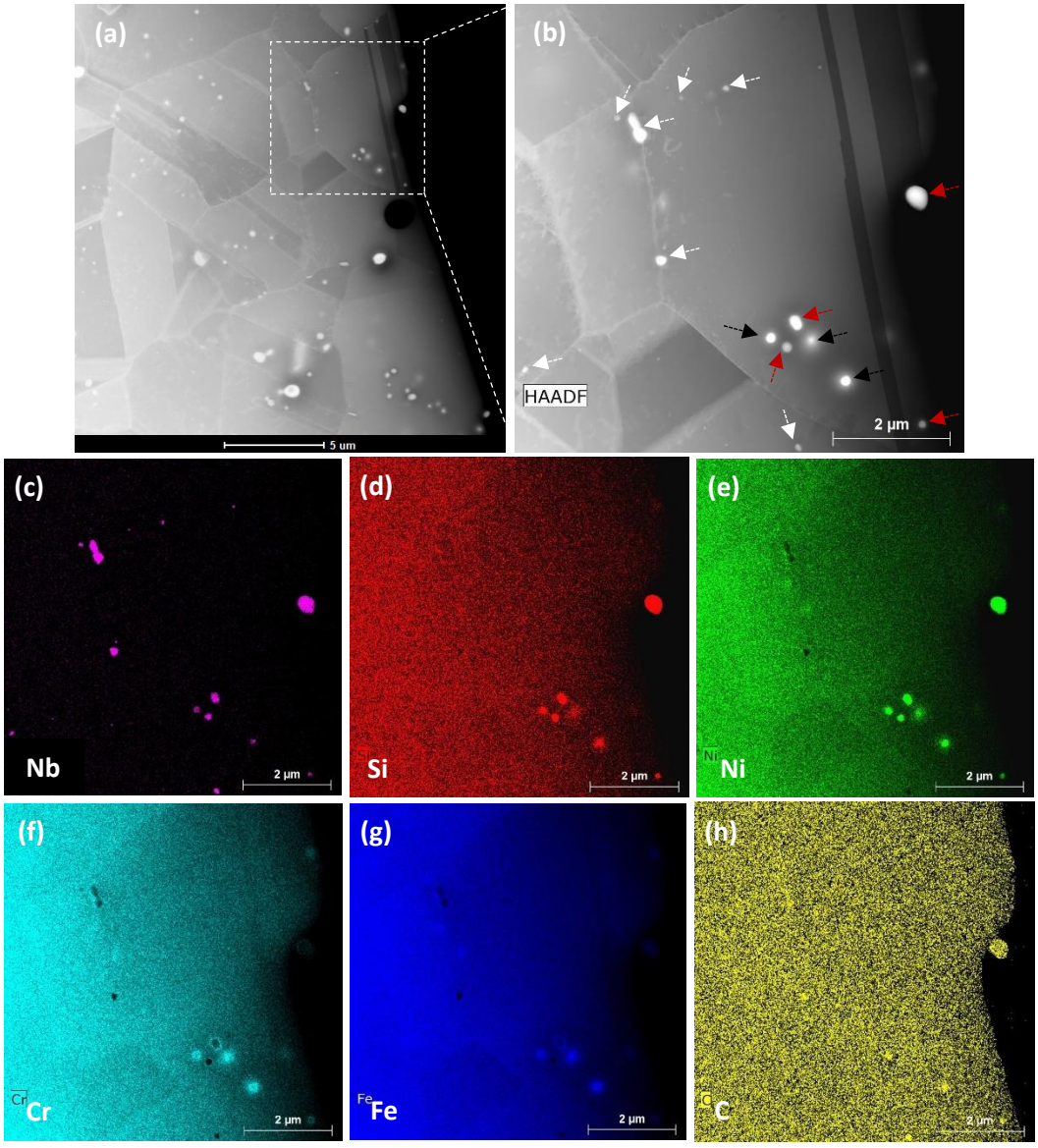

Figure 4-13 (a)(b) HAADF images obtained from alloy C solution annealed at 1050 °C, (c)-(h) EDS maps of Nb, Si, Ni, Cr, Fe and C, respectively.

The precipitates at the grain boundaries in alloy C after solution annealing at 1050 °C and then ageing for 200 hours at 650 °C are shown in Figure 4-14. Figure 4-14(a) shows that many precipitates nucleated after 200 hours ageing at 650 °C and their compositions are identified by compared the EDS maps in Figure 4-14(b)-(f). In Figure 4-14(a), the precipitates at the grain boundary indicated by blue and red arrows are $M_{23}C_6$ precipitates and G phase, respectively. We can see that most of the precipitates at the grain boundary are G phase which might have formed from niobium carbides [53].

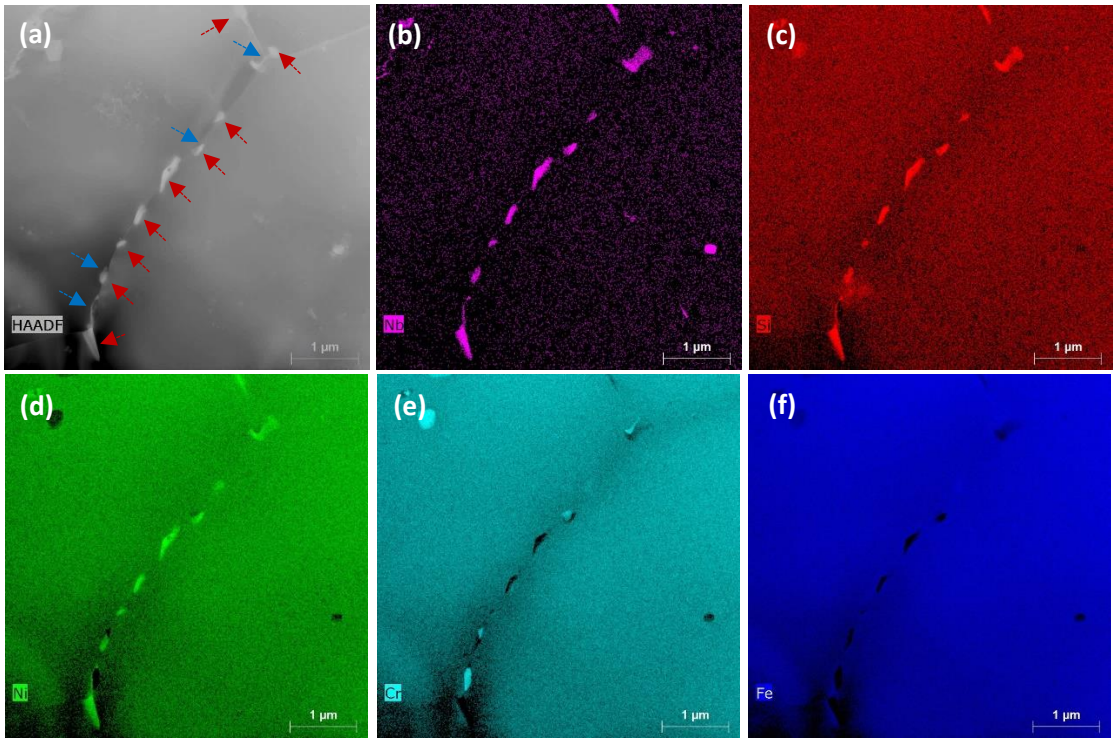

Figure 4-14 (a) HAADF image obtained from alloy C aged at 650 °C for 200 hours, (b)-(f) EDS maps of Nb, Si, Ni, Cr and Fe, respectively.

4.2 Chromium depletion profiles in thermally sensitised model alloy

Before studying chromium depletion in different alloys over a range of ageing times, chromium depletion was studied in details on 24 hours aged and 5 hours aged samples to acquire a general view of chromium depletion in the sensitised samples.

4.2.1 Chromium depletion at grain boundaries with different misorientation

Figure 4-15(a) is a HAADF image obtained from alloy A aged for 24 hours at 650 °C, which shows many chromium carbides at the grain boundaries. Figure 4-15(b) is a selected area of Figure 4-15(a), which shows the misorientation angle, measured by TKD in SEM, of two selected grain boundaries. $M_{23}C_6$ precipitates are observed at both grain boundary and triple junction. Chromium depletion profiles at the grain boundaries α and β are shown in Figure 4-15(c) and (d). Approximately the same magnitude of chromium depletion was obtained at the grain boundaries α and β which have misorientation angles of 40° and 30°, respectively. Thus, in terms of the grain boundaries α and β, no obvious difference in chromium depletion was detected.

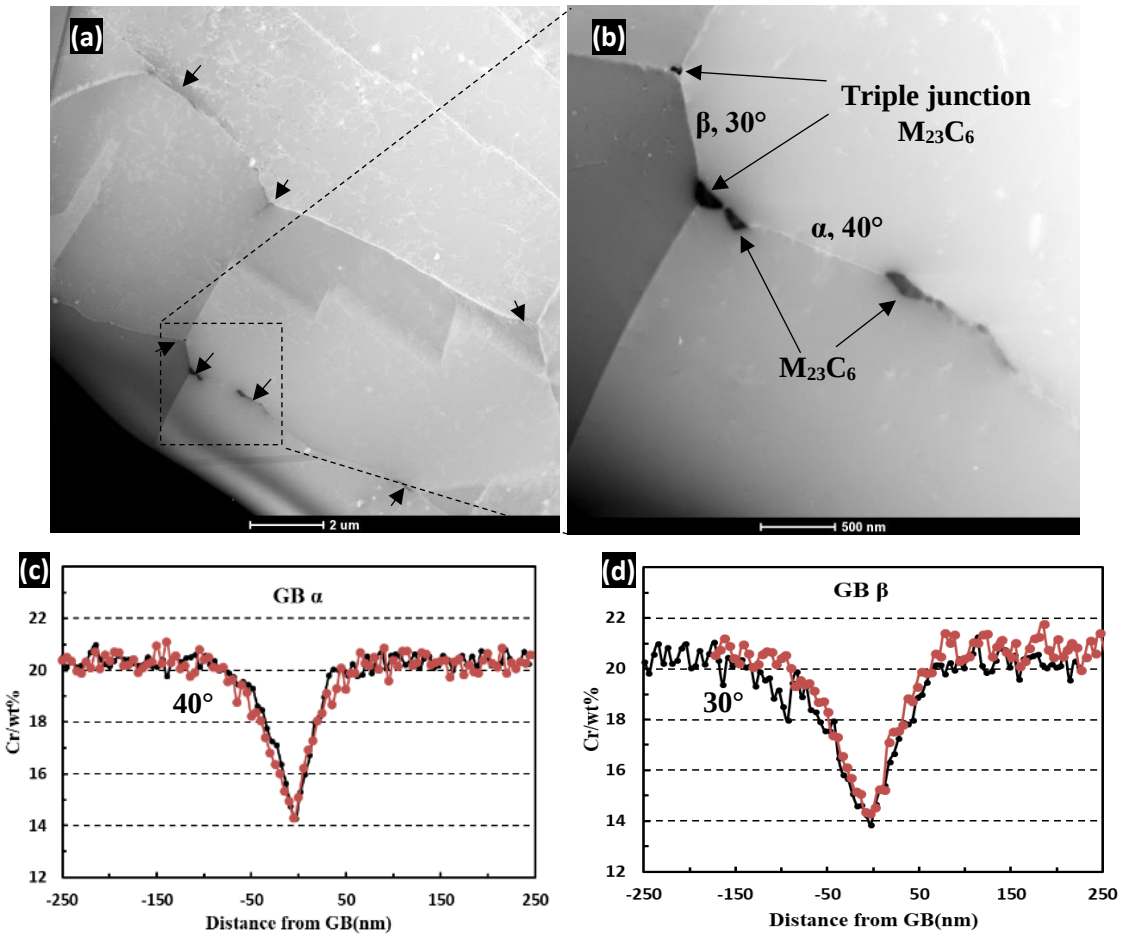

Figure 4-15 (a) and (b) HAADF images obtained from alloy A solution annealed at 1050 °C and then aged for 24 hours at 650 °C showing $M_{23}C_6$ precipitation at two selected grain boundaries α

and β. (c) and (d) are chromium depletion profiles across the grain boundaries α and β, with misorientation angles 40° and 30° respectively.

As we know that TEM sample prepared by twin-jet polishing have a wedge shape, sample thickness increases from the central hole towards the disk edge. Elemental segregation measurement by STEM-EDS is sensitive to sample thickness due to the beam interaction volume changing with different thickness. To minimised the thickness effect on segregation measurement, a FIB sample was lifted out from alloy A solution annealed at 1050 °C and then aged for 5 hours at 650 °C, which has relatively uniform thickness throughout the whole sample compared with the twin-jet prepared TEM sample. As illustrated in Figure 4-16(a), which is a HAADF image of the whole sample, $M_{23}C_6$ precipitates indicated by red arrows are found at grain boundaries. The grain boundary misorientation angle was measured by TKD in SEM as depicted in Figure 4-16(a)(b). Figure 4-16(c)-(g) are chromium depletion profiles across five grain boundaries GB-1 to GB-5. GB-1 and GB-2 are random HAGBs (black) whose misorientation angles are 27° and 34°, respectively. They have similar chromium depletion profiles in both magnitude and width. The width of chromium profile in this thesis is the range of the neighbouring grain boundary area which has lower chromium concentration than the matrix.The lowest chromium concentrations for GB-1 and GB-2 are 12.1 wt.% and 12.3 wt.%, respectively. GB-4 and GB-5 are identified as Σ11 and Σ17 boundaries with misorientation angle 27° and 61° whose lowest chromium concentrations are 13.7 wt.% and 13.8 wt.%, respectively, higher than the two HAGBs (GB-1 and GB-2). GB-3 is a Σ3 boundary that is classified as a special grain boundary and no chromium depletion is detected. As described in section 2.3.2.2, coincidence site lattice Σ grain boundaries have lower energy than the random HAGBs, which lead Σ grain boundaries to show less chromium depletion and better

resistance to intergranular attack, especially for the Σ3 boundary that is entirely immune to the corrosion test conducted in this thesis.

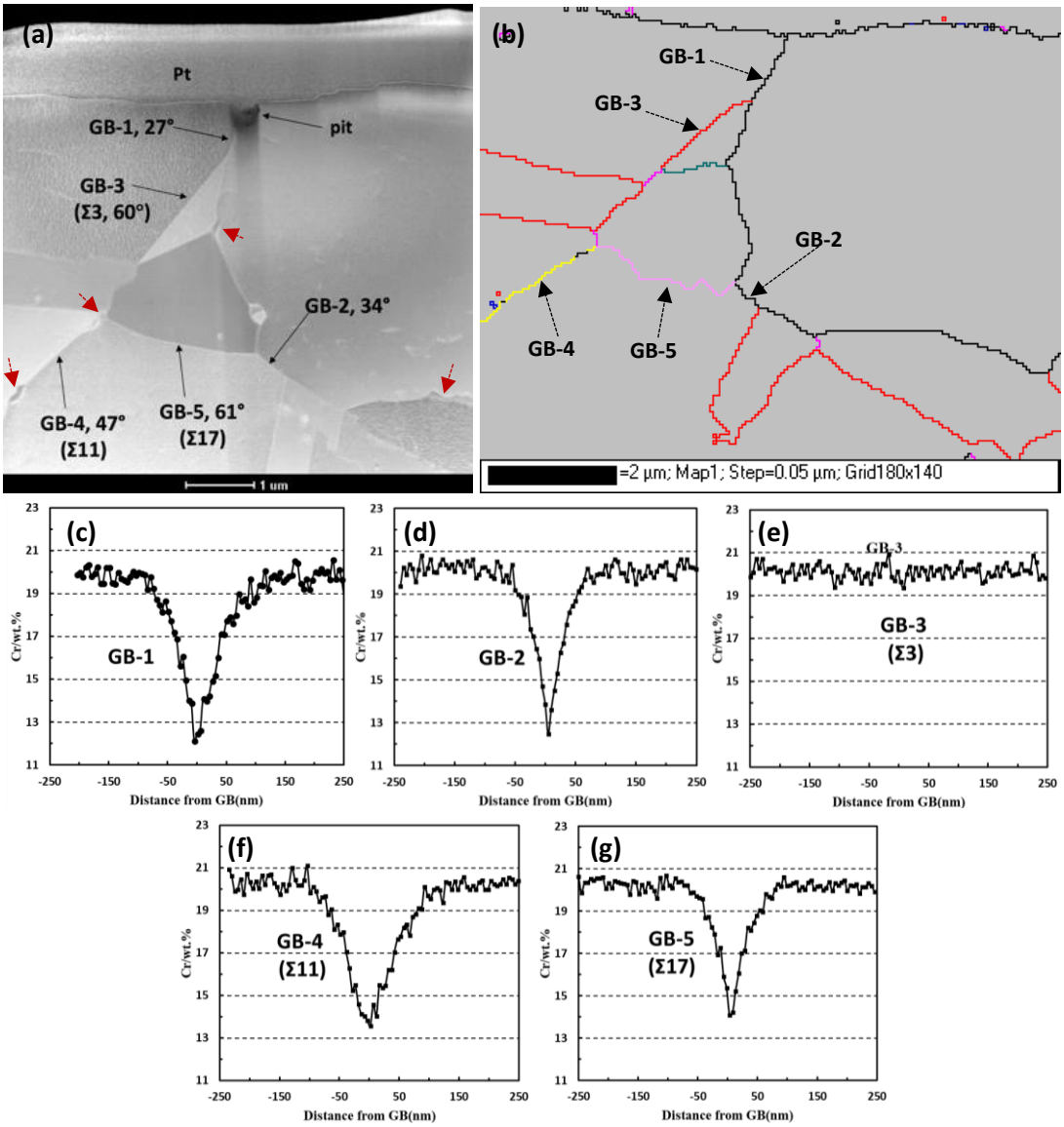

Figure 4-16 (a) HAADF image obtained from the TEM lamella which was lifted out from alloy A solution annealed at 1050 °C and then aged for 5 hours at 650 °C, (b) a grain boundary map of the FIB sample acquired by TKD showing the grain boundary type and misorientation angle, (c)-(g) the grain boundary chromium depletion profiles measured by STEM-EDS.

4.2.2 Effect of proximity to chromium carbide on chromium depletion

Figure 4-17(a), which is a schematic of the grain boundary α in Figure 4-15(b), shows the position of STEM-EDS line scans at the grain boundary from line 1 to line 4. Line 1 crosses the $M_{23}C_6$ precipitate. Line 2, Line 3 and Line 4 are about 30 nm, 292 nm and 585 nm, respectively, away from the $M_{23}C_6$ precipitate. The chromium depletion line scans are shown in Figure 4-17(b)-(e). Figure 4-17(b) shows that only one of the chromium carbide interfaces with that matrix shows obvious chromium depletion. This is supposed to be the incoherent interface. Figure 4-17(c) is line scan 2 which is very close to the $M_{23}C_6$ precipitate, about 30 nm, which shows the lowest chromium concentration is about 13.5 wt.% and chromium profile has a relative flat top. Approximately the same chromium depletion magnitude is acquired from Line-3 and Line-4 in Figure 4-17(d) and (e), which implies no obvious effect of the proximity to the $M_{23}C_6$ precipitate on the magnitude of chromium depletion.

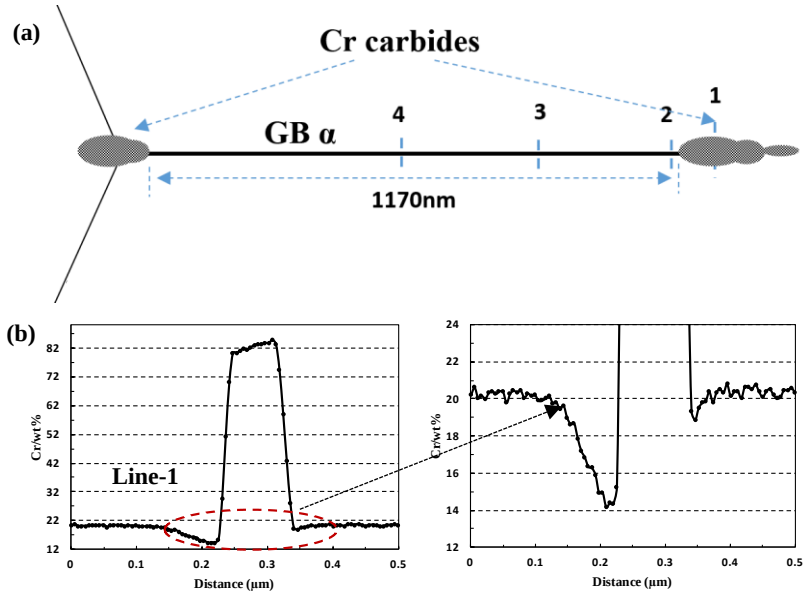

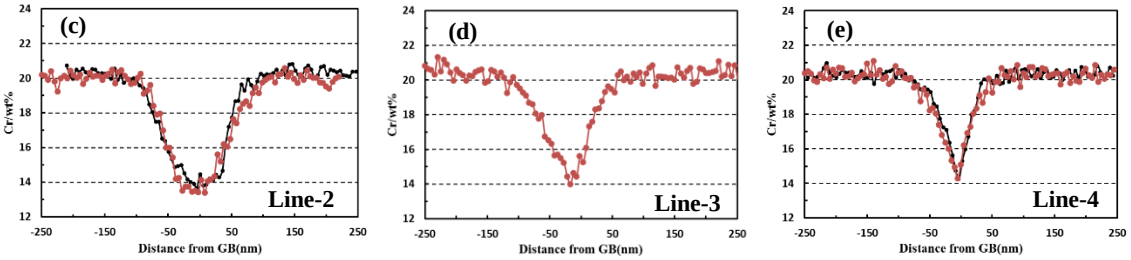

Figure 4-17 (a) Schematic of the grain boundary α in Figure 4-15 (b) showing STEM-EDS line scan positions, indicated by numbers 1 to 4 in the figure, in alloy A aged for 24 hours at 650 °C, (b)-(e) are chromium depletion profiles obtained from positions 1-4 in (a).

Figure 4-18(a) is a HAADF image of alloy A aged for the longer time of 200 hours at 650 °C. $M_{23}C_6$ precipitates are observed at the grain boundary. The selected area diffraction pattern in [011] zoon axis at the top right of Figure 4-18(a) is acquired from the coherent interface area, indicated by a white dashed circle, of the $M_{23}C_6$ precipitate, which shows the d-spacing of chromium carbide is three times that of the matrix. Thus, the interface at the right side of the chromium carbide Figure 4-18(a) is coherent; correspondingly the other side is incoherent. Figure 4-18(b) is the chromium profile across the $M_{23}C_6$ precipitate which shows that no chromium depletion is observed either at the coherent or incoherent interface. However, obvious chromium depletion is observed at the chromium carbide interface in alloy A aged for 24 hours in Figure 4-17(b). This suggests that the chromium depletion at the $M_{23}C_6$ precipitate interface has been healed by a long time ageing.

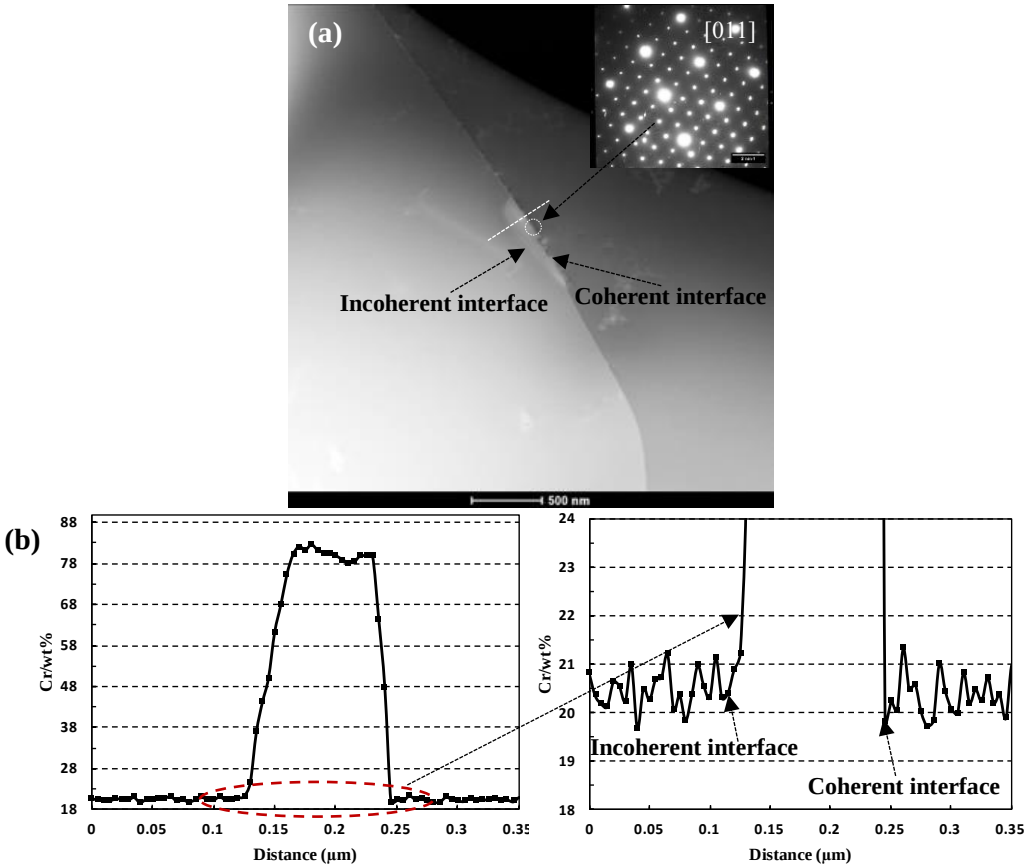

Figure 4-18 Chromium profile cross a $M_{23}C_6$ precipitate at a grain boundary in alloy A solution annealed at 1050 °C then aged for 200 hours at 650 °C: (a) HAADF image, (b) chromium profile.

4.3 Chromium depletion in model alloys with various Si contents

To investigate the effect of silicon on the chromium depletion at grain boundaries, chromium depletion was measured on the model alloys (alloy A, alloy B and alloy C) with three different silicon concentrations, namely, 0 wt.%, 0.56 wt.% and 2.25 wt.% Si, respectively. All model alloys were solution annealed at 1050 °C for 30 minutes then aged at 650 °C for a range of times from 10 minutes to 200 hours.

4.3.1 $M_{23}C_6$ precipitation and chromium depletion profile in model alloys

The $M_{23}C_6$ precipitation at the grain boundary over a range of ageing times is shown in Figure 4-19 and Figure 4-20. $M_{23}C_6$ precipitates are indicated by white arrows. As shown

in Figure 4-19(a)-(c), without ageing, no $M_{23}C_6$ precipitates are found at the grain boundary in the solution annealed samples. Figure 4-19(d) shows that $M_{23}C_6$ precipitate still not presents in alloy A after 10 minutes ageing at 650 °C while small $M_{23}C_6$ precipitates are found in alloys B and C as shown in Figure 4-19(e) and (f). As illustrated in Figure 4-19 (g)-(l) and Figure 4-20, the $M_{23}C_6$ precipitates grow and their number increases with ageing time. Figure 4-20(f), (i) and (l) show that, in alloy C, a number of precipitates with white contrast form at the grain boundary when the ageing time increases to 24 hours. The majority of these precipitates are G phase.

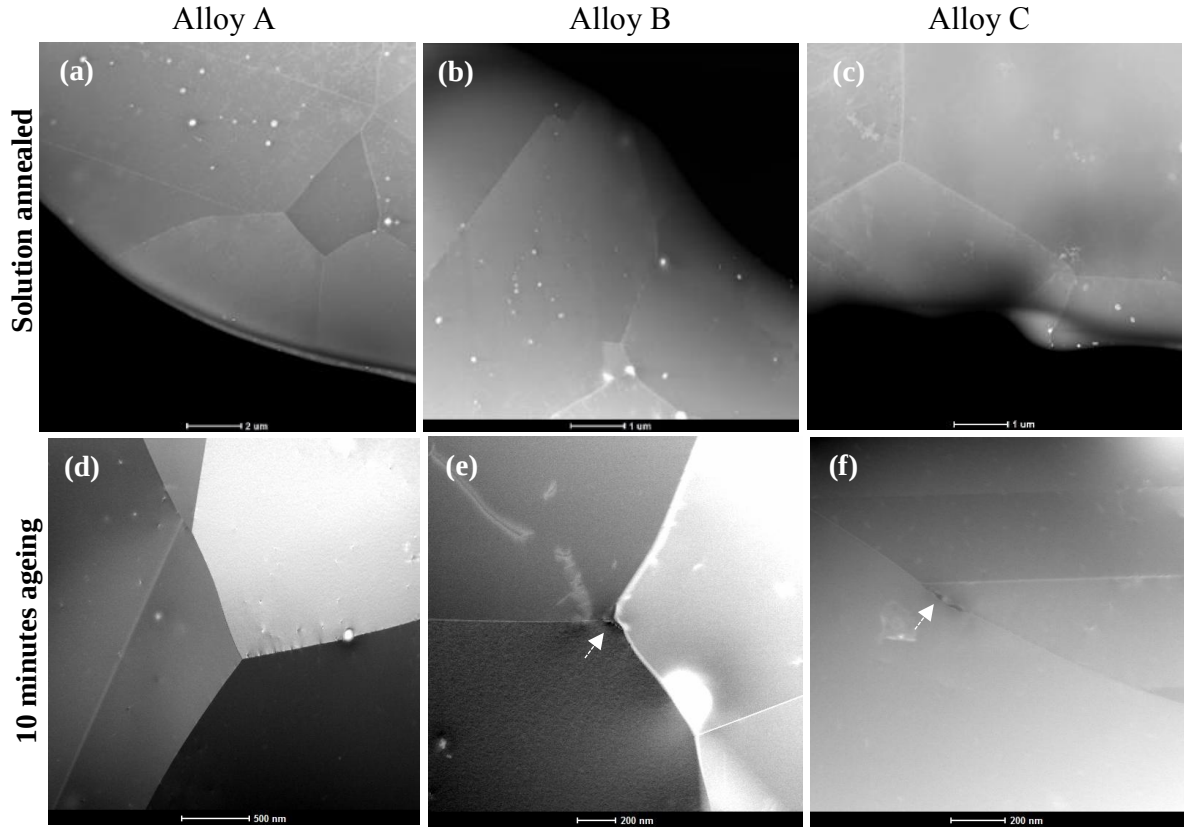

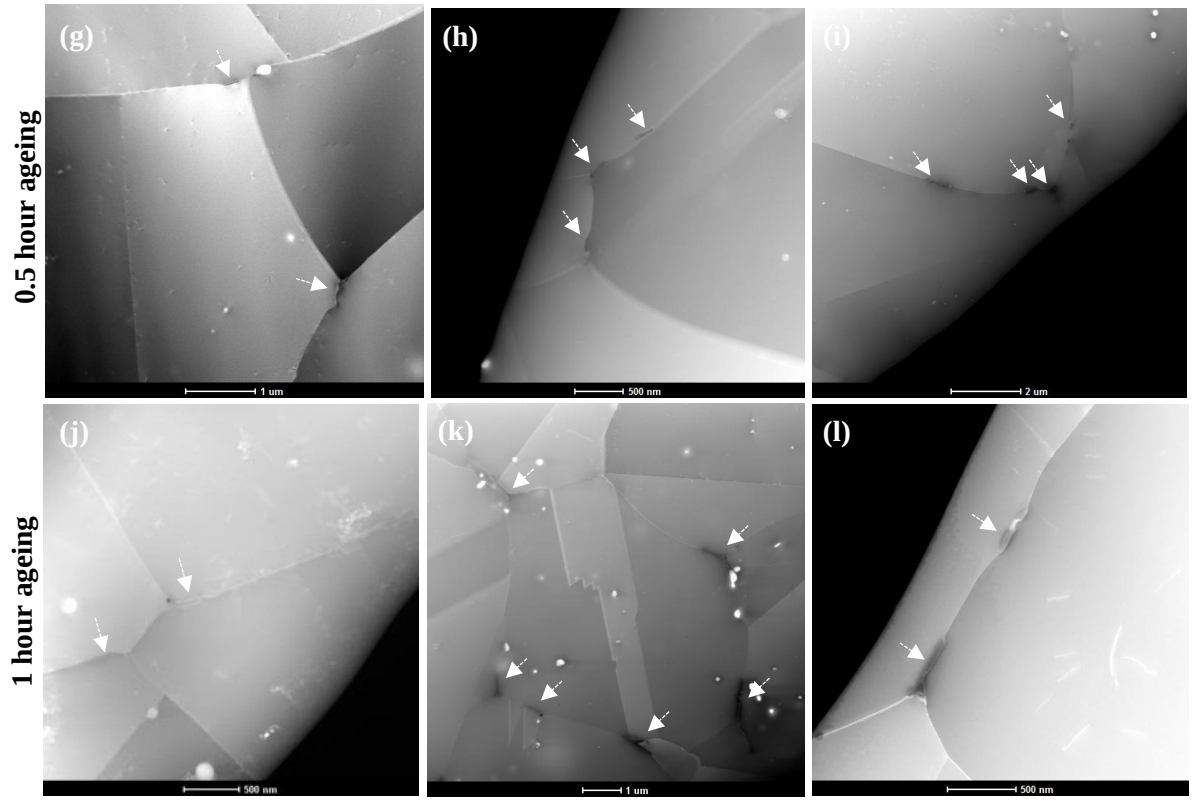

Figure 4-19 HAADF images obtained from model alloys aged at 650 °C for: (a)-(c) 1050 °C solution annealed, (d)-(f) 10 minutes, (g)-(i) 0.5 hour and (j)-(l) 1 hour.

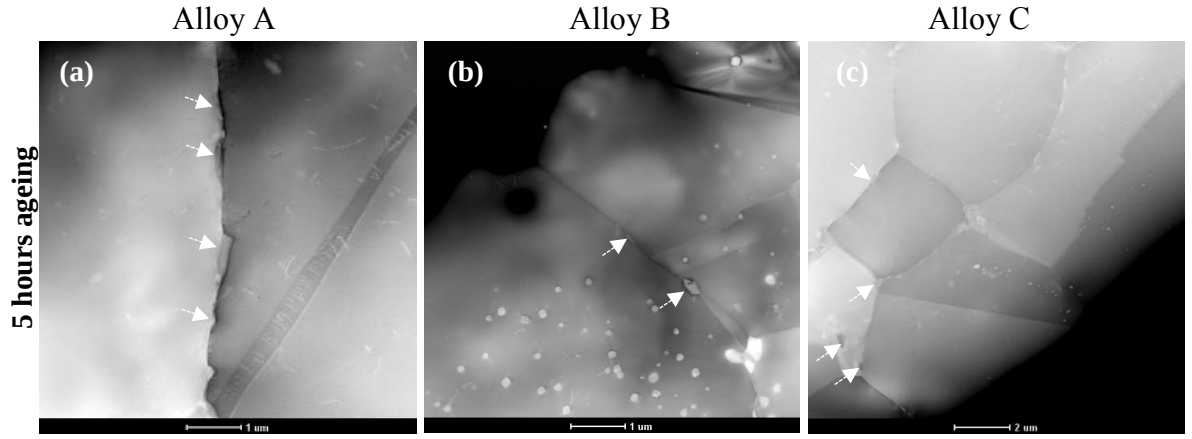

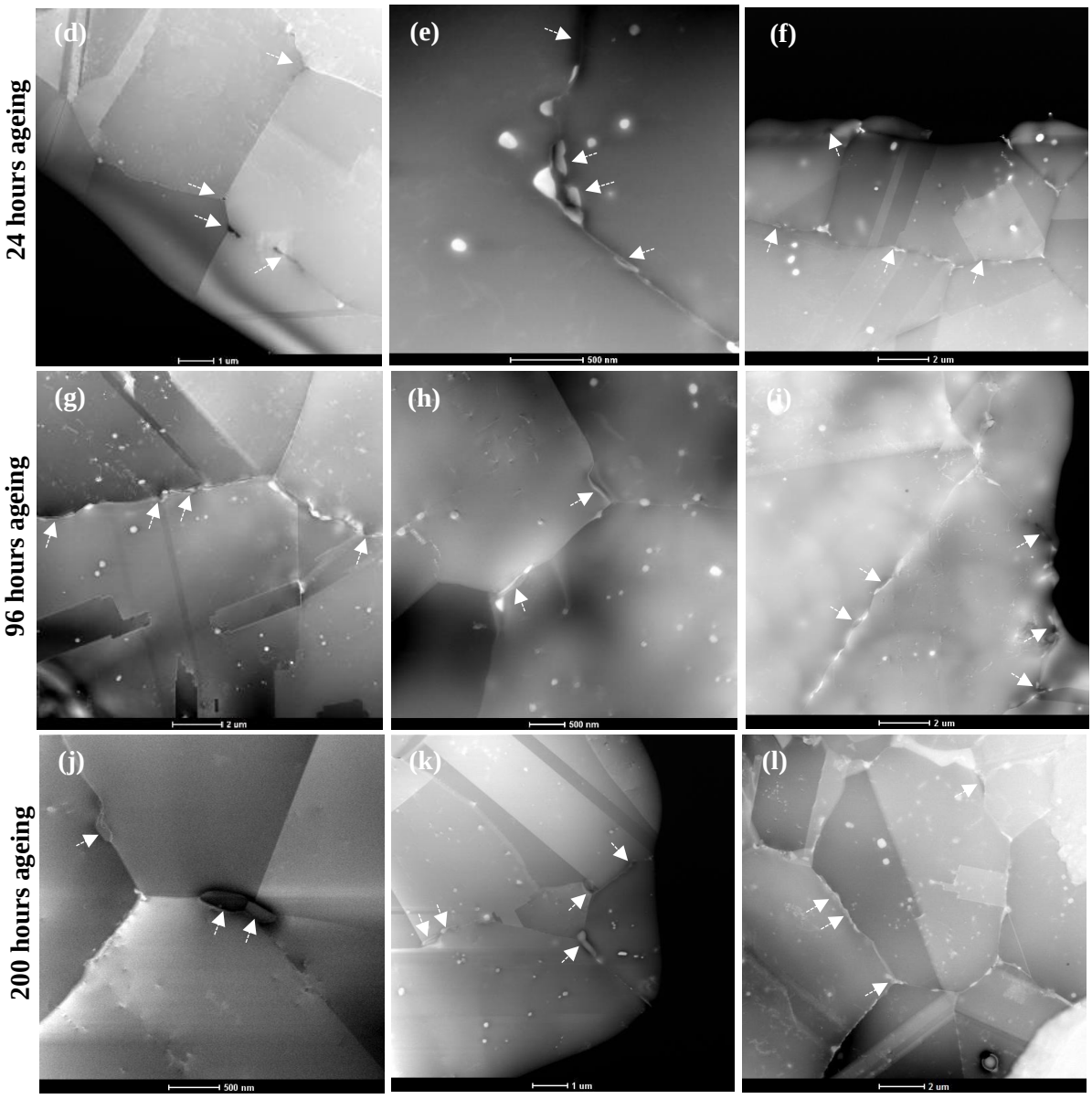

Figure 4-20 HAADF images obtained from model alloys aged at 650 °C for: (a)-(c) 5 hours, (d)-(f) 24 hours, (g)-(i) 96 hours and (j)-(l) 200 hours.

Figure 4-21 and Figure 4-22 show chromium depletion profiles at the grain boundary in all three model alloys, annealed at 1050 °C with subsequent ageing at 650 °C for a range of times from 10 minutes to 200 hours. Figure 4-19 and Figure 4-20 show that the chromium carbide distribution at the grain boundary in the aged sample is not uniform and that some of the grain boundaries are free from $M_{23}C_6$ precipitates. To make the measurements from

different grain boundaries comparable, all chromium profiles were acquired at grain boundaries with a similar chromium carbide distribution keeping the same distance between the EDS line scan position and the nearest chromium carbide. As shown in Figure *4-21*(a), (b) and (c), for 1050 °C annealed samples, without ageing, no chromium depletion is detected at the grain boundary as the cooling rate of water quenching is very high and there is no time for the formation of chromium carbide. In Figure 4-22(d), (e) and (f) are chromium profiles of model alloys aged for only 10 minutes. No chromium depletion is observed in alloy A while chromium depletion is detected in alloy B and alloy C. Alloy C shows more chromium depletion than for alloy B. As the ageing time increases to 0.5 hour, chromium depletion starts to be detected also in alloy A and the magnitude of chromium depletion increases in alloys B and C. Alloy C has the largest magnitude of chromium depletion at the grain boundary after 0.5 hour ageing. After 1 hour ageing, all three alloys exhibit a high magnitude of chromium depletion, which indicates that intergranular attack can be serious in 1 hour aged samples. The alloy C, containing 2.25% Si, shows a lower chromium concentration at the grain boundary than alloy A or alloy B. The chromium depletion width is still narrow, only about 60 nm, which might be because there is not enough time for chromium atoms to migrate from the matrix toward the grain boundary. As ageing time increases to 5 hours, Figure 4-22(a) shows that the chromium concentration at the grain boundary in alloy A continues to decrease to about 12 wt.% while the chromium depletion in alloy B and alloy C start to be mitigated. The chromium depletion width

increases massively from 60 nm to 150 nm. The magnitude of chromium depletion decreases in all three model alloys as the ageing time increases to 24 hours. Alloy C has the lowest magnitude of chromium depletion at the grain boundary compared with alloy A and alloy B, which is opposite with the 0.5 hour and 1 hour aged samples shown in Figure 4-22(g)-(l). Chromium depletion continues to be mitigated (or healed) as the ageing time increases to 96 hours and 200 hours. In general, chromium depletion in alloy B and alloy C reaches a maximum at 1 hour ageing at 650 °C and then they enter the healing process as the ageing time increases. For alloy A, chromium depletion reaches the maximum at 5 hours ageing which is delayed compared with alloys B and C.

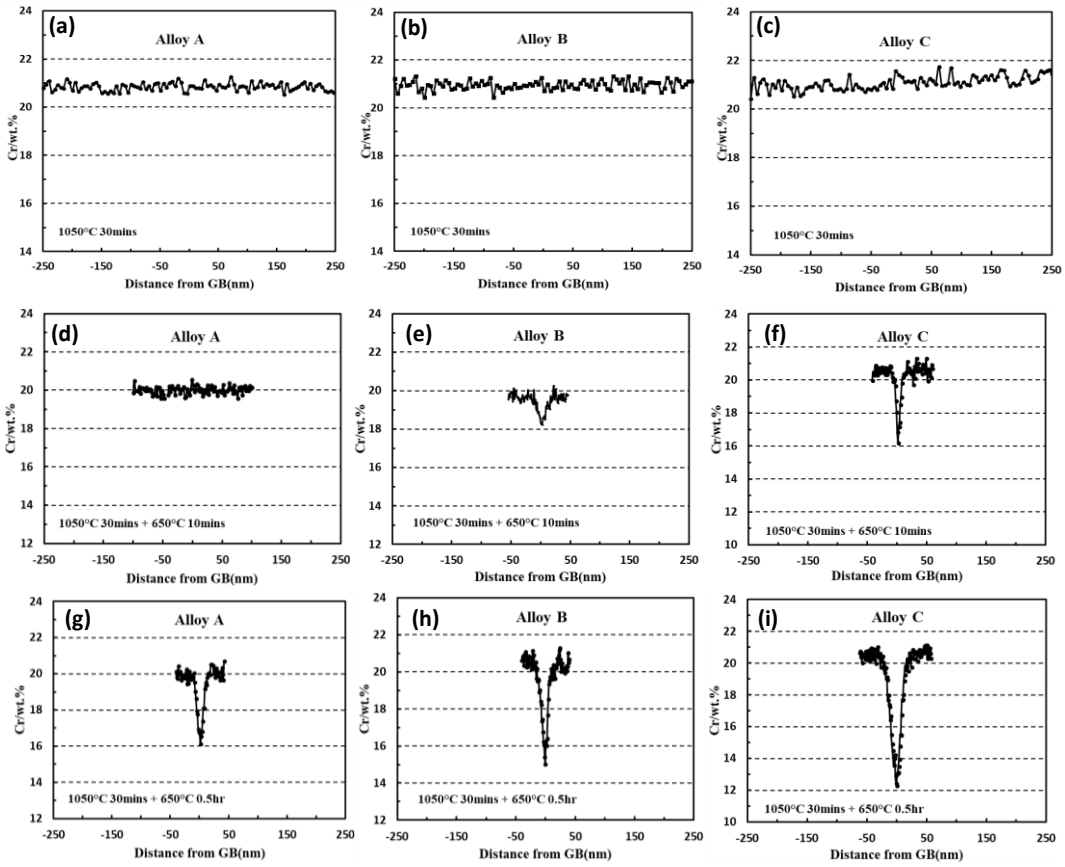

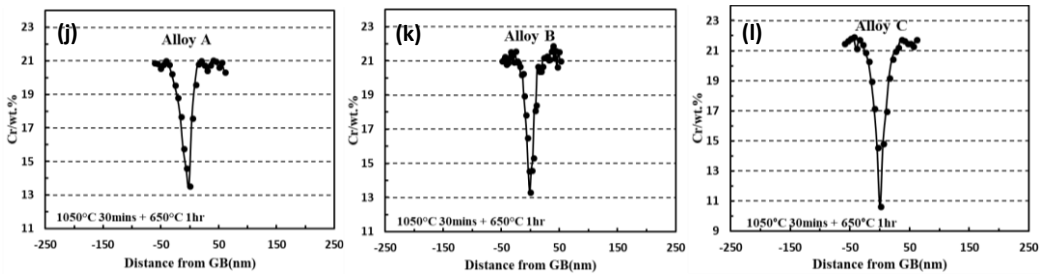

Figure 4-21 Typical chromium depletion profiles at the grain boundary in model alloys aged at 650 °C for a range of times: (a)(b)(c) solution annealed without ageing, (d)(e)(f) 10 minutes, (g)(h)(i) 0.5 hour, (j)(k)(l) 1 hour.

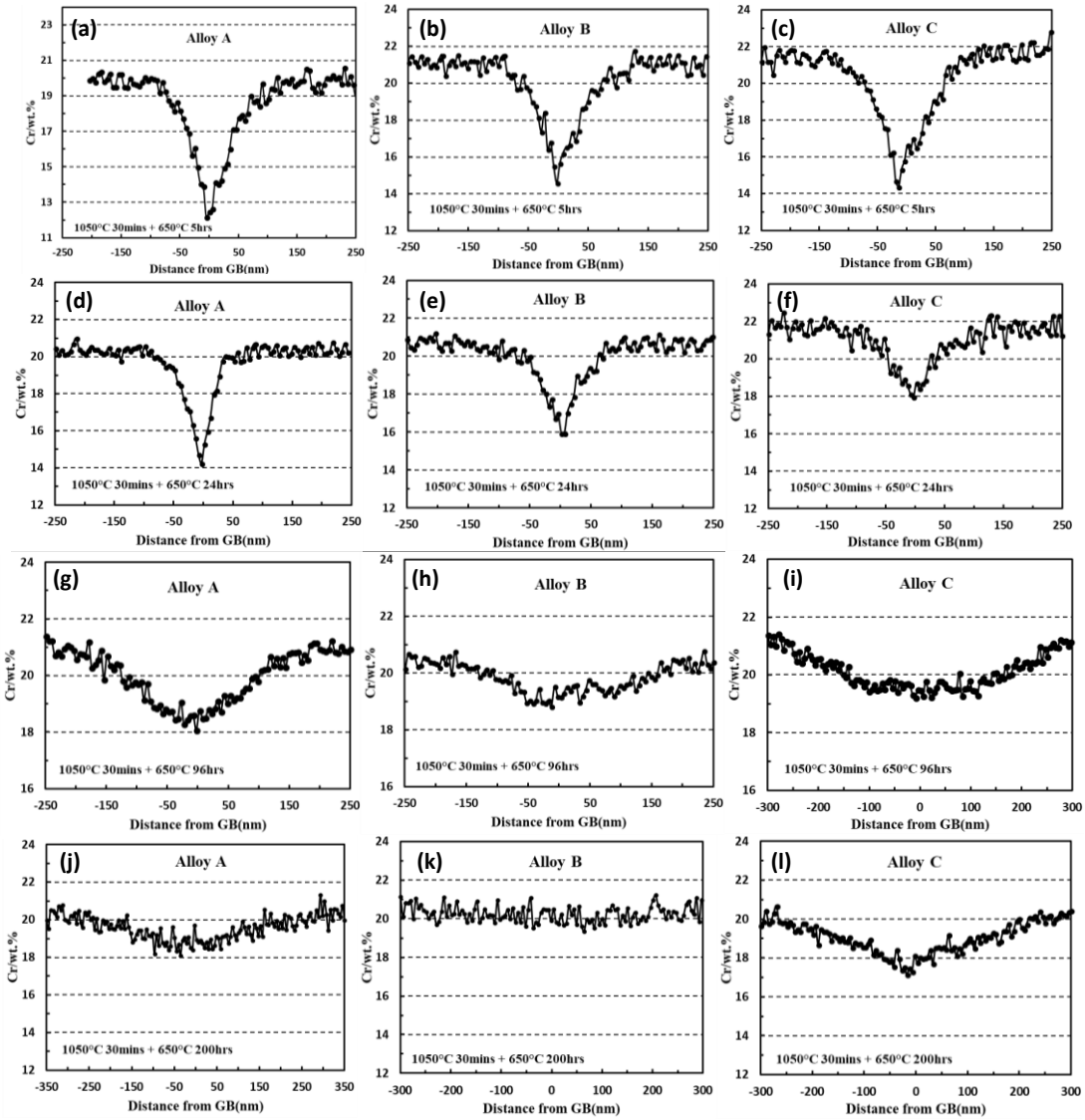

Figure 4-22 Typical chromium depletion profiles at the grain boundary of model alloys aged at 650 °C for a range of times: (a)(b)(c) 5 hours, (d)(e)(f) 24 hours, (g)(h)(i) 96 hours, (j)(k)(l) 200 hours.

4.3.2 The effect of silicon on the extent of chromium depletion

Figure 4-21 and Figure 4-22 show the typical chromium depletion profiles at the grain boundary in the model alloys annealed at 1050 °C and then aged at 650 °C for a range of times from 10 minutes to 200 hours. However, the chromium carbide precipitation might be varying from grain boundary to grain boundary, which could cause the difference in the magnitude of chromium depletion at different grain boundaries. Thus, to determine the average magnitude of chromium depletion at the grain boundary, chromium concentration was measured from at least three grain boundaries in each heat-treated sample and for each grain boundary two measurements were carried out. The average magnitude of chromium depletion is reproduced in Figure 4-23 with error bars attached, which shows the chromium decrement (ΔCr, which is the chromium concentration of the matrix subtract the lowest chromium concentration at the grain boundary) and depletion width as a function of ageing time in the model AGR fuel cladding alloys. Figure 4-23(a) shows that alloy A has the lowest magnitude of chromium depletion while alloy C has the highest after 10 minutes ageing at 650 °C. As ageing time increases, the magnitude of chromium depletion continues to increase and reaches the maximum after 1 hour ageing in alloy B and alloy C while alloy A reaches a maximum after 5 hours' ageing. Then, chromium depletion starts to be mitigated with further ageing time. Alloy C has the lowest magnitude of chromium depletion when ageing time increases to 24 hours. As ageing time increases to 96 hours, silicon bearing alloys show a lower chromium depletion magnitude at the grain boundary compared with the silicon free alloy A. In alloy B, chromium depletion is fully healed after 200 hours ageing while slight chromium depletion is still detected in alloy A. In alloy C, the magnitude of chromium depletion increases as the ageing time increases from 96 hours to 200 hours, which is an abnormal trend as the depletion supposed to be mitigated when

increasing the ageing time. The silicon effect on the width of chromium depletion is shown in Figure 4-23(b). In general, the width of chromium depletion increases with increasing ageing time in the model alloys. Silicon doped alloys show a larger chromium depletion width than the silicon free alloy.

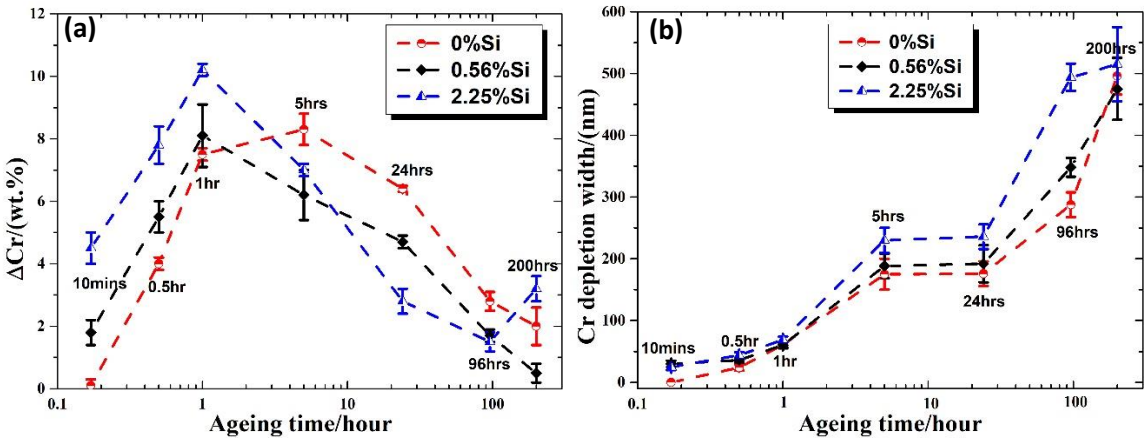

Figure 4-23 Chromium depletion behaviour in model alloys as a function of ageing time: (a) the magnitude of chromium depletion, (b) the width of chromium depletion; the results are depicted by markers with different colours as shown by the legend.

4.4 DOS in model alloys with various silicon contents

The DL-EPR test provides a quantitative method to measure the DOS of sensitised materials. To study the effect of silicon on sensitisation in 20/25/Nb AGR fuel cladding materials, DL-EPR test was carried out in model alloys A, B and C, which were thermally sensitised at 650 °C for various times. Then, the surface morphology of the DL-EPR tested samples was characterised using SEM.

4.4.1 DOS measurement by the DL-EPR test

Figure 4-24 shows the polarisation curves of the DL-EPR test in the model alloys which were solution annealed then aged at 650 °C for various times: 1 hour, 5 hours, 24 hours

and 200 hours. In all three model alloys, the solution annealed sample, without ageing, shows the lowest maximum reactivation current density (I_r) during the reverse scan. A substantial increase in I_r is observed when ageing is carried out. In Alloy A, I_r reaches a maximum after 5 hours ageing while in alloys B and C, I_r reaches a maximum after 1 hour ageing. As ageing time continues to increase, I_r starts to decrease which suggests that sensitisation begins to be healed by further ageing.

Table 4-1 is the DL-EPR test matrix and results. It includes heat treatment parameters, maximum activation and reactivation current density and the calculated DOS. At each heat treatment condition, two samples were tested. The DOS was determined by taking the ratio of maximum reactivation current density to maximum activation current density from the polarisation curves of the DL-EPR test in Figure 4-24.

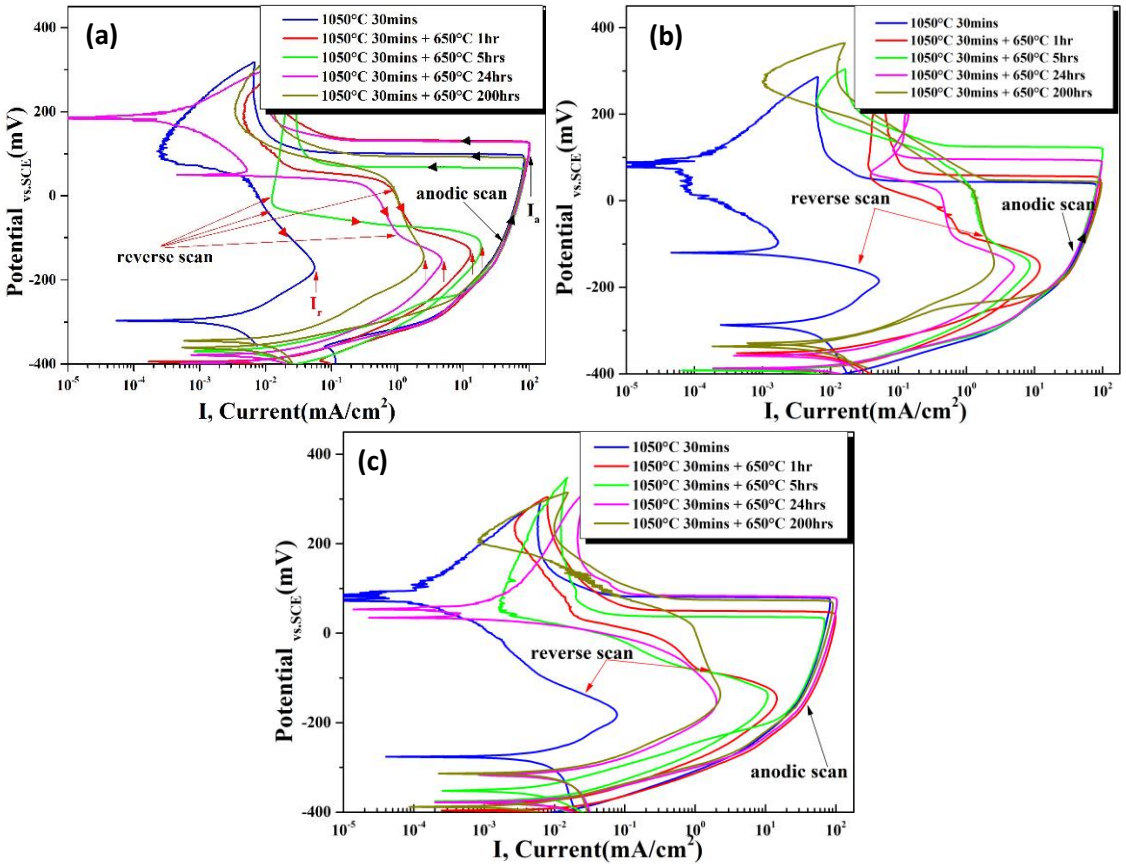

Figure 4-24 Polarisation curves of DL-EPR test on: (a) alloy A, (b) alloy B, (c) alloy C aged at 650 °C for various times, the results are depicted by curves with different colours as interpreted in the legend.

Table 4-1 Results of the DL-EPR test on model alloys aged for various times at 650 °C.

Material	Solution annealing	Ageing time at 650 °C (hours)	Maximum anodic, reactivation current and their ratio						Average [DOS]
			Test1			Test2			
			I_a (mA/cm^2)	I_r (mA/cm^2)	I_r/I_a [DOS]	I_a (mA/cm^2)	I_r (mA/cm^2)	I_r/I_a [DOS]	
Alloy A	1050 °C 30 minutes	0	84.072	0.055	0.001	70.287	1.289	0.018	0.010
		1	102.00	13.03	0.128	104.64	12.325	0.118	0.123
		5	85.826	18.8	0.219	85.081	16.742	0.197	0.208
		24	99.060	2.001	0.020	101.56	4.738	0.047	0.034
		200	90.029	2.536	0.028	92.542	2.448	0.026	0.027
Alloy B		0	68.652	0.037	0.001	82.386	0.052	0.001	0.001
		1	83.210	9.074	0.109	93.967	12.053	0.128	0.119
		5	73.630	5.196	0.071	101.58	8.573	0.084	0.078
		24	64.810	1.208	0.019	98.63	5.013	0.051	0.035
		200	99.960	2.691	0.027	99.062	2.553	0.026	0.027
Alloy C		0	67.114	0.032	0.000	82.946	0.077	0.001	0.001
		1	84.780	8.359	0.099	98.934	14.549	0.147	0.123
		5	59.480	5.594	0.094	84.491	10.786	0.128	0.111
		24	103.52	2.012	0.019	96.664	0.614	0.006	0.012
		200	76.920	1.750	0.023	90.651	2.278	0.025	0.024

The average DOS in Table 4-1 as a function of ageing time is plotted in Figure 4-25. The solution annealed samples, without ageing, have the lowest DOS. The DOS increases rapidly to about 0.125 after 1 hour ageing and no obvious difference of DOS is found between the model alloys containing various silicon contents. As the ageing time increases to 5 hours, the DOS of alloy A increases to about 0.220 while those of alloys B and C start to decrease. Thus, the DOS reaches a maximum after 1 hour ageing for alloy B and alloy C while the DOS of alloy A reaches a maximum after 5 hours ageing. The DOS of all three model alloys decreases to less than 0.04 when the ageing time increases to 24 hours, which means that the sensitisation has been substantially mitigated. When the ageing time increases to 200 hours, the DOS of all three alloys is only about 0.025 which is very close to the DOS of the solution annealed alloys.

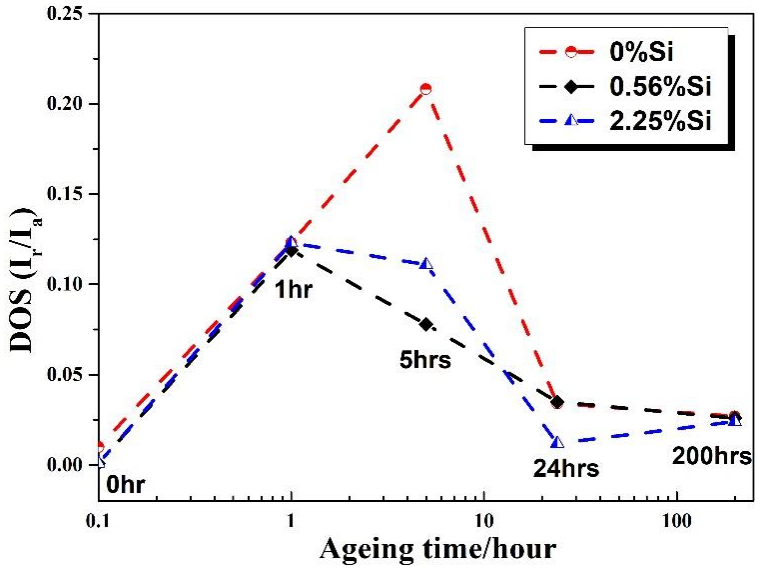

Figure 4-25 Average value of DOS from the DL-EPR test on the model alloys showing the dependence of DOS on ageing time. The results are depicted by markers with different colours as defined in the legend.

4.4.2 The examination of attack morphology after the DL-EPR test

Figure 4-26 shows the surface morphology of alloy A, aged for various times, after the DL-EPR test. Without ageing, the solution annealed sample only shows 'step' structures after the test as illustrated in Figure 4-26(a) and (b), which means the intergranular corrosion rate is similar to that of matrix. Whereas, a number of intergranular pits are observed in sample aged for 1 hour after the test in Figure 4-26(c) and (d). Most of the pits are at triple junctions. As ageing time increases to 5 hours, the size of the corrosion features increases and 'ditch' like attack are observed along the grain boundary in Figure 4-26(e) and (f), which suggests that the DOS increases compared with the 1 hour aged sample; this agrees with its reactivation current in Figure 4-24. However, only a few large pits are observed when ageing time increases to 24 hours, which indicates that sensitisation is substantially mitigated after longer time ageing. Sensitisation is entirely healed after 200 hours ageing as shown in Figure 4-26(e) where no intergranular corrosion is observed and only the step structure is present.

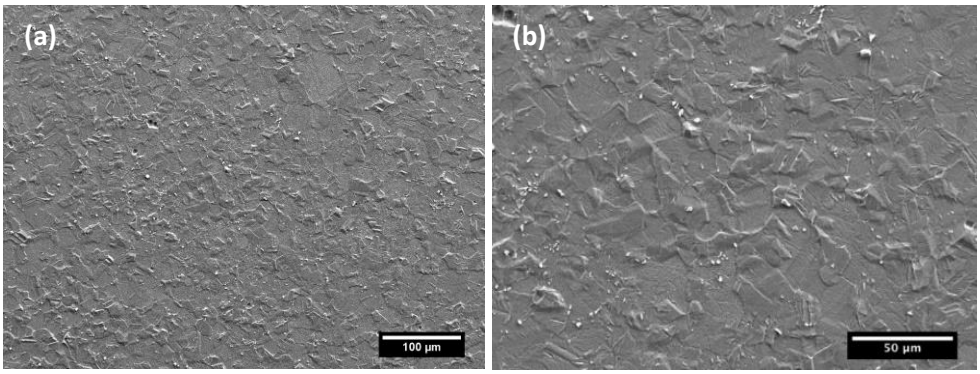

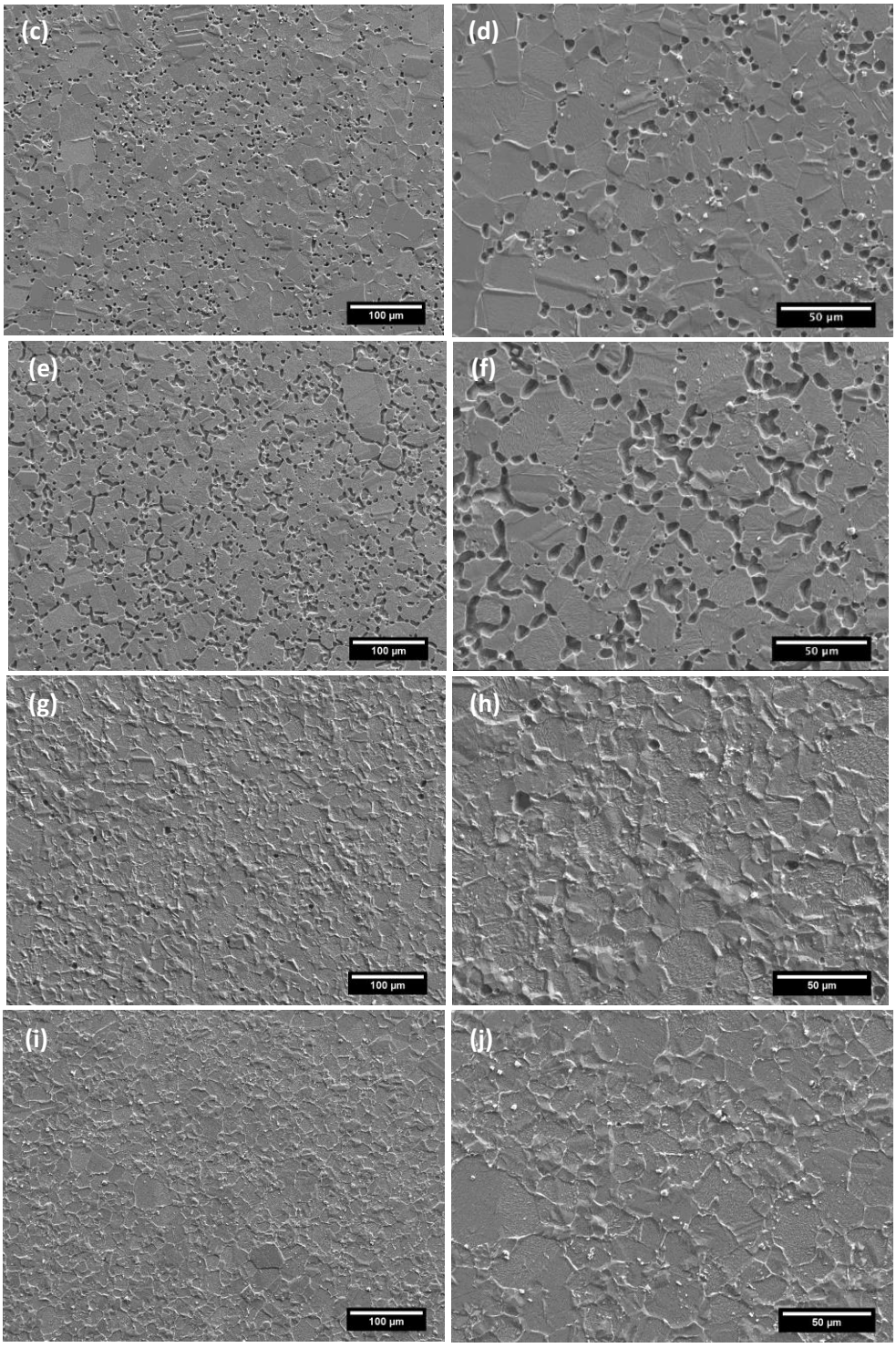

Figure 4-26 Surface morphology micrographs obtained from DL-EPR tested alloy A age at 650 °C for various times: (a)(b) solution annealed without ageing, (c)(d) 1 hour, (e)(f) 5 hours, (g)(h) 24 hours, (i)(j) 200 hours.

Figure 4-27 is the surface morphology of DL-EPR tested alloy B aged for various times at 650 °C. Without ageing, only a step structure is observed at the grain boundary after the solution annealing at 1050 °C as shown in Figure 4-27(a) and (b), except for a few attacks observed around the big niobium carbides, which was discussed in Phuah's work [31]. Lots of corrosion features are observed after 1 hour ageing, as shown in Figure 4-27(c) and (d). Both discrete pits and ditches are found at grain boundaries. However, the size of the pits decreases when the ageing time increases to 5 hours as shown in Figure 4-27(e) and (f), which indicates sensitisation starting to be healed. Figure 4-27(g) and (h) show that sensitisation continues to be healed further when the ageing time increases to 24 hours as the amount of intergranular corrosion decreases much compared to the 5 hour aged sample. Sensitisation is entirely healed after 200 hours' ageing as shown in Figure 4-27(i) and (j). The flake-like features decorating grain boundaries in Figure 4-27(j) are chromium carbides.

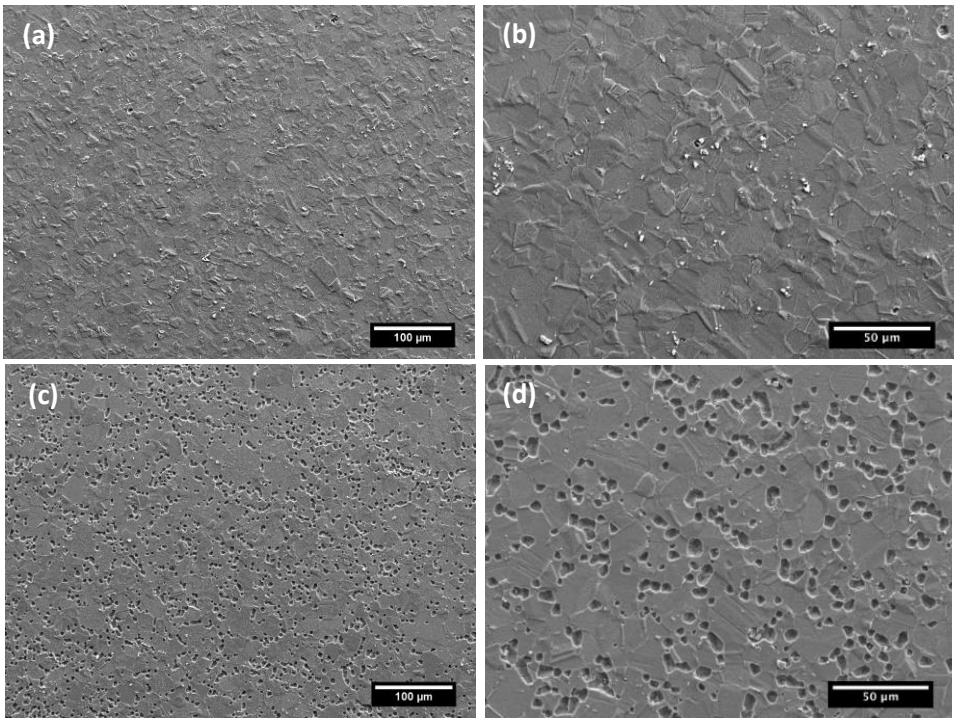

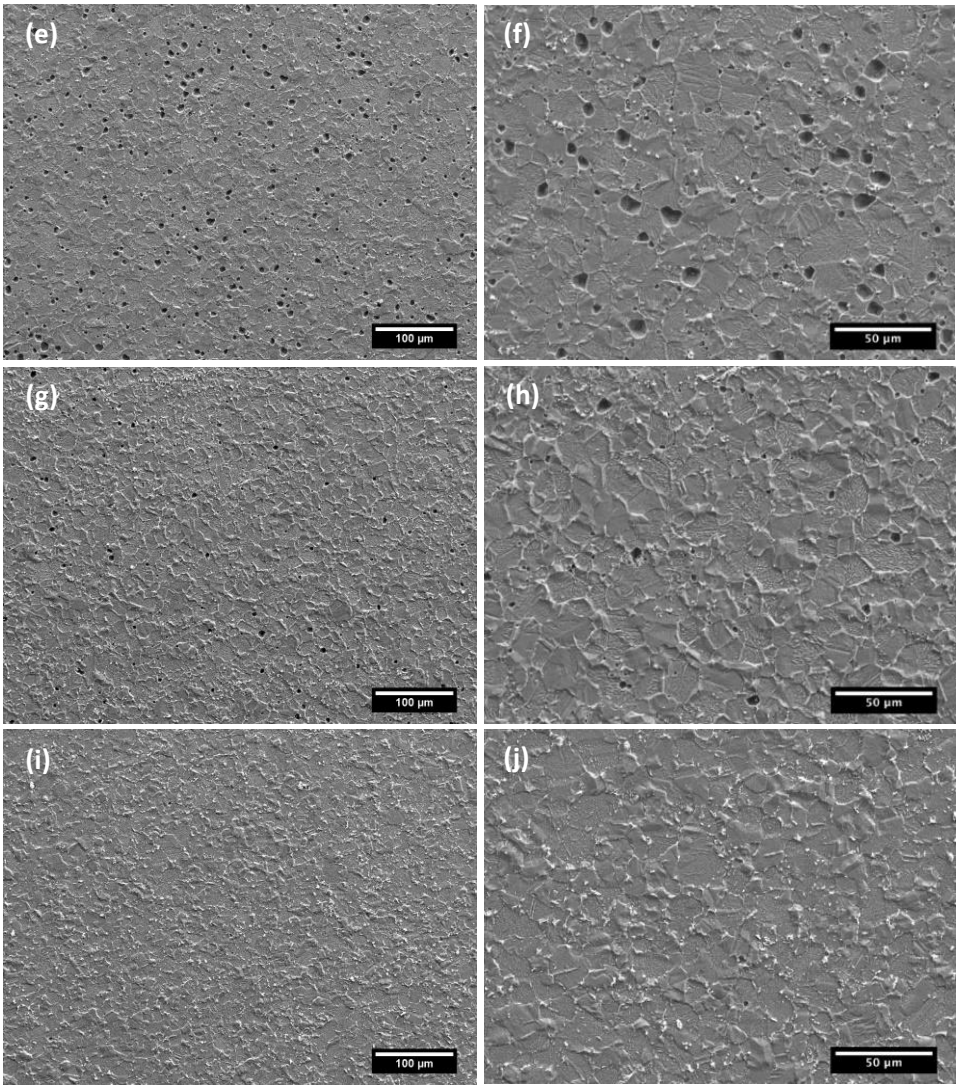

Figure 4-27 Surface morphology micrographs obtained from DL-EPR tested alloy B age at 650 °C for various times: (a)(b) solution annealed without ageing, (c)(d) 1 hour, (e)(f) 5 hours, (g)(h) 24 hours, (i)(j) 200 hours.

Figure 4-28 shows the surface morphology of DL-EPR tested alloy C aged at 650 °C for various times. The 1050 °C solution annealed sample, without ageing, only has a step structure after the DL-EPR test as shown in Figure 4-28(a) and (b), which suggests that it is unsensitised. The sample after 1 hour ageing is seriously attacked after the test as shown in Figure 4-28(c) and (d). The majority of grain boundaries display ditches. Ditch-like attack features are observed on the boundaries of both large and small grains. Sensitisation

is partly healed when the ageing time increases to 5 hours as shown in Figure 4-28(e) and (f). The majority of sensitisation at grain boundaries of the small grains have been healed while ditch-like attack features still present at the boundaries of the large grains, which suggests that grain size plays a role in sensitisation. As ageing time increases to 24 hours and then to 200 hours, Figure 4-28(g)(h) and Figure 4-28(i)(j) show no attack features at the grain boundary, which indicates that sensitisation has been healed entirely. Many flake-like particles are observed at the grain boundaries especially around the small grains. Most of the particles are chromium carbides. G phase was also observed due to the high silicon content in alloy C.

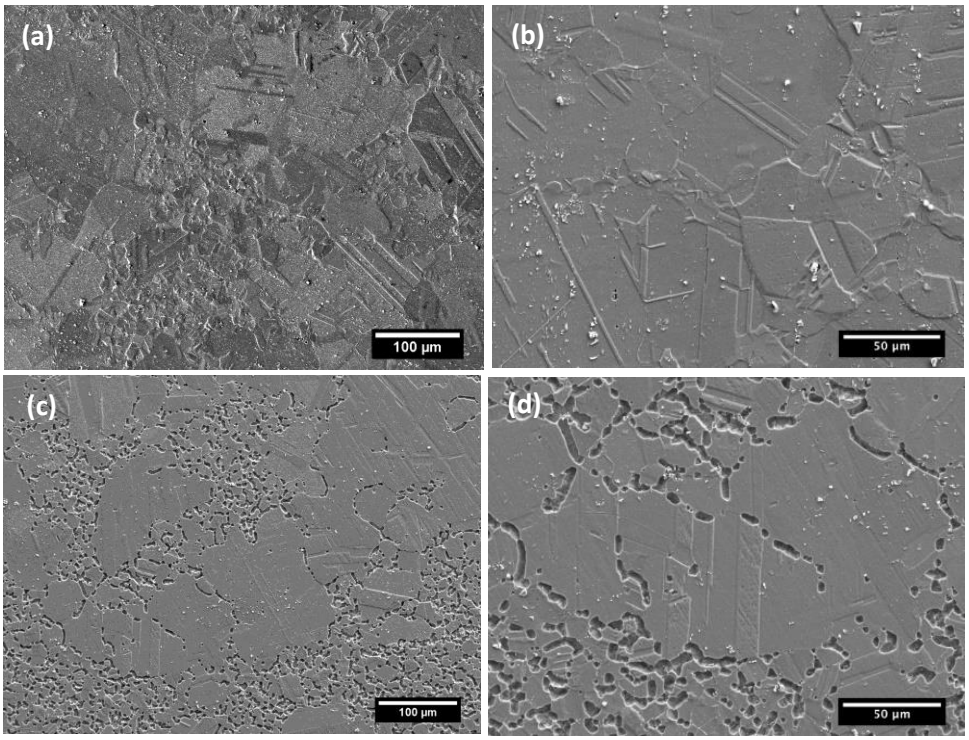

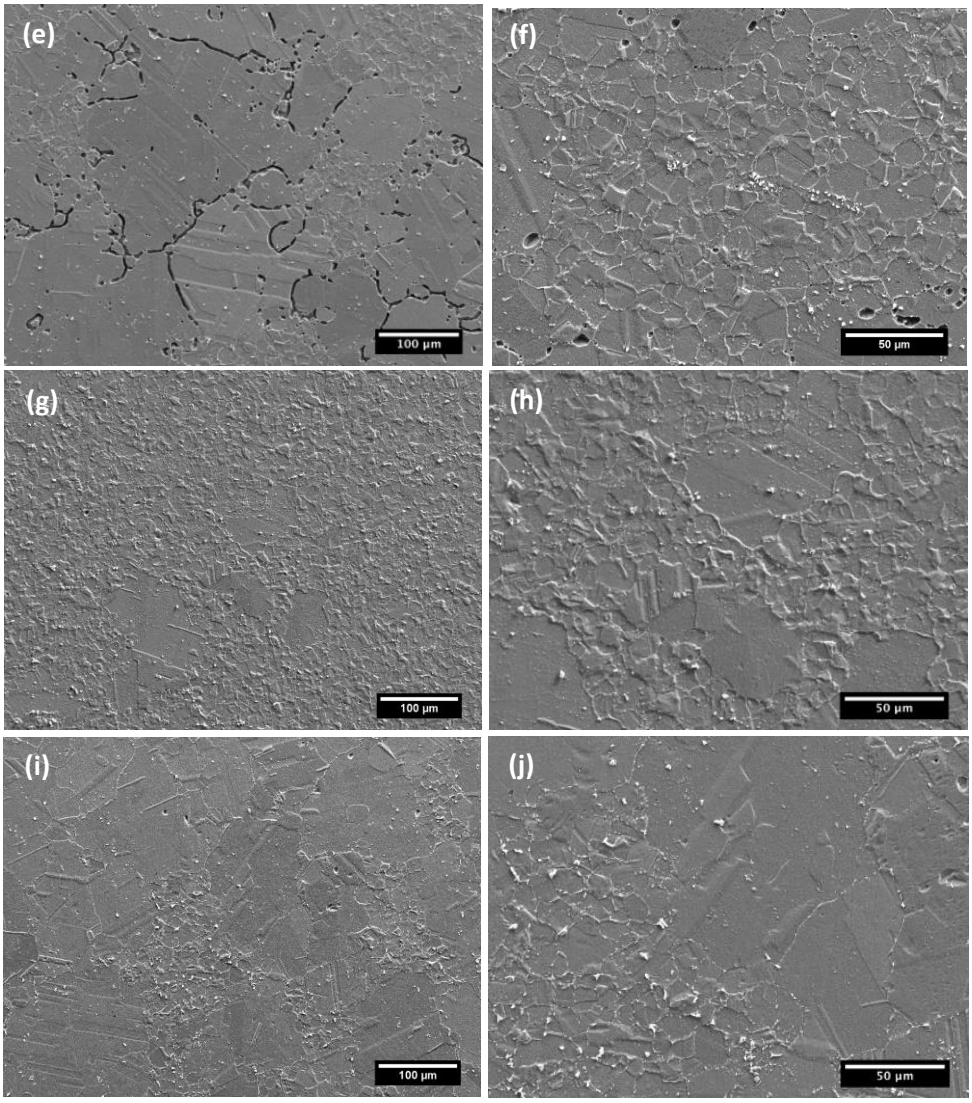

Figure 4-28 Surface morphology micrographs obtained from DL-EPR tested alloy C age at 650 °C for various times: (a)(b) solution annealed without ageing, (c)(d) 1 hour, (e)(f) 5 hours, (g)(h) 24 hours, (i)(j) 200 hours.

4.5 Discussion

4.5.1 Material characterisation

Alloy A and alloy B have the same grain structure; their grain size are similar and uniform throughout the whole sample. Large variation of grain size presents in alloy C. There is no grain growth after ageing at 650 °C for various times up to 200 hours. The grain boundaries are dominated by Σ3 boundaries.

Niobium carbides are found in all heat-treated alloys. The solution annealed alloys are absent from chromium carbides nucleation, but chromium carbides are found at the grain boundaries after aging. These chromium carbides are proven to be $M_{23}C_6$ precipitates. G phase is more likely found in alloy C that has high silicon concentration.

4.5.1.1 Grain structure of the investigated alloys

The grain sizes of alloys A and B are similar and uniform while the grain size in alloy C is non-uniform (Figure 4-1). No grain growth was found in the model alloys after ageing up to 200 hours at 650 °C (Figure 4-2 - Figure 4-4) as grain growth in stainless steel generally needs temperature higher than 850 °C [185]. Sensitisation is affected by grain size [106]. Beltran et al [107] found that the decreasing grain size can accelerate the sensitisation and desensitisation. The absence of grain growth leaves the grain boundary area fraction the same after the ageing for various times. The DOS is measured using the DL-EPR test in this work and corrosion takes place on the grain boundaries during the test [24], therefore, DOS determined by this test is very sensitive to the grain boundary area fraction. Thus, the same grain structure makes the DOS value comparable among different ageing treatments. The small grains in alloy C are very similar to the grains in alloys A and B, which makes their sensitisation very similar when subjected to the same heat treatment. Niobium carbide at the grain boundary can pin the grain boundary to prevent it from migrating and thus inhibit the grain from growing. Thus, less niobium carbide at the grain boundary might cause grain growth. The huge variation of grain size (Figure 4-1(e)) might be due to a non-uniform distribution of niobium carbides at the grain boundaries in alloy C. EBSD maps in Figure 4-5 show the grain boundaries are dominated by Σ3 boundaries that are immune to

intergranular corrosion because their low energy means no chromium depletion. This grain structure makes these alloys possess good resistance to sensitisation.

4.5.1.2 Precipitates

The 20/25/Nb alloy is used for AGR fuel cladding because of its good creep and oxidation resistance at elevated temperature. As a stable precipitate, NbC remain in the alloys throughout the whole annealing and ageing process. The nucleation of niobium carbides in stainless steel commences with the heterogeneous nucleation of particles on lattice defects such as dislocations and grain boundaries [186,187]. The lattice parameter of NbC precipitates is 4.41 Å, they have spherical morphology in the matrix while elongated shape at the grain boundary (Figure 4-8(b)). The formation of niobium carbides consumes free carbon in the matrix, which mitigates the sensitisation by decreasing the nucleation of chromium carbides at the grain boundary. Niobium carbides at the grain boundary also act as a pin to prohibit the growth of the grains. Niobium is a stronger carbide former than chromium. Thus, carbon is captured by Nb in preference to form chromium carbides which are detrimental to corrosion properties. Many large NbC precipitates (Figure 4-6(a)) are also found in the model alloys after the solution anneal at 1050 °C. The large NbC precipitates have detrimental effects on the material such as worsening creep and corrosion properties [31]. They can fall out and leave a void on the surface where pitting corrosion can take place. Crevice corrosion can also happen at sites where the large niobium carbides stick out of the sample surface. The dispersion of a large number of fine NbC precipitates (Figure 4-6(b)) in the matrix not only improves the resistance to corrosion but also increases creep strength through precipitation hardening.

Solution annealed samples, without ageing, are free from chromium carbides at the grain boundaries (Figure 4-9). Figure 2-15 shows the calculated dissolution behaviour of niobium carbide as a function of temperature, which suggests that part of the niobium carbides dissolve after annealing at 1050 °C. A number of chromium carbides are formed at the random grain boundary after ageing at 650 °C which twin grain boundaries are still free from carbides (Figure 4-10). Carbon used to form chromium carbides is from the dissolved niobium carbides. Chromium carbides have a preference for nucleating on large misorientation grain boundaries (>= 15°), where the energy is the highest, rather than on incoherent portions of twin boundaries, where the energy is lower. Normally, carbide nucleation does not occur at twin boundaries due to their low energy. Trillo and Murr [188] proposed that there is a critical energy for the nucleation of precipitates at grain boundaries. The critical energy lies between 16 mJ/m^2 and 265 mJ/m^2 which corresponds to the energies of non-coherent and coherent twin boundaries. The d-spacings of chromium carbides in [011] axis is three time than of the matrix (Figure 4-11), which confirms these carbides are $M_{23}C_6$ precipitates. It has been reported by Moss and Sykes [32] that chromium carbides at the grain boundary in AGR fuel cladding material is $M_{23}C_6$ (16Cr + 7Fe + 6C) with a lattice parameter of a = 10.65 Å. The $M_{23}C_6$ precipitates at the grain boundary are coherent with one of the adjacent grains to minimise the activation energy for nucleation. As ageing time increases, the $M_{23}C_6$ precipitates grow further with preferential migration of incoherent $M_{23}C_6$/austenite interface with higher interfacial energy [26].

Alloy C, containing 2.25 wt.% Si, which is a very high silicon concentration for stainless steel, has many G phase precipitates in the matrix (Figure 4-13). The precipitates at the

grain boundary in Figure 4-14 are dominated by G phase which might be be transformed from NbC precipitates[53]. In niobium stabilized 20/25/Nb cladding material, G phase has the chemical composition $Ni_{16}Nb_6Si_7$ [53]. Nb can be replaced by Ti, Mn, V, Ta, Zr or Hf [189]. The crystal structure of the G phase is a variant of face centred cubic (FCC), which has 116 atoms per unit cell with a lattice parameter of 11.2 Å. The lattice parameter is exactly four times that of BCC ferrite [190]. The growth of G phase consumes niobium which causes less niobium carbides to be formed at the grain boundary and it has been considered as a strengthening phase [191,192].

4.5.2 Chromium depletion in a sensitised sample

Chromium depletion is detected in a thermally sensitised sample due to the formation of chromium carbides at the grain boundary (Figure 4-15). In general, the magnitude of chromium depletion increases with ageing time and reaches the maximum when chromium carbides at the grain boundary stop growing. Then chromium depletion is mitigated by further ageing because of the diffusion of chromium atoms from the matrix towards grain boundary. Compared with the 24 hours aged sample, chromium depletion at the random HAGBs are more serious in the 5 hours aged sample. Thus, chromium carbides have stop growing after 24 hours ageing in alloy A and chromium depletion is being healed.

Chromium depletion is affected by grain boundary misorientation (Figure 4-16). Σ3 boundary is free from chromium depletion while the other two CSL boundaries (Σ11 and Σ17) exhibit less chromium depletion than the random HAGBs, which might be because the CSL boundaries have lower energy than the random HAGBs resulting in less chromium carbides nucleation on the CSL boundary.

The driving force of chromium depletion is the nucleation of chromium carbide that takes chromium from the grain boundary. Chromium depletion is more serious at that location that is very close to the chromium carbide, whereas, the carbide influence can be neglected if the distance away from the carbides is long enough (Figure 4-17). This might be because the elemental diffusion rate at grain boundary can be a few orders higher than in the matrix [193], chromium depletion at the grain boundary is homogenised quickly.

The magnitude of chromium depletion at the interfaces between the chromium carbide and the adjacent grains is different in the 24 hours age alloy A (Figure 4-17(b)). Chromium carbide nucleated at the grain boundary is coherent with one of the adjacent grains (Figure 4-11). The coherent interface might have lower energy than the incoherent interface, which leads to less chromium depletion at the coherent than the incoherent interface. Chromium depletion at the chromium carbide interfaces is healed entirely when ageing time increases to 200 hours (Figure 4-18) due to the migration of chromium atoms from the matrix towards the interface.

4.5.3 The effect of Si on chromium depletion at grain boundary

The dependence of the magnitude of chromium depletion at the grain boundary on ageing time is shown in Figure 4-23(a). The magnitude of chromium depletion increases with ageing time and reaches a maximum and then starts to be healed with further ageing. A kinetic theory has been proposed to explain the chromium depletion at the grain boundary due to the nucleation of chromium carbides [79,80]. The magnitude of chromium depletion at the grain boundary is determined by the net amount of chromium captured by chromium carbide precipitation and the amount diffused towards the grain boundary from the grain

matrix. At the beginning of ageing, chromium carbides grow quickly due to a high free carbon content and more chromium is taken by the carbide than diffuses to the grain boundary, which leads to a decrease of the grain boundary chromium concentration. As ageing proceeds, the chromium carbide growth slows down due to the decreasing free carbon content and there is a point where chromium carbide growth is slow enough that chromium taken by the carbide is balanced by the chromium diffused to the grain boundary from the grain matrix where upon the grain boundary chromium concentration reaches the minimum. As ageing time continues to increase, the amount of chromium captured by the carbides is less than the amount diffusing from the grain matrix. The chromium concentration starts to increase until the grain boundary chromium concentration reaches the same level as the grain interior.

Chromium depletion in all three model alloys has similar trend but reaches the maximum at different times (Figure 4-23(a)). The magnitude of chromium depletion at the grain boundary increases as the ageing time increases from 10 minutes and reaches the maximum after 1 hour ageing in alloy B and C. It then starts to decrease with increasing ageing time. Whereas, in alloy A, chromium depletion reaches a maximum after 5 hours ageing, which is slower to reach the maximum compared with alloy B and alloy C. Thus, the silicon bearing alloys show a higher magnitude of chromium depletion at the grain boundary before the depletion reaches the maximum, and alloy C (2.25 wt.% Si) exhibits higher magnitude of chromium depletion at the grain boundary than alloy B (0.56 wt.% Si). However, this trend starts to reverse; the silicon free alloy (alloy A) exhibits more chromium depletion than silicon bearing alloys (alloy B and alloy C) after chromium depletion reaches the maximum and begins to be healed. The process before the magnitude

of chromium depletion reaches its maximum is classified as the 'sensitisation stage' and the decrease of the magnitude of chromium depletion is classified as the 'desensitisation stage'. If we assume that silicon increases the diffusion rate of chromium towards the grain boundary in 20/25/Nb alloys, alloy A shows less chromium depletion than alloy B and alloy C during the sensitisation stage and more chromium depletion during the desensitisation stage. Assassa and Guiraldenq [133] investigated the influence of silicon content on the diffusion of Fe, Cr and Ni in austenitic stainless steels containing 0.07 wt.%, 1 wt.% and 4 wt.% Si using the residual activity method [194,195]. Their results suggested that the chromium diffusion coefficient is the highest in the 1 wt.% Si alloy when below a certain temperature as shown in Figure 2-33, whereas the 4 wt.% Si alloy has the lowest chromium diffusion coefficient. The activation energy obtained from the diffusion coefficient using the Arrhenius equation in the silicon-doped alloys is shown in Table 4-2. The alloy with 1 wt.% Si addition has the lowest activation energy.

Table 4-2 Activation energy of Ni, Cr and Fe for diffusion in austenitic stainless steel doped different amount of silicon [133].

Tracer	**^{63}Ni**			**^{51}Cr**			**^{59}Fe**		
Silicon, %	0.1	1	4	0.1	1	4	0.1	1	4
Q_j, kJ at. g^{-1}	174 (± 4)	159 (± 2)	257 (± 4)	193 (± 4)	172 (± 4)	276 (± 6)	245 (± 6)	195 (± 6)	314 (± 6)

In this thesis, the silicon content in silicon bearing alloys are 0.56 wt.% and 2.25 wt.% which are close to the 1 wt.% Si alloy in Assassa and Guiraldenq's work. Thus, a higher magnitude of chromium depletion in silicon bearing alloys during the sensitisation stage but a lower magnitude of chromium depletion during the desensitisation stage when exposed to the same ageing time might be due to the silicon decreasing the activation energy of chromium.

The magnitude of chromium depletion in alloy C aged for 200 hours, as shown in Figure 4-23(a), is abnormal. It is supposed to decrease during the desensitisation stage when increasing the ageing time. Figure 4-14 shows that the grain boundary precipitates are dominated by G phase which could be transformed from NbC [53]. G phase does not contain carbon; thus, carbon can be released from NbC after NbC transforms to G phase. The elevated free carbon content after 200 hours ageing in alloy C can continue to form $M_{23}C_6$, consequently, decrease the chromium concentration at the grain boundary.

The chemical compositions of the model alloys in Table 3-1 show alloy A, B and C have very similar carbon content. If the same amount of carbon was released back into the matrix after the solution annealing at 1050 °C, the maximum magnitude of chromium depletion will be very close. However, Figure 4-23(a) shows that alloy C has the highest maximum magnitude of chromium depletion at the grain boundary after 1 hour's ageing while alloys A and B have similar maximum magnitude of chromium depletion. Figure 4-13 shows that many G phase precipitates already exists after the solution annealing. G phase captures niobium from the matrix resulting in less niobium to capture carbon by forming NbC. Thus, the free carbon content in alloy C might be higher than that in alloys A and B after the solution anneal, which could explain why alloy C has a higher maximum magnitude of chromium depletion. As shown in Figure 4-23(b), as regard the chromium depletion width at the grain boundary, silicon bearing alloys showed a wider depletion range because of the higher chromium diffusion coefficient in these alloys.

The precipitation behaviour of 20/25/Nb alloy has been studied over the temperature range 500-850 °C by Powell et al. [53]. The time-temperature-precipitation (TTP) diagram of the

AGR fuel cladding material was plotted as shown in Figure 2-14. The TTP diagram suggests that the ageing time needed for formation of chromium carbide is about 40 hours. However, the nucleation of chromium carbide at the grain boundary in the alloys studied this thesis happened after only 10 minutes ageing at 650 °C (Figure 4-19(e) and (f)). This difference might be due to the different annealing conditions. In Powell's work, samples were solution annealed at 1050 °C followed by 30% cold work and then subjected to 930 °C annealing and 3% cold work. During the 930 °C annealing, the free carbon was captured by niobium and reduced due to the formation of niobium carbides, which delayed the nucleation of chromium carbide at the grain boundary. In this thesis, the as received samples were solution annealed at 1050 °C prior to the ageing, which leaves a higher free carbon content in the matrix and thus chromium carbide nucleation at the grain boundary in a shorter time.

4.5.4 The effect of Si on sensitisation

It is well known that sensitisation in austenitic stainless steel is due to chromium depletion at the grain boundary. As discussed in section 4.5.2, a small amount of silicon addition could increase the diffusion rate of chromium and thus sensitisation in silicon bearing alloys can reach its maximum and be healed more quickly than in silicon free alloys. Figure 4-25 shows that the DOS of alloys B and C reach the maximum (after 1 hours ageing) more quickly than alloy A (after 5 hours ageing). The maximum DOS values of alloys B and C are 0.119 and 0.123, respectively, which are lower than the maximum DOS value (0.208) of alloy A. However, the increasing diffusion rate of chromium due to the addition of silicon to alloys B and C can only reduce the time needed for the alloy to reach the maximum DOS. It cannot account for the higher maximum DOS of alloy A than that of

alloys B and C. In the DL-EPR test, the repassivation process in the forward scan forms a layer of thin protective chromium oxide film to resist the attack from the acid solution. Recently, Laurent et al. [125,127] investigated the influence of silicon on passive and transpassive dissolution in nitric acid using an electrochemical method. They suggested that the passive film consisted of two layers, a silicon-rich outer layer and a chromium-rich inner layer. Silicon increases the activation potential of the passive film as it contains less chromium and more silicon, which suggests that silicon decrease the affinity of the stainless steel for oxygen. If the alteration of chemical composition in the passive film due to silicon addition can improve the corrosion resistance to intergranular attack, the lower DOS of silicon bearing alloys than for the silicon free alloy as shown in Figure 4-25 is expected.

The surface morphology of the DL-EPR tested sample in Figure 4-26, Figure 4-27 and Figure 4-28 agrees well with the magnitude of chromium depletion at the grain boundary in Figure 4-21 and Figure 4-22, which shows that a higher magnitude of chromium depletion at the grain boundary corresponds to a higher extent of attack on the sample surface. Silicon bearing alloys show much less intergranular attack than the silicon free alloy after 5 hours' ageing, which is in agreement with the smaller I_r/I_a value compared with the silicon free alloy (Figure 4-25). In alloy C, containing 2.25 wt.% Si, the grain size is not uniform (Figure 4-4 and Figure 4-28). To make the I_r/I_a value reflect the degree of sensitisation better, a normalised value should have been acquired by measuring the attacked grain boundary network [84]. However, the attacked features in these alloys consist of discrete pits at the grain boundary instead of ditches along the whole boundary, which makes it difficult to normalise the I_r/I_a value to the grain boundary network. Thus, it

is not accurate to take the ratio of I_r to I_a as the degree of sensitisation, which is shown in Figure 4-25. However, we still can see that the silicon bearing alloy shows a much lower I_r/I_a value after 5 hours' ageing and the corresponding surface micrographs, in Figure 4-27(f) and Figure 4-28(e), show less attack than the surface micrograph of the silicon free alloy in Figure 4-26(f).

In alloy C, the sensitisation of small grains has been healed substantially after 5 hours ageing, however, the boundaries of the large grains are still severely sensitised (Figure 4-28(e)). The sensitised boundaries of both the large and small grains are healed entirely after 24 hours ageing (Figure 4-28(g)). Thus, sensitisation of the boundaries of small grains can be healed more quickly than that of the large grains. Pascali et al. [106] reported that the initiation of sensitisation at low temperature is delayed as the grain size increases from 17 μm to 68 μm and that desensitisation is also delayed. In Beltran's work [107], he found that, comparing with the material of 15 μm grains, the strained material of 150 μm grains increases carbide nucleation and accelerates the sensitisation-desensitisation process, which might be because the average length of carbon atoms diffusing from the mid-grain to the grain boundary decreases for smaller grain material.

4.6 Summary

4.6.1 Material characterisation

In alloys A and B, the grain size is about 15-20 μm and its distribution is uniform after solution annealing at 1050 °C. No obvious grain growth was found after ageing at 650 °C for up to 200 hours. The grain size is non-uniform in alloy C where the small grain size is about 20 μm while the large grain size is up to about 150 μm. The grain boundary is

dominated by the Σ3 boundary. This grain boundary network makes the 20/25/Nb alloys possess a better resistance to intergranular attack. NbC precipitates present both at the grain boundary and in the matrix throughout the heat treatments. Solution annealed alloys are free from $M_{23}C_6$ precipitation, however, many $M_{23}C_6$ precipitates were found at the grain boundary after ageing at 650 °C. The carbon used to form $M_{23}C_6$ is from the dissolution of NbC during the solution anneal at 1050 °C. In alloy C, many G phase precipitates were observed both at the grain boundary and in the matrix in the solution annealed sample due to the high Si concentration.

4.6.2 Silicon effect

In the range of ageing times from 10 minutes to 200 hours, chromium depletion exhibits two stages (sensitisation and desensitisation), which agrees well with the kinetic theory. Silicon bearing alloys showed a higher magnitude of chromium depletion in the sensitisation stage but less depletion in the desensitisation stage, and the ageing time needed for alloys B and C to reach the maximum magnitude of chromium depletion is less than that for alloy A. This might be because silicon increases the diffusion rate of chromium towards the grain boundary. DOS measured by DL-EPR test showed that silicon-bearing alloys experienced less attack than the silicon free alloy after 5 hours ageing. However, no evident difference was found under the other sensitisation treatments. The morphology of the DL-EPR tested sample agreed well with the magnitude of chromium depletion. Sensitisation of small grains can be healed more quickly than that of large grains.

5 Thermally induced sensitisation and chromium depletion on the commercial alloy

20/25/Nb alloy is used as cladding material in AGRs. The exposure to intense neutron irradiation might cause chromium depletion at the grain boundary during in-reactor service, and the sensitised fuel cladding might be vulnerable to intergranular corrosion when the spent fuel is removed from the reactor and stored in the post-process cooling pond. Thus, to predict the sensitisation behaviour of the spent fuel cladding stored in the cooling pond, it is necessary to measure the irradiation induced chromium depletion at the grain boundary. As an irradiation facility was not available to me, thermally induced chromium depletion and sensitisation were carried out to replicate irradiation induced chromium depletion and sensitisation. Chromium depletion and sensitisation in a 20/25/Nb commercial alloy (alloy D) at two different annealing temperatures are reported here.

5.1 Characterisation of the commercial alloy

Figure 5-1 shows the grain structure of alloy D annealed at 930°C and 1050 °C for 30 minutes. The grain size of the 1050 °C annealed sample is about 40-50 μm while it is only about 20 μm in the 930 °C annealed sample. There is thus obvious grain growth in the 1050 °C annealed sample as compared with the 930 °C annealed sample. As illustrated in Figure 5-1(a) and (c), the grain structure is uniform throughout the whole sample for both heat treatments. Figure 5-1(b) and (d) show a number of twins present intragranularly in the grain. Many large (1-5 μm) white niobium carbide precipitates with irregular shape are also found. Figure 5-2 is EBSD maps obtained from the alloy D annealed at 1050 °C. Figure 5-2(a) confirms that there exists many twins in the material. Figure 5-2(b) shows

that the grain boundaries are dominated by Σ3 boundaries. Figure 5-2(c) shows the network of random grain boundaries after excluding the CSL boundaries, which confirms that the average grain size is about 40 μm.

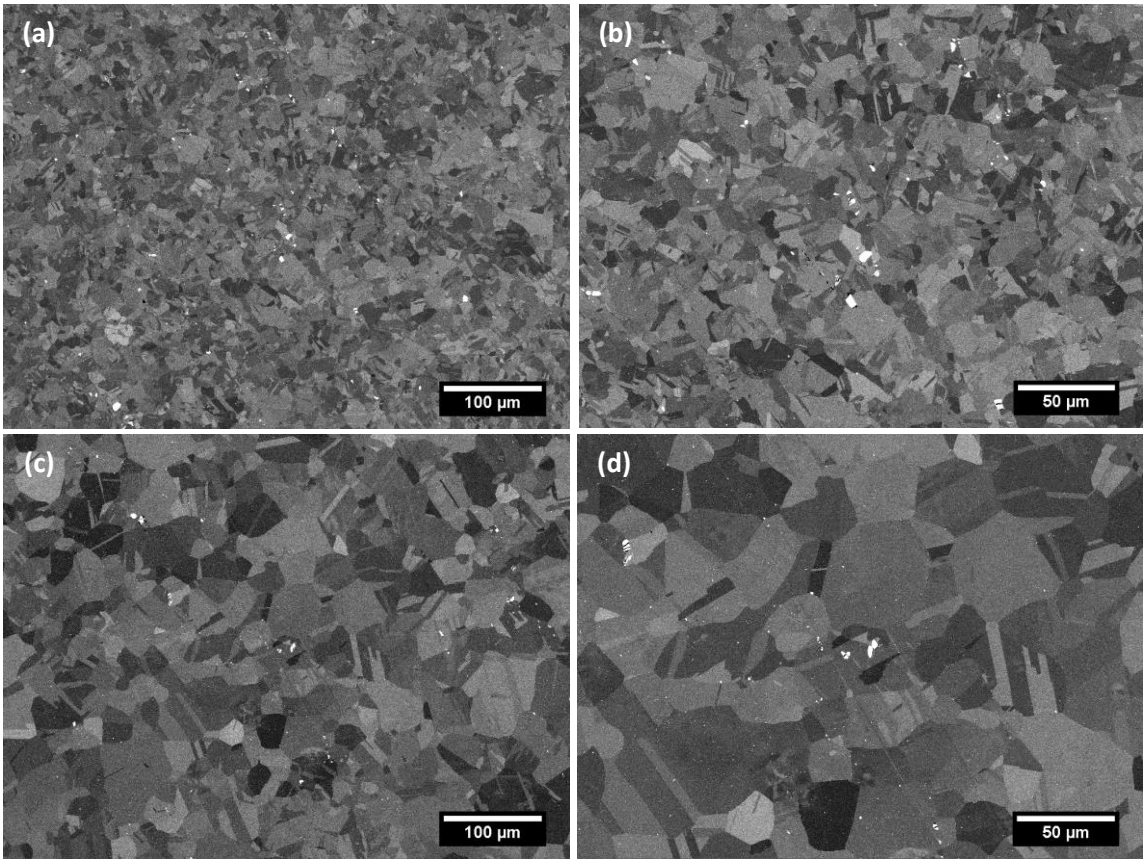

Figure 5-1 BSE images obtained from alloy D annealed for 30 minutes at: (a)(b) 930 °C, (c)(d) 1050 °C.

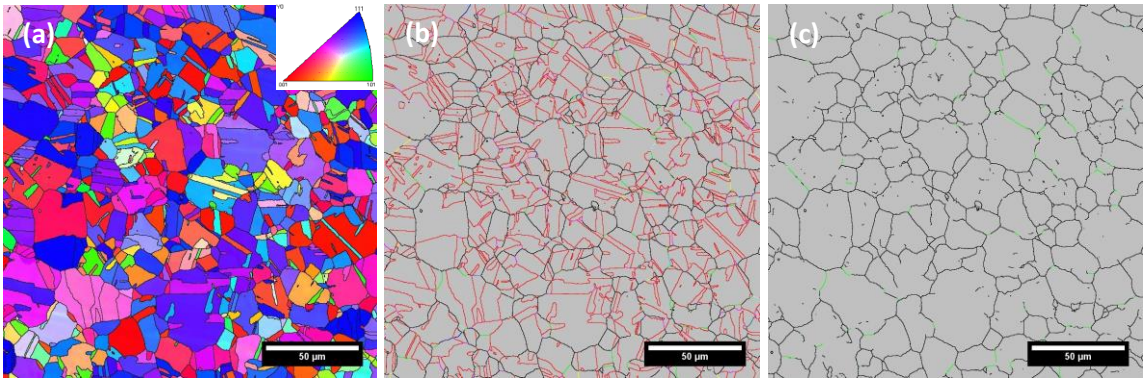

Figure 5-2 EBSD maps obtained from alloy D annealed at 1050 °C for 30 minutes: (a) orientation map in the Y direction and the top-right inset indicates the colour code; (b) grain boundary segments shown in various colour: Σ3 and Σ9 boundaries are red and pink, random HAGBs and

LAGBs are black and lime green, (c) random grain boundary map which excludes the CSL boundaries.

Figure 5-3(a) is a BSE image of alloy D solution annealed at 1050 °C, which includes a large niobium carbide precipitate (about 3 µm) and a number of small (about 100-500 nm) niobium carbides. Figure 5-3(b) is an EDS line scan spectrum, indicated by a dashed line, across the large precipitate. It shows that the niobium and carbon counts increase as the electron beam scans across the precipitate while no nitrogen counts are found, which suggests that the large precipitate is a NbC precipitate rather than Nb(CN).

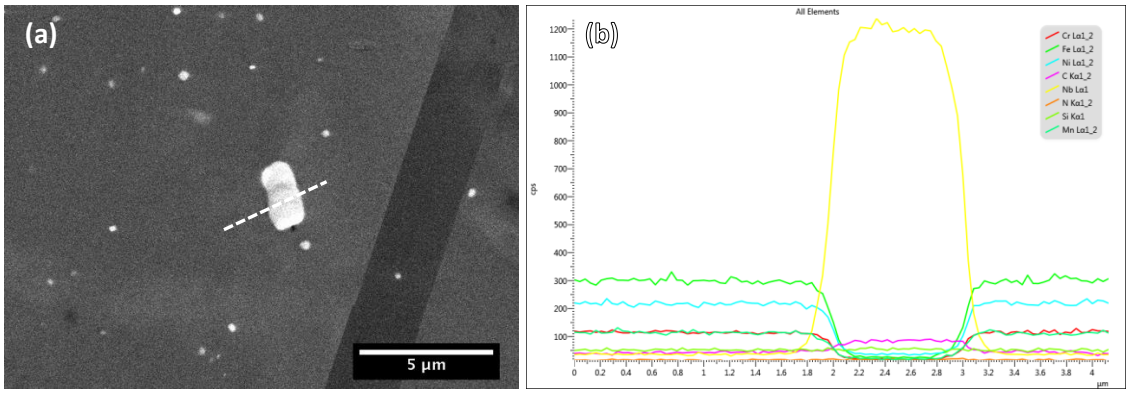

Figure 5-3 (a) is a BSE image obtained from alloy D solution annealed at 1050 °C, (b) is an EDS line scan across a large Nb carbide.

Figure 5-4 shows the microstructure of alloy D after 24 hours ageing at 650 °C. It shows that the grain size distribution is uniform. The grain structure is similar to the solution annealed sample in Figure 5-2. Compared with the solution annealed sample, there is no obvious grain growth in the ample with subsequent 24 hours ageing at 650 °C. A number of intragranular twins are observed, similar to the model alloys (Figure 4-1). As shown in Figure 5-4(d), a number of chromium carbides (indicated by white arrows) are observed at the grain boundaries and on the triple junctions. Many NbC precipitates are also found both intergranularly and intragranularly.

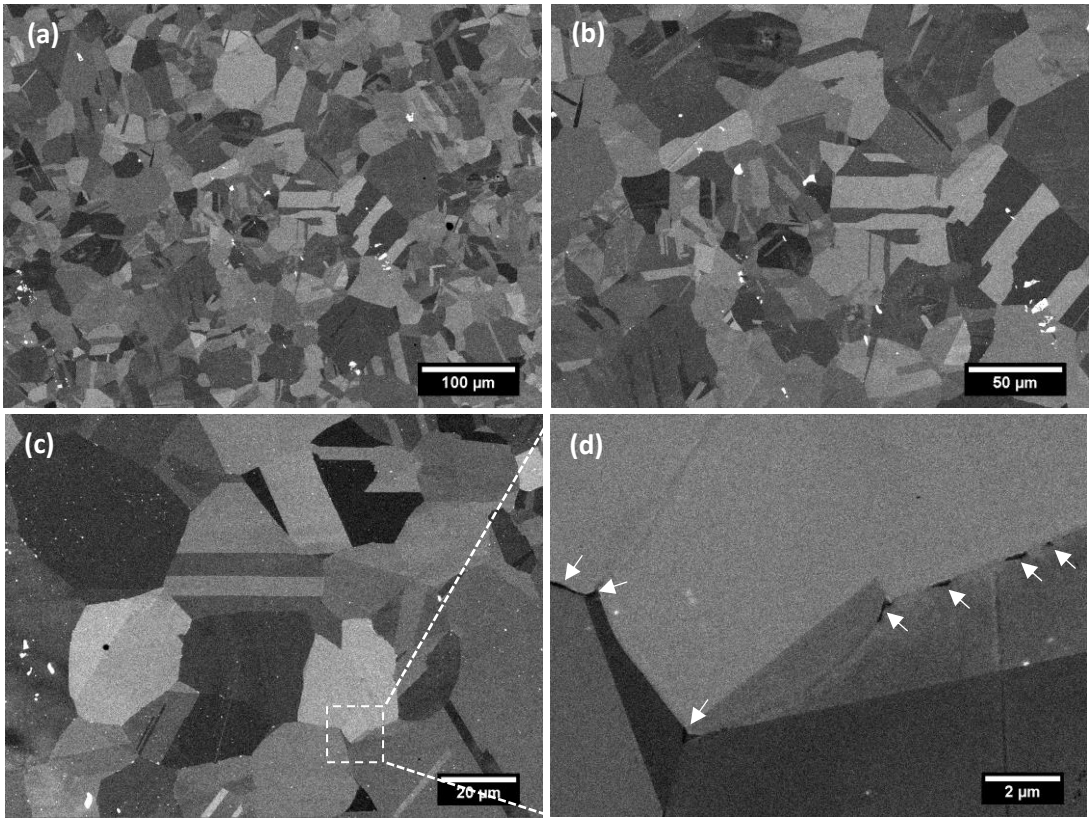

Figure 5-4 BSE images obtained from alloy D solution annealed at 1050 °C and then aged at 650 °C for 24 hours: (a)-(d) are images acquired at different magnification.

BF and high resolution TEM images were acquired from the interfaces between a $M_{23}C_6$ precipitate and the neighbouring grains as illustrated in Figure 5-5. Figure 5-5(a) and (b) are TEM BF images to show the morphology of $M_{23}C_6$ precipitates at the grain boundary. The EDS spectrum at the bottom-left of Figure 5-5(a) was acquired from the precipitate to confirm that it is a chromium carbide. Figure 5-5(c) and (d) are high resolution TEM images of the interface between the chromium carbide and grain B. It shows that the $M_{23}C_6$ precipitate is coherent with grain B. The interface is indicated by a white dashed line in Figure 5-5(d). Misfit strain is observed adjacent to the coherent interface in Figure 5-5(c) due to the mismatch of the lattice constant between the chromium carbide and the matrix [26]. Figure 5-5(e) and (f) are high resolution TEM images of the interface between $M_{23}C_6$

precipitate and grain A, which shows that the $M_{23}C_6$ precipitate is incoherent with grain A. The interface is indicated by a dashed curve in Figure 5-5(f).

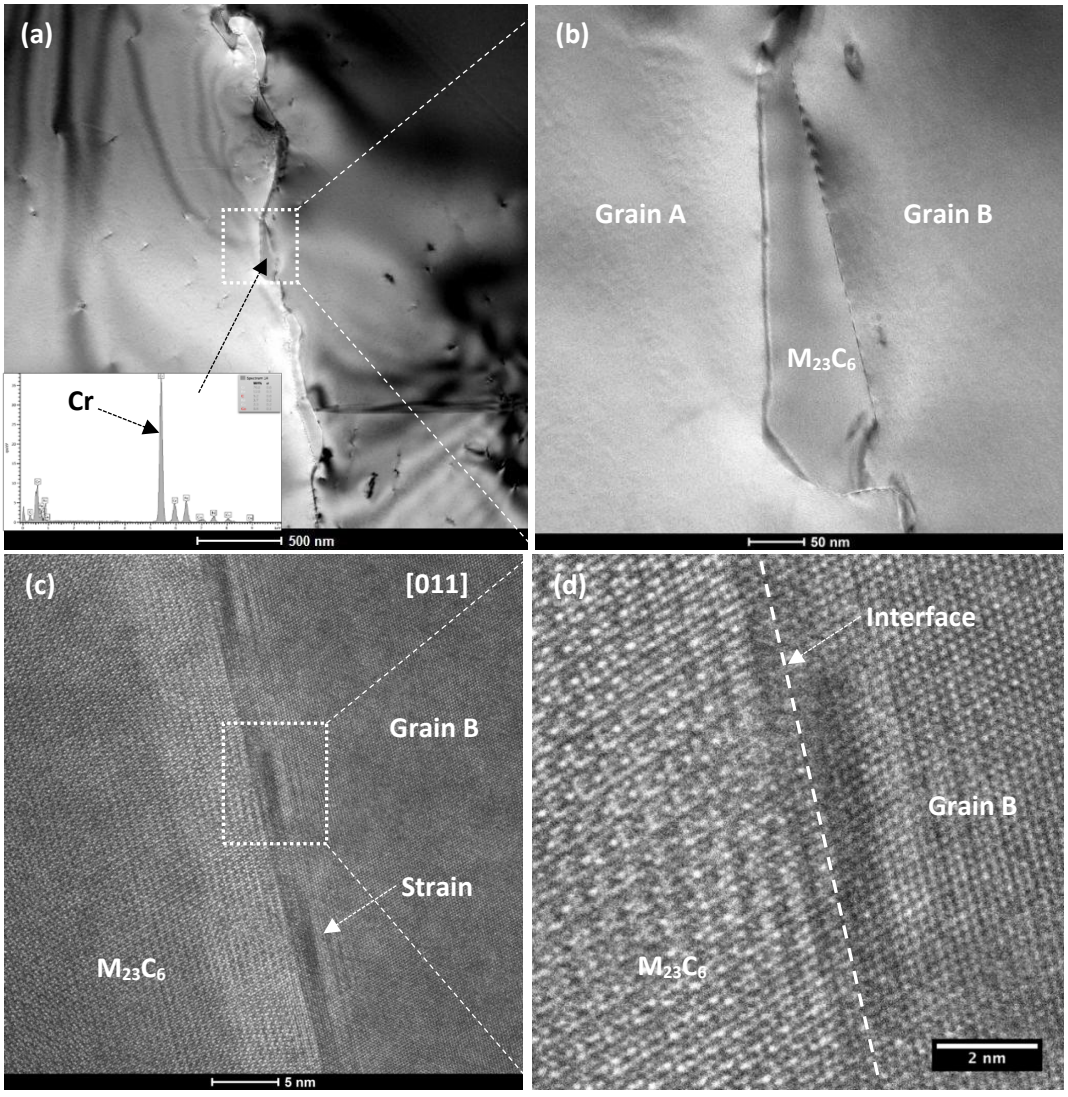

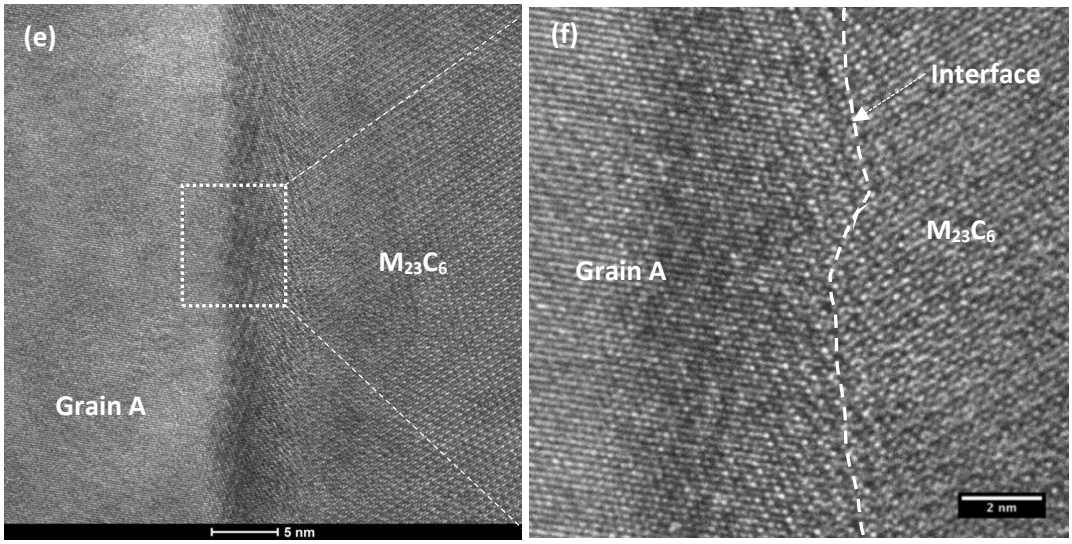

Figure 5-5 TEM BF images and high-resolution images of $M_{23}C_6$ at the grain boundary in alloy D after 24 hours' ageing at 650 °C; (a) BF image showing a grain boundary decorated by $M_{23}C_6$, (b) a $M_{23}C_6$ precipitate at grain boundary, (c)-(f) high resolution images showing the interfaces between the $M_{23}C_6$ precipitate and the matrix.

5.2 Chromium depletion measurement in alloy D annealed at different temperatures

Alloy D was annealed at two temperatures, namely 930 °C and 1050 °C. The 930 °C annealed samples were aged subsequently at 650 °C for 24 hours, 96 hours and 200 hours. The 1050 °C annealed samples were aged subsequently at 650 °C for 1 hour, 5 hours, 24 hours, 96 hours and 200 hours.

5.2.1 Microstructure of alloy D after heat treatment

Figure 5-6 is HAADF images of alloy D after annealing at 930 °C and then ageing at 650 °C for various times, which shows that no $M_{23}C_6$ precipitate is nucleated at the grain boundary in any of the aged samples up to 200 hours. Only NbC precipitates are found both at the grain boundary and in the matrix, which are white particles in the images. Thus, NbC precipitates did not dissolve under annealing at 930 °C resulting in the absence of free

carbon in the matrix, which leads to the grain boundaries are free from $M_{23}C_6$ precipitate nucleation.

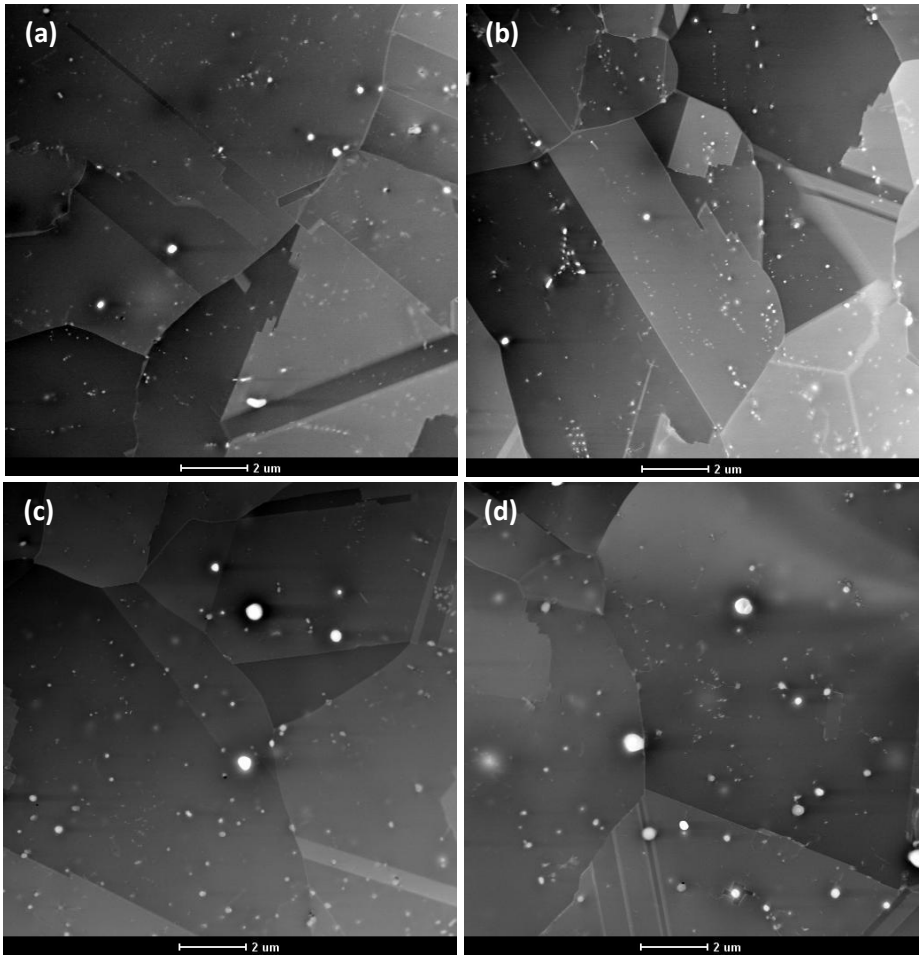

Figure 5-6 TEM HAADF images obtained from alloy D annealed at 930 °C and then aged for various times: (a) annealed, (b) 24 hour, (c) 96 hours, (d) 200 hours.

Figure 5-7 is HAADF images of alloy D after annealing at 1050 °C with subsequent ageing at 650 °C for various times. Compared with the 930 °C annealed samples in Figure 5-6, much less NbC precipitates are observed in the samples annealed at 1050 °C as part of the NbC precipitates dissolve at 1050 °C while they remain intact at 930 °C. The solution annealed sample, without ageing, does not show any $M_{23}C_6$ precipitates at the grain boundary as depicted in Figure 5-7(a). In the 1 hour aged sample (Figure 5-7(b)), only a few $M_{23}C_6$ precipitates are observed at the grain boundary which implies a low degree of

sensitisation in the sample. The size and number of $M_{23}C_6$ precipitates increase with ageing time from 1 hour to 96 hours. $M_{23}C_6$ precipitates are indicated by white arrows at the grain boundary. The shape of the $M_{23}C_6$ precipitates are irregular. The spacing between the chromium carbides is still large even after 200 hours ageing, which means the chromium carbides did not form a continuous film at the grain boundary. No obvious increase in the amount of chromium carbides is observed between 96 hours and 200 hours, which indicates that $M_{23}C_6$ precipitation reaches a maximum after 96 hours ageing. Some of the precipitates (indicated by black arrows) with white contrast at the grain boundary are G phases which might be transformed from niobium carbide [53] after a long time of ageing at 650 °C.

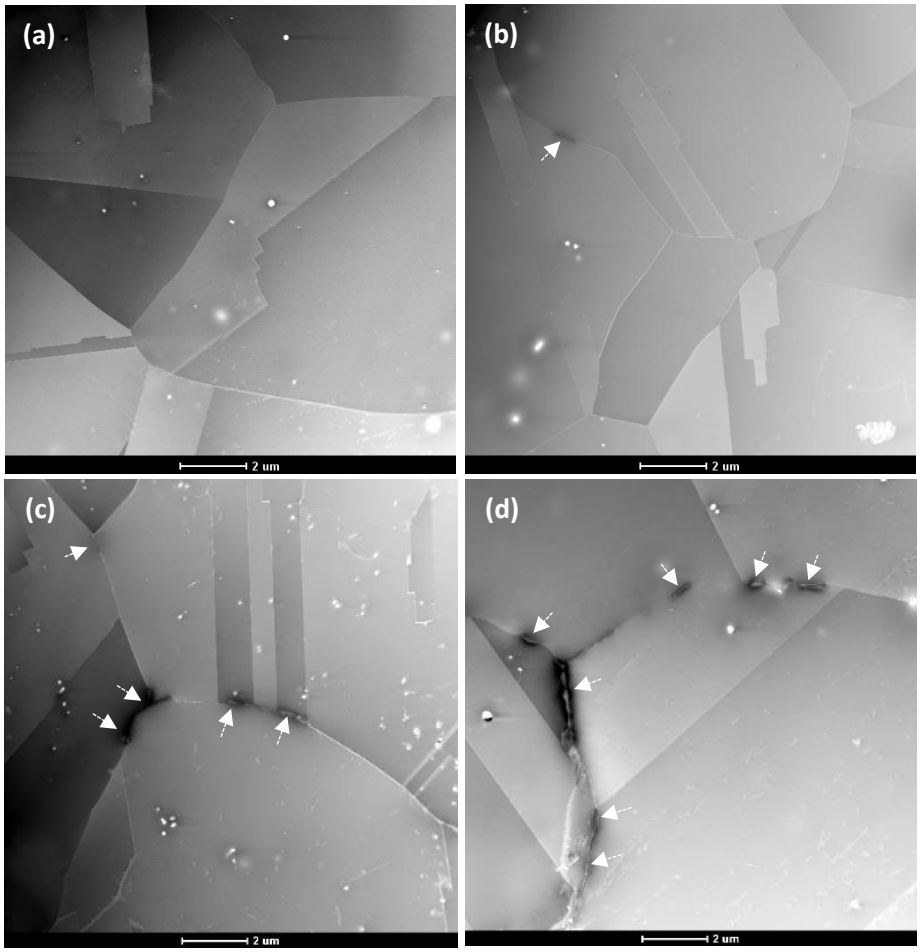

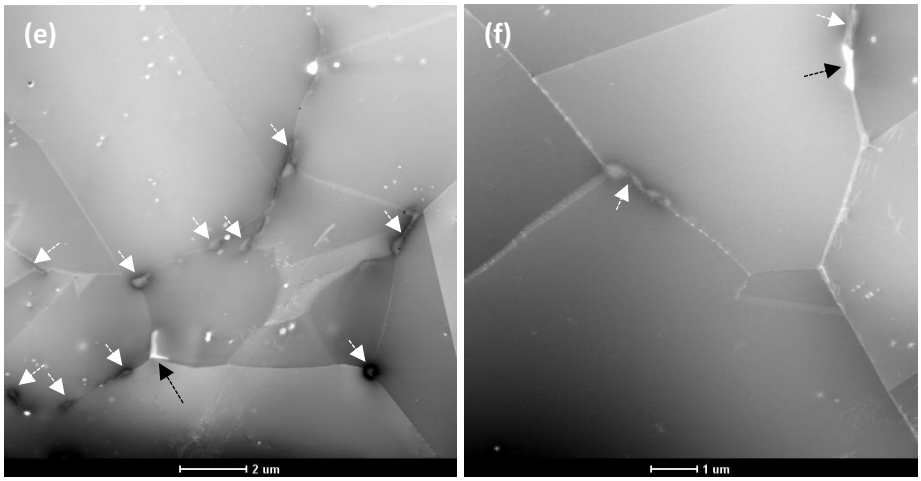

Figure 5-7 TEM HAADF images obtained from alloy D after annealing at 1050 °C and then aged at 650 °C for various times: (a) solution annealed without ageing, (b) 1 hour, (c) 5 hours, (d) 24 hours, (e) 96 hours, (f) 200 hours.

5.2.2 The measurement of chromium depletion

Figure 5-8(a) is a HAADF image of alloy D after annealing at 1050 °C and then aged for 24 hours at 650 °C. A $M_{23}C_6$ precipitate, indicated by a black arrow, is found at the grain boundary. A number of small NbC precipitates indicated by white arrows are formed at the grain boundary. The dissolution of NbC precipitates on annealing at 1050 °C increases the concentration of niobium in the matrix. The migration of niobium towards the grain boundary forms niobium carbide. The white dashed line indicates the EDS line scan position, which is about 150 nm away from the $M_{23}C_6$ precipitate to avoid the influence of the precipitate on segregation measurement. Figure 5-8(b) shows typical elemental segregation profiles at the grain boundary. Chromium is seriously depleted with a lowest concentration of 12.0 wt.% and a depletion width of 400 nm at the grain boundary, Ni and Fe are enriched, and no Si segregation is detected. For RIS, silicon is enriched at the grain boundary because of the interstitial-solute dragging mechanism. However, silicon segregation is not observed in the aged sample as the equilibrium vacancy concentration does not increase during the ageing process. A twin peak is observed on the Fe profile, which might be because of the relative narrow enrichment profile of Ni. It makes Fe

enrichment at the grain boundary less than in the adjacent areas. The twin peak Fe segregation profile is observed in most samples with severer chromium depletion. As this thesis focuses on the sensitisation of AGR fuel cladding alloys, which is induced by chromium depletion at the grain boundary, only the chromium profile is shown in the following figures.

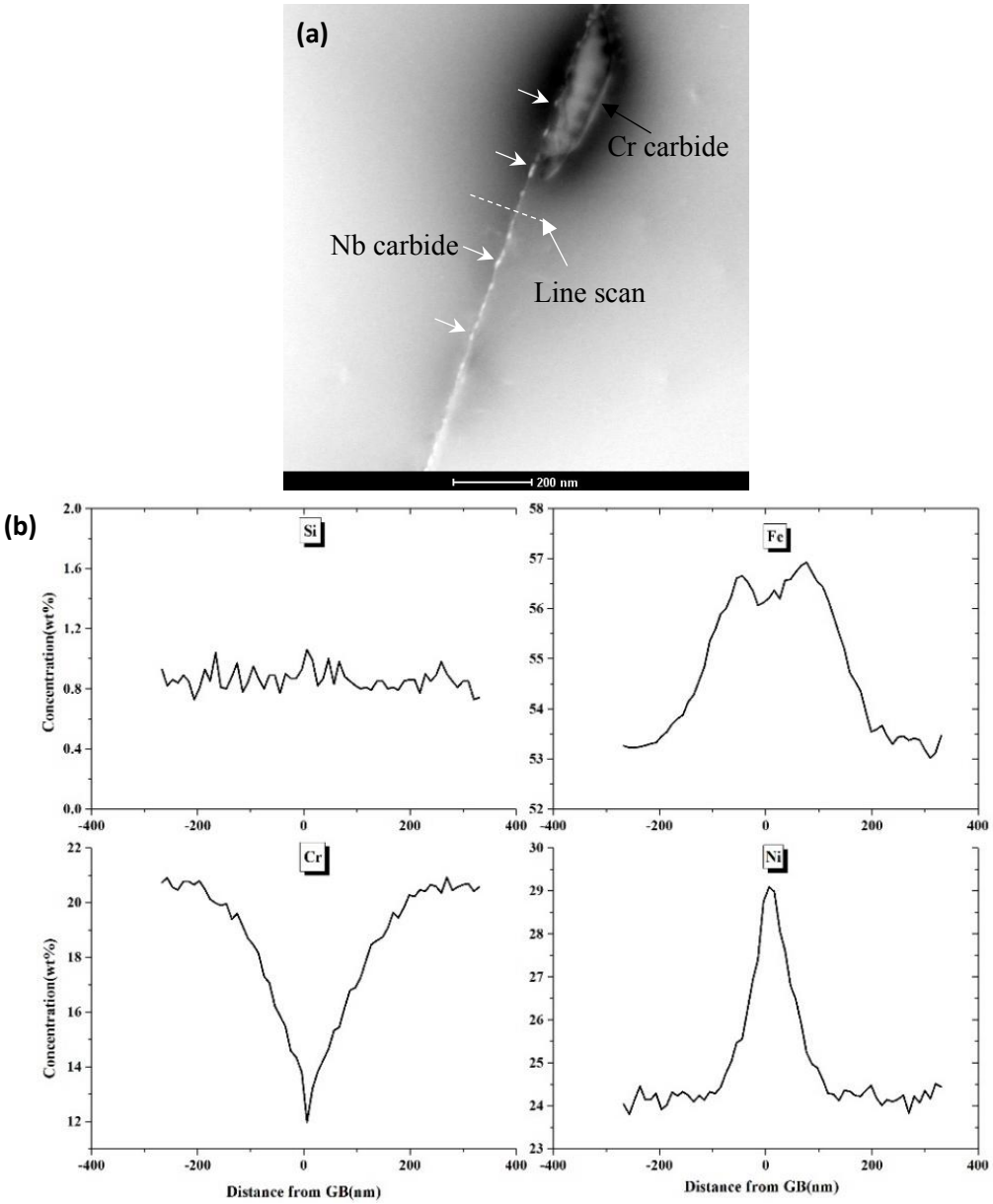

Figure 5-8 A typical grain boundary elemental profiles obtained from alloy D solution annealed at 1050 °C and then aged for 24 hours at 650 °C: (a) HAADF image, (b) elemental segregation profiles.

Chromium depletion profiles across the grain boundary in alloy D annealed at 930 °C and 1050 °C with subsequent ageing are shown in Figure 5-9. No chromium depletion is detected in the 930 °C or 1050 °C annealed sample (without ageing) as illustrated in Figure 5-9(a). Figure 5-9(b) shows that chromium depletion at the grain boundary starts to emerge after 1 hour ageing in the 1050 °C annealed sample. The lowest chromium concentration at the grain boundary is about 16 wt.% with a narrow depletion width, about 30 nm. The mild chromium deletion is because the $M_{23}C_6$ precipitation at the grain boundary is rare in the 1 hour aged sample as shown in Figure 5-7(b). Compared with the 1 hour aged sample, both the magnitude and width of the chromium depletion increase after 5 hours' ageing as depicted in Figure 5-9(c). In the samples annealed at 930 °C, no chromium depletion is detected at the grain boundary after 24 hours, 96 hours or 200 hours ageing (Figure 5-9(d)-(f)) due to the absence of $M_{23}C_6$ precipitates in these samples as shown in Figure 5-6. Serious chromium depletion is present at the grain boundary in the sample annealed at 1050 °C and then aged for 24 hours shows as shown in Figure 5-9(d). The lowest chromium concentration is only 12 wt.% with a large segregation width of about 400 nm. The chromium depletion is healed when the ageing time increases to 96 hours and 200 hours as shown in Figure 5-9(e) and (f). The samples annealed at 930 °C shows a slightly higher chromium concentration in the matrix after 96 hours and 200 hours ageing compared with the 1050 °C annealed sample, which might be because the formation of chromium carbides at the grain boundary after the 1050 °C anneal consumes chromium from the matrix.

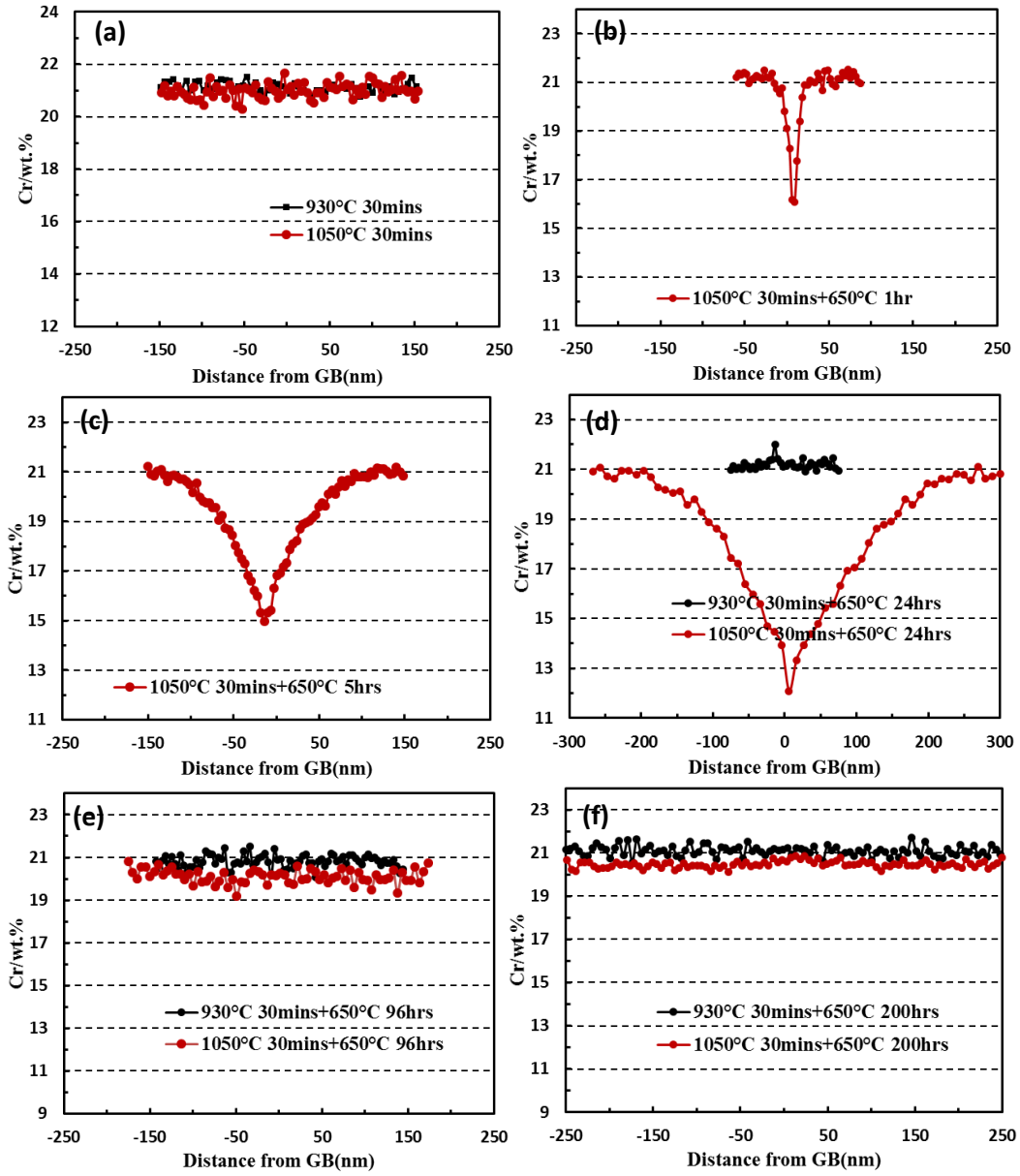

Figure 5-9 The comparison of chromium depletion at the grain boundary in alloy D annealed at 930 °C and 1050 °C, and then aged at 650 °C for various times: (a) annealed, (b) 1 hour, (c) 5 hours, (d) 24 hours, (e) 96 hours, (f) 200 hours.

To further characterise the chromium concentration at the grain boundary, STEM-EDS point measurements were conducted on three grain boundaries and on each grain boundary two measurements were made. Figure 5-10 shows the chromium concentration at the grain boundary as a function of ageing time in the samples annealed at 930 °C and 1050 °C. The error is calculated over six data points on each sample and an error bar is included in the

figure. In the samples annealed at 930 °C, no chromium depletion is detected at the grain boundaries regardless of the ageing time, even up to 200 hours. For samples annealed at 1050 °C, the most serious chromium depletion at the grain boundary is detected in the 24 hours' aged sample. Increasing the ageing time to 96 hours or 200 hours, chromium depletion is healed almost entirely, which might indicate that the free carbon has been consumed to form chromium carbides at the grain boundary after 24 hours ageing and further ageing will lead to the initiation of desensitisation. After 24 hours ageing, the largest chromium concentration gradient forms between the matrix and the grain boundary. Thus, the chromium concentration in the sample is inhomogeneous and there is no driving force to maintain it as there is no further formation of chromium carbides. As the ageing time increases, chromium in the matrix diffuses towards grain boundary to cancel out the chromium depletion. Finally, the chromium concentration in the whole sample becomes homogeneous again.

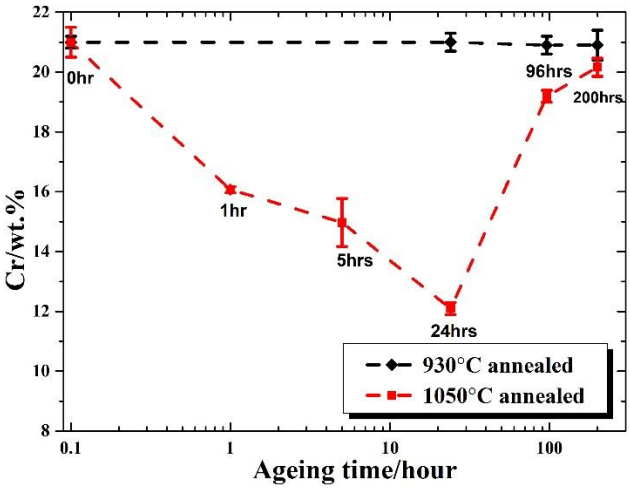

Figure 5-10 Chromium concentration at the grain boundary in alloy D annealed at 930 °C and 1050 °C as a function of ageing time at 650 °C.

5.3 DOS of alloy D annealed at different annealing temperatures

In this section, the DOS of alloy D annealed at 930 °C and 1050 °C was measured by the DL-EPR test with a subsequent surface morphology examination using SEM. To have a better understanding of the attack features after the DL-EPR test, localized corrosion features were also analyzed.

5.3.1 DOS measurement

Figure 5-11 shows the polarisation curves of the DL-EPR tests on alloy D after ageing at 650 °C for various times. It shows that the 24 hours aged sample has the highest maximum reverse current density (I_r) while the 200 hours aged sample has the lowest maximum I_r. During the reverse scan, the more serious the attack at the grain boundary the higher reverse current density will be. The I_r increases as ageing time increases from 1 hour to 24 hours and reaches a maximum after 24 hours ageing. Thus, the most serious attack morphology is expected in the 24 hours aged sample. As ageing time increases to 96 hours or 200 hours, I_r starts to decrease, which means that sensitisation starts to be healed. The solution annealed sample (without ageing) shows the lowest reverse current which indicates no intergranular attack at the grain boundary. In Figure 5-11(b), the polarisation curves from the DL-EPR tests on alloy D annealed at 930 °C are sketched together with those from the 1050 °C annealed samples. The maximum reverse current density (I_r) of the 1050 °C annealed samples is higher than that of the 930 °C annealed samples.

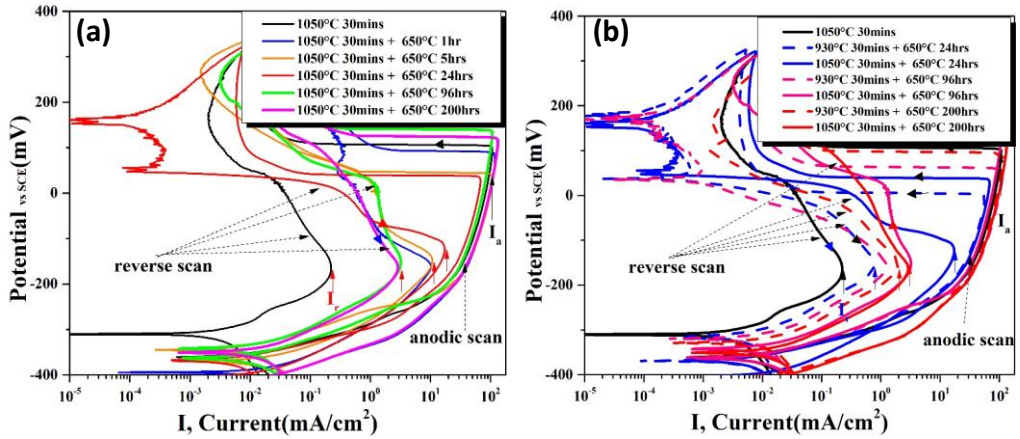

Figure 5-11 Polarisation curves of DL-EPR test in alloy D aged at 650 °C for various ageing times after annealing at different temperatures: (a) 1050 °C, (b) comparison of 1050 °C and 930 °C.

Two samples were tested by the DL-EPR test after each heat treatment. Table 5-1 summarises the DL-EPR test results on alloy D. DOS is determined by the ratio of maximum reactivation current density (I_r) to maximum activation current density (I_a) and the average DOS of the two tested samples under each heat treatment is plotted in Figure 5-12. For the 1050 °C annealed samples, the DOS increases as the ageing time increases and reaches the maximum after 24 hours ageing. DOS decreases as the ageing time increases to 96 hours and 200 hours. In the 930 °C annealed samples, the DOS in all aged samples is at a very low level and less than that in the samples annealed at 1050 °C.

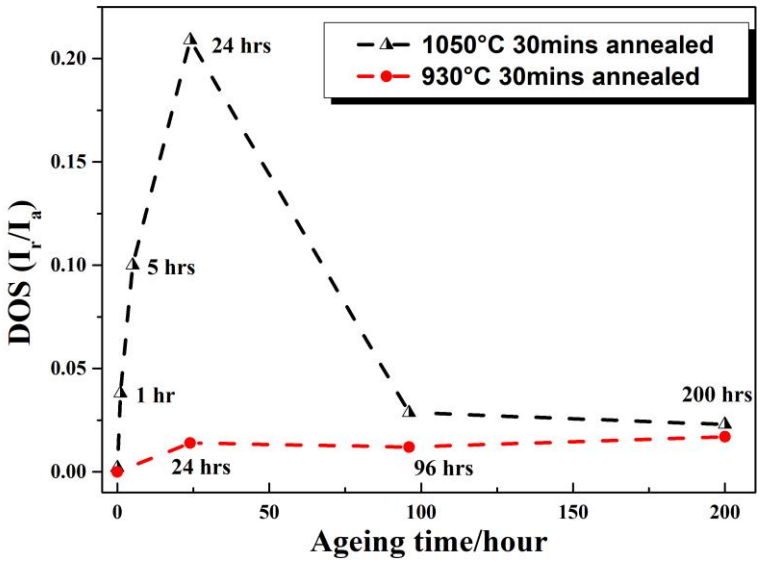

Figure 5-12 The value of I_r/I_a showing the dependence of DOS on ageing time in alloy D.

Table 5-1 Results of the DL-EPR test on alloy D annealed at 930 °C or 1050 °C and then aged for various times.

Material	Annealing temperature (°C)	Ageing time at 650 °C (hours)	Maximum anodic and reactivation current						Average [DOS]
			Test1			Test2			
			I_a (mA/cm^2)	I_r (mA/cm^2)	I_r/I_a [DOS]	I_a (mA/cm^2)	I_r (mA/cm^2)	I_r/I_a [DOS]	
Alloy D	930	0	109.7	0.022	0.000	100.6	0.021	0.000	0.000
		24	56.8	0.772	0.014	67.9	0.977	0.014	0.014
		96	136.1	1.789	0.013	115.6	1.224	0.011	0.012
		200	127.3	2.205	0.017	115.8	1.958	0.017	0.017
	1050	0	108.1	0.223	0.002	-	-	-	0.002
		1	88.47	3.384	0.038	118.2	10.161	0.086	0.062
		5	107.8	10.774	0.100	136.8	24.385	0.178	0.139
		24	68.2	14.292	0.209	-	-	-	0.209
		96	135.6	3.763	0.028	108.5	3.211	0.030	0.029
		200	133.7	2.889	0.022	119.5	2.716	0.023	0.022

5.3.2 Surface morphology examination

To explain the DOS obtained from the DL-EPR test on the aged samples, the sensitisation morphology of the tested samples was examined using SEM. Figure 5-13 shows the morphology of the 930 °C annealed samples after DL-EPR testing. All the 930 °C annealed samples with subsequent ageing to various times up to 200 hours are absent from attack. Only 'step' structure is observed throughout the sample. This indicates that they are not subject to sensitisation, which agrees with the low reverse current density shown in Figure 5-11(b). The particles remaining on the sample surface after the DL-EPR test are NbC precipitates due to their high corrosion resistance to the test solution.

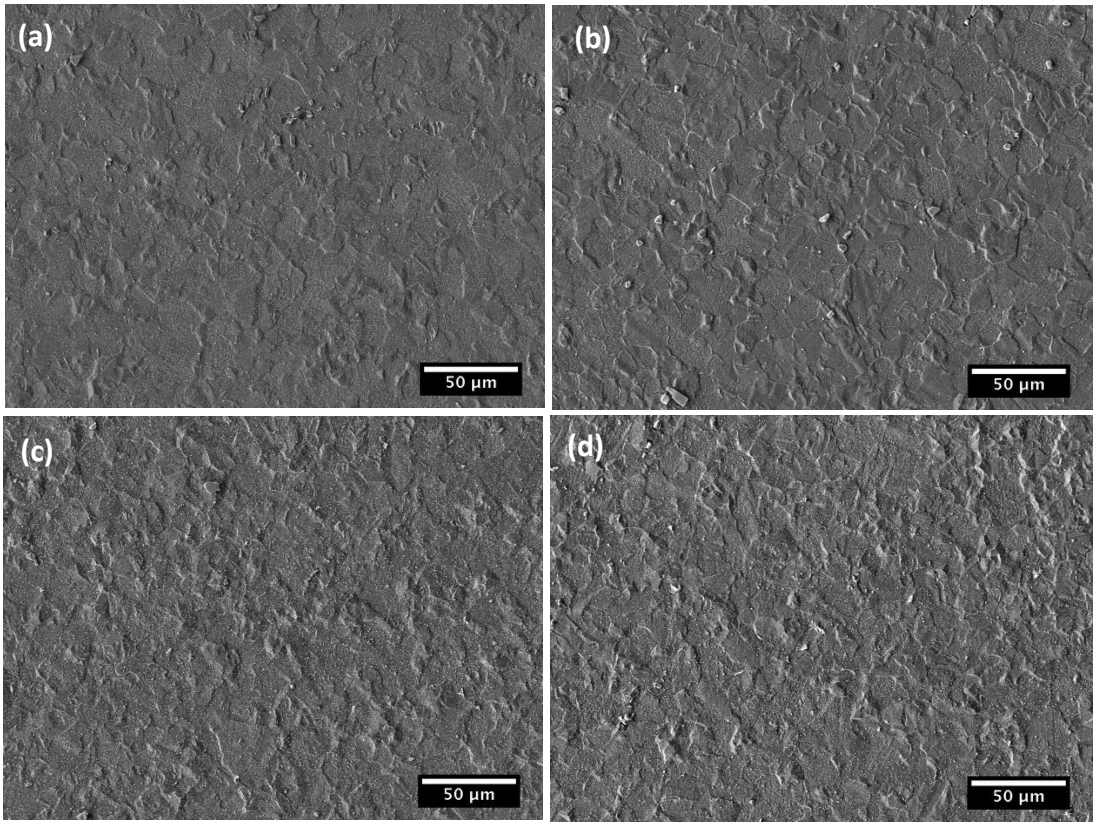

Figure 5-13 Surface morphology micrographs obtained from alloy D annealed at 930 °C and the aged at 650 °C for various times after DL-EPR testing: (a) annealed without ageing, (b) 24 hours, (c) 96 hours, (d) 200 hours.

Figure 5-14 shows the surface attack morphology in low and high magnifications of alloy D after the DL-EPR test, which was solution annealed at 1050 °C with subsequent ageing at 650 °C for various times. Figure 5-14(a) and (b) are surface morphology images of the solution annealed sample without ageing, which show that the sample is free from attack and only 'step' structure is observed. In the 1 hour aged sample, as shown in Figure 5-14(c) and (d), a number of discrete pits are present at the grain boundaries and most of them seems likely on triple junctions, which indicates that lots of chromium carbides nucleate at the triple junctions and cause severe chromium depletion at adjacent area of the carbide-matrix interface. When the ageing time increases to 5 hours, as shown in Figure 5-14(e) and (f), more pits are observed at the grain boundary and the size of the pits increases. Meanwhile, many small pits start to emerge on the grain boundaries. As shown in Figure 5-14(g) and (h), the intergranular attack gets more serious when the ageing time increases to 24 hours. Most of the attack is ditches at the grain boundary. Large numbers of pits are also present at the grain boundaries. Some of them are individual pits and others tend to connect together to be a ditch. The intergranular attack is mitigated as ageing time increases further to 96 hours and 200 hours, as shown in Figure 5-14(i)-(l). Only a few pits are left after 96 hours ageing which means the sensitisation has been substantially healed (Figure 5-14(i) and (j)). The sensitisation is healed entirely when the ageing time increased to 200 hours (Figure 5-14(k) and (l)). Many flake-like features remaining at the grain boundary are proved to be chromium carbides in the following section. However, the surface morphology of the sample annealed at 930 °C and then aged for 200 hours shows no flake-like feature observed at the grain boundaries (Figure 5-13(d)), which indicates chromium

carbides nucleation do not take place in the 930 °C annealed sample even after a long time aging.

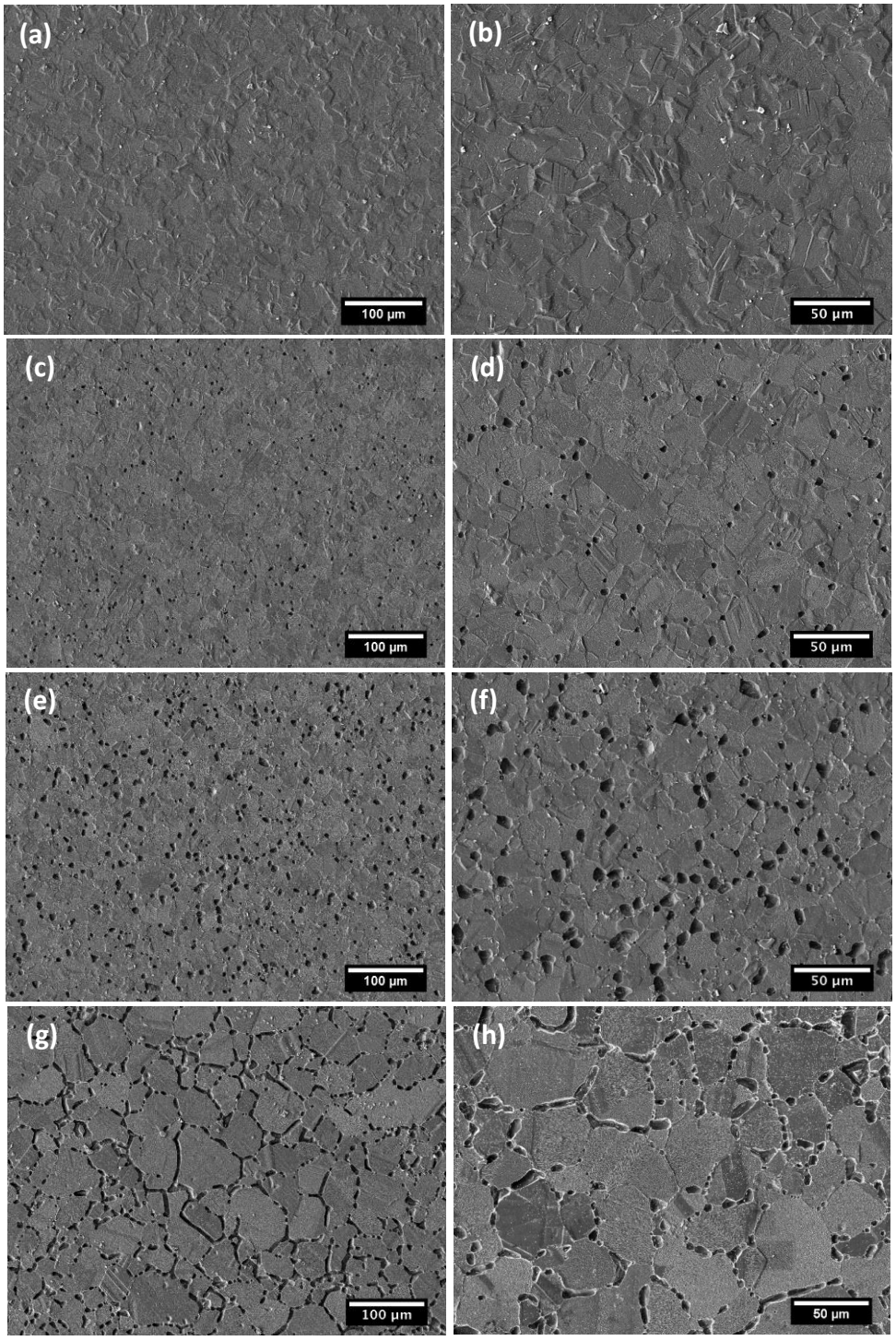

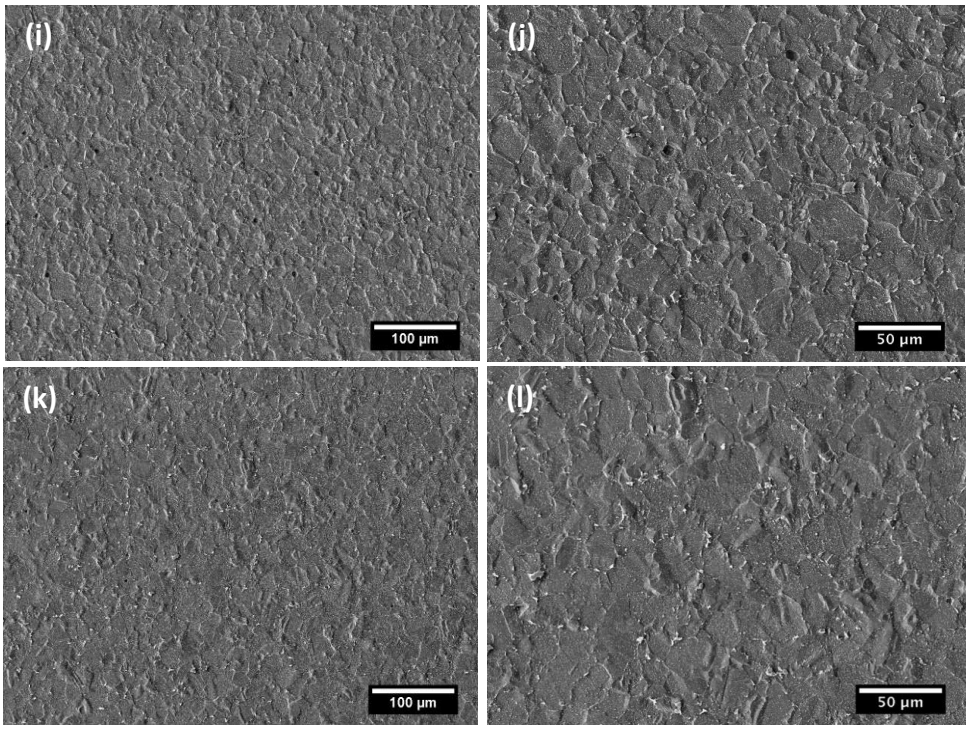

Figure 5-14 Surface morphology micrographs obtained from alloy D annealed at 1050 °C with various ageing time scale after DL-EPR test, (a)(b) solution anneal, (c)(d) 1 hour, (e)(f) 5 hours, (g)(h) 24 hours, (i)(j) 96 hours and (k)(l) 200 hours.

5.3.3 Characterisation of the attack features on alloy D after the DL-EPR test

As shown in Figure 5-15, the surface and grain boundary attack morphology of the DL-EPR test on alloy D solution annealed at 1050°C with subsequent 24 hours ageing were examined by SEM and EBSD. The appearance of the sensitised sample surface presents an abundance of corrosion features. As illustrated in Figure 5-15(a), sensitisation is uniform throughout the whole sample. Figure 5-15(b) shows a representative surface morphology of the 24 hours aged sample. Almost all sites attacked during the DL-EPR test are at the grain boundary. Most of the attack appears as discrete pits at the grain boundaries and triple junctions. Some of the large pits tend to connect together to form a ditch at the grain boundary. In terms of pit number and size, the extent of attack varies from grain boundary to grain boundary. Figure 5-15(c) and Figure 5-15(d) are localised areas of Figure 5-15(b)

indicated by area A and area B, respectively. They show that Σ3 coherent twin boundaries and LAGBs are immune to intergranular attack, while most of the random HAGBs are attacked and the extent of attack varies from grain boundary to grain boundary. Figure 5-15(e) and Figure 5-15(f) are grain orientation and grain boundary distribution maps, which were acquired from the same area in Figure 5-15(b). Figure 5-15(e) confirms that all attack, decorated with a black colour, are at the grain boundaries. Figure 5-15(f) shows that there is a large number of Σ3 boundaries, delineated by red lines, and they are immune to intergranular attack. A few LAGBs are identified in the sample and they are immune to attack either. However, almost the entire HAGBs are attacked to various extents.

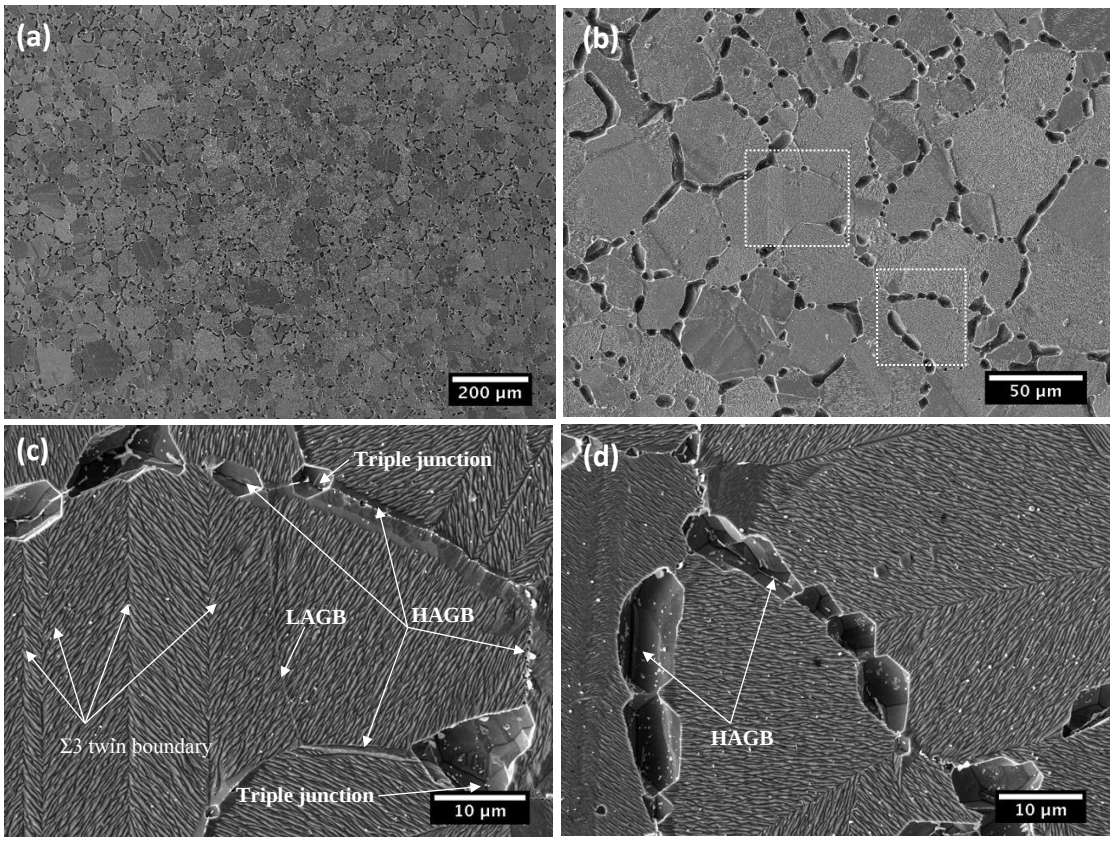

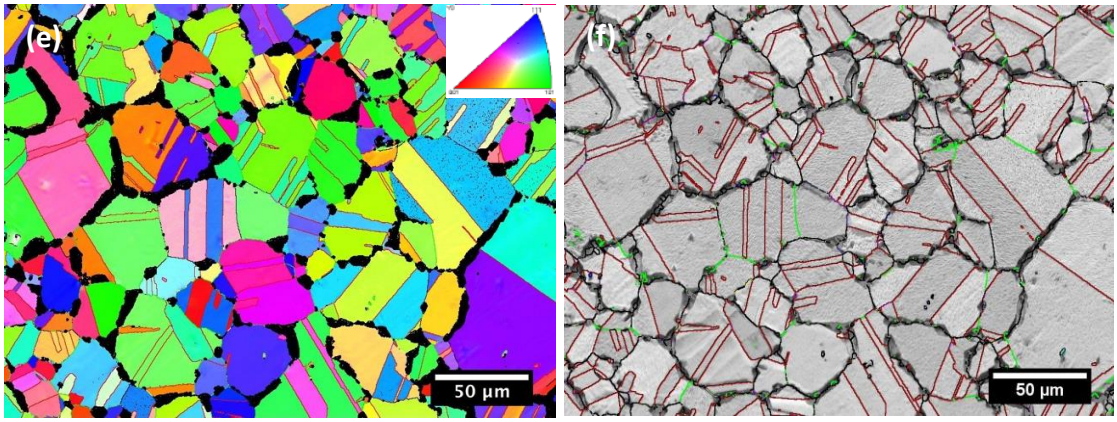

Figure 5-15 DL-EPR tested sample obtained from alloy D annealed at 1050 °C and then aged for 24 hours at 650 °C: (a), (b), (c) and (d) are SEM images of the sample surface, (e) orientation map in the Y direction, (f) grain boundary segments are shown in various colours: Σ3 and Σ9 boundaries red and pink, random HAGBs and LAGBs are black and green.

Figure 5-16(a) is a micrograph of several attacked grain boundaries. The attack exhibits as ditches at the grain boundaries and a number of chromium carbides are distributed along the grain boundary inside the ditch, and they tend to connect together. Figure 5-16(b) shows another grain boundary with discrete pits rather than a ditch, which means this grain boundary is less sensitised than that in Figure 5-16(a). Lots of chromium carbides are found on the grain boundary. To confirm this precipitates are chromium carbides, EDS maps on the grain boundary area are obtained. As shown in the EDS maps (Figure 5-16(c)), chromium and carbon counts increase at the sites of these precipitates while iron and nickel counts decrease. This suggests that these precipitates are chromium carbides instead of niobium carbides. Thus, chromium carbides remain intact during the DL-EPR test.

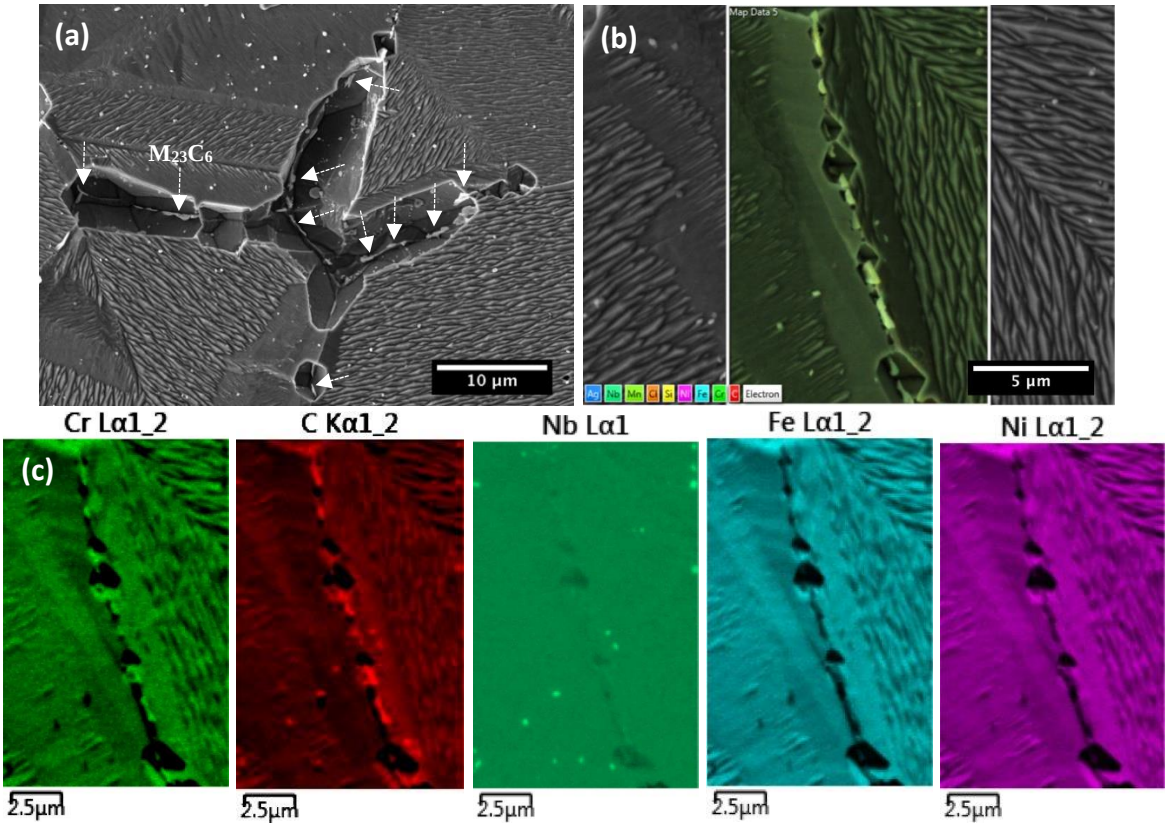

Figure 5-16 Chromium carbides remain at the grain boundary after the DL-EPR test on alloy D annealed at 1050 °C and then aged for 24 hours at 650 °C: (a) SEM images, (b) EDS mapping area, (c) EDS maps acquired from the area in (b)

As shown in Figure 5-17(a), coherent twin boundaries are immune to attack while incoherent twin boundaries are partly free from attack. Figure 5-17(b) shows a localised area of Figure 5-17(a), which shows that no chromium carbide is observed at the coherent twin boundary while many small chromium carbides are seen on the incoherent twin boundary. One large pit, indicated by a black arrow, is also observed at the incoherent twin boundary. Figure 5-17(c) is a comparison of EDS spectra acquired from the precipitate and matrix. The grey spectrum is from the precipitate at an incoherent twin boundary indicated by a white arrow in Figure 5-17(b) while the red spectrum is from the matrix. Compared with the matrix, the X-ray counts of chromium and carbon from the precipitate are higher, which indicates these precipitates are chromium carbides.

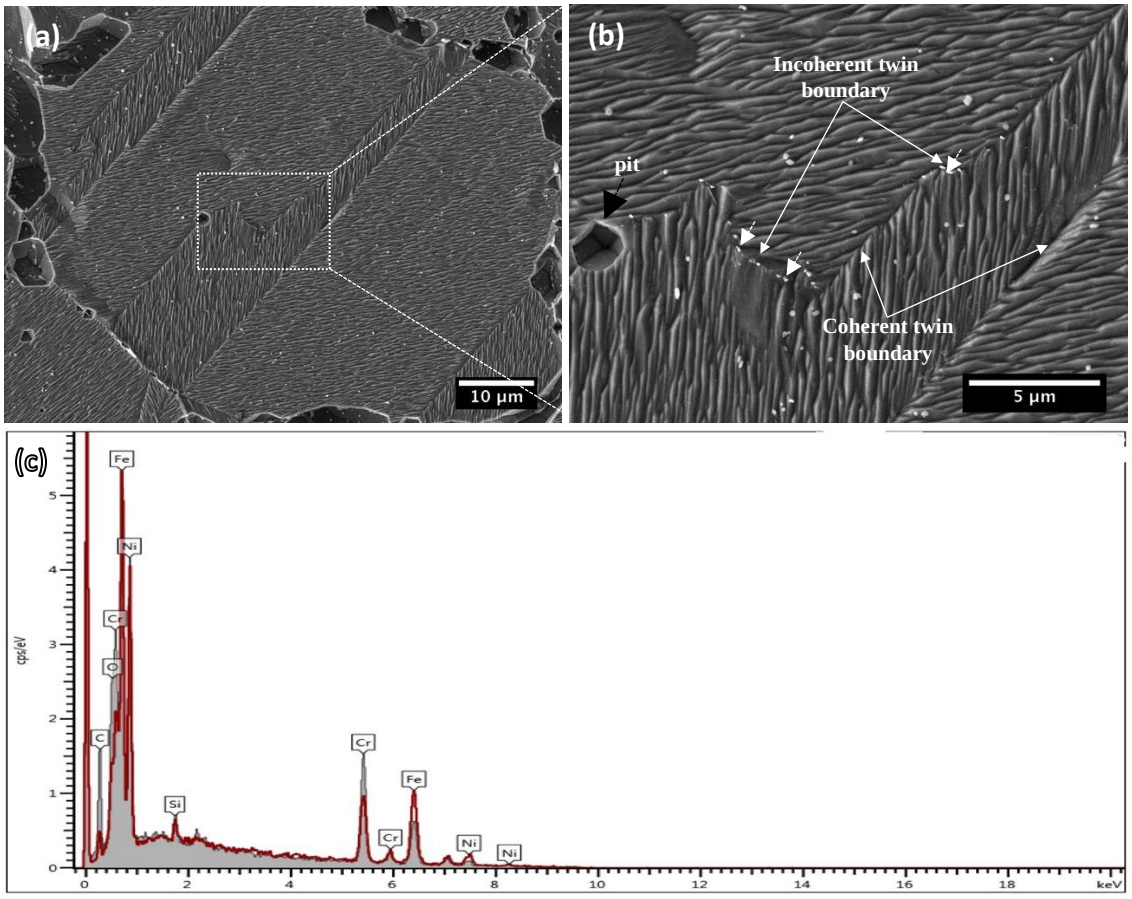

Figure 5-17 (a) and (b) show the morphology after the DL-EPR test on alloy D annealed at 1050 °C and then aged for 24 hours at 650 °C, (c) EDS spectra acquired from a precipitate at an incoherent twin boundary (grey) and from the matrix (red).

The effect of NbC precipitates on the corrosion of AGR fuel cladding material was studied in Phuah's thesis [31]. The corrosion of the matrix surrounding the NbC is examined in Figure 5-18. Figure 5-18(a) is an area where both large and small NbC precipitates are present in the matrix. Figure 5-18(b), (c) and (d) are three localised areas in Figure 5-18(a), where various extents of attack are observed around the NbC precipitates. As shown in Figure 5-18(b) and (c), attack is observed around the large NbC precipitates while no corrosion is observed around the small (around 200 nm) NbC. However, not all large NbC have their surrounding alloy attacked, as shown in Figure 5-18(d).

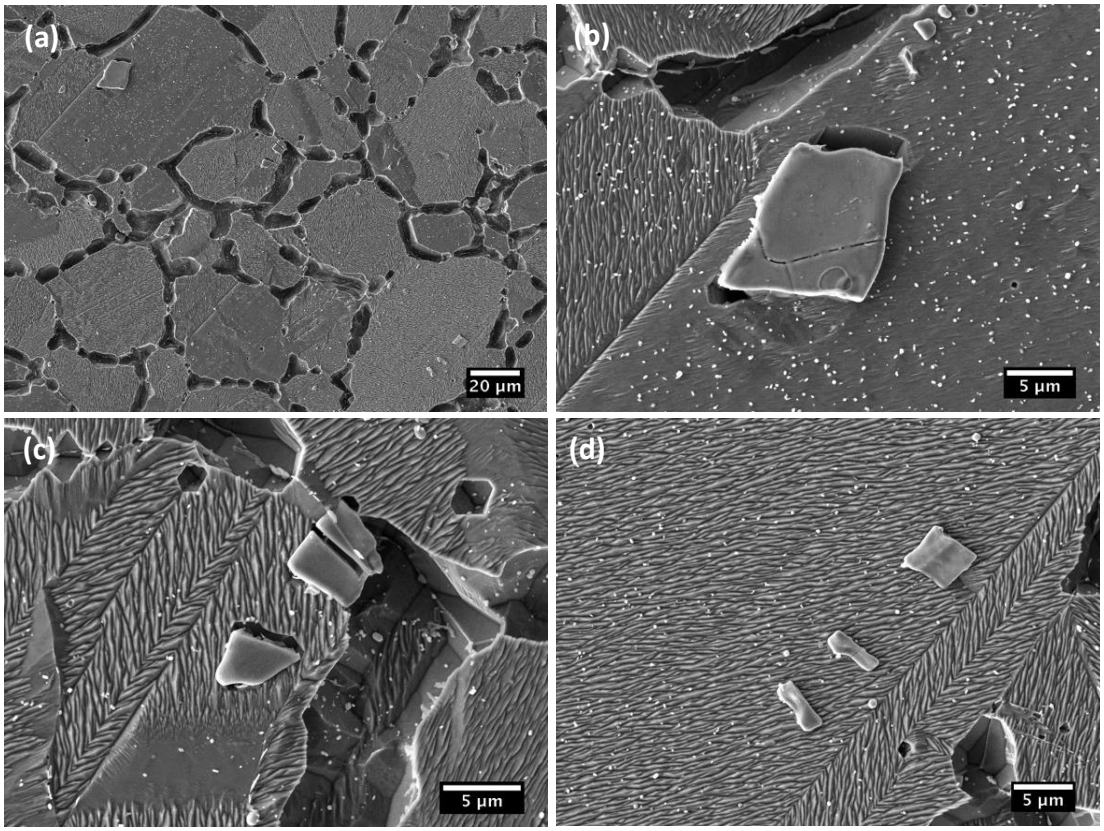

Figure 5-18 (a) SEM images of alloy D aged for 24 hours showing the corrosion around large niobium carbides, (b), (c) and (d) are localised images of the niobium carbides in (a).

To investigate the corrosion behaviour around chromium carbides at the grain boundary, a comparison of the same area before and after the DL-EPR test is obtained as shown in Figure 5-19. Figure 5-19(a) is a BSE image of alloy D aged at 650 °C for 5 hours before the DL-EPR test. It shows that many chromium carbides, indicated by white arrows, are found along the grain boundaries. There is a large niobium carbide top-left. The same area was found after the DL-EPR test as shown in Figure 5-19(b). The large niobium carbide is prominent after the test, which means the dissolution of matrix was severe during the forward scan in the DL-EPR test. The shapes of the niobium carbide before and after the DL-EPR test are similar, which indicates that niobium carbides remain intact during the

test due to their high corrosion resistance. Grain A, which has many chromium carbides around its boundaries, is selected to compare the corrosion behaviour of chromium carbides. The EDS maps shown in Figure 5-19(c)-(f) indicate that chromium carbides remain at the grain boundaries after the DL-EPR test. Compared with the location of chromium carbides in Figure 5-19(a), some of the chromium carbides newly emerged in Figure 5-19(b) suggests that these chromium carbides are revealed after the test. Some of the chromium carbides observed in Figure 5-19(a) have disappeared. They might have dropped into the test solution because the matrix dissolution depth might be larger than the size of the chromium carbides. In the EDS mapping area, one small pit (indicated by black arrow) is present at the grain boundary while a large pit (indicate by red arrow) is more likely nucleated at a triple junction. No attack is found around the other chromium carbides at the grain boundary or the other triple junctions.

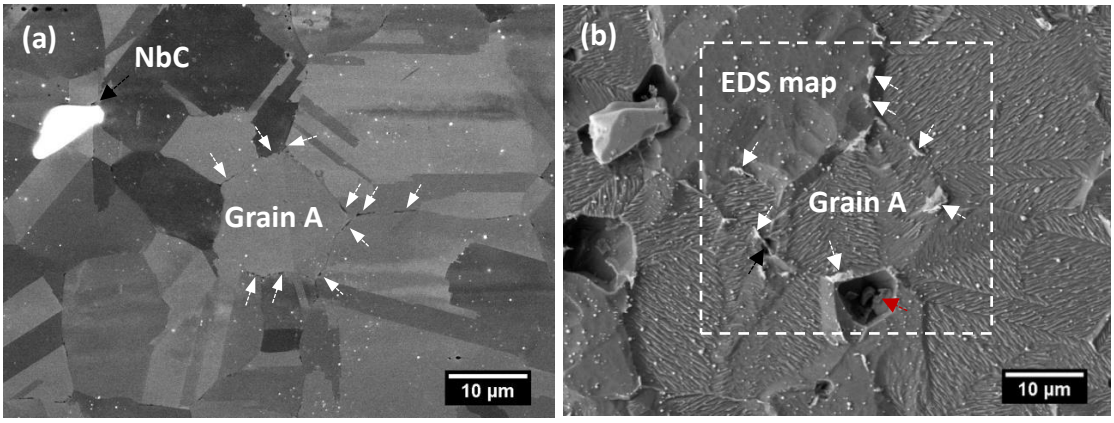

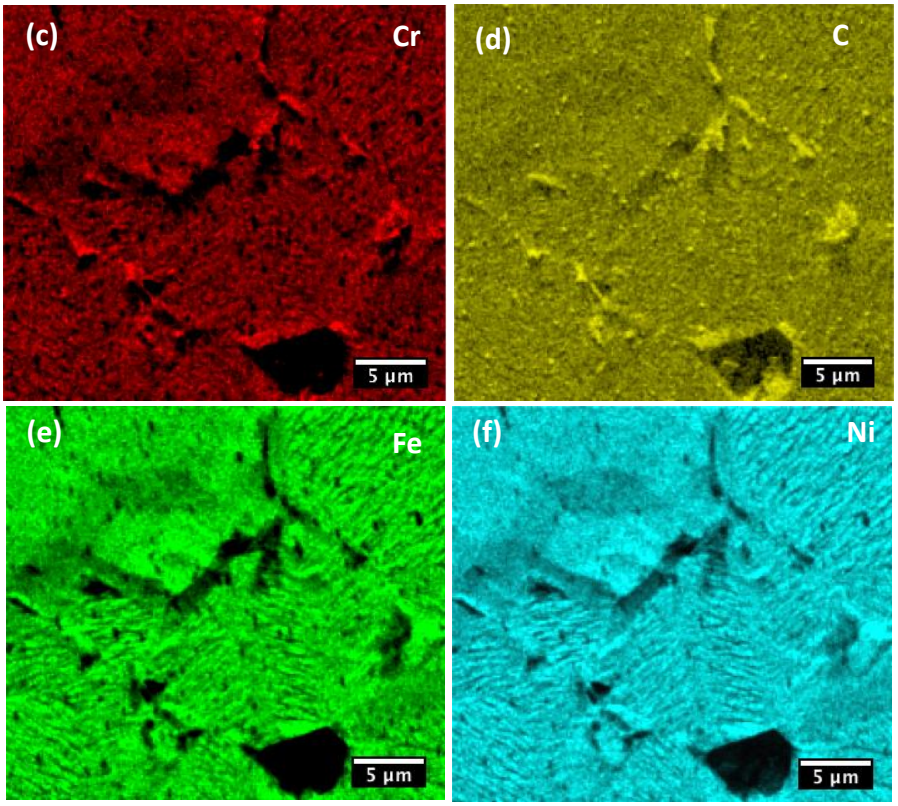

Figure 5-19 SEM micrographs and EDS maps obtained from alloy D annealed at 1050 °C and then aged for 5 hours: (a) before DL-EPR test, (b) the same location as (a) after DL-EPR test. (c) - (f) are EDS maps of chromium, carbon, iron and nickel, respectively.

5.4 Discussion

5.4.1 Material characterisation

The grain size of the 930 °C annealed sample is smaller than that of the 1050 °C annealed sample (Figure 5-1) because higher annealing temperatures can facilitate the grain growth [185]. The grain boundary is dominated by the Σ3 boundaries which are free from carbide precipitation and immune to intergranular attack due to their low boundary energy [23]. The grain structure of alloy D is very similar to the grain structure of the model alloys in Figure 4-1. This grain boundary network makes the commercial 20/25/Nb alloy possess excellent intergranular corrosion resistance. The 20/25/Nb alloy is niobium stabilised. Carbon is fixed by niobium carbides, which can dramatically improve its intergranular

corrosion resistance. Niobium carbides dissolve at high annealing temperature (1050 °C in this work) and the amount of niobium carbide dissolved depends on the temperature and the duration of annealing [55]. This explains the number of remaining niobium carbides in the 930 °C annealed sample (Figure 5-1(a) and (b)) is higher than that in the 1050 °C annealed sample (Figure 5-1(c) and (c)). Niobium carbides in 20/25/Nb AGR fuel cladding material were reported to be Nb(CN) by Powell et al. [53]. However, no nitrogen counts have detected as illustrated in Figure 5-3. Thus, the niobium carbides in the alloys studied in this thesis are NbC, not Nb(CN).

A number of chromium carbides are found in the sample annealed at 1050 °C followed by ageing at 650 °C for 24 hours (Figure 5-4), which might hint the sensitisation of alloy D after 24 hours ageing and susceptibility to intergranular corrosion on exposure to an aggressive environment. The carbon used to form chromium carbides is from the dissolved niobium carbides at high annealing temperature. The nucleation of $M_{23}C_6$ has been widely investigated. Its distribution and morphology are sensitive to grain boundary misorientation [196,197]. The nucleation of $M_{23}C_6$ takes place at HAGBs, especially at random HAGB. LAGB and Σ3 coherent twin boundaries are usually free from chromium carbide precipitation because of their low grain boundary energy compared with random HAGB. $M_{23}C_6$ formed during the ageing process should have a similar orientation relationship to one of the adjacent grains which could minimise the activation energy for nucleation [23,26]. Therefore, $M_{23}C_6$ precipitates formed at the grain boundary is coherent with one of the adjacent grains (Figure 5-5) [198].

5.4.2 Chromium depletion and sensitisation of alloy D at different annealing temperatures

The results of thermally induced chromium depletion at the grain boundary and sensitisation in alloy D annealed at 930 °C or 1050 °C and then aged have been reported in section 5.2 and section 5.3. 930 °C is stabilisation annealing which can maximise the formation of niobium carbides and make the alloy have better corrosion property. 1050 °C is solution annealing which can dissolve some of the niobium carbides making the alloy ready to be sensitised by the subsequent ageing.

The amount of the NbC precipitates dissolved depends on the annealing time at 1050 °C. For the annealed samples, both at 930 °C and 1050 °C, without ageing, no attack is observed after the DL-EPR test as no chromium carbide or chromium depletion is observed at the grain boundary in Figure 5-6 (a), Figure 5-7 (a) and Figure 5-9(a). No chromium carbide formation or chromium depletion was observed at the grain boundary after the ageing even up to 200 hours in the 930 °C annealed samples, which leads to no intergranular attack being present in these samples after the DL-EPR test.

The alloys investigated in this thesis are all niobium stabilized to fix carbon in the austenite matrix. The precipitation of niobium carbide in 20/25/Nb alloy is thought to take place around 900 °C-950 °C [13]. Thus, annealing at 930 °C carried out during the fabrication of AGR fuel cladding material to maximise the formation of niobium carbide, which could increase the creep properties and avoid the sensitisation induced by chromium depletion due to chromium carbides formation at the grain boundary. For the 930 °C annealed samples, no free carbon can be used to form chromium carbides at the grain boundary as

carbon is fixed by niobium carbides and therefore no chromium depletion was detected after ageing at 650 °C even up to 200 hours.

At a solution annealing temperature of 1050 °C, part of the niobium carbides dissolve and carbon is released back to the austenite matrix. The high cooling rate in water quenching leaves the dissolved carbon as supersaturated solute in the matrix owning to lower carbon solubility at lower temperature. When the supersaturated alloy is thermally aged at the sensitisation temperature range from 450 °C to 850 °C, aged at 650 °C in this thesis, the precipitation of chromium carbides at the grain boundary occurs due to the high diffusion rate of carbon towards the grain boundary and the high affinity of carbon and chromium. Thus, chromium carbides are found in all aged samples (Figure 5-7).

In the initial stage of ageing, the amount of $M_{23}C_6$ precipitates nucleated at the grain boundary increases as the free carbon in the matrix diffuses towards the grain boundary to form $M_{23}C_6$ precipitates. As the ageing proceeds, the increase of $M_{23}C_6$ precipitate at the grain boundary causes a decreasing of chromium concentration. Thus, the chromium concentration at the grain boundary decreases in alloy D as the ageing time increases from 0 to 24 hours (Figure 5-10). The net amount of chromium depletion at the grain boundary equals the amount taken by the $M_{23}C_6$ precipitates subtract the amount diffuses towards grain boundary from matrix. Thus, the chromium concentration reaches a minimum when the amount of chromium taken by $M_{23}C_6$ is exactly balanced by the amount diffuse towards grain boundary from the matrix. In alloy D, the chromium concentration is at the lowest and sensitisation is the most serious in the 24 hours aged sample. As ageing continues, the depleted chromium is gradually replenished by the chromium in matrix and sensitisation is mitigated until the chromium concentration equals the matrix content and sensitisation

is completely healed. There is a delay of reaching the minimum chromium concentration at the grain boundary in alloy D during the ageing process, which means lowest chromium concentration is reached after a finite time (24 hours for alloy D) rather than at the beginning of chromium carbide nucleation according to reaction theory [71].

Chromium depletion was firstly applied to explain sensitisation by Bain et al [67]. Sensitisation happens due to the chromium carbide precipitation induced chromium depletion at the grain boundary to a level that passivation is not feasible. In the DL-EPR test, a thin chromia film is produced during the passivation stage to protect the sample from being attacked. However, the chromia film is not protective any more when the grain boundary chromium concentration is less than a critical value (about 13 wt.% for stainless steel). As shown in Figure 5-12 and Figure 5-14, the DOS agrees well with the magnitude of chromium depletion at the grain boundary in Figure 5-9. A number of pits are observed in the 1 hour and 5 hours aged samples even though their chromium concentrations are higher than the critical value. This might be because the chromium concentration at the carbide interface is lower than that at the grain boundary. The DOS reaches a maximum and the most severe intergranular attack is shown after 24 hours' ageing when the chromium depletion concentration (12.0 wt.%) is less than the critical value. The DOS decreases massively and only a few pits are observed on the DL-EPR tested sample surface after 96 hours' ageing and chromium depletion is healed substantially. DOS is the lowest and no attack features are observed after 200 hours' ageing when chromium depletion has been healed entirely.

As shown in Figure 5-8 and Figure 5-15, the width of the attack is more than ten times the chromium depletion width at the grain boundary. Thus, the chromium depletion profile is

not directly linked to the attack width. This might be because crevice corrosion takes place after a groove forms during the dissolution of the chromium depleted zone just as stainless steel is susceptible to crevice corrosion when exposed to the potentials used in the DL-EPR test. The height difference on different grain face, as shown in Figure 5-15(b), is due to the dependence of dissolution rate on grain orientation [199,200]. As shown in Figure 5-15(b), in each individual grain, the surface topography is not smooth but decorated by 'step-like' textures, because grains dissolve preferentially on the plane with the lowest surface free energy and not always perpendicular to the exposed grain surface [201,202].

5.4.3 Chromium depletion in AGR cladding: irradiation versus thermal treatment

Only limited neutron irradiation induced segregation and sensitisation data can be found in the online databases, which might be due to the difficulty of handling highly radioactive neutron irradiated AGR cladding material. Norris et al. [18] investigated neutron irradiation induced segregation and sensitisation at different temperatures on AGR cladding retracted from the reactor as shown in Figure 2-3, Figure 2-4 and Figure 2-5. They reported the lowest chromium concentrations at the grain boundary varying from 10.0 wt.% to 14.8 wt.% over the irradiation temperature range 348 °C - 530 °C and local dose range 1.4 dpa - 5.4 dpa. In this work, the sample solution annealed at 1050 °C followed by 24 hours ageing at 650 °C has the lowest chromium concentration of 12 wt.% at the grain boundary, which is within the depletion range of irradiated 20/25/Nb reported by Norris et al [18]. If ageing was conducted over a series of ageing time and temperature on the solution annealed samples, the lowest chromium concentration at grain boundary can have higher possibility to match the irradiation induced chromium depletion. Then, the thermally sensitised sample which has similar levels of chromium depletion to the irradiated sample can be used to

simulate corrosion property degradation induced by irradiation, which could avoid dealing with the highly radioactive samples while assessing their intergranular corrosion or stress corrosion cracking properties during post storage in the water pond.

However, there are obvious differences between thermal and irradiation induced chromium depletion. Thermally induced chromium depletion is due to the formation of $M_{23}C_6$ at the grain boundary while irradiation induced chromium depletion is because of the IK effect. The chromium depletion width of irradiated sample is only about 10-20 nm while, in the thermally treated sample, the depletion width can be higher than 150 nm. Besides, there are other differences between irradiation and thermal treatment, which have been mentioned at the end of section 2.2.2. These differences might have an effect on the replication of irradiation induced sensitisation by thermal treatment. Attempt has been made by Whillock et al. [29] and Al-Shater et al. [33] to study the stress corrosion cracking behaviour of thermally sensitised 20/25/Nb alloy in a cooling pond environment to simulate the outcome of neutron irradiation effects on sensitisation.

5.5 Summary

Thermally induced chromium depletion at the grain boundary and sensitisation at different annealing temperatures have been reported in this chapter. In the 930 °C annealed samples, neither chromium carbide nor chromium depletion is detected at the grain boundary in samples aged even up to 200 hours at 650 °C. The values of DOS measured by DL-EPR are very low and no intergranular corrosion is observed on examining the surface morphology after the electrochemical test, which suggests that samples annealed at 930 °C will not be sensitised by subsequent ageing at 650 °C. In 1050 °C annealed samples, lots

of discrete pits and ditches are observed at the grain boundaries in sensitised samples (1 hour, 5 hours and 24 hours aged) while desensitised (or healed) samples (96 hours or 200 hours aged) are free from intergranular attack. Thus, NbC carbides can dissolve at the annealing temperature of 1050 °C to release carbon back to the matrix and cause the depletion of chromium at the grain boundary due to the formation of chromium carbides. The magnitude of chromium depletion in the 1050 °C annealed and then aged for 24 hours is similar to the neutron irradiation induced chromium depletion reported by Norris et al. [18]. Thus, with regard to chromium depletion caused sensitisation in AGR fuel cladding during storage in a cooling pond, it might be feasible to apply certain heat treatments to replicate the extent of chromium depletion induced by irradiation. Then, the irradiation induced sensitisation behaviour could be studied by analysing the thermally sensitised material, which could avoid the handling of the high radioactive material.

6 The correlation between sensitisation, chromium depletion and misorientation angle

For a sensitised stainless steel, the extent of attack at the grain boundary might be different from grain boundary to grain boundary after a electrochemical test, which has been reported by different researchers [25,109,179,180]. An attempt has been made to understand the cause of this difference from the perspective of the grain boundary misorientation angle [179]. However, no reported work has attempted to correlate the chromium depletion directly to the specific grain boundary that has a certain extent of attack. The magnitude of chromium depletion might be varying from grain boundary to grain boundary due to the variation of number and morphology of $M_{23}C_6$ precipitates among the grain boundaries. Thus, it is interesting to know the correlation between the sensitisation (or intergranular attack), the grain boundary misorientation and the chromium depletion. In this study, sensitisation at individual random grain boundary was studied and the sensitisation structure was obtained using DL-EPR test TEM samples were directly lifted from the individual grain boundaries that have various extent of attack using FIB to measure its chromium depletion. In this way, chromium depletion at individual grain boundary can be directly linked to its extent of attack.

6.1 Surface morphology of alloy D after DL-EPR test

Figure 6-1 shows the polarisation curves and surface morphology images of two DL-EPR tested samples of alloy D; one sample is only solution annealed at 1050 °C for 30 minutes and the other is solution annealed followed by ageing at 650 °C for 24 hours. The maximum reverse current density (I_r) in the reverse scan of the 24 hours aged sample is much higher than that of the solution annealed sample. The DOS is determined by the ratio of maximum reactivation current density to maximum activation current density (I_r/I_a). The DOS of the

solution annealed and aged samples are 0.002 and 0.209, respectively. Usually, the sample is categorised as sensitised when DOS is higher than 0.01 [176]. Thus, the solution annealed sample is not sensitised while the 24 hours aged sample is severely sensitised. During the reverse scan, the more serious attack at grain boundaries the higher reverse current will be. Thus, serious attack is expected on the 24 hours aged sample that has much higher reverse current, but no attack in the solution annealed sample, which is in agreement with the morphology observed in Figure 6-1(b) and Figure 6-1(c). Only a 'step' structure is presented in Figure 6-1(b) while both discrete pits and ditches are observed in Figure 6-1(c). The height difference at different grain surfaces is due to the dependence of dissolution rate on grain orientation.

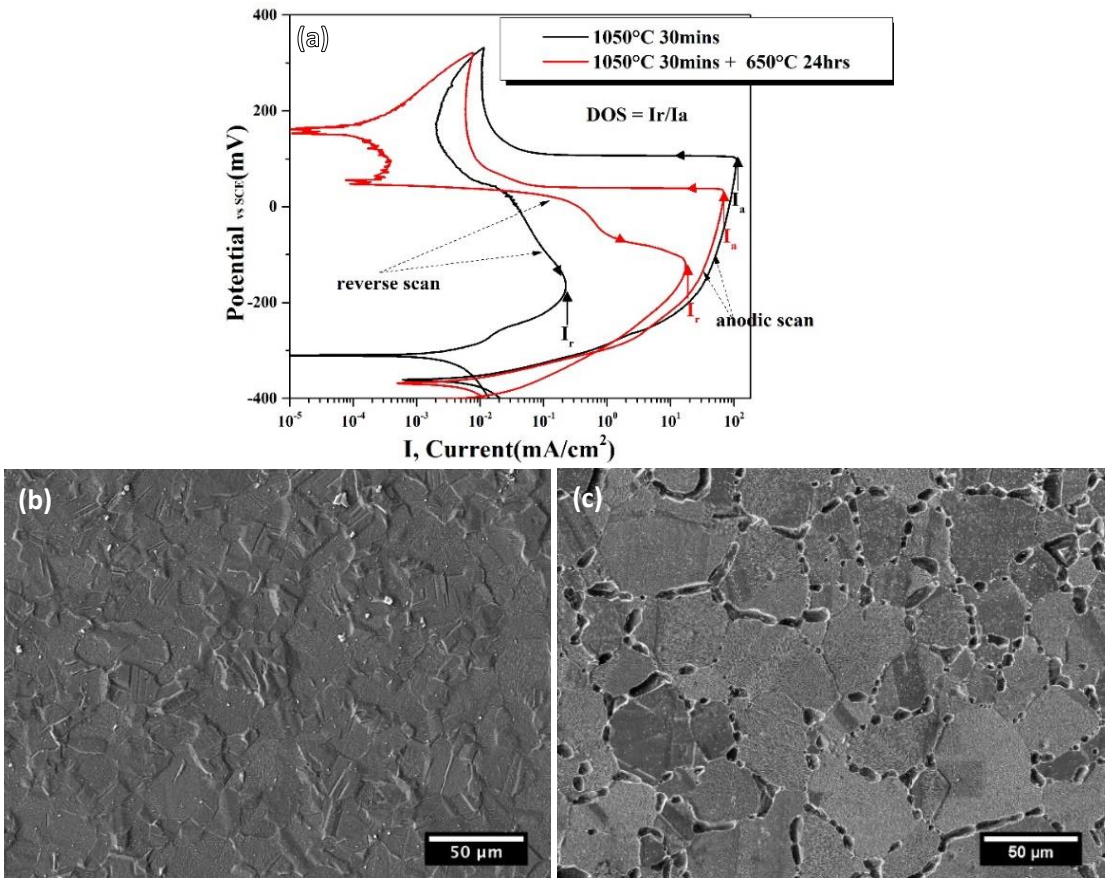

Figure 6-1 (a) Polarisation curves of the two DL-EPR tests, (b) and (c) surface morphology after DL-EPR test on the sample solution annealed at 1050 °C and sample solution annealed then aged for 24 hours at 650 °C, respectively.

6.2 The effect of misorientation angle on the extent of attack at the grain boundary

Large variation in the extent of attack among the random grain boundaries have been observed after the test in Figure 6-1(c). To observe the individual grain boundary further, 5 random grain boundaries are selected from the area of Figure 6-1(c) and their attack structures are shown in Figure 6-2. The misorientation angles of these grain boundaries are acquired from the EBSD map in Figure 6-3(c). The grain boundary indicated by white arrows in Figure 6-2(a) is a LAGB is less likely to be distinguished after the test due to a low misorientation angle of 8.7°. It is free from carbide precipitation and intergranular attack. The grain boundaries in Figure 6-2(b)-(e) are all HAGBs. Only two small pits indicated by white arrows are observed on the grain boundary in Figure 6-2(b). There is a number of small white precipitates distributed along the grain boundary, which are chromium carbides. Compared with the grain boundary in Figure 6-2(b), the number and size of the pits on the grain boundary in Figure 6-2(c) are larger. Many larger chromium carbides are also observed on the grain boundary. Large pits are observed on the grain boundary in Figure 6-2(e) and these pits tend to connect together to form a ditch. The grain boundary is divide into two segments by a Σ3 boundary that is indicated by white arrows. The misorientation angle of the two segments are 52.7° and 18.2°. Their average pits size is similar although they have large difference on misorientation angle. Many chromium carbides indicated by black arrows are also observed on the grain boundary. The grain boundary in Figure 6-2(e) is attacked into a ditch. In terms of the extent of attack, noticeable difference is observed between the grain boundary in Figure 6-2(c) and (e) even though they have similar misorientation angles. Figure 6-2(f) shows the EDS spectra of chromium,

niobium and carbon, which are acquired from the grain boundary area in Figure 6-2(c). It shows that the white precipitates are all chromium carbides and there are no niobium carbides on the grain boundary. The small white precipitates in the matrix are niobium carbides. In each individual grain, the surface topography is not smooth but decorated by 'step-like' textures, and these small facets are aligned along the same direction.

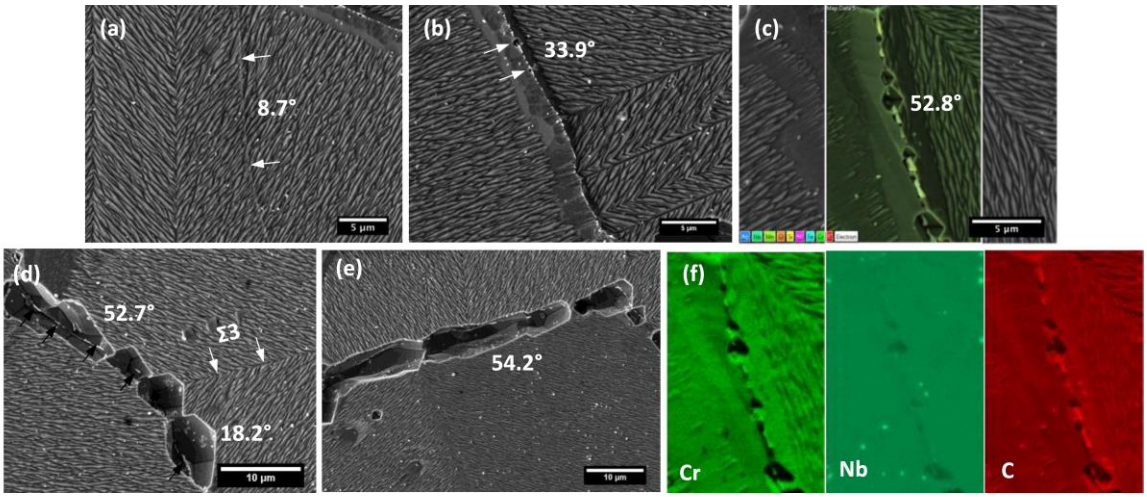

Figure 6-2 (a) a selected typical area of alloy D aged for 24 hours at 650 °C after DL-EPR test, (b), (c) and (d) are three selected random LAGBs with different extent of attack.

To investigate the relationship of the extent between attack and the misorientation angle at the grain boundary, four areas (Area A, Area B, Area C and Area D) were randomly selected and EBSD mapping was carried out as shown in Figure 6-3. Figure 6-3(a), (d), (g) and (j) are SEM images of the DL-EPR tested sample surfaces, which show that almost the entire attack (pits or ditches) is at the grain boundaries. Figure 6-3(b), (e), (h) and (k) are EBSD inverse pole figures to illustrate grain orientation via different colours, which further confirms the attack are at the grain boundary. Figure 6-3(c), (f), (i) and (l) are grain boundary maps. Grain boundaries shown by red curves are Σ3 boundaries that are immune to attack in the test solution. Black curves are random HAGBs and lime green curves are LAGBs (<15°). The grey areas along the grain boundary are zero solution during the EBSD

scanning, which show the location of intergranular attack in the sample after DL-EPR test. Generally, in all four selected areas, most of the HAGBs are attacked by the solution while LAGBs and Σ3 boundaries are immune to attack.

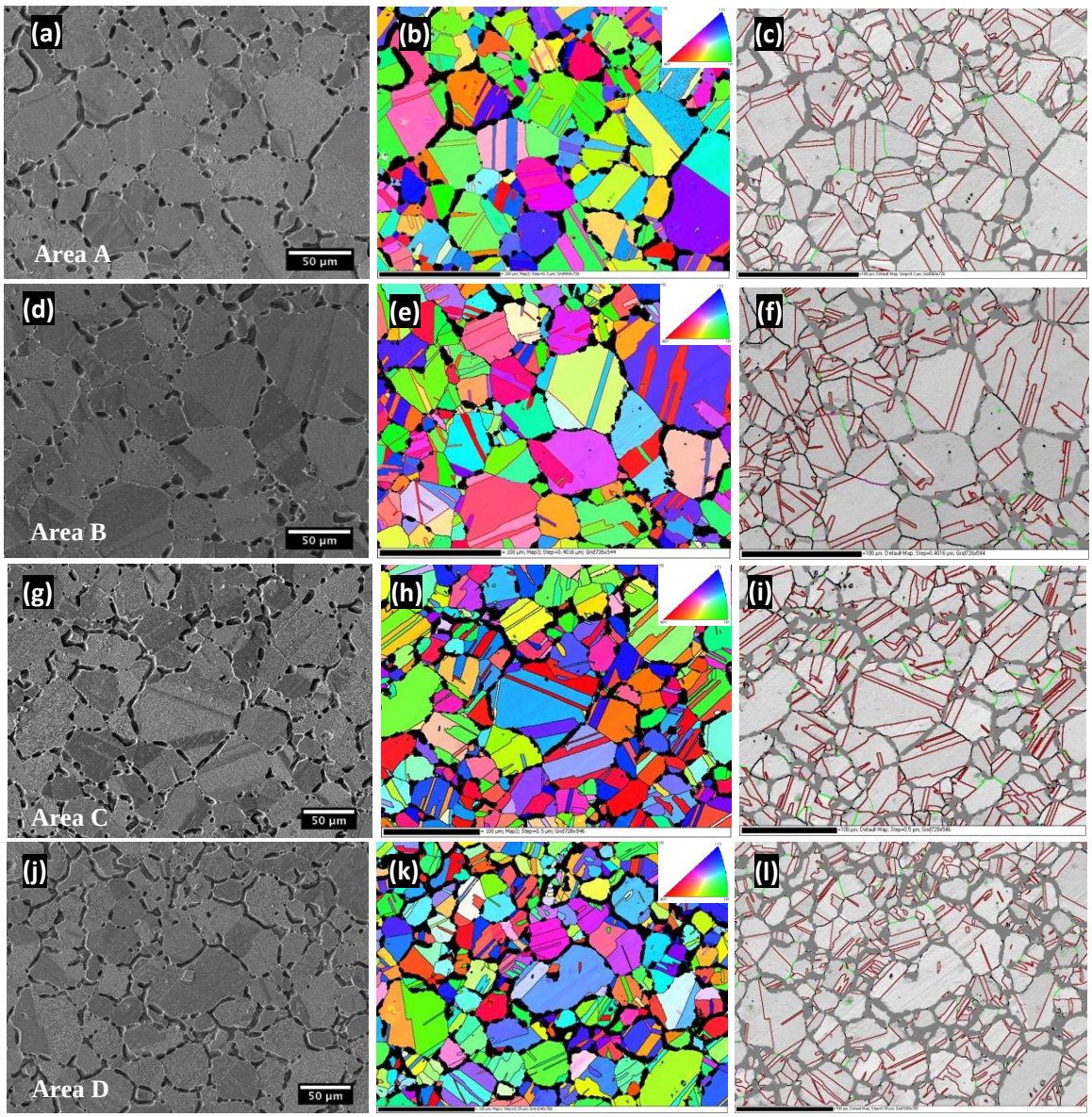

Figure 6-3 The grain boundary misorientation measurement in four areas by EBSD on DL-EPR tested alloy D aged for 24 hours at 650 °C; (a), (d), (g) and (j) are SEM images of the four selected areas; (b), (e), (h) and (k) are orientation maps in the Y direction, (c), (f), (i) and (l) are the grain boundary distribution; red curves, black curves and lime green curves are Σ3 boundaries, random HAGBs and LAGBs, respectively.

Different extents of attack have been observed on the grain boundaries that have different misorientation angle. To understand the dependence of extent of attack on misorientation angle on random grain boundaries, 35 random grain boundaries with various extents of attack were selected from four different areas as depicted in Figure 6-3. Their extent of attack was determined by the average pits width at grain boundary and misorientation angles were measured by EBSD. The extent of attack as a function of misorientation angle is plotted in Figure 6-4. According to the commonly used Brandon criterion [203], the transition angle between LAGB and HAGB is 15°, which is indicated by a black dashed line in the figure. A threshold angle is also suggested, which is indicated by a red dashed line. It shows that the extent of attack distribution exhibits a high level of scatter over the whole large misorientation angle range. Both high and low extent of attack can be found on the grain boundaries which have similar misorientation angle. Thus, no obvious correlation between misorientation angle and the extent of attack can be drawn. The red data points are grain boundaries that have a misorientation angle lower that the threshold angle. They are free from attack. The two grain boundaries indicated by black arrows have a miorientation angle of 14.0° and 14.3° and their morphology of attack are shown in Figure 6-5(b) and Figure 6-8(a), respectively. They show that attack presents even though it locates in the low angle range. The GB indicated by a blue arrow has a misorientation angle of 15.4° and its morphology of attack is shown in Figure 6-5(a), where a large ditch is present. Many chromium carbides indicated by white arrows are shown in the ditch. The two grain boundaries indicated by red arrows have a miorientation angle of 17.6° and 58.0° and their morphology of attack are shown in Figure 6-5(c) and Figure 6-7(b), respectively.

No intergranular attack is observed on these two grain boundaries, which suggest that not all random HAGBs are subject to attack after the test.

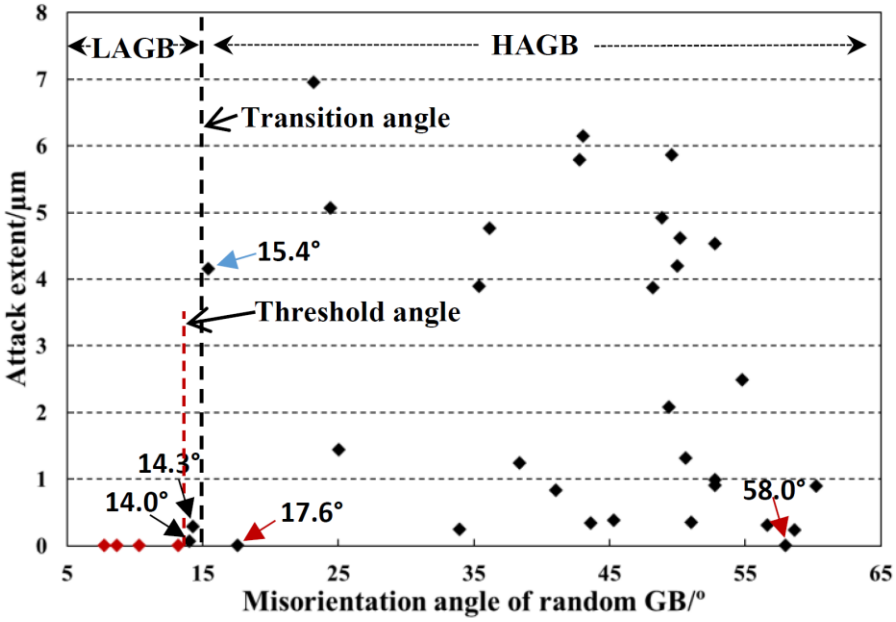

Figure 6-4 The dependence of attack extent at random grain boundaries on misorientation angle.

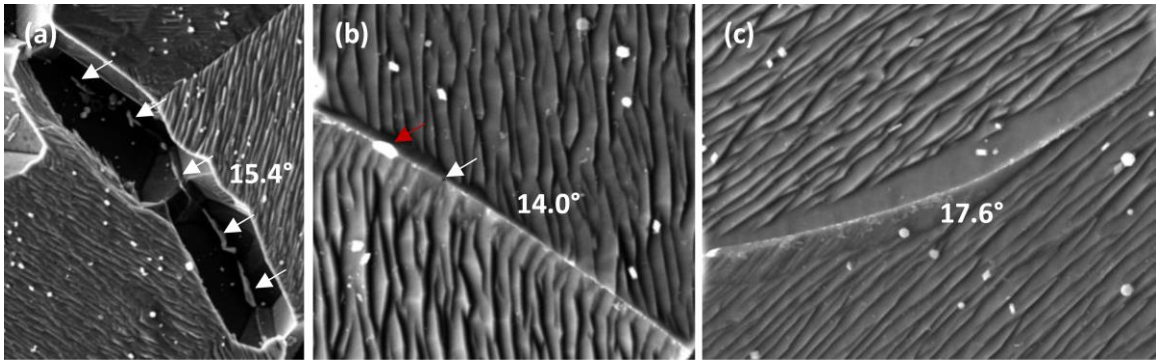

Figure 6-5 The morphology of grain boundaries whose misorientation angle is close to the transition angle: (a) 15.4°, chromium carbides are indicated by whites arrows; (b) 14.0°, a small pit and a chromium carbide were indicated by white and red arrows, respectively; (c) 17.6°.

6.3 Chromium depletion at selected grain boundaries with different extents of attack

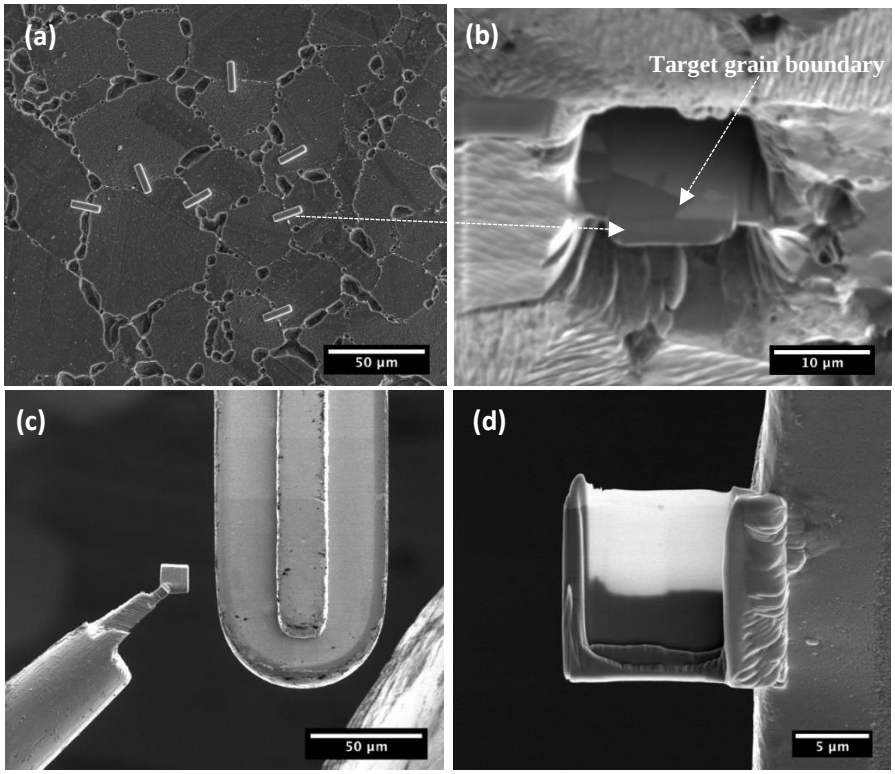

Figure 6-6 (a) Pt deposition on the four selected grain boundaries, (b) trench digging for sample lift out, (c) samples is about to be attached to TEM grid, (d) FIB sample thin enough for TEM observation.

To study the dependence of extent of attack on the magnitude of chromium depletion at the grain boundary, several grain boundaries with various extents of attack were selected and chromium depletion was measured on these grain boundaries. To measure chromium profile at a specific grain boundary, TEM samples were prepared by FIB as shown in Figure 6-6. FIB samples were lifted out from the four areas in Figure 6-3. Figure 6-6(a), which is an SEM micrograph of a DL-EPR test sample of alloy D aged for 24 hours at 650 °C, shows several selected grain boundaries deposited with platinum. Figure 6-6(b), which is a FIB SEM ion image, shows a FIB sample with the target grain boundary in the middle of the sample. Figure 6-6(c) shows a FIB sample about to be attached to the pin of a copper

grid. Figure 6-6(d) is a FIB sample with an electron transparent thin area including the grian boundary which is ready for measuring chromium depleiton using STEM-EDS.

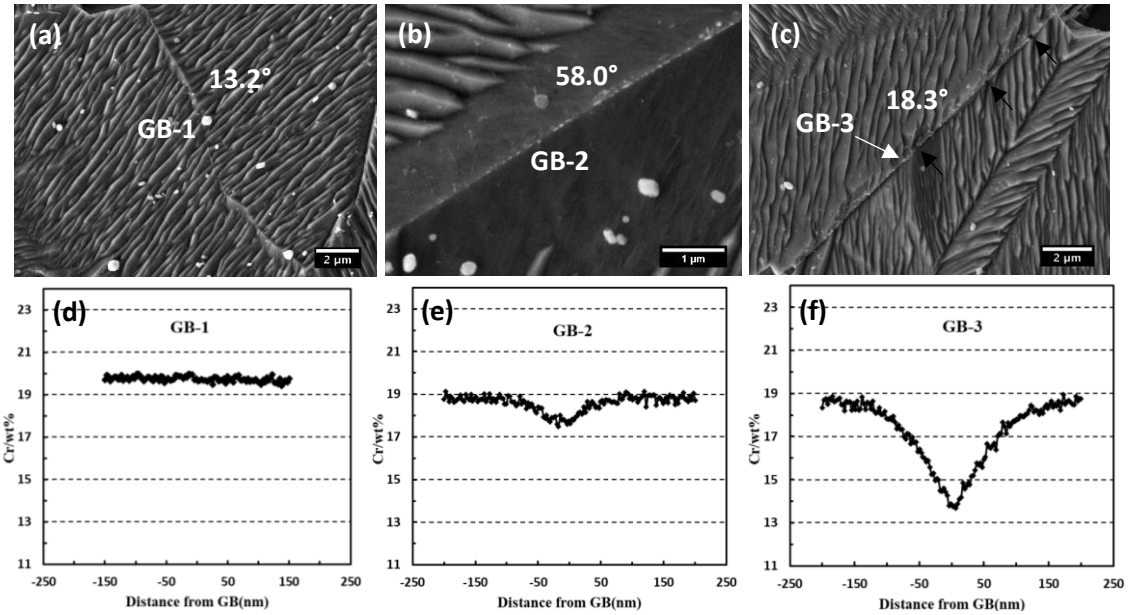

Figure 6-7 (a), (b) and (c) are SEM images obtained from the selected grain boundaries, (d), (e) and (f) are the corresponding chromium depletion profiles at the grain boundary.

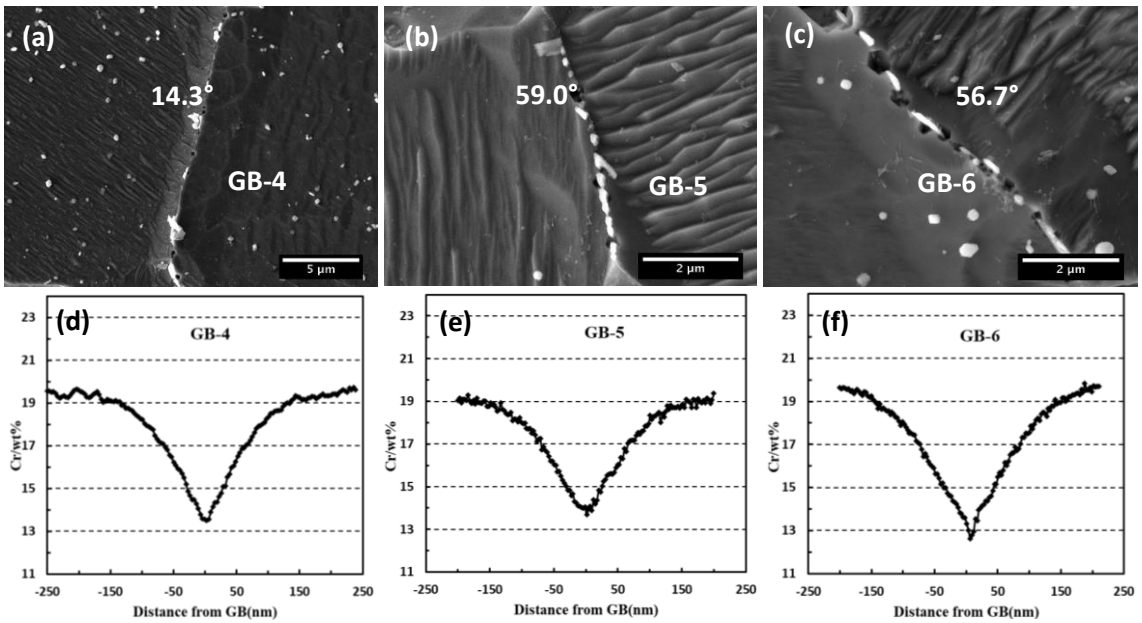

Figure 6-8 (a), (b) and (c) are SEM images obtained from the selected grain boundaries, (d), (e) and (f) are the corresponding chromium depletion profiles at the grain boundary.

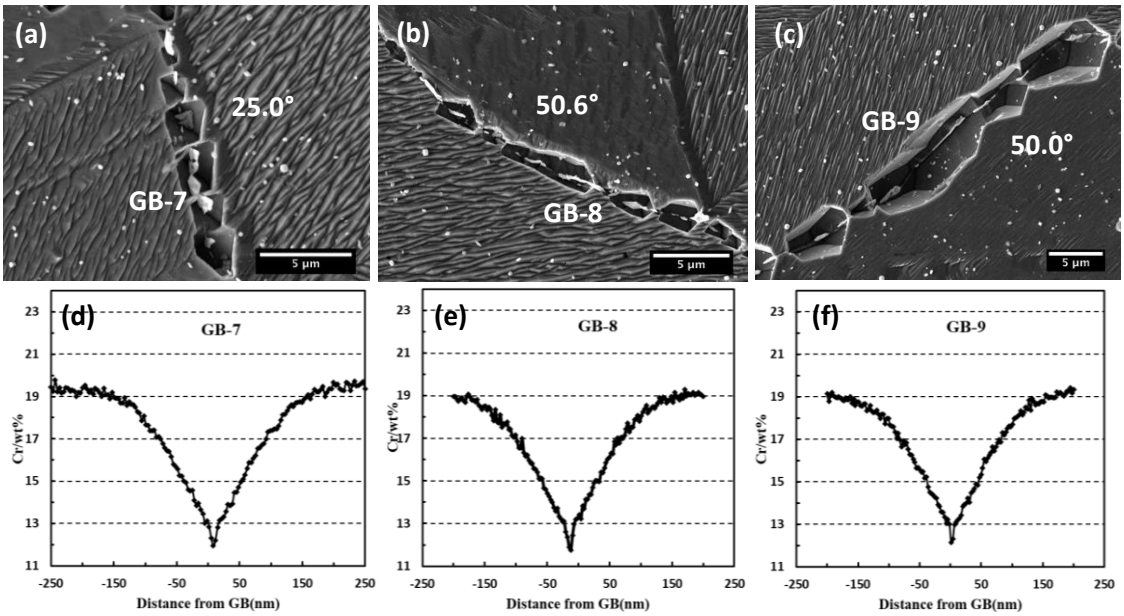

Figure 6-9 (a), (b) and (c) are SEM images obtained from the selected grain boundaries, (d), (e) and (f) are the corresponding chromium depletion profiles at the grain boundary.

Nine random grain boundaries, termed GB-1 to GB-9, with various extents of attack, were selected to study the correlation of grain boundary attack and chromium depletion. To measure the chromium depletion at the grain boundary, one FIB sample was lifted out from each selected grain boundary. Before lifting out the FIB sample from the selected grain boundaries, an SEM image was taken to measure the extent of attack, which is shown in Figure 6-7(a), (b) and (c) - Figure 6-9(a), (b) and (c). In Figure 6-10, STEM BF images show the carbide precipitation at the grain boundaries in the FIB sample. A chromium depletion profile at the grain boundary was measured using STEM-EDS, shown in Figure 6-7(d), (e) and (f) - Figure 6-9(d), (e) and (f). As shown in Figure 6-7(a), Figure 6-7(d) and Figure 6-10(a), GB-1 is a LAGB that is immune to attack during the DL-EPR test; no chromium depletion or chromium carbide precipitation is detected. The only precipitate visible is a niobium carbide indicated by a red arrow. No grain boundary attack is observed at GB-2 which is a HAGB with slight chromium depletion. No chromium carbides are observed at GB-2 in Figure 6-7(b) but one $M_{23}C_6$ precipitate is present in Figure 6-10(b). Only a few

small pits (about 0.14 μm in width) are observed on GB-3, indicated by black arrows in Figure 6-7(c). The chromium concentration at GB-3 is about 13.8 wt.%. Large $M_{23}C_6$ precipitates, about 300 nm in width, are observed in Figure 6-10(c). GB-4 to GB-6 are grain boundaries with mild attack (small discrete pits) as shown in Figure 6-8(a), (b) and (c). Many $M_{23}C_6$ precipitates are observed, especially on GB-5 and GB-6, both in SEM and STEM BF images. GB-7 to GB-9 are grain boundaries with serious attack (large pits connected together as a ditch-like feature) as shown in Figure 6-9(a), (b) and (c), due to the high magnitude of chromium depletion, as observed in Figure 6-9(d), (e) and (f), and lots of $M_{23}C_6$ precipitates remain inside the ditch at the grain boundary due to their high resistance to corrosion [178]. The morphology of attack on GB-7 to GB-9, in terms of attack shape and size, is different. As shown in Figure 6-9 (c), the average width of the attack is about 5 μm which is more than ten times the corresponding width of chromium depletion shown in Figure 6-9(f). GB-3, GB-4 and GB-5 have similar magnitudes of chromium depletion while the proximity of $M_{23}C_6$ precipitation is different, which indicates that chromium carbide might not be the only factor that affects chromium depletion at the grain boundary. GB-7, GB-8 and GB-9 show that serious grain boundary attack takes place when the chromium concentration is less than about 12 wt.%. $M_{23}C_6$ precipitates are observed at the grain boundary. Part of the sample was damaged while thinning the FIB sample lifted out from GB-9. Thus, the grain boundary in Figure 6-10(i) only shows a small area of GB-9 where no $M_{23}C_6$ is present. In fact, lots of $M_{23}C_6$ were observed when preparing the sample. Chromium carbide was seen at all large grain boundaries. Chromium concentration, attack size, misorientation angle and rotation axis at the 9 selected grain boundaries are summarised in Table 6-1.

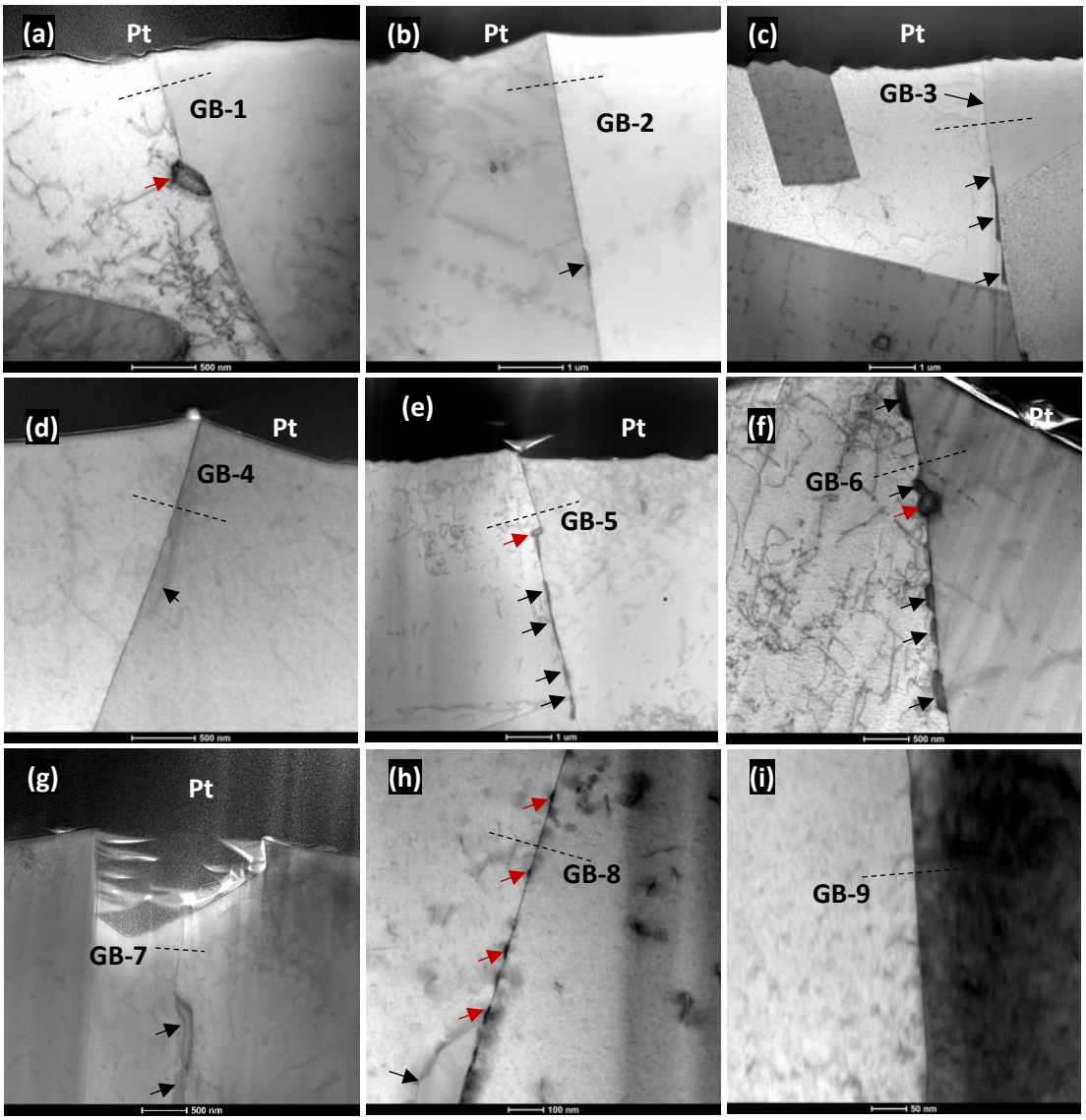

Figure 6-10 STEM BF images of FIB samples lifted out from the nine selected grain boundaries, precipitates at the grain boundary indicated by red and black arrows are NbC and $M_{23}C_6$ precipitates, respectively; Line scan position is marked by a black dash line cross the grain boundary.

Table 6-1 Summary of chromium concentration, attack extent and misorientation on the selected grain boundaries with FIB sample lifted.

Boundary ID	Boundary type	Cr content at GB (wt.%)	Extent of attack (μm)	Mis. angle (°)	Mis. axis
GB-1	LAGB	19.6	0.00	13.2	[-1 -4 4]
GB-2	HAGB	18.2	0.00	58.0	[2 2 -3]
GB-3		13.9	0.13	18.3	[-2 1 0]
GB-4	LAGB	14.3	0.29	14.3	[-1 -4 1]
GB-5	HAGB	13.9	0.25	59.0	[-3 3 -4]
GB-6		13.0	0.31	56.7	[4 4 1]
GB-7		11.2	1.45	25.0	[-1 2 -3]
GB-8		11.5	1.31	50.6	[2 4 -3]
GB-9		11.9	4.20	50.0	[0 3 2]

Figure 6-11(a), the average extent of attack as a function of chromium concentration at grain boundary, shows that attack starts to initiate when the chromium concentration is about 13.0 to 14.3 wt.%. The grain boundary area was not attacked by the solution when the chromium concentration is higher than 14.3 wt.% as the passive chromia film is strong enough to protect grain boundary from attack during the reactivation period. Whereas, substantial attack, in terms of attack width and depth, are observed at the grain boundary when chromium concentration is less than 12 wt.% which might due to the thickness of passive film is not strong enough to combat the attack from the test solution. The red data points were acquired from two LAGBs, which suggests that grain boundary attack is still likely if the misorientation angle of the LAGB is close to the transition angle as illustrated in Figure 6-8(a), but the absence of attack is more likely when the misorientation angle is further less than the transition angle (Figure 6-7(a)). Figure 6-11(b), which is the chromium concentration as a function of misorientation angle, shows no obvious relationship between chromium depletion and misorientation can be drawn, which seems likely that misorientation angle does not play a role in chromium segregation.

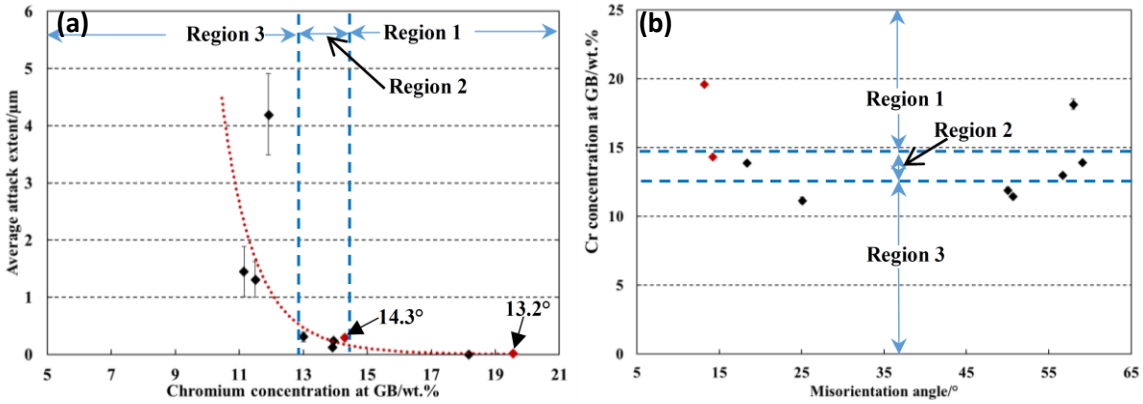

Figure 6-11 (a) the dependence of average attack extent on chromium concentration at the grain boundary, the red data point is from the LAGBs while the black data points are from random HAGBs; (b) the dependence of chromium concentration on misorientation angle.

6.4 Discussion

6.4.1 Misorientation effect on grain boundary attack

The effect of grain boundary structure on chromium segregation and sensitisation has been widely investigated by different people [23,74,103,180]. Laws and Goodhew [102] studied the effects of misorientation and grain boundary plane on chromium carbide precipitation and chromium depletion at the grain boundaries in a sensitised 316 stainless steel. They identified a few CSL boundaries (Σ3, Σ11, Σ13a, Σ13b) as 'favoured' boundaries that have much less chromium depletion compared with other types of HAGBs. They also found that there is no correlation between the boundary plane normal and either the width of the chromium profile or the lowest chromium concentration at the grain boundary even though the activation energy for the formation of a chromium carbide might be reduced if the boundary plane is close to {111}. Low angle (<15°) and CSL Σ3 coherent twin boundaries are immune to sensitisation. The other CSL grain boundaries are partly immune to sensitisation and have better resistance to sensitisation than random HAGBs. Random HAGBs are easily attacked compared with other types of grain boundary when exposed to a sensitisation environment due to their higher grain boundary energy. Increasing the

fraction of CSL and twin boundaries in stainless steel can significantly improve the resistance to sensitisation due to their low grain boundary energy [109].

The extent of attack after DL-EPR testing at individual random HAGBs is different from boundary to boundary (Figure 6-1(c) and Figure 6-2), even though they are on the same sample and subject to the same test condition. The widely accepted transition angle between HAGB and LAGB is near 15°. This transition angle can be determined experimentally by the sharp change of activation enthalpy between HAGB and LAGB [204], and it can be at different angles for different grain boundary axis. For grain boundary sensitisation, there is a threshold angle [179], below this angle the grain boundaries are unlikely to be sensitised, above this angle the grain boundaries are subject to sensitisation and high variation the DOS exists among these grain boundaries. This threshold angle can be different in different alloys and heat treatment conditions. The threshold angle can also be different with the transition angle. In this study, the threshold angle is between 13.2° and 14.0°, below which the grain boundaries are free from attack as illustrated by the red data points in Figure 6-4. The statistics of attack extent as a function of misorientation angle shows that there is no particular correlation between the extent of attack and the misorientation angle over a wide range of angles from the threshold angle to 60°. Conspicuous variation of extent of attack was observed on the grain boundaries whose misorientation angle slightly higher than the threshold angle (Figure 6-2(a) and (b)). Similar observations were also reported in austenitic and ferritic alloys by Bennett and Pickering [179]. They suggested that either grain boundary energy or the habit plane contribution might explain the different extent of attack at different grain boundaries. Higher grain boundary energy facilitates the nucleation of chromium carbide which

promotes the rapid depletion of chromium at the grain boundary area. A grain boundary plane close to a habit plane is expected to have a relatively higher precipitation rate [205]. Up to now, however, no universal theory has been proposed to depict the energy of HAGBs. Many experimental and calculated results have shown that special boundaries at certain misorientations exhibits lower grain boundary energy for which the atomic fit is better than that for random HAGBs. Whereas, the disordered atomic structure of random HAGB leads to their energy being at a maximum and approximately constant with angle. Thus, the various attack extents at different random HAGBs more likely can be explained by the behaviour of chromium carbides precipitation, however, only from the perspective of misorientation angle is not feasible. The morphology of the two grain boundaries (Figure 6-2(c) and Figure 6-7(b)), indicated by two red arrows in Figure 6-4, makes the statement even more convincible.

6.4.2 Chromium depletion effect on grain boundary attack

As discussed in section 6.4.1, the extent of attack did not show a strong relation with the misorientation angle on random HAGBs. An attempt to relate the attack on random GBs to chromium depletion is made in this section by analysing the FIB samples which were directly lifted from 9 grain boundaries that have various extents of attack. Sensitisation behaviour is divided into three regions as shown in Figure 6-11. In region 1 (GB-1 and GB-2), the grain boundaries are free from attack due to a high level of chromium concentration at the grain boundary, which leads the chromia film formed during the repassivation period thick enough to protect the grain boundary from being attacked. These grain boundaries tend to be absent from chromium carbides (GB-1), resulting in no chromium depletion, or present a small amount of chromium carbides with a large spacing

(GB-2), resulting in slight chromium depletion. Sensitisation enters region 2 (GB-3 to GB-6) when chromium depleted to a level between 13.0 wt.% and 14.3 wt.% that makes the intergranular attack starts to initiate. In this region, the morphology of attack exhibits likely to be small discrete pits along the grain boundary. This might be because the thickness of the passive film formed at the grain boundary is not uniform due to the variation of chromium concentration along an individual grain boundary. In region 3 (GB-7 to GB-9), substantial attack emerges on the grain boundary when chromium concentration is less than a value of 12 wt.%. The passive film breaks down easily during the reactivation process due to the low chromium concentration at the grain boundary. The attack features in this region tend to be large pits and these pits are about to connect together to form a ditch at the grain boundary (Figure 6-9(a) and (b)) or directly to be a ditch is also likely (Figure 6-9(c)). The chromium carbides nucleated on these grain boundaries are large and the spacing between two carbides is small. Therefore, the magnitude of chromium depletion at the grain boundary might be the main reason that accounts for the various extents of attack on the random grain boundaries. As discussed above, the extent of attack is controlled by chromium depletion. No evident correlation can be drawn between misorientation angle and the extent of attack in Figure 6-4. Thus, it is reasonable to expect that there is no obvious correlation between chromium depletion and misorientation angle as shown in Figure 6-11(b).

The GB-1 (LAGB) is absent from chromium carbide precipitation and chromium depletion because of its low boundary energy [23]. The mild chromium depletion at GB-2 is due to the nucleation of a small amount of $M_{23}C_6$ precipitates present in the cross-section image of GB-2 in Figure 6-10(b). Chromium carbides remain at the grain boundaries of GB-3 to

GB-9 after the DL-EPR test due to their higher resistance to corrosion. The morphology and distribution of chromium carbides on these grain boundaries show that the grain boundary with large chromium carbides and a small spacing between the carbides exhibit a higher magnitude of chromium depletion. Thus, chromium depletion is strongly affected by the number and morphology of chromium carbides nucleated at the grain boundary. The reported work [26,188,206] suggests that the formation of chromium carbides is affected by the grain boundary misorientation. Trillo and Murr [188] found that increasing misorentation angle might increase the grain boundary energy which will facilitate the formation of chromium carbide. However, this has not been observed here. This might be because chromium carbide formation on random HAGBs is affected by not only misorientation angle but also the boundary plane. The activation energy for the formation of a chromium carbide might be reduced on certain grain boundary planes, which facilitate the growth of chromium carbide.

Evident difference of extent of attack between GB-7, GB-8 and GB-9 was found (Figure 6-9(a), (b) and (c)) even though they have very similar lowest chromium concentration. This indicates that the morphology of attack might also be affected by the local geometry of the chromium carbide which might affect the corrosion potential of its surrounding alloy. The attack width observed is much larger than the depletion width of chromium which indicates that the attack width is not simply determined by chromium depletion width. Bennett and Pickering [179] suggested that in the early stages, the attack features formed by dissolution of the chromium depletion zone, especially at the $M_{23}C_6$ precipitate-matrix interface area, might have a geometry and dimensions to function as a crevice. Then the

alloy is subject to crevice corrosion in the DL-EPR test condition, expanding the attack width.

6.5 Summary

In the present study, the variation of extent of attack was found among the random grain boundaries after the DL-EPR test on a sensitised sample of 20/25/Nb stainless steel. The reasons for this variation were studied from the perspective of misorientation angle and chromium depletion at the grain boundary and the following results can be drawn:

There exists a threshold angle that grain boundaries less than this angle are immune to intergranular attack while grain boundaries higher than this angle are subject to attack and the extent of attack is various from grain boundary to grain boundary. The threshold angle in this study is between 13.2° and 14.0° that is slightly smaller than the commonly used transition angle, 15°, of LAGB and HAGB. The statistics over a number of random grain boundaries found that no obvious correlation between the extent of attack and the misorientation angle could be drawn.

Sensitisation, for random grain boundaries, is more likely determined by the magnitude of chromium depletion rather than the misorientation angle. For the 20/25/Nb alloy studied in this work, the grain boundaries were protected from attack when chromium concentration was higher than 14.3 wt.%. The grain boundary attack started to initiate when chromium concentration was about 13 wt.% to 14 wt.% and serious attack took place when it was less than 12 wt.%. No correlation between chromium depletion and misorientation angle was found either. The chromium depletion is affected by the number and spacing of $M_{23}C_6$ precipitation.

7 Conclusions and suggestions future work

7.1 Conclusions

The thermally induced sensitisation, due to chromium depletion at grain boundary, on AGR fuel cladding austenitic stainless steel has been studied in this work. The following conclusions are drawn:

7.1.1 The influence of Si on chromium depletion and sensitisation of model alloys (chapter 4)

In alloys A and B, the grain size is about 20 μm and its distribution is uniform after solution annealing at 1050 °C. There is no obvious grain growth during the ageing process at 650 °C for up to 200 hours. Solution annealed alloys are free from $M_{23}C_6$ precipitates nucleation, but $M_{23}C_6$ precipitates are found at the random HAGBs in the samples with subsequent ageing at 650 °C and their size and number increase with ageing time until no free carbon left in the matrix.

The magnitude of chromium depletion reaches a maximum after 1 hour ageing in 0.56 wt.% and 2.25 wt.% Si alloys and starts to decrease as ageing time continue to increase. Whereas the magnitude of chromium depletion in 0 wt.% Si alloy reaches a maximum after 5 hours' ageing. Thus, the addition of silicon can decrease the time needed for reaching the maximum chromium depletion at grain boundary. Chromium depletion is healed dramatically after 96 hours or longer ageing in these model alloys. In the range of ageing times from 10 minutes to 200 hours, chromium depletion exhibits two stages (sensitisation and desensitisation) and the trend agrees well with the kinetic theory. Compared with silicon free (0 wt.% Si) alloy, during the sensitisation stage, silicon bearing alloys (0.56

wt.% Si and 2.25 wt.% Si) show more chromium depletion at the grain boundary when aged to the same time scale. On the contrary, during the desensitisation stage (healing process) silicon free alloy shows less chromium depletion than silicon bearing alloys. This might be because of the addition of silicon increasing the diffusion rate of chromium.

The DOS measured by DL-EPR test shows that silicon bearing alloys experience less attack than the silicon free alloy after 5 hours ageing. However, no obvious difference was observed under the other sensitisation treatments. The trend of DOS acquired from DL-EPR testing is in agreement with the magnitude of chromium depletion. The morphology of the DL-EPR tested sample agrees well with the magnitude of chromium depletion. The DL-EPR tests show that silicon bearing alloys do not show an obviously better resistance to sensitisation than the silicon free alloy.

7.1.2 Thermally induced sensitisation and chromium depletion on the commercial alloy (chapter 5)

The grain size of the 930 °C annealed sample of alloy D is smaller than that of the 1050 °C annealed sample. The number of remaining niobium carbides in the 930 °C annealed sample is higher than that in the 1050 °C annealed sample because niobium carbides dissolve at high annealing temperature (1050 °C in this work) and the amount of niobium carbide dissolved depends on the temperature and the duration of annealing. $M_{23}C_6$ precipitates formed at the grain boundary are coherent with one of the adjacent grains, which could minimise the activation energy for nucleation.

In the 930 °C annealed samples, neither chromium carbide nor chromium depletion is detected at the grain boundary in samples aged even up to 200 hours at 650 °C. The values of DOS measured by DL-EPR are very low and no intergranular corrosion is observed by

examining the surface morphology after the electrochemical test, which suggests that samples annealed at 930 °C will not be sensitised by subsequent ageing at 650 °C.

In 1050 °C annealed samples, a number of discrete pits and ditches are found at the grain boundaries in sensitised samples (1 hour, 5 hours and 24 hours aged) while desensitised samples (96 hours or 200 hours aged) are free from intergranular attack. Thus, NbC carbides can dissolve at the annealing temperature of 1050 °C to release carbon back to the matrix and cause the depletion of chromium at the grain boundary due to the formation of chromium carbides.

The magnitude of chromium depletion in the 1050 °C annealed and then aged for 24 hours is similar to the reported neutron irradiation induced chromium depletion in 20/25/Nb alloy. Thus, it might be feasible to apply certain heat treatments to replicate the extent of chromium depletion induced by irradiation. Then, the irradiation induced sensitisation behaviour could be studied by analysing the thermally sensitised material, which could avoid handling the high radioactive material.

7.1.3 The correlation between sensitisation, chromium depletion and misorientation angle (chapter 6)

Different extents of attack were observed at individual grain boundaries in the sensitised sample after the DL-EPR test. There exists a threshold angle that grain boundaries less than this angle are immune to intergranular attack while grain boundaries higher than this angle are subject to attack and the extent of attack is various from grain boundary to grain boundary. The threshold angle in this study is between 13.2° and 14.0° which is slightly smaller than the commonly used transition angle, 15°, of LAGB and HAGB. The statistics

over a number of random grain boundaries find that no obvious correlation between the extent of attack and the misorientation angle can be drawn.

The magnitude of chromium depletion at 9 selected grain boundaries with various extents of attack was measured and linked directly to its extent of attack. Sensitisation, for random grain boundaries, is found more likely to be determined by the magnitude of chromium depletion rather than the misorientation angle. For the 20/25/Nb alloy studied in this work, the grain boundaries are protected from attack when chromium concentration was higher than 14.3 wt.%. The grain boundary attack starts to initiate when chromium concentration is about 13 wt.% to 14 wt.% and serious attack take place when it was less than 12 wt.%. No correlation between chromium depletion and misorientation angle is found either. The chromium depletion is controlled by the number and spacing of $M_{23}C_6$ precipitation.

7.2 Suggestions for future work

Thermally induced sensitisation on 20/25/Nb was studied in this thesis using the DL-EPR test and STEM-EDS for DOS and chromium depletion measurement, respectively. An attempt was made to replicate irradiation induced sensitisation by thermal treatment of the commercial AGR fuel cladding (Alloy D in this thesis), but there are differences between thermally and irradiation induced sensitisation as stated at the end of section 2.2.2. Thus, proton irradiation could be used to study the sensitisation of AGR fuel cladding material in future work after this thesis. Was et al. [17] examined the feasibility of using proton irradiation to simulate the neutron irradiation. They found that proton irradiation provided an excellent simulation of neutron irradiation effects on RIS, irradiation hardening and irradiation assisted stress corrosion cracking. After removal from the reactor core, the AGR fuel cladding has been exposed to high dose (a few dpa) of neutron irradiation. To acquire

such a high irradiation dose, the linear accelerator, Dynamitron, located in the physics department at University of Birmingham can be utilised. The Dynamitron can provide large beam current to achive a high damage dose in a relatively short time. Figure 7-1 is the beam line station and material irradiation the chamber of Dynamitron. The proton irradiation dose can be calculated using the SRIM software.

The effect of silicon on chromium depletion at the grain boundary and on sensitisation was studied in this thesis on the thermally treated AGR fuel cladding model alloys. No obvious silicon segregation was detected in the thermally sensitised alloy, but obvious enrichment of silicon (via interstitial-solute dragging mechanism) was observed in the irradiated material. Thus, it might be interesting to know the effect of silicon on irradiation induced chromium depletion at the grain boundary and then make comparison with the thermally induced depletion studied in this thesis.

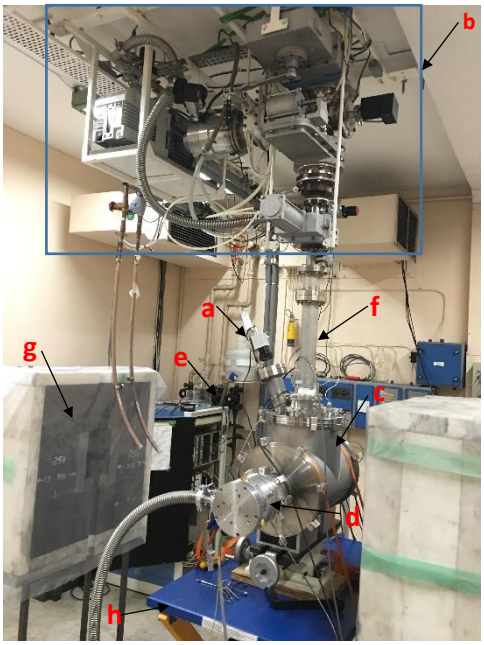

Figure 7-1 The beam line station and irradiation chamber of the Dynamitron: (a) Infra-red camera, (b) part of Dynamitron vacuum and valve system, (c) chamber body, (d) diffusion pump, (e) cooling water supply, (f) beam line tube, (g) gamma ray shield, (h) supporting trolley.

References

[1] Reactor Database, World Nuclear Association, Http://www.world-Nuclear.org/. (2018).

[2] Nuclear Power in the United Kingdom, World Nuclear Association, Http://www.world-Nuclear.org/. (2018).

[3] S. Chu, A. Majumdar, Opportunities and challenges for a sustainable energy future, Nature. 488 (2012) 294–303.

[4] V.S. Arunachalam, E.L. Fleischer, The Global Energy Landscape and Materials Innovation, MRS Bulletin. 33 (2008) 264–288.

[5] W. Hoffelner, Materials for nuclear plants: From safe design to residual life assessments, 2013.

[6] C.R.F. Azevedo, Selection of fuel cladding material for nuclear fission reactors, Engineering Failure Analysis. 18 (2011) 1943–1962.

[7] J. Kyffin, The Technical Case for Interim Storage of AGR Fuel, Sustainable Nuclear Energy Conference. (2014).

[8] S.J. Zinkle, G.S. Was, Materials challenges in nuclear energy, Acta Materialia. 61 (2013) 735–758.

[9] E.E. Bloom, J.T. Busby, C.E. Duty, P.J. Maziasz, T.E. McGreevy, B.E. Nelson, B.A. Pint, P.F. Tortorelli, S.J. Zinkle, Critical questions in materials science and engineering for successful development of fusion power, Journal of Nuclear Materials. 367–370 A (2007) 1–10.

[10] J. Knaster, A. Moeslang, T. Muroga, Materials research for fusion, Nature Physics. 12 (2016) 424–434.

[11] A.D. Marwick, Segregation in irradiated alloys: The inverse Kirkendall effect and the effect of constitution on void swelling, Journal of Physics F: Metal Physics. 8 (1978) 1849–1861.

[12] Z. Balogh, G. Schmitz, Diffusion in Metals and Alloys, in: Physical Metallurgy, Fifth Edition, 2014: pp. 387–559.

[13] W. Walters, T. Atkins, R. Boothby, C. Donohoe, S. Dumbill, H. Sims, Replication of reactor-induced sensitisation of AGR fuel cladding，NNL report, 2012.

[14] M. Adam, The characteristics of failed AGR fuel, NNL report, 2010.

[15] A.H. Mir, M. Toulemonde, C. Jegou, S. Miro, Y. Serruys, S. Bouffard, S. Peuget, Understanding and simulating the material behavior during multi-particle irradiations, Scientific Reports. 6 (2016).

[16] J.A. Hinks, A review of transmission electron microscopes with in situ ion irradiation, Nuclear Instruments and Methods in Physics Research, Section B: Beam Interactions with Materials and Atoms. 267 (2009) 3652–3662.

[17] G.S. Was, J.T. Busby, T. Allen, E.A. Kenik, A. Jensson, S.M. Bruemmer, J. Gan,

A.D. Edwards, P.M. Scott, P.L. Andreson, Emulation of neutron irradiation effects with protons: Validation of principle, Journal of Nuclear Materials. 300 (2002) 198–216.

[18] D.I.R. Norris, C. Baker, C. Taylor, J.M. Titchmarsh, Radiation-Induced Segregation in 20Cr/25Ni/Nb Stainless Steel, Effects of Radiation on Materials: 15th International Symposium, ASTM STP 1125. 603 (1992) 603–620.

[19] M.A. Ashworth, D.I.R. Norris, I.P. Jones, Radiation-induced segregation in Fe-20Cr-25Ni-Nb based austenitic stainless steels, Journal of Nuclear Materials. 189 (1992) 289–302.

[20] D. Norris, Compositional profiles at grain boundaries in 20%Cr/25%Ni/Nb stainless steel, in: Proceedings of the Symposium on Radiation-Induced Sensitisation of Stainless Steels, 1986: pp. 86–98.

[21] T. Onchi, K. Dohi, N. Soneda, M. Navas, M.L. Castaño, Mechanism of irradiation assisted stress corrosion crack initiation in thermally sensitized 304 stainless steel, Journal of Nuclear Materials. 340 (2005) 219–236.

[22] T.M. Devine, The mechanism of sensitization of austenitic stainless steel, Corrosion Science. 30 (1990) 135–151.

[23] E.A. Trillo, L.E. Murr, Effects of carbon content, deformation, and interfacial energetics on carbide precipitation and corrosion sensitization in 304 stainless steel, Acta Materialia. 47 (1998) 235–245.

[24] P. Ahmedabadi, V. Kain, K. Arora, I. Samajdar, S.C. Sharma, P. Bhagwat, Radiation-induced segregation in desensitized type 304 austenitic stainless steel, Journal of Nuclear Materials. 416 (2011) 335–344.

[25] M. Matula, L. Hyspecka, M. Svoboda, V. Vodarek, C. Dagbert, J. Galland, Z. Stonawska, L. Tuma, Intergranular corrosion of AISI 316L steel, Materials Characterization. 46 (2001) 203–210.

[26] K. Kaneko, T. Fukunaga, K. Yamada, N. Nakada, M. Kikuchi, Z. Saghi, J.S. Barnard, P.A. Midgley, Formation of $M_{23}C_6$-type precipitates and chromium-depleted zones in austenite stainless steel, Scripta Materialia. 65 (2011) 509–512.

[27] M. Grimston, W.J. Nuttall, G. Vaughan, The siting of UK nuclear reactors., Journal of Radiological Protection : Official Journal of the Society for Radiological Protection. 34 (2014) R1–R24.

[28] E. Nonbel, Description of the Advanced Gas Cooled Type of Gas Cooled Reactor (AGR), Report, 1996.

[29] G.O.H. Whillock, B.J. Hands, T.P. Majchrowski, D.I. Hambley, Investigation of thermally sensitised stainless steels as analogues for spent AGR fuel cladding to test a corrosion inhibitor for intergranular stress corrosion cracking, Journal of Nuclear Materials. 498 (2018) 187–198.

[30] C.M. Chan, To Provide a Mechanistic Understanding of In-Pond Corrosion of Advanced Gas-cooled Reactor Fuel Cladding, Thesis, University of Manchester, 2016.

[31] C. Phuah, Corrosion of thermally-aged advanced gas reactor fuel cladding, Thesis, University of Manchester, 2012.

[32] C. Moss, J. Sykes, Thermal sensitisation on 20%Cr/25%Ni/Nb stainless steel, in: Proceedings of the Symposium on Radiation-Induced Sensitisation of Stainless Steels, 1986: pp. 43–59.

[33] A. Al-Shater, D. Engelberg, S. Lyon, C. Donohoe, S. Walters, G. Whillock, A. Sherry, Characterization of the stress corrosion cracking behavior of thermally sensitized 20Cr-25Ni stainless steel in a simulated cooling pond environment, Journal of Nuclear Science and Technology. 54 (2017) 742–751.

[34] R.C. Lobb, Observations on the microstructure of 20Cr-25Ni-Nb stainless steel after exposure to iodine vapor during creep at 750°C, Oxidation of Metals. 15 (1981) 147–167.

[35] P.A. Tempest, R.K. Wild, Oxidation pretreatment to reduce corrosion of 20%Cr-25%Ni-Nb stainless steel. I. Weight gain and oxide thickness measurements, Oxidation of Metals. 30 (1988) 209–230.

[36] D. Powell, R. Pilkington, D. Miller, Influence of thermal ageing on creep properties of 20/25/Nb-stabilized steel, in: Proceedings of the Stainless Steels, 1985: pp. 382–390.

[37] R.C. Ecob, R.C. Lobb, V.L. Kohler, The formation of G-phase in 20/25/Nb stainless steel AGR fuel cladding alloy and its effect on creep properties, Journal of Materials Science. 22 (1987) 2867–2880.

[38] D. Powell, R. Pilkington, D. Miller, The effect of pre-strain on the creep and creep fatigue properties of a 20%Cr-25%Ni-Nb-stabilized stainless steel, in: Proceedings of the 2nd International Conference on Creep and Fracture of Engineering Materials and Structures, 1984: pp. 989–1001.

[39] Westinghouse Electric Company Brochure, Nuclear Fuel Manufacture at Springfields，Westinghouse Electric Company, (2008).

[40] T. Michler, Austenitic Stainless Steels, in: Reference Module in Materials Science and Materials Engineering, 2016.

[41] J.M. Perks, A.D. Marwick, C.A. English, A computer code to calculate radiation induced segregation in concentrated ternary alloys, UKAEA report AERE-R-12121, 1986.

[42] J.M. Perks, A.D. Marwick, C.A. English, Fundamental aspects of radiation-induced segregation in Fe-Cr-Ni alloys, in: Proceedings of the Symposium on Radiation-Induced Sensitisation of Stainless Steels, 1986: pp. 15–34.

[43] T.R. Allen, G.S. Was, Modeling radiation-induced segregation in austenitic Fe-Cr-Ni alloys, Acta Materialia. 46 (1998) 3679–3691.

[44] D. Norris, Predictions of a model for radiation-induced sensitisation of 20/25/Nb CAGR fuel pin cladding, CEGB report TPRD/B/PC/0292/M87, (AGR/FPWG/P(87)936), 1987.

[45] M. Nastar, F. Soisson, Radiation-induced segregation, Comprehensive Nuclear Materials. 1 (2012) 471–496.

[46] N.D. Authority, Review of Radiation-Induced Sensitisation of AGR Fuel Cladding, (2009) 1–22.

[47] E.A. Kenik, T. Inazumi, G.E.C. Bell, Radiation-induced grain boundary segregation and sensitization of a neutron-irradiated austenitic stainless steel, Journal of Nuclear Materials. 183 (1991) 145–153.

[48] C. Taylor, An examination of irradiated WAGR MK 2 clad fuel pins which failed during post-irradiation storage in air, UKAEA report ND-R-407(W), 1979.

[49] I. Wilson, T. Banks, Examination of CAGR fuel after storage in station pond and B27 pond, Sellafield (demineralised water), Windscale report AEA_RS_3111, 1991.

[50] C. Donohoe, D. Potter, W. Walters, Long term storage of AGR fuel in caustic-dosed pond water to inhibit corrosion, NNL (11) 11406. Issue 1., 2011.

[51] C. Taylor, D. Rhodes, An examination and assessment of WAGR fuel pins stored in the B27 pond at Windscale – UKAEA report ND-R-120(W), 1978.

[52] I. Wilson, A. King, Post-Storage Examination of Pond Stored CAGR Fuel: Progress Report on Work Carried Out at WL - UKAEA Report., 1988.

[53] D.J. Powell, R. Pilkington, D.A. Miller, The precipitation characteristics of 20% Cr/25% Ni/Nb stabilised stainless steel, Acta Metallurgica. 36 (1988) 713–724.

[54] Y. Matsukawa, T. Takeuchi, Y. Kakubo, T. Suzudo, H. Watanabe, H. Abe, T. Toyama, Y. Nagai, The two-step nucleation of G-phase in ferrite, Acta Materialia. 116 (2016) 104–113.

[55] H. Lee, K. Park, J. Lee, Y. Heo, Dissolution behaviour of NbC during slab reheating, ISIJ International. 54 (2014) 1677–1681.

[56] H.M. Chung, W.J. Shack, Irradiation-Assisted Stress Corrosion Cracking Behavior of Austenitic Stainless Steels Applicable to LWR Core Internals, 2006.

[57] K. Fukuya, Current understanding of radiation-induced degradation in light water reactor structural materials, Journal of Nuclear Science and Technology. 50 (2013) 213–254.

[58] G.S. Was, D. Farkas, I.M. Robertson, Micromechanics of dislocation channeling in intergranular stress corrosion crack nucleation, Current Opinion in Solid State and Materials Science. 16 (2012) 134–142.

[59] A. Hojná, Irradiation-assisted stress corrosion cracking and impact on life extension, in: Corrosion, 2013: pp. 964–974.

[60] G.S. Was, Fundamentals of radiation materials science: Metals and alloys, second edition, 2016.

[61] T. Miura, K. Fujii, K. Fukuya, Y. Ito, Characterization of deformation structure in ion-irradiated stainless steels, Journal of Nuclear Materials. 386–388 (2009) 210–213.

[62] G.S. Was, P. Ampornrat, G. Gupta, S. Teysseyre, E.A. West, T.R. Allen, K. Sridharan, L. Tan, Y. Chen, X. Ren, C. Pister, Corrosion and stress corrosion cracking in supercritical water, Journal of Nuclear Materials. 371 (2007) 176–201.

[63] M.G. Fontana, N.D. Greene, J. Klerer, Corrosion Engineering, Journal of The Electrochemical Society. 115 (1968) 142C.

[64] O. Okada, K. Nakata, S. Kasahara, Effects of thermal sensitization on radiation-induced segregation in type 304 stainless steel irradiated with He-ions, Journal of Nuclear Materials. 265 (1999) 232–239.

[65] R. Cowan, C. Tedmon, Intergranular Corrosion of Iron-Nickel-Chromium Alloys, Advances in Corrosion Science and Technology, vol. 3, Plenum Press, New York, 1973.

[66] R.K. Dayal, N. Parvathavarthini, B. Raj, Influence of metallurgical variables on sensitisation kinetics in austenitic stainless steels, International Materials Reviews. 50 (2005) 129–155.

[67] E.C. Bain, R.H. Aborn, J. J. Rutherford, The Nature and Prevention of Intergranular Corrosion in Austenitic Stainless Steels, Trans. Am. Soc. Steel Treating. (1933) 481–509.

[68] C. Strawstrom, M. Hillert, An improved depleted-zone theory of intergranular corrosion of 18-8 stainless steel, J. Iron Steel Inst. (1969) 77–85.

[69] L. Jinlong, L. Tongxiang, D. Limin, W. Chen, Influence of sensitization on microstructure and passive property of AISI 2205 duplex stainless steel, Corrosion Science. 104 (2016) 144–151.

[70] I. Taji, M.H. Moayed, M. Mirjalili, Correlation between sensitisation and pitting corrosion of AISI 403 martensitic stainless steel, Corrosion Science. 92 (2015) 301–308.

[71] Y. Yin, R.G. Faulkner, P. Moreton, I. Armson, P. Coyle, Grain boundary chromium depletion in austenitic alloys, Journal of Materials Science. 45 (2010) 5872–5882.

[72] S. Lin, Intergranular Corrosion of Austenitic Stainless, Applied Mechanics and Materials. 229–231 (2012) 14–17.

[73] R. Jones, V. Randle, Sensitisation behaviour of grain boundary engineered austenitic stainless steel, Materials Science and Engineering A. 527 (2010) 4275–4280.

[74] H. Sahlaoui, K. Makhlouf, H. Sidhom, J. Philibert, Effects of ageing conditions on the precipitates evolution, chromium depletion and intergranular corrosion susceptibility of AISI 316L: Experimental and modeling results, Materials Science and Engineering A. 372 (2004) 98–108.

[75] J.J. Kai, M.N. Liu, The effects of heat treatment on the carbide evolution and the chromium depletion along grain boundary of inconel 690 alloy, Scripta Metallurgica. 23 (1989) 17–22.

[76] G.S. Was, H.H. Tischner, R.M. Latanision, The influence of thermal-treatment on the chemistry and structure of grain-boundaries in Inconel 600, Metallurgical Transactions A-Physical Metallurgy and Materials Science. 12 (1981) 1397–1408.

[77] J.J. Kai, G.P. Yu, C.H. Tsai, M.N. Liu, S.C. Yao, The effects of heat treatment on the chromium depletion, precipitate evolution, and corrosion resistance of INCONEL alloy 690, Metallurgical Transactions A. 20 (1989) 2057–2067.

[78] J.J. Kai, C.H. Tsai, T.A. Huang, M.N. Liu, The effects of heat treatment on the sensitization and SCC behavior of INCONEL 600 alloy, Metallurgical Transactions A. 20 (1989) 1077–1088.

[79] Y.F. Yin, R.G. Faulkner, Model predictions of grain boundary chromium depletion in Inconel 690, Corrosion Science. 49 (2007) 2177–2197.

[80] H. Sahlaoui, H. Sidhom, J. Philibert, Prediction of chromium depleted-zone evolution during aging of Ni-Cr-Fe alloys, Acta Materialia. 50 (2002) 1383–1392.

[81] A.P. Majidi, M.A. Streicher, Four Nondestructive Electrochemical Tests for Detecting Sensitization in Type 304 and 304L Stainless Steels, Nuclear Technology. 75 (1986) 356–369.

[82] N. Lopez, M. Cid, M. Puiggali, I. Azkarate, A. Pelayo, Application of double loop electrochemical potentiodynamic reactivation test to austenitic and duplex stainless steels, Materials Science and Engineering: A. 229 (1997) 123–128.

[83] G.S. Was, V.B. Rajan, On the relationship between the epr test, sensitization, and igscc susceptibility, Corrosion. 43 (1987) 576–579.

[84] S. Rahimi, D.L. Engelberg, T.J. Marrow, A new approach for DL-EPR testing of thermo-mechanically processed austenitic stainless steel, Corrosion Science. 53 (2011) 4213–4222.

[85] T. Amadou, H. Sidhom, C. Braham, Double loop electrochemical potentiokinetic reactivation test optimization in checking of duplex stainless steel intergranular corrosion susceptibility, Metallurgical and Materials Transactions A. 35 (2004) 3499–3513.

[86] X.R. Qian, Y.T. Chou, Correlation between grain boundary corrosion and grain boundary energy in niobium bicrystals, Philosophical Magazine A: Physics of Condensed Matter, Structure, Defects and Mechanical Properties. 45 (1982) 1075–1079.

[87] G. Palumbo, K.T. Aust, Structure-dependence of intergranular corrosion in high purity nickel, Acta Metallurgica Et Materialia. 38 (1990) 2343–2352.

[88] H. Kokawa, M. Shimada, Y.S. Sato, Grain-boundary structure and precipitation in sensitized austenitic stainless steel, JOM. 52 (2000) 34–37.

[89] V. Randle, G. Owen, Mechanisms of grain boundary engineering, Acta Materialia. 54 (2006) 1777–1783.

[90] C. Cheung, U. Erb, G. Palumbo, Application of grain boundary engineering concepts to alleviate intergranular cracking in Alloys 600 and 690, Materials

Science and Engineering A. 185 (1994) 39–43.

[91] S. Spigarelli, M. Cabibbo, E. Evangelista, G. Palumbo, Analysis of the creep strength of a low-carbon AISI 304 steel with low-Σ grain boundaries, Materials Science and Engineering A. 352 (2003) 93–99.

[92] M. Michiuchi, H. Kokawa, Z.J. Wang, Y.S. Sato, K. Sakai, Twin-induced grain boundary engineering for 316 austenitic stainless steel, Acta Materialia. 54 (2006) 5179–5184.

[93] M. Shimada, H. Kokawa, Z.J. Wang, Y.S. Sato, I. Karibe, Optimization of grain boundary character distribution for intergranular corrosion resistant 304 stainless steel by twin-induced grain boundary engineering, in: Acta Materialia, 2002: pp. 2331–2341.

[94] P. Ahmedabadi, V. Kain, M. Gupta, I. Samajdar, S.C. Sharma, P. Bhagwat, R. Chowdhury, The role of niobium carbide in radiation induced segregation behaviour of type 347 austenitic stainless steel, Journal of Nuclear Materials. 415 (2011) 123–131.

[95] H. Wiedersich, P.R. Okamoto, N.Q. Lam, A theory of radiation-induced segregation in concentrated alloys, Journal of Nuclear Materials. 83 (1979) 98–108.

[96] R. Boothby, Review of reactor-induced sensitisation of AGR fuel cladding, NNL report, 2009.

[97] E.P. Simonen, L.A. Charlot, S.M. Bruemmer, Quantification of defect-solute coupling from inverse-Kirkendall segregation, Journal of Nuclear Materials. 225 (1995) 117–122.

[98] J.P. Wharry, G.S. Was, The mechanism of radiation-induced segregation in ferritic-martensitic alloys, Acta Materialia. 65 (2014) 42–55.

[99] Z. Lu, R.G. Faulkner, G. Was, B.D. Wirth, Irradiation-induced grain boundary chromium microchemistry in high alloy ferritic steels, Scripta Materialia. 58 (2008) 878–881.

[100] J.P. Wharry, G.S. Was, A systematic study of radiation-induced segregation in ferritic-martensitic alloys, Journal of Nuclear Materials. 442 (2013) 7–16.

[101] S.M. Bruemmer, E.P. Simonen, P.M. Scott, P.L. Andresen, G.S. Was, J.L. Nelson, Radiation-induced material changes and susceptibility to intergranular failure of light-water-reactor core internals, Journal of Nuclear Materials. 274 (1999) 299–314.

[102] M.S. Laws, P.J. Goodhew, Grain boundary structure and chromium segregation in a 316 stainless steel, Acta Metallurgica et Materialia. 39 (1991) 1525–1533.

[103] N. Sakaguchi, M. Endo, S. Watanabe, H. Kinoshita, S. Yamashita, H. Kokawa, Radiation-induced segregation and corrosion behavior on Σ3 coincidence site lattice and random grain boundaries in proton-irradiated type-316L austenitic stainless steel, Journal of Nuclear Materials. 434 (2013) 65–71.

[104] S.K. Mannan, R.K. Dayal, M. Vijayalakshmi, N. Parvathavarthini, Influence of deformation on sensitization kinetics and its microstructural correlation in a nuclear grade 316 stainless steel, Journal of Nuclear Materials. 126 (1984) 1–8.

[105] C.S. Tedmon, D.A. Vermilyea, D.E. Broecker, Technical note Effect of cold work on intergranular corrosion of sensitized stainless steel, Corrosion. 27 (1971) 104–106.

[106] R. Pascali, A. Benvenuti, D. Wenger, Carbon content and grain size effects on the sensitization of AISI type 304 stainless steels, Corrosion. 40 (1984) 21–32.

[107] R. Beltran, J.G. Maldonado, L.E. Murr, W.W. Fisher, Effects of strain and grain size on carbide precipitation and corrosion sensitization behavior in 304 stainless steel, Acta Materialia. 45 (1997) 4351–4360.

[108] A.H. Advani, D.G. Atteridge, L.E. Murr, S.M. Bruemmer, R. Chelakara, Deformation effects on chromium diffusivity and grain boundary chromium depletion development in type 316 stainless steels, Scripta Metallurgica et Materiala. 25 (1991) 461–465.

[109] P.M. Ahmedabadi, V. Kain, B.K. Dangi, I. Samajdar, Role of grain boundary nature and residual strain in controlling sensitisation of type 304 stainless steel, Corrosion Science. 66 (2013) 242–255.

[110] E.A. Trillo, R. Beltran, J.G. Maldonado, R.J. Romero, L.E. Murr, W.W. Fisher, A.H. Advani, Combined effects of deformation (strain and strain state), grain size, and carbon content on carbide precipitation and corrosion sensitization in 304 stainless steel, Materials Characterization. 35 (1995) 99–112.

[111] H.E. Evans, D.A. Hilton, R.A. Holm, S.J. Webster, Influence of silicon additions on the oxidation resistance of a stainless steel, Oxidation of Metals. 19 (1983) 1–18.

[112] T.D. Nguyen, J. Zhang, D.J. Young, Effects of silicon on high temperature corrosion of Fe-Cr and Fe-Cr-Ni alloys in carbon dioxide, Oxidation of Metals. 81 (2014) 549–574.

[113] A.M. Emsley, M.P. Hill, Intergranular oxidation of silicon in 20Cr-25Ni niobium-stabilized stainless steel at 1140-1230 K, Oxidation of Metals. 34 (1990) 351–360.

[114] B.E. Wilde, Influence of silicon on the intergranular corrosion behavior of 18Cr-8Ni stainless steels, Corrosion. 44 (1988) 699–704.

[115] J.S. Armijo, B.E. Wilde, Influence of Si content on the corrosion resistance of austenitic Fe-Cr-Ni alloys in oxidizing acids, Corrosion Science. 8 (1968) 649–664.

[116] R. Robin, F. Miserque, V. Spagnol, Correlation between composition of passive layer and corrosion behavior of high Si-containing austenitic stainless steels in nitric acid, Journal of Nuclear Materials. 375 (2008) 65–71.

[117] P.L. Andresen, P.H. Chou, M.M. Morra, J.L. Nelson, R.B. Rebak, Microstructural and Stress Corrosion Cracking Characteristics of Austenitic Stainless Steels Containing Silicon, Metallurgical and Materials Transactions A. 40 (2009) 2824–

2836.

[118] P.H. Chou, P.L. Andresen, M.L. Pollick, R.B. Rebak, Repassivation behavior and stress corrosion cracking susceptibility of stainless steels containing silicon, NACE - International Corrosion Conference Series. (2010).

[119] G.F. Li, Y.F. Kaneshima, T. Shoji, Effects of impurities on environmentally assisted crack growth of solution-annealed austenitic steels in primary water at 325°C, Corrosion. 56 (2000) 460–469.

[120] P.L. Andresen, Factors Influencing SCC and IASCC of Stainless Steels in High Temperature Water, in: Proceedings of the American Society of Mechanical Engineers - ASME, Pressure Vessels and Piping Division Conference, 2004: pp. 185–192.

[121] P.L. Andresen, M.M. Morra, Effects of Si on SCC of Irradiated and Unirradiated Stainless Steel and Nickel Alloys, in: Proceedings of the 12th International Environmental Degradation of Materials in Nuclear Power System- Water Reactors-, 2005: pp. 87–108.

[122] H. Kajimura, N. Usuki, H. Nagano, Dual layer corrosion protective film formed on Si bearing austenitic stainless steel in highly oxidizing nitric acid, in: Symposium on Passivity and Its Breakdown, 1997: pp. 332–343.

[123] O. V. Kasparova, Peculiarities of intergranular corrosion of silicon-containing austenitic stainless steels, Protection of Metals. 40 (2004) 425–431.

[124] B. Laurent, N. Gruet, B. Gwinner, F. Miserque, M. Tabarant, K. Ogle, A Direct Measurement of the Activation Potential of Stainless Steels in Nitric Acid, Journal of The Electrochemical Society. 164 (2017) C481–C487.

[125] B. Laurent, N. Gruet, B. Gwinner, F. Miserque, K. Rousseau, K. Ogle, The kinetics of transpassive dissolution chemistry of stainless steels in nitric acid: The impact of Si, Electrochimica Acta. 258 (2017) 653–661.

[126] A. Desestret, M. Froment, P. Guiraldenq, Application des Radioéléments à l'étude de l'influence du silicium sur quelques propriétés des joints de grains d'aciers inoxydables austénitiques, Mém. Sci. Rev. Métall. (F). 66 (1969) 389–405.

[127] B. Laurent, N. Gruet, B. Gwinner, F. Miserque, K. Rousseau, K. Ogle, Dissolution and Passivation of a Silicon-Rich Austenitic Stainless Steel during Active-Passive Cycles in Sulfuric and Nitric Acid, Journal of The Electrochemical Society. 164 (2017) C892–C900.

[128] B. Esmailzadeh, A. Kumar, F.A. Garner, The influence of silicon on void nucleation in irradiated alloys, Journal of Nuclear Materials. 133–134 (1985) 590–593.

[129] G. Mahon, A. Nichols, I. Jones, C. English, T. Williams, Radiation-induced segregation in ferritic steels, in: Proceedings of the Symposium on Radiation-Induced Sensitisation of Stainless Steels, 1986: pp. 99–115.

[130] H.W. Allison, H. Samelson, Diffusion of aluminum, magnesium, silicon, and zirconium in nickel, Journal of Applied Physics. 30 (1959) 1419–1424.

[131] R.A. Swalin, A. Martin, R. Olson, Diffusion of magneisum, silicon, and molybdenum in nickel, Journal of Metals. 9 (1957) 936–939.

[132] G.R. Johnston, Diffusion of chromium and silicon in nickel solid-solution alloys of the ni-cr-si system, High Temperatures - High Pressures. 14 (1981) 695–707.

[133] W. Assassa, P. Guiraldenq, Bulk and grain boundary diffusion of 59Fe, 51Cr, and 63Ni in austenitic stainless steel under influence of silicon content, Metal Science. 12 (1978) 123–128.

[134] F.A. Garner, W.G. Wolfer, The effect of solute additions on void nucleation, Journal of Nuclear Materials. 102 (1981) 143–150.

[135] J. Katz, H. Wiedersich, Nucleation of voids in materials supersaturated with vacancies and interstitials, Journal of Chemical Physics. 55 (1971) 1414.

[136] K.C. Russell, Nucleation of voids in irradiated metals. II. The general case, Scripta Metallurgica. 6 (1972) 209–214.

[137] B. Esmailzadeh, A.S. Kumar, Influence of composition on steady state void nucleation in irradiated alloys, in: Effects of Radiation on Materials : 12th International Symposium, ASTM STP 870, 1985: pp. 468–480.

[138] D. Wolf, J.F. Lutsko, On the geometrical relationship between tilt and twist grain boundaries, Zeitschrift Fur Kristallographie - New Crystal Structures. 189 (1989) 239–262.

[139] D. McLean, Grain boundaries in metals, Clarendon Press, Oxford, 1957.

[140] V. V. Bulatov, B.W. Reed, M. Kumar, Grain boundary energy function for fcc metals, Acta Materialia. 65 (2014) 161–175.

[141] F.J. Humphreys, M. Hatherly, The structure and energy of grain boundaries, in: Recrystallization and Related Annealing Phenomena, 1995: pp. 57–83.

[142] A. Sutton, R. Balluffi, Interfaces in Crystalline Materials Clarendon, 1995.

[143] J.M. Burgers, Geometrical considerations concerning the structural irregularities to be assumed in a crystal, Proceedings of the Physical Society. 52 (1940) 23–33.

[144] G.I. Taylor, The Mechanism of Plastic Deformation of Crystals. Part I. Theoretical, Proceedings of the Royal Society A: Mathematical, Physical and Engineering Sciences. 145 (1934) 362–387.

[145] M.E. Glicksman, C.L. Vold, Heterophase dislocations - An approach towards interpreting high temperature grain boundary behavior, Surface Science. 31 (1972) 50–67.

[146] P. Lejček, Grain Boundaries: Description, Structure and Thermodynamics BT - Grain Boundary Segregation in Metals, in: Grain Boundary Segregation in Metals, 2010: pp. 5–24.

[147] P.H. Pumphrey, G.A. Chadwick, D.A. Smith, Grain boundary structure and properties, Academic Press, London, 1976.

[148] D.G. Brandon, B. Ralph, S. Ranganathan, M.S. Wald, A field ion microscope

study of atomic configuration at grain boundaries, Acta Metallurgica. 12 (1964) 813–821.

[149] R.C. Newman, K. Sieradzki, H.S. Isaacs, Stress-corrosion cracking of sensitized type 304 stainless steel in thiosulfate solutions, Metallurgical Transactions A. 13 (1982) 2015–2026.

[150] H.Y. Bi, H. Kokawa, Z.J. Wang, M. Shimada, Y.S. Sato, Suppression of chromium depletion by grain boundary structural change during twin-induced grain boundary engineering of 304 stainless steel, Scripta Materialia. 49 (2003) 219–223.

[151] E.A. West, G.S. Was, IGSCC of grain boundary engineered 316L and 690 in supercritical water, Journal of Nuclear Materials. 392 (2009) 264–271.

[152] S. Rahimi, D.L. Engelberg, J.A. Duff, T.J. Marrow, In situ observation of intergranular crack nucleation in a grain boundary controlled austenitic stainless steel, Journal of Microscopy. 233 (2009) 423–431.

[153] C. Hu, S. Xia, H. Li, T. Liu, B. Zhou, W. Chen, N. Wang, Improving the intergranular corrosion resistance of 304 stainless steel by grain boundary network control, Corrosion Science. 53 (2011) 1880–1886.

[154] E.P. Butler, M.G. Burke, Chromium depletion and martensite formation at grain boundaries in sensitised austenitic stainless steel, Acta Metallurgica. 34 (1986) 557–570.

[155] B. Weiss, R. Stickler, Phase instabilities during high temperature exposure of 316 austenitic stainless steel, Metallurgical Transactions. 3 (1972) 851–866.

[156] T.S. Duh, J.J. Kai, F.R. Chen, Effects of grain boundary misorientation on solute segregation in thermally sensitized and proton-irradiated 304 stainless steel, Journal of Nuclear Materials. 283–287 (2000) 198–204.

[157] J.J. Kai, F.R. Chen, T.S. Duh, Effects of Grain Boundary Misorientation on Radiation-Induced Solute Segregation in Proton Irradiated 304 Stainless Steels, Materials Transactions. 45 (2004) 40–50.

[158] S. Watanabe, Y. Takamatsu, N. Sakaguchi, H. Takahashi, Sink effect of grain boundary on radiation-induced segregation in austenitic stainless steel, Journal of Nuclear Materials. 283–287 (2000) 152–156.

[159] C.M. Barr, G.A. Vetterick, K.A. Unocic, K. Hattar, X.M. Bai, M.L. Taheri, Anisotropic radiation-induced segregation in 316L austenitic stainless steel with grain boundary character, Acta Materialia. 67 (2014) 145–155.

[160] G.G. Lee, H.H. Jin, Y.B. Lee, J. Kwon, Observation and rate theory modeling of grain boundary segregation in Σ3 twin boundaries in ion-irradiated stainless steel 316, Journal of Nuclear Materials. 449 (2014) 234–241.

[161] C.M. Barr, L. Barnard, J.E. Nathaniel, K. Hattar, K.A. Unocic, I. Szlurfarska, D. Morgan, M.L. Taheri, Grain boundary character dependence of radiation-induced segregation in a model Ni-Cr alloy, Journal of Materials Research. 30 (2015) 1290–1299.

[162] C.A. Hampel, Rare Metals Handbook, 2nd edition, 1961.

[163] C.M. Parish, K.G. Field, A.G. Certain, J.P. Wharry, Application of STEM characterization for investigating radiation effects in BCC Fe-based alloys, Journal of Materials Research. 30 (2015) 1275–1289.

[164] J.M. Titchmarsh, I.A. Vatter, Measurement of radiation induced segregation profiles by high spatial resolution electron microscopy, in: Proceedings of the Symposium on Radiation-Induced Sensitisation of Stainless Steels, 1986: pp. 74–85.

[165] T.F. Kelly, M.K. Miller, Atom probe tomography, Review of Scientific Instruments. 78 (2007) 31101–44904.

[166] E.A. Marquis, Atom probe tomography applied to the analysis of irradiated microstructures, Journal of Materials Research. 30 (2015) 1222–1230.

[167] M. Herbig, M. Kuzmina, C. Haase, R.K.W. Marceau, I. Gutierrez-Urrutia, D. Haley, D.A. Molodov, P. Choi, D. Raabe, Grain boundary segregation in Fe-Mn-C twinning-induced plasticity steels studied by correlative electron backscatter diffraction and atom probe tomography, Acta Materialia. 83 (2015) 37–47.

[168] S. Mandal, K.G. Pradeep, S. Zaefferer, D. Raabe, A novel approach to measure grain boundary segregation in bulk polycrystalline materials in dependence of the boundaries' five rotational degrees of freedom, Scripta Materialia. 81 (2014) 16–19.

[169] M. Herbig, D. Raabe, Y.J. Li, P. Choi, S. Zaefferer, S. Goto, Atomic-scale quantification of grain boundary segregation in nanocrystalline material, Physical Review Letters. 112 (2013) 126103.

[170] T. Toyama, Y. Nozawa, W. Van Renterghem, Y. Matsukawa, M. Hatakeyama, Y. Nagai, A. Al Mazouzi, S. Van Dyck, Grain boundary segregation in neutron-irradiated 304 stainless steel studied by atom probe tomography, Journal of Nuclear Materials. 425 (2012) 71–75.

[171] Standard Practices for Detecting Susceptibility to Intergranular Attack in Austenitic Stainless Steels, A262-14, ASTM Publications, 2015.

[172] ASTM G108-94: Standard Test Method for Electrochemical Reactivation (EPR) for Detecting Sensitization of AISI Type 304 and 304L Stainless Steels, ASTM Standards. (2010).

[173] S. Frangini, A. Mignone, Modified Electrochemical Potentiokinetic Reactivation Method for Detecting Sensitization in 12 wt% Cr Ferritic Stainless Steels, Corrosion. 48 (1992) 715–726.

[174] G.H. Aydoğdu, M.K. Aydinol, Determination of susceptibility to intergranular corrosion and electrochemical reactivation behaviour of AISI 316L type stainless steel, Corrosion Science. 48 (2006) 3565–3583.

[175] V. Cihal, R. Stefec, T. Shoji, Y. Watanabe, V. Kain, Electrochemical potentiodynamic reactivation: development and applications of the EPR test., Key Engineering Materials. 261–263 (2004) 855–864.

[176] H. Sidhom, T. Amadou, C. Braham, Evaluation by the double loop electrochemical potentiokinetic reactivation test of aged ferritic stainless steel intergranular corrosion susceptibility, Metallurgical and Materials Transactions A: Physical Metallurgy and Materials Science. 41 (2010) 3136–3150.

[177] S. Haupt, H.H. Strehblow, A combined surface analytical and electrochemical study of the formation of passive layers on Fe Cr alloys in 0.5 M H2SO4, Corrosion Science. 37 (1995) 43–54.

[178] V. Kain, Y. Watanabe, Development of a single loop EPR test method and its relation to grain boundary microchemistry for alloy 600, Journal of Nuclear Materials. 302 (2002) 49–59.

[179] B.W. Bennett, H.W. Pickering, Effect of grain boundary structure on sensitization and corrosion of stainless steel, Metallurgical Transactions A. 18 (1991) 1117–1124.

[180] C. Hu, S. Xia, H. Li, T. Liu, B. Zhou, W. Chen, N. Wang, Improving the intergranular corrosion resistance of 304 stainless steel by grain boundary network control, Corrosion Science. 53 (2011) 1880–1886.

[181] S. Suzuki, Features of transmission EBSD and its application, JOM. 65 (2013) 1254–1263.

[182] R.R. Keller, R.H. Geiss, Transmission EBSD from 10 nm domains in a scanning electron microscope, Journal of Microscopy. 245 (2012) 245–251.

[183] J. Wu, Microstructure and Mechanical Properties of Mg-Zn-(Y/Gd) alloys, PhD thesis, University of Birmingham, 2016.

[184] ISO, Steels — Micrographic Determination of the Apparent Grain Size, (2003).

[185] E. Khzouz, Grain Growth Kinetics in Steels, Report, 2011.

[186] J.M. Silcock, W.J. Tunstall, Partial dislocations associated with NbC precipitation in austenitic stainless steels, Philosophical Magazine. 10 (1964) 361–389.

[187] A.R. Jones, P.R. Howell, B. Ralph, The precipitation of niobium carbide at grain boundaries in an austenitic stainless steel, Journal of Materials Science. 11 (1976) 1593–1599.

[188] E.A. Trillo, L.E. Murr, A TEM investigation of $M_{23}C_6$ carbide precipitation behaviour on varying grain boundary misorientations in 304 stainless steels, Journal of Materials Science. 33 (1998) 1263–1271.

[189] J.M. Vitek, G-Phase Formation in Aged Type 308 Stainless Steel, Metallurgical Transactions A. 18 (1987) 154–156.

[190] Y. Matsukawa, T. Takeuchi, Y. Kakubo, T. Suzudo, H. Watanabe, H. Abe, T. Toyama, Y. Nagai, The two-step nucleation of G-phase in ferrite, Acta Materialia. 116 (2016) 104–113.

[191] M. Yang, C. Wang, S. Yang, Z. Shi, X. Liu, New insights into the precipitation strengthening of ferritic steels: Nanoscale G-phase particle, Materials Letters. 209 (2017) 134–137.

[192] W.W. Sun, R.K.W. Marceau, M.J. Styles, D. Barbier, C.R. Hutchinson, G phase precipitation and strengthening in ultra-high strength ferritic steels: Towards lean "maraging" metallurgy, Acta Materialia. 130 (2017) 28–46.

[193] M. Mizouchi, Y. Yamazaki, Y. Iijima, K. Arioka, Low temperature grain boundary diffusion of chromium in SUS316 and 316L stainless steels, Materials Transactions. 45 (2004) 2945–2950.

[194] P.L. Gruzin, Self-diffusion in gamma iron, Dokl. Akad. Nauk S.S.S.R. 86 (1952) 289.

[195] F.S. Buffington, K. Hirano, M. Cohen, Self diffusion in iron, Acta Metallurgica. 9 (1961) 434–439.

[196] J.P. Adamson, J.W. Martin, The nucleation of $M_{23}C_6$ carbide particles in the grain boundaries of an austenitic stainless steel, Acta Metallurgica. 19 (1971) 1015–1018.

[197] M. Ochi, R. Kawano, T. Maeda, Y. Sato, R. Teranishi, T. Hara, M. Kikuchi, K. Kaneko, Three-dimensional studies of intergranular carbides in austenitic stainless steel, Microscopy. 66 (2017) 89–94.

[198] Marshall，P, Austenitic stainless steels: microstructure and mechanical properties, in: Elsevier Applied Science Publishers, London, 1984: pp. 31–55.

[199] L. Lapeire, E. Martinez Lombardia, K. Verbeken, I. De Graeve, L.A.I. Kestens, H. Terryn, Effect of neighboring grains on the microscopic corrosion behavior of a grain in polycrystalline copper, Corrosion Science. 67 (2013) 179–183.

[200] P.G. Ulyanov, D.Y. Usachov, A. V. Fedorov, A.S. Bondarenko, B. V. Senkovskiy, O.F. Vyvenko, S. V. Pushko, K.S. Balizh, A.A. Maltcev, K.I. Borygina, A.M. Dobrotvorskii, V.K. Adamchuk, Microscopy of carbon steels: Combined AFM and EBSD study, Applied Surface Science. 267 (2013) 216–218.

[201] S. Wang, J. Wang, Effect of grain orientation on the corrosion behavior of polycrystalline Alloy 690, Corrosion Science. 85 (2014) 183–192.

[202] D.J. Horton, A.W. Zhu, J.R. Scully, M. Neurock, Crystallographic controlled dissolution and surface faceting in disordered face-centered cubic FePd, MRS Communications. 4 (2014) 1–7.

[203] D.G. Brandon, The structure of high-angle grain boundaries.pdf, Acta Metallurgica. 14 (1966) 1479–1484.

[204] M. Winning, A.D. Rollett, Transition between low and high angle grain boundaries, Acta Materialia. 53 (2005) 2901–2907.

[205] J.K. Lee, H.I. Aaronson, Influence of faceting upon the equilibrium shape of nuclei at grain boundaries-II. Three-dimensions, Acta Metallurgica. 23 (1975) 809–820.

[206] R. Hu, G. Bai, J. Li, J. Zhang, T. Zhang, H. Fu, Precipitation behavior of grain boundary $M_{23}C_6$ and its effect on tensile properties of Ni-Cr-W based superalloy, Materials Science and Engineering A. 548 (2012) 83–88.